DESIGN AND FABRICATION OF FLUORESCENT PROBES FOR BIOMEDICAL APPLICATIONS: POTENTIAL TOOL FOR *IN VITRO* AND *IN VIVO* BIOIMAGING, SENSING AND siRNA DELIVERY FOR CANCER THERAPY

HEMA SANTHAKUMAR

PhD THESIS

2021

SREE CHITRA TIRUNAL INSTITUTE FOR
MEDICAL SCIENCES AND TECHNOLOGY,
THIRUVANANTHAPURAM

DESIGN AND FABRICATION OF FLUORESCENT PROBES FOR BIOMEDICAL APPLICATIONS: POTENTIAL TOOL FOR *IN VITRO* AND *IN VIVO* BIOIMAGING, SENSING AND siRNA DELIVERY FOR CANCER THERAPY

A THESIS PRESENTED BY

HEMA SANTHAKUMAR

TO

THE SREE CHITRA TIRUNAL INSTITUTE FOR MEDICAL
SCIENCES AND TECHNOLOGY, THIRUVANANTHAPURAM

IN PARTIAL FULFILMENT OF THE REQUIREMENTS
FOR THE AWARD OF
DOCTOR OF PHILOSOPHY

2021

CERTIFICATE

I, **Hema Santhakumar**, hereby certify that I had personally carried out the work depicted in the thesis entitled "**Design and fabrication of fluorescent probes for biomedical applications: potential tool for *in vitro* and *in vivo* bioimaging, sensing and siRNA delivery for cancer therapy**". No part of the thesis contains any matter previously published or written by another person, nor any material that has been submitted for the award of any other degree or diploma of any University or Institute of higher learning, except where due acknowledgment has been made in the text.

Signature

Name: Hema Santhakumar

Registration no: 2015/PhD/07

Place: Thiruvananthapuram

Date: 09.11.2021

Dr. R. S. Jayasree
Division of Biophotonics and Imaging
Department of Biomaterial Sciences and Technology
BMT Wing, SCTIMST

This is to certify that **Ms. Hema Santhakumar**, in the Division of Biophotonics and Imaging of this Institute has fulfilled the requirements prescribed for the PhD degree of the Sree Chitra Tirunal Institute for Medical Sciences and Technology, Thiruvananthapuram.

The thesis entitled, "**Design and fabrication of fluorescent probes for biomedical applications: potential tool for *in vitro* and *in vivo* bioimaging, sensing and siRNA delivery for cancer therapy**" was carried out under my direct supervision. No part of the thesis was submitted for the award of any degree or diploma prior to this date.

*Clearance was obtained from the Institutional Ethics Committee/ Institutional Animal Ethics Committee for carrying out the study.

Date: 09.11.2021

Dr. R.S. Jayasree
(Research Supervisor)

The thesis entitled

DESIGN AND FABRICATION OF FLUORESCENT PROBES FOR BIOMEDICAL APPLICATIONS: POTENTIAL TOOL FOR *IN VITRO* AND *IN VIVO* BIOIMAGING, SENSING AND siRNA DELIVERY FOR CANCER THERAPY

Submitted by

HEMA SANTHAKUMAR

For the degree of

Doctor of Philosophy

of

SREE CHITRA TIRUNAL INSTITUTE FOR
MEDICAL SCIENCES AND TECHNOLOGY,
Thiruvananthapuram

Is evaluated and approved by

09/11/21

Dr. R. S. Jayasree
(SCTIMST, Trivandrum)
....
Name of the guide

Prof. Amit Kumar Dinda
(AIIMS, New Delhi)
....
Name of thesis examiner

ACKNOWLEDGEMENTS

I owe my deep sense of gratitude to my beloved father Mr. S. Santhakumar, my mother Mrs. S. Maheswari and my sister Mrs. S. Syama for their affection, patience and support, which smoothly paved the path towards the successful completion of the work.

I owe my sincere gratitude to The Director, SCTIMST and Head BMT Wing for providing all the facilities during the course of my PhD work. I extend my thanks to Dean, Associate Dean (PhD affairs), Registrar, Deputy Registrar and all members of academic division and Director's office for their support and help.

I would like to express my sincere gratitude to my research guide, Dr. R. S. Jayasree for her continuous support and valuable suggestions during the entire course of my PhD work. I am thankful to her for all the moral support she has given me throughout my days in the lab.

I am extremely thankful to my doctoral advisory committee members, Dr. Anoopkumar Thekkuveettil, Dr. T.R. Santhosh Kumar and Dr. P.R. Anil Kumar for their suggestions and critical comments. I am grateful to the Department of Biotechnology, New Delhi for the Junior Research Fellowship and Senior Research Fellowship and SCTIMST, Trivandrum for the financial support.

I thank Dr. A. Ajayaghosh, Director, CSIR-NIIST, Trivandrum and his team member Dr. Divya Philips for the help and suggestions in molecular probe work. I also extend my sincere thanks to Dr. K. K. Maiti for providing SERS facility, Dr. Saju Pillai for XPS analysis, Dr. Karunakaran Venugopal for lifetime measurements.

I thank Dr. Reji Varghese, IISER-TVM for extending HR-TEM facility.

I sincerely acknowledge Dr. Sachin J Shenoy, Mr. Manoj, Mr. Anoop and Mr. Sunil of DLAS for helping me in animal experiments. I thank Dr. Maya Nandkumar, Mr. Pradeepkumar, Keerthi S Varier and Amalu Navas of MIC for the help in using microplate reader. I sincerely thank Dr. Anoopkumar T, Dr. Pradeep Punnakal and *all students of MOM for providing vibratome and lab facility. I am grateful to Dr. Rekha M R, BST for the moral support and Zeta size analyzer facility. I thank Dr. Prabha D Nair for extending the facility of fluorescence spectrometer. I thank Dr. Roy Joseph, Dr. Sunitha and Dr. Renjith P for fluorescence spectrometer and LC-MS facility. I thank Dr. Manoj Komath and Ms. Susan Mani for TEM facility. I thank Dr. Lizymol PP and Ms. Dhanya for Zeta size analyzer facility. I thank Dr. Anugya Bhatt for plate reader facility. I thank Mr. Willi Paul for the SERS studies in hippocampal slices.*

I extend my gratitude to Mr. Sanal Das, Olympus for the help in microscopy.

My sincere thanks also goes to former and present fellows at Division of Biophotonics and Imaging, Dr. Ariya Saraswathy, Dr. Shaiju S Nazeer, Dr. Lakshmi V Nair, Dr. Parvathy RS, Dr. Resmi V Nair, Dr. Jibin K, Dr. Rekha CR, Ms. Shania, Ms. Nimi, Ms. Nisha, Ms. Marina, Mr. Jayaram, Ms. Renuka, Ms. Dhanya, Ms Resmi AN, Ms. Rinta, Mr. Jijo, Mr. Sarath, Mr. Dhushyanthan, and Ms. Anjana. I also thank all staff of BMT Wing, who directly or indirectly helped me for my PhD program. The help from the divisions of accounts, store and library is greatly acknowledged. I also thank the security staff for their kind support.

TABLE OF CONTENTS

Declaration by student....................i
Certificate of guide....................ii
Approval of thesis....................iii
Acknowledgements....................iv
Table of contents....................vi
List of figures....................xi
List of tables....................xvii
Abbreviations....................xviii
Synopsis....................xxi
1. Introduction....................1
  1.1. Fluorescence imaging....................2
  1.2. Fluorescent probes for biomedical applications....................4
  1.3. Fluorescent probes for biosensing....................5
    1.3.1. Mechanisms of fluorescent probes for sensing....................5
    1.3.2. Fluorescent probes for ion sensing....................9
  1.4. Fluorescent probes for bioimaging....................9
    1.4.1. Fluorescent nanoprobes for bioimaging....................10
    1.4.2. Fluorescent gold nanoclusters....................11
    1.4.3. Fluorescence mechanism of gold nanoclusters....................13
  1.5. Fluorescent nanoprobes for cancer therapy....................14
    1.5.1. Cancer and apoptosis....................14
    1.5.2. Photodynamic therapy....................16
      1.5.2.1. Nanoparticle based PDT....................17
    1.5.3. Gene therapy....................18
      1.5.3.1. Mechanism of RNA interference....................19
      1.5.3.2. Advantages of RNA interference....................21
      1.5.3.3. Barriers to siRNA delivery....................22
  1.6. Hypothesis....................24
  1.7. Objectives....................24
2. Literature Review....................25
  2.1. Fluorescent molecular probe for zinc ion sensing....................26
    2.1.1. Importance of Zn^{2+} *sensing*....................26
      2.1.1.1. Zn^{2+} in human body....................26
      2.1.1.2. Zn^{2+} in brain....................27
      2.1.1.3. Zn^{2+} in diseases....................27
    2.1.2. Fluorescent probes for Zn^{2+} *sensing*....................28
      2.1.2.1. Optical methods of Zn^{2+} sensing....................28
      2.1.2.2. Fluorescent probes for Zn^{2+} sensing....................29
    2.1.3. Ratiometric probes and imaging....................30
  2.2. Fluorescent nanoprobe for cancer imaging and therapy....................34
    2.2.1. Gold based fluorescent nanoprobes....................34
    2.2.2. Fluorescence enhancement in metal nanoclusters....................35
    2.2.3. Peptide stabilized Gold nanoclusters....................37
    2.2.4. Gold nanoclusters for bioimaging and cancer therapy....................40

2.3. Fluorescent nano gene downregulator for cancer imaging cum therapy 43
    - *2.3.1. Genes upregulated in cancer* 43
    - *2.3.2. siRNA delivery for cancer* 44
    - *2.3.3. Nanoparticles for siRNA delivery* 45
    - *2.3.4. Gold nanoclusters for siRNA delivery* 48

3. Materials and Methods 50
  - 3.1. Fluorescent molecular probe for zinc ion sensing 51
    - *3.1.1. Chemicals* 51
    - *3.1.2. Imaging system and Instrumentation* 51
    - *3.1.3. Synthesis and characterization of molecular probe* 52
    - *3.1.4. In vitro studies* 52
      - 3.1.4.1. Cell culture 52
      - 3.1.4.2. Cytocompatibility study 53
      - 3.1.4.3. Cellular imaging and Zn^{2+} sensing 53
      - 3.1.4.4. Hippocampal slice preparation 53
      - 3.1.4.5. Zn^{2+} sensing in acute hippocampal slices 54
      - 3.1.4.6. Induction of epileptic condition *in vitro* 55
      - 3.1.4.7. Zn^{2+} sensing in hippocampal slice using Raman Spectroscopy 55
      - 3.1.4.8. Ratiometric imaging 56
    - *3.1.5. In vivo studies* 56
      - 3.1.5.1. Quantification of Zn^{2+} in rat brain 57
      - 3.1.5.2. Establishing epilepsy rat model 57
      - 3.1.5.3. Intra-carotid artery infusion, Hyperosmolar BBB disruption 58
      - 3.1.5.4. *In vivo* Zn^{2+} imaging 59
  - 3.2. Fluorescent nano probe for cancer imaging and therapy 59
    - *3.2.1. Chemicals and Reagents* 59
    - *3.2.2. Synthesis and characterization of tripeptides* 60
    - *3.2.3. Synthesis of tripeptide-gold nanoclusters* 62
    - *3.2.4. Characterization of tripeptide-gold nanoclusters* 63
    - *3.2.5. In vitro cell studies* 65
      - 3.2.5.1. Cell culture 65
      - 3.2.5.2. Cytocompatibility study 65
      - 3.2.5.3. Cellular uptake and accumulation study 66
      - 3.2.5.4. Analysis of intracellular ROS level 67
      - 3.2.5.5. Mitochondrial membrane potential (ΔΨm) analysis 67
      - 3.2.5.6. Analysis of cell death 68
    - *3.2.6. Statistical analysis* 69
  - 3.3. Fluorescent nano gene downregulator for cancer imaging cum therapy 69
    - *3.3.1. Chemicals and Reagents* 69
    - *3.3.2. Construction of fluorescent nano gene downregulator and its characterization* 70
    - *3.3.3. Synthesis and characterization of oligopeptides* 70
    - *3.3.4. Synthesis of oligopeptide-gold nanoclusters* 72
    - *3.3.5. Characterization of oligopeptide-gold nanoclusters* 73
    - *3.3.6. In vitro cell studies* 74
      - 3.3.6.1. Cell culture 74

3.2.6.2. *In vitro* cytocompatibility study............................75
3.2.6.3. Cellular uptake study..75
3.3.7. siRNA complexation to oligopeptide-gold nanoclusters..........76
3.3.7.1. Characterization of oligopeptide gold nanocluster-siRNA complex...76
3.3.8. In vitro cell studies..77
3.3.8.1. siRNA transfection..77
3.3.8.2. Cytocompatability of different siRNA transfection methods...77
3.3.8.3. Endosomal/lysosomal escape of oligopeptide-GNC-siRNA complex...78
3.3.8.4. Immunocytochemistry..78
3.3.8.5. Quantitative RT-PCR..79
3.3.8.6. Wound healing assay..80
3.3.8.7. Apoptosis assay...80
3.3.8.8. Live dead assay...80
3.3.8.9. Caspase assay...81
3.3.9. Her2 conjugation to oligopeptide-GNC-siRNA complex...82
3.3.9.1. Evaluation of uptake of oligopeptide-GNC-Her2-siRNA complex in co-culture model..........................82
3.3.10. Statistical analysis..83
4. Results and Discussions...84
4.1. Fluorescent molecular probe for zinc ion sensing...............................85
4.1.1. Design of molecular probe for Zn^{2+} sensing.......................85
4.1.2. Characterization of molecular probe towards Zn^{2+} sensing....86
4.1.3. In vitro studies...88
4.1.3.1. Cytocompatibility..88
4.1.3.2. Fluorescence imaging and Zn^{2+} sensing.................89
4.1.3.2.1. Imaging and Zn^{2+} sensing in C6 glioma cells......89
4.1.3.2.2. Imaging and Zn^{2+} sensing in hippocampal slice..90
4.1.3.2.3. Imaging Zn^{2+} dynamics under *in vitro* epileptic condition...92
4.1.3.3. Studying Zn^{2+} dynamics using Raman spectroscopy.95
4.1.3.4. Ratiometric imaging...98
4.1.3.4.1. Ratiometric imaging of Zn^{2+} in C6 glioma cells.98
4.1.3.4.2. Ratiometric imaging of Zn^{2+} dynamics in epileptic hippocampal slice...................................99
4.1.4. In vivo studies..101
4.1.4.1. Zn^{2+} quantification in rat brain...............................101
4.1.4.2. Epileptic behavioural changes.............................101
4.1.4.3. *In vivo* Zn^{2+} imaging in epileptic rat brain............102
4.2. Fluorescent nano probe for cancer imaging and therapy......................103
4.2.1. Synthesis and characterization of tripeptides.........................104
4.2.2. Synthesis of tripeptide-gold nanoclusters..............................108
4.2.3. Physico-chemical characterization of tripeptide-gold nanoclusters..110

4.2.3.1. Optical properties..110
4.2.3.2. Size, surface charge and surface chemistry.............116
4.2.3.3. Stability of tripeptide-gold nanoclusters.................124
4.2.4. Biological evaluation of tripeptide-gold nanoclusters...........127
4.2.4.1. *In vitro* cytocompatibility of tripeptide-gold nanoclusters..128
4.2.4.2. Cellular uptake and accumulation of tripeptide-gold nanoclusters..131
4.2.4.3. *In vitro* PDT of tripeptide-gold nanoclusters: Photoinduced ROS generation...............................136
4.2.4.4. *In vitro* PDT of tripeptide-gold nanoclusters: Photoinduced change in mitochondrial membrane potential (ΔΨm)..140
4.2.4.5. *In vitro* PDT of tripeptide-gold nanoclusters: Photoinduced cell death..142
4.3. Fluorescent nano gene downregulator for cancer imaging cum therapy...146
4.3.1. Construction of fluorescent nano gene downregulator..........146
4.3.2. Synthesis and characterization of oligopeptides....................147
4.3.3. Synthesis of oligopeptide-gold nanoclusters..........................151
4.3.4. Physico-chemical characterization of oligopeptide-gold nanoclusters...154
4.3.4.1. Optical properties..154
4.3.4.2. Size, surface charge and surface chemistry.............159
4.3.4.3. Stability of oligopeptide-gold nanoclusters.............164
4.3.5. Biological evaluation of oligopeptide-gold nanoclusters.......167
4.3.5.1. *In vitro* cytocompatibility of oligopeptide-gold nanoclusters..168
4.3.5.2. Cellular uptake of oligopeptide-gold nanoclusters..169
4.3.6. Complexation of siRNA to oligopeptide-gold nanoclusters...171
4.3.6.1. Characterization of oligopeptide-GNC-siRNA complex..171
4.3.7. In vitro evaluation of siRNA delivery using oligopeptide-gold nanoclusters........176
4.3.7.1. Cellular uptake of siRNA using different transfection Methods..176
4.3.7.2. Cytocompatibility of different siRNA carriers........178
4.3.7.3. Endosomal escape effect of oligopeptide-GNC-siRNA complex..180
4.3.8. Evaluation of survivin and Her2 overexpression in cancer cells..181
4.3.9. Evaluation of gene silencing/knockdown by oligopeptide-GNC-siRNA complex..183
4.3.10. Anti-migration or anti-metastatic effect of oligopeptide-GNC-siRNA complex...184
4.3.11. Effect of oligopeptide-gold nanocluster-siRNA complex in inducing apoptosis...186

        4.3.12. Evaluation of caspase 3/7 activity..189
        4.3.13. Her2 conjugation to GNC-siRNA complex...........................190
        4.3.14. Evaluation of GNC-Her2-siRNA complex uptake in co-culture model..192

5. Summary and Conclusion..194
    5.1. Summary...195
    5.2. Conclusion..199

Bibliography..201

List of publications..215

Conferences...216

LIST OF FIGURES

Figure No.	Captions	Page no.
1	A simplified jablonski diagram explaining the fluorescence principle	3
2	Electromagnetic spectrum	3
3	General mechanisms of a fluorescent biosensor	6
4	Mechanism of PET based fluorescent sensor	6
5	a) Spectral overlap of two fluorophores b) Mechanism of FRET based fluorescent sensor	7
6	Schematic representation of ICT process	8
7	Different kinds of fluorescent nanoparticles used in bioimaging	11
8	Synthetic approaches of fluorescent gold nanoclusters and effect of ligands on their fluorescence	13
9	Molecular mechanisms of apoptosis	15
10	Evasion of apoptosis and carcinogenesis	16
11	PDT mechanism of action	17
12	Nanoparticle based PDT to treat cancer	18
13	Gene expression and gene silencing	20
14	Detailed RNAi mechanism	21
15	Extracellular and intracellular barriers encountered by siRNA following systemic administration	23
16	Fluorescence response of ZnAFs sensing extracellularly released Zn^{2+}, with varying affinity towards Zn^{2+}	30
17	Fluorescence ratiometric imaging of intracellular Zn^{2+} and Zn^{2+} in rat hippocampal slice using ZnIC	31
18	A naphthalimide-azide based colorimetric and ratiometric fluorescent probe, NAP-1, for selective and sensitive detection of hydrogen sulphide	32
19	Schematic representation of FQ1, absorption and emission spectra of FQ1 with response to Zn^{2+} and confocal fluorescence images of intracellular Zn^{2+} in NIH 3T3 cells with FQ1	33
20	Schematic representation of binding of TOA to $Au_{22}(SG)_{18}$ clusters and fluorescence spectra of $Au_{22}(SG)_{18}$ in water and TOA-Au_{22} clusters in toluene	36
21	Aggregation induced emission of Au-thiolate nanoclusters	37
22	Schematic diagram showing the synthesis and application of fluorescent peptide-mercaptoundecanoic acid co-stabilized gold nanoclusters (peptide-MUA/AuNCs) for the sensing of metalloproteinase-9	38
23	Schematic representation of peptide templated gold nanocluster inducing apoptosis through enzyme like catalysis, Absorbance and fluorescence spectra of gold nanocluster	39

24	Different colour emitting gold quantum clusters (QC) under UV light developed by thiol containing dipeptide (Leu-Cys) as stabilizing agent and sodium borohydride/trisodium citrate as reducing agent	40
25	Gold clusters nanoassembly (Au CNA) for near-infrared fluorescent imaging and photodynamic therapy (PDT) *in vitro* and *vivo*	42
26	a) Schematic illustration of PDT of cancer by AuNC@DHLA, b) Two-Photon and One-Photon Exciatation images of HepG2 cells treated with AuNC@DHLA, c) ROS generation measured by DCFH-DA in control and AuNC@DHLA treated cells irradiated with laser, d) cell viability using Calcein-AM/Propidium Iodide in AuNC@DHLA treated laser irradiated cells, e) Tumor growth curve of HepG2-tumor-bearing nude mice in different treatment groups within 28 days	42
27	Timeline of discoveries in the field of siRNA	44
28	Schematic representation of MN-NIRF-siGFP probe with magnetic nanoparticles labelled with NIR Cy5.5 dye linked to membrane translocation peptides (MPAP) and siRNA molecules targeting GFP (siGFP). MN-NIRF-siGFP probe for simultaneous MR imaging (a), NIR imaging (b) and siRNA mediated tumour therapy (c & d - RT-PCR analysis of survivin mRNA expression & apoptotic nuclei)	46
29	Preparation of Polyvalent RNA-AuNP Conjugates (a), cellular uptake of Cy5RNA-Au NPs (b), knockdown of luciferase expression treated with RNA-AUNPs (c)	47
30	Schematic diagram of laser triggered release of siRNA from gold nanoshell (a), Downregulation of GFP in H1299 cells by siRNA using nanoshell poly-L-lysine (NS-PLL) delivery vectors (b)	47
31	(a) Schematic diagram of the preparation of GNC–siRNA complex, (b) delivery mechanism of GNC–siRNA complex for NGF silencing and pancreatic cancer therapy, (c) Cellular uptake of free siRNA and GNC–siRNA into Panc-1 cells (siRNA labelled with Cy5 dye for visualization), (d) RT-PCR analysis of NGF mRNA expression after treatment, (e) western blot analysis of NGF protein expression after treatment	49
32	Flowchart of peptide synthesis	60
33	Synthesis of six different tripeptides (DCG, DCS, DCH, SCG, HCS, HCG)	61,62
34	Synthesis of three different oligopeptides $(HR)_3C(HR)_3$, $(HK)_3C(HK)_3$ and $(H)_3C(H)_3$	71
35	Structure of BP and BP•Zn^{2+} complex	86
36	Frontier orbitals of models of BP and BP•Zn^{2+} complex	86
37	SERS spectra of BP and BP•Zn^{2+} complex	87
38	FTIR spectra of BP and BP•Zn^{2+} complex	87
39	a) Absorption spectra of BP and BP•Zn^{2+} complex, b) Fluorescence spectra of BP and BP•Zn^{2+} complex with $ZnCl_2$ @	88

	different conc. (µM), CaEDTA (50 µM). Arrow indicates the reversal of fluorescence shift on addition with CaEDTA.	
40	Cell viability (%) of C6 glioma with different concentration of BP	89
41	Imaging and Zn^{2+} sensing in C6 Glioma cells using BP	90
42	Detailed lamellar anatomy of hippocampal slice sectioned perpendicular to the septo-temporal axis	90
43	Imaging and sensing endogenous Zn^{2+} in hippocampal slice. Slices incubated with a) BP, b) Fluozin-3 AM and c) TSQ	91
44	Effect of CaEDTA and TPEN on vesicular Zn^{2+}, imaged with BP	92
45	Imaging Zn^{2+} dynamics under *in vitro* epileptic condition using BP (a) and Fluozin-3 AM (b)	94
46	Raman Spectra from the hilar region of unstimulated (control) and stimulated (epileptic) hippocampal slices incubated with BP	96
47	Ratiometric time lapse imaging of Zn^{2+} in C6 Glioma cells using BP	98
48	Average emission intensity ratio ($R=I_{620}/I_{570}$) according to the corresponding ratiometric images of cells in Figure 47	99
49	Ratiometric imaging of endogenous Zn^{2+} and its dynamics in hippocampal slices	100
50	Average emission intensity ratio ($R=I_{620}/I_{570}$) according to corresponding ratiometric images of slices in figure 49	100
51	Quantification of total free Zn^{2+} in rat brain weighing 2.4 g. The standard plot shows the pixel intensity ratio with reference to different concentration of BP•Zn^{2+} complex	101
52	*In vivo* imaging of brain Zn^{2+} in epileptic rat using BP @ 430 nm excitation	103
53	Kaiser test results of peptide synthesis	104
54	Chemical structure of tripeptides with Ball and stick model	105
55	LC-MS of synthesized tripeptides with its respective mass	106,107
56	Pictorial representation of the synthesis of six tripeptide-gold nanoclusters (DCG-GNC, DCS-GNC, DCH-GNC, SCG-GNC, HCS-GNC and HCG-GNC)	109,110
57	UV-Vis Absorption, Emission & Excitation spectra of different tripeptide-gold nanoclusters.	111
58	Emission spectra of different tripeptide-gold nanoclusters upon different excitation	113
59	Fluorescence lifetime of tripeptide-gold nanoclusters at their respective emission maximum and @ 375 nm excitation	115
60	Relative amplitude of long lifetime component (τ_2) for different tripeptide-gold nanoclusters with λ_{ex} = 375 nm with their respective emission maximum	116
61	HR-TEM image and size distribution of tripeptide-gold nanoclusters	117,118
62	Surface charge of tripeptide-gold nanoclusters	119
63	FTIR spectra of tripeptides and its respective gold nanoclusters	120,121
64	High resolution XPS spectra of tripeptide-gold nanoclusters	123

	showing the binding energies of Au 4f and Ag 3d	
65	Influence of different pH on the fluorescent stability of tripeptide-gold nanoclusters	125
66	Photobleaching measurements of tripeptide-gold nanoclusters and Rhodamine 6G after continuous UV illumination	126
67	Effect of storage time on the fluorescence stability of tripeptide-gold nanoclusters	126
68	Group separation for the cellular interaction studies of tripeptide-gold nanoclusters	127
69	*In vitro* cytocomapatibility study of tripeptide-gold nanoclusters in cancer and normal cells showing the percentage of cell viability at different concentrations	129,130
70	Cellular uptake and accumulation of tripeptide-gold nanoclusters in respective cells after 3,6, 12 and 24 h incubation	132
71	Cellular uptake mechanism of tripeptide-gold nanoclusters evaluated at different temperature.	133,134
72	Microscopic images of ROS generation in tripeptide-gold nanocluster treated cancer cells with and without laser irradiation	138
73	Quantitative measurement of ROS generation by tripeptide-gold nanoclusters in respective cancer cells with and without laser irradiation	139,140
74	Microscopic images of mitochondrial membrane potential change in tripeptide-gold nanoclusters treated cancer cells with and without laser irradiation	141
75	Live dead imaging of tripeptide-gold nanocluster treated cancer cells with and without laser irradiation	143,144
76	Quantitative measurement of cell death in tripeptide-gold nanocluster treated cells with and without laser irradiation using MTT assay	145
77	Pictorial representation of fluorescent nano gene downregulator	147
78	Kaiser test results of peptide synthesis	148
79	Chemical structure of oligopeptides with Ball and stick model	149,150
80	MALDI-MS of synthesized oligopeptides showing the respective mass	150,151
81	Pictorial representation of the synthesis of three oligopeptide-gold nanoclusters: (HR)$_3$C(HR)$_3$-GNC, (HK)$_3$C(HK)$_3$-GNC and (H)$_3$C(H)$_3$-GNC	153
82	UV-Vis absorption and emission spectra of different oligopeptide-gold nanoclusters, (HR)$_3$C(HR)$_3$-GNC, (HK)$_3$C(HK)$_3$-GNC and (H)$_3$C(H)$_3$-GNC	155
83	Emission spectra of different oligopeptide-gold nanoclusters (HR)$_3$C(HR)$_3$-GNC, (HK)$_3$C(HK)$_3$-GNC and (H)$_3$C(H)$_3$-GNC upon different excitation	156
84	Fluorescence lifetime of oligopeptide-gold nanoclusters @ 610 nm emission and @ 375 nm excitation	158

85	Relative amplitude of long lifetime component (τ_2) for different oligopeptide-gold nanoclusters @ 375 nm excitation and 610 nm emission	158
86	HR-TEM image and size distribution of oligopeptide-gold nanoclusters	160
87	Surface charge of oligopeptide-gold nanoclusters	161
88	FTIR spectra of oligopeptides and its respective gold nanoclusters	162
89	High resolution XPS spectra of oligopeptide-gold nanoclusters showing the binding energies of Au 4f and Ag 3d	164
90	Influence of different pH on the fluorescent stability of oligopeptide-gold nanoclusters	165
91	Photobleaching measurements of oligopeptide-gold nanoclusters and Rhodamine 6G after continuous UV illumination	166
92	Effect of storage time on the fluorescence stability of oligopeptide-gold nanoclusters	167
93	*In vitro* cytocomapatibility study of oligopeptide-gold nanoclusters in SK-BR-3 cancer cells showing the percentage of cell viability at different concentrations	169
94	Cellular uptake and accumulation of oligopeptide-gold nanoclusters in SK-BR-3 cells after 3 h of incubation	170
95	Charge reversal study using zeta potential analysis showing the siRNA loading capacity of three different oligopeptide-gold nanoclusters	172
96	FTIR spectra of oligopeptide-gold nanoclusters and their complexation with siRNA	173
97	High resolution XPS spectra showing the binding energies of major elements in $(HR)_3C(HR)_3$-GNC and $(HK)_3C(HK)_3$-GNC and their siRNA complex formation	174,175
98	Fluorescent images of the cellular internalization of NSsiRNA-FITC by different transfection methods	178
99	Quantification of cellular uptake of NSsiRNA-FITC using different transfection methods	178
100	Cytocompatibility study of oligopeptide-gold nanocluster siRNA carrier compared with the commercially available lipofectamine siRNA carrier	179
101	Fluorescent microscopic images showing the endosomal escape effect of oligopeptide-goldnanoclusters-siRNA complexes in SK-BR-3 cells at different time points	181
102	Fluorescent microscopic images showing the survivin over expression in SK-BR-3 cells at different stages of cell cycle	182
103	Fluorescent microscopic images showing the survivin under expression in WI-38 cells	182
104	Fluorescent microscopic images showing the Her2 over and under expression in SK-BR-3 and WI-38 cells respectively	182
105	Relative mRNA expression of survivin in SK-BR-3 cells with different siRNA delivery vectors analyzed by qRT-PCR	184

106	Wound healing assay showing the migration of SK-BR-3 cells after transfection with different survivin siRNA carriers for 1, 24 and 48 h	185
107	Extent of Gap closure % shown by SK-BR-3 cells in migration assay after 24 and 48 h treatment with GNC-SURsiRNA complexes and free-SURsiRNA	185
108	Fluorescence microscopic images of SK-BR-3 cells stained with Annexin-Alexa Fluor 488 & PI and with acridine orange/ethidium bromide dual staining after 48 h of different SURsiRNA delivery transfection methods	188
109	Quantitative cell viability percentage by MTT assay after 48 h treatment with different siRNA delivery carriers	188
110	Relative fluorescent intensity showing caspase 3/7 activity in SK-BR-3 cells treated with different siRNA transfection methods	190
111	UV visible absorption spectra of Her2, $(HR)_3C(HR)_3$-GNC-siRNA and $(HR)_3C(HR)_3$-GNC-Her2-siRNA complex	191
112	FTIR spectra of $(HR)_3C(HR)_3$-GNC-siRNA and $(HR)_3C(HR)_3$-GNC-siRNA-Her2 complexes	191
113	Evaluation of GNC-Her2-siRNA complex uptake in co-culture model. Red and white arrow indicates SK-BR-3 cells and WI-38 cells respectively	192
114	Summary of fluorescent molecular probe property and its application	196
115	Summary of fluorescent nano probe property and its application	197
116	Summary of fluorescent nano gene downegulator property and its application	199
117	Illustration showing potential biomedical applications of fluorescent probes used in this study	200

LIST OF TABLES

Table No.	Captions	Page no.
1	Different synthetic approaches of gold nanoclusters and its fluorescence quantum yield	35
2	Composition of ACSF and PSF for hippocampal slice preparation	54
3	Stages of seizure activity according to Racine scale	58
4	Chemical composition for the synthesis of different tripeptide-gold nanoclusters	63
5	Chemical composition for the synthesis of different oligopeptide-gold nanoclusters	72
6	Sequences of primers used for qRT-PCR	79
7	Raman peak assignments of control and epileptic hippocampal slices incubated with BP	97
8	Stages of epileptic seizures observed under video recording	102
9	Excitation and emission maximum of different tripeptide-gold nanoclusters	112
10	Quantum yield of six different tripeptide-gold nanoclusters	114
11	Summary of lifetimes of tripeptide-gold nanoclusters @ λ_{ex} = 375 nm with their respective emission maximum	114
12	The binding energies of Au $4f_{7/2}$, Au $4f_{5/2}$, Ag $3d_{5/2}$ and Ag $3d_{3/2}$ in respective tripeptide-gold nanoclusters	123
13	Quantum yield of three different oligopeptide-gold nanoclusters calculated using the comparative method with Rhodamine 6G	157
14	Summary of lifetimes of oligopeptide-gold nanoclusters @ 375 nm excitation and 610 nm emission	158
15	The binding energies of Au $4f_{7/2}$, Au $4f_{5/2}$, Ag $3d_{5/2}$ and Ag $3d_{3/2}$ in respective oligopeptide-gold nanoclusters	164

ABBREVIATIONS

@	:	At
µg	:	Micro gram
µl	:	Micro litre
µm	:	Micro metre
µM	:	Micro molar
AFM	:	Atomic force microscopy
AIE	:	Aggregation induced emission
Asp	:	Aspartic acid
BBB	:	Blood Brain Barrier
BSA	:	Bovine Serum Albumin
CaEDTA	:	Ethylenediaminetetraaceticacid disodium calcium salt
CO_2	:	Carbondioxide
CT	:	Computerized tomography
Cys	:	Cysteine
DAPI	:	4, 6-Diamidino-2-Phenylindole
DCM	:	Dichloromethane
DIEA	:	N,N-Diisopropylethylamine
DMEM	:	Dulbecco’s Modifed Eagle’s Medium
DMEM/F12	:	Dulbecco’s Modifed Eagle’s Medium/Nutrient mixture F12 Ham, 1:1
DMF	:	Dimethyl formamide
DMSO	:	Dimethyl Sulfoxide
DNA	:	Deoxyribo nucleic acid
EPR	:	Enhanced permeation and retention
EtBr	:	Ethidium Bromide
FBS	:	Fetal Bovine Serum
FITC	:	Fluorescein Isothyocyanate
FTIR	:	Fourier Transform Infra Red Spectroscopy
GFP	:	Green fluorescent protein
Gly	:	Glycine
GNC	:	Gold nanocluster
h	:	Hours
HBTU	:	O-(Benzotriazol-1-yl)-N,N,N′,N′-tetramethyluronium hexafluorophosphate
H_2DCFH-DA	:	2,7-Dichlorodihydrofluorescein diacetate
H_2O_2	:	Hydrogen peroxide
$HAuCl_4$	:	chloroauric acid
His	:	Histidine
HOMO	:	Highest occupied molecular orbital

IAEC : Institutional Animal Ethics Committee
ICP-MS : Inductively coupled plasma mass spectrometry
ICT : Intramolecular charge transfer
kg : Kilo gram
LUMO : Lowest unoccupied molecular orbital
M : Molar
MALDI-MS : Matrix-Assisted Laser Desorption/Ionization-mass Spectrometry
MFI : Mean fluorescence intensity
mg : Milli gram
min : Minutes
miRNA : microRNA
ml : Milli litre
mM : Milli molar
MMP : Mitochondrial membrane potential
MRI : Magnetic resonance imaging
mRNA : messenger RNA
MTT : 3-(4,5-dimethyl thiazol-2-yl)-2,5-diphenyl tetrazolium Bromide
NADH : Nicotinamide Adenine Dinucleotide Hydrogen
NADPH : Nicotinamide Adenine Dinucleotide Phosphate
NIR : Near Infra-red
nm : Nanometer
NP : Nanoparticle
NSsiRNA : Non-specific siRNA
PBS : Phosphate Buffered Saline
PCR : Polymerase Chain Reaction
PDT : Photo dynamic therapy
PEI : Polyethylenimine
PET : Photo-induced electron transfer
PFS : Phosphate free saline
pH : potential of hydrogen
PS : Photosensitizer
qPCR : Quantitative PCR
QY : Quantum yield
RES : Reticuloendothelial system
RNA : Ribo nucleic acid
RNAi : RNA interference
ROI : Region of interest
ROS : Reactive Oxygen Species
Rpm : Rotations per minute
RT : Room temperature

SD	:	Standard Deviation
Sec	:	Seconds
SEM	:	Scanning Electron Microscopy
Ser	:	Serine
SERS	:	Surface Enhanced Raman scattering
siRNA	:	Short interfering RNA/small interfering RNA/silencing RNA
SPECT	:	Single-photon emission computed tomography
TEM	:	Transmission Electron Microscopy
TEMED	:	Tetramethylethylenediamine
TFA	:	Trifluoroacetic acid
THF	:	Tetrahydrofuran
TIPS	:	Triisopropyl silane
TPEN	:	N,N,N′,N′-tetrakis(2-pyridylmethyl)ethylenediamine
Trypsin-EDTA	:	Trypsin-ethylenediaminetetraacetic acid
TSQ	:	N-(6-Methoxy-8-Quinolyl)-p-Toluenesulfonamide
U	:	Units
UV	:	Ultra Violet
Vis	:	Visible
Zn^{2+}	:	Zinc (II) ion

SYNOPSIS

Imaging is a kind of photography in most people’s perception. But scientific imaging goes far beyond this, in which images can be created by diverse methods such as chemical imaging, molecular imaging, mechanical methods (AFM), scanning methods (ICP-MS, MALDI-MS), medical imaging (Radioimaging, CT, MRI, SPECT, Ultrasound), etc. Most of these imaging methods are destructive or they require extensive sample preparation, while others are non-destructive and are well suited for imaging intact tissues and living systems. Among the imaging techniques, optical imaging finds special attraction in biomedical field because of their several advantages. Among optical imaging techniques, fluorescence imaging is a powerful technique as it is highly sensitive, selective, versatile, less hazardous and rich in contrast. Other advantages of fluorescence imaging include rapid signal acquisition, multicolour for multiplexed imaging and so on.

Fluorescence imaging is of two different kinds: imaging based on intrinsic biochemical species inside cells like NADPH and imaging based on addition of synthetic probes. Thus the main barrier of fluorescence imaging is the autofluorescence from biological specimens, which mostly emit in blue and green of visible region in electromagnetic spectrum. To overcome this, fluorescent probes with red emission properties are generally preferred. A molecule which has the ability to fluorescence is called fluorescent probe. These fluorescent probes can be used for bioimaging including plain imaging, targeted imaging and for sensing of different analytes. Organic dyes are commonly used as fluorescent probes as it is economical, easily available and versatile. Nowadays, nanoprobes are replacing organic dyes because of its photostability, virtually inert nature, high surface to volume ratio and non-toxicity. Because of their unique optical properties, nanoprobes/nanoparticles find special application in medical field for bioimaging, tissue engineering, biosensors, photothermal therapy, gene delivery, drug delivery, etc. Among fluorescent nanoparticles, noble metal nanoparticles are attractive because of their non-toxic nature and excellent fluorescent property. These fluorescent nanoparticles can replace organic dye molecules for bioimaging including cancer imaging. Moreover, the high surface to volume ratio of nanoparticles allows conjugation of different drugs/genes for efficient delivery in cancer cells for their treatment. Cancer cells evade apoptosis by different mechanisms and these mechanisms can be focussed to construct a therapeutic agent. In brief, nanoprobes can be designed to have the desired properties for both disease diagnosis and its treatment. Based on these backgrounds, a hypothesis is proposed to design fluorescent probes which will act as a potential candidate for simultaneous bioimaging, biosensing and therapeutic purpose. The thesis mainly deals with the design and development of two classes of fluorescent probes: Fluorescent molecular probe and fluorescent nanoprobe for simultaneous bioimaging, sensing and cancer therapy.

The main objectives of the thesis are as follows:

1. To study the bioimaging and sensing potential of a fluorescent ratiometric molecular probe and exploitation of this probe to study the dynamics of Zn^{2+} under epileptic condition *in vitro* and *in vivo*
2. Development of fluorescent nanoprobe for cancer imaging cum therapy
    - a) Design and synthesis of different tripeptides using solid phase synthesis
    - b) Synthesis of tripeptide stabilized fluorescent gold nanoclusters
    - c) *In vitro* evaluation of tripeptide stabilized fluorescent gold nanoclusters for simultaneous imaging cum photodynamic therapy of cancer
3. Development of fluorescent nano gene downregulator for cancer imaging cum therapy
    - a) Design and synthesis of different oligopeptides using solid phase synthesis
    - b) Synthesis of oligopeptide stabilized fluorescent gold nanoclusters
    - c) Construction of fluorescent nano gene downregulator with oligopeptide-gold nanoclusters, siRNA and cancer targeting ligand
    - c) *In vitro* evaluation of fluorescent nano gene downregulator for simultaneous imaging and siRNA based cancer therapy

The thesis is mainly divided into five chapters viz., introduction, literature review, materials & methods, results & discussion and conclusion. The first chapter is the general **Introduction**, which describes the importance and principle of fluorescence imaging, applications of fluorescent probes in biomedical field, biosensing and bioimaging of fluorescent molecular probe and mechanism of biosensing. The advantage of fluorescent nanoparticles over organic dyes and its use in bioimaging is described. In addition, the pros of metal nanoparticles, especially gold nanoclusters and its mechanism of fluorescence are explained. The use of nanoparticle in photodynamic therapy of cancer is highlighted. RNA interference (RNAi) therapy for cancer is also explained.

The second chapter is the **Literature review**, which describes in detail about the role of Zn^{2+} in physiological, pathological condition and importance of its sensing. Various fluorescent probes for Zn^{2+} sensing and a brief review on ratiometric imaging of Zn^{2+} are described. Fluorescent gold nanoclusters for cancer imaging and therapy are reviewed. Literature review on different peptide stabilized gold nanoclusters, fluorescence enhancement in gold nanoclusters through different approaches and gold nanoclusters with photodynamic therapy are reviewed in detail. In addition, genes targeted in siRNA delivery for cancer therapy and different nanoparticles for siRNA delivery are discussed. Gold nanocluster based gene therapy is also reviewed.

The third chapter describe the **Materials and methods** followed for the completion of objectives. The methods include the optical property evaluation of BP molecular probe in physiological buffer, bioimaging, ratiometric imaging and Zn^{2+} sensing in C6 glioma cells and rat hippocampal slices. Methods for inducing epilepsy in rat and the *in vivo* imaging of Zn^{2+} are also described. Protocol for custom designed and manual synthesis of different tripeptides and the preparation of respective gold nanoclusters are described. Methods for physico-chemical characterization of tripeptide-gold nanoclusters are also included in this section. Methods for evaluating the cellular uptake and therapeutic efficiency (PDT) of these tripeptide-gold nanoclusters in different cancer cells are included. Protocol for custom designed and manual synthesis of different oligopeptides and its respective gold nanoclusters preparation are described. Methods for the physico-chemical characterization of oligopeptide-gold nanoclusters were included. Protocol for construction of fluorescent nano gene downregulator using oligopeptide-gold nanoclusters, siRNA and Her2 antibody are described. Methods for the physico-chemical characterization of fluorescent nano gene downregulator are explained. Methods for evaluating the cellular uptake and therapeutic efficiency (siRNA based cancer therapy) of fluorescent nano gene downregulator in cancer cells are mentioned.

The fourth chapter describe the **Results and Discussion** section of major experimental findings, which is subdivided into three main sections. First section deals with the characterization of fluorescent molecular probe for Zn^{2+} sensing, it's *in vitro* (cellular, hippocampal slice) and *in vivo* application for bioimaging and Zn^{2+} sensing under neurodegenerative condition. Second section deals with the synthesis and characterization of fluorescent nanoprobe and their application in cancer cells for simultaneous imaging and photodynamic therapy. Third section deals with the synthesis and characterization of fluorescent nanoprobe and their application in cancer cells for simultaneous imaging and siRNA based cancer therapy.

In detail, the first section in results and discussion focuses on studying the optical properties of fluorescent molecular probe, bipyridine bridged bispyrrole (BP) in physiological buffer condition, whose green emission upon Zn^{2+} binding shifts to red. The cellular imaging, Zn^{2+} sensing and ratiometric imaging potential of BP were studied in C6 glioma cells with the addition of exogenous Zn^{2+}. The endogenous Zn^{2+} sensing and the ratiometric imaging potential of BP in hippocampal slices were also confirmed. The dynamics of Zn^{2+} under neuropathological condition was also studied using BP in chemically stimulated rat brain slices. The *in vivo* brain Zn^{2+} quantification and imaging was also proved by BP. BP is a dual function molecular probe with its change in emission from green to red upon Zn^{2+} binding, which allows clear visualization of Zn^{2+} sensing, avoids autofluorescence and the ratiometric imaging potential shown by BP allows quantification of Zn^{2+} eliminating the artifacts from fluorescence imaging. The deep tissue imaging potential of BP is proved *in vivo*.

The second section in results and discussion focuses on the design and development of fluorescent tripeptide stabilized gold nanoclusters for simultaneous cancer imaging and therapy. Six different tripeptides were designed and manually synthesized towards this. These custom designed tripeptides were used to synthesize gold nanoclusters with different emission properties in near red region to overcome autofluorescence. These tripeptide-gold nanoclusters have ultra small size, excellent red and near red fluorescent property, high quantum yield, long lifetime, photostability, non-toxic nature and good cellular internalization. Hence the tripeptide-gold nanoclusters act as outstanding bioimaging agent. The cellular internalization of tripeptide-gold nanoclusters is highly influenced by their surface charge and cell type. These tripeptide-gold nanoclusters have limited dark toxicity but exert photoinduced ROS generation in cancer cells with 532 nm laser irradiation, leading to mitochondrial membrane potential loss followed by photoinduced cell death. Thus these tripeptide-gold nanoclusters can itself act as an efficient photosensitizer for photodynamic therapy (PDT). The image guided PDT efficiency of tripeptide-gold nanoclusters was confirmed *in vitro*.

The third section in results and discussion focuses on the design and development of fluorescent nano gene downregulator for simultaneous cancer imaging and siRNA based cancer therapy. Three different oligopeptides were designed and manually synthesized towards this. These custom designed oligopeptides were used to synthesize gold nanoclusters with different emission properties in near red region to overcome autofluorescence and to provide sufficient positive charge for the complexation of siRNA. Hence, the fluorescent nano gene downregulator was constructed using oligopeptide-gold nanoclusters, survivin siRNA and Her2 antibody for cancer targeting, imaging and RNAi therapy. The oligopeptide-gold nanoclusters have ultra small size, excellent red fluorescent property, high quantum yield, long lifetime, photostability, non-toxic nature and good cellular internalization. Hence the oligopeptide-gold nanoclusters act as outstanding bioimaging agent. The oligopeptide-gold nanoclusters fabricated with positively charged amino acids like histidine, arginine and lysine provided them excellent siRNA complexation efficiency and these siRNA carriers could efficiently escape endosome for effective siRNA delivery. These fluorescent nano gene downregulator caused effective knockdown of the overexpressed survivin in cancer cells, thus leading to apoptosis induction in cancer cells. The image guided siRNA delivery and cancer gene therapy of fluorescent nano gene downregulator is confirmed *in vitro*.

The final chapter of the thesis summarizes the work of three different fluorescent probes and its simultaneous application for bioimaging, sensing and cancer therapy. The thesis starts with the use of basic fluorescent molecular probe for bioimaging and sensing and ends with an advanced fluorescent nanoprobe for bioimaging and futuristic gene therapy for cancer. The future perspective of the study is to make these fluorescent probes available for clinical application along with the *in vivo* study.

CHAPTER 1: INTRODUCTION

1. INTRODUCTION

1.1. Fluorescence imaging

Imaging is a kind of photography in most people's perception. But scientific imaging goes far beyond this, wherein images can be created by diverse methods like chemical imaging, molecular imaging, optical imaging, mechanical methods (AFM), Scanning methods (ICP-MS, MALDI-MS), medical imaging (radioimaging, MRI, CT, SPECT, ultrasound imaging), etc. Most of these imaging methods require extensive sample preparation; others are non-destructive and are well suited to image intact tissues or living system. Among the imaging techniques, optical imaging finds special attraction in biomedical field owing to its several advantages. Optical imaging uses visible/ultraviolet/infrared light to acquire detailed images of molecules/cells/tissues/organs and thus reduces the patient exposure to harmful radiation like x-rays. Therefore it can be used for prolonged and repeated procedures over time to visualize soft tissues without causing any damage. It is non-invasive, significantly faster and can be used to monitor different properties of cells/tissues/organs at the same time with the usage of multiple colours of light. Some of the examples of optical imaging include photoacoustic imaging, endoscopy, Raman spectroscopy, fluorescence imaging, optical coherence tomography, etc.

Among the optical imaging techniques, fluorescence imaging is the most powerful technique as it is simple, highly selective, sensitive, versatile, low hazardous and rich in contrast. Other advantages include rapid signal acquisition, multiple colours for multiplexed imaging, localized signal and so on. The term fluorescence was first introduced by G. G. Stokes in a paper entitled 'On the change of refrangibility of light' in 1852. Fluorescence is an event which occurs when a molecule upon illumination, absorbs light at a specific wavelength and re-emits light at a longer wavelength. The molecule which has the potential to fluoresce is called fluorophore. The principle of fluorescence is explained in the Jablonski diagram (Figure 1). The electrons in a molecule reside in the lowest energy state (ground state - S_0) before excitation. When the molecule is hit with the photon of certain energy, the electrons absorb the energy and jumps to the highest energy state (S_2). Generally the excited electrons relax toward the lowest vibrational energy level (S_1) within the electronic excited state and lose some energy dissipated as heat. And then to return to the ground state (S_0), the electron releases the additional energy in the form of emission photon (Fluorescence). The energy of this emission photon is less than the excitation energy and hence it has the longer wavelength and appears in different colour. The wavelength of emitted light ($\lambda_{emission}$) is determined by the equation below:

$$\lambda_{emission} = hc/E_{emission}$$

where, h = Planck's constant, c = the speed of light, $E_{emission}$ = the energy difference between the energy levels of the two states.

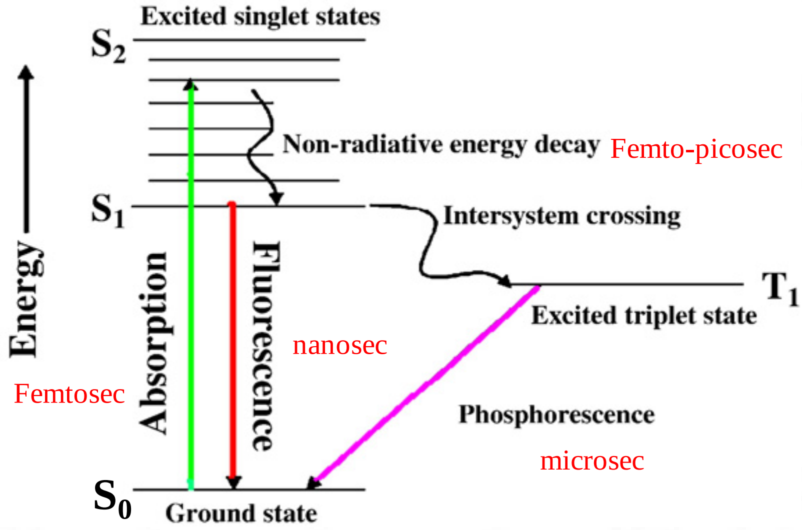

Figure 1: A simplified Jablonski diagram explaining the fluorescence principle.

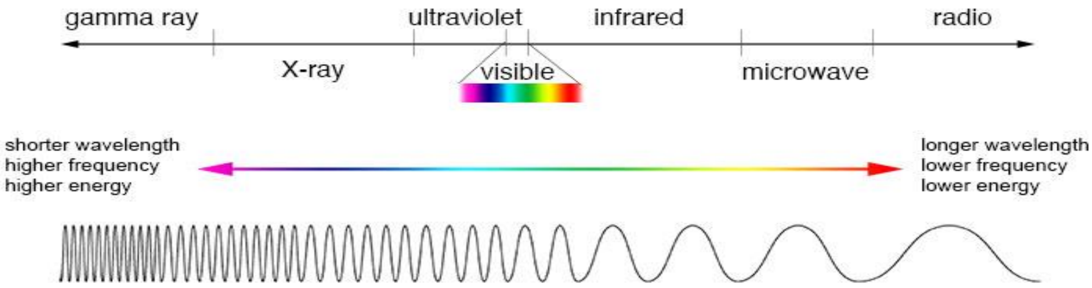

Figure 2: Electromagnetic spectrum.

The emitted photon is usually in the visible region of electromagnetic spectrum (Figure 2) and the emitted light should be intense enough to view under a microscope/imaging system. The factors affecting the fluorescence intensity are quantum yield, extinction coefficient, photostability and fluorescence lifetime of fluorophores as well as the excitation wavelength intensity. Fluorescence imaging techniques have experienced rapid development in the past decade and emerged as a vital tool in the area of clinical diagnostics. Fluorescence imaging allow us to visualize the dynamics of various molecular processes occurring inside living cells, including gene expression, protein expression, molecular interactions, etc. Fluorescence imaging is of two kinds:

- imaging based on intrinsically fluorescent (bio)chemical species such as NADH in tissues, chlorophyll in plants, etc.
- imaging based on addition of synthetic fluorescent probes, labels, nanoparticles or nanosensors

1.2. Fluorescent probes for biomedical applications

Even though fluorescence imaging finds special attraction in biomedical field, there are some barriers which need to be considered for successful *in vivo* fluorescence imaging. Autofluorescence is the main issue faced by fluorescence imaging. Intrinsic/endogenous molecules like collagen, elastin, NAPDH, flavins, etc. will absorb light in UV to blue region (355-488 nm) and emit blue to green fluorescence (350-550 nm). Thus fluorescent probes with red emission are preferable for biological imaging. Over the years, the design and development of different fluorescent probes for various biological applications improved our understanding of biological systems. Fluorescent probes are designed to localize to a specific region within a biological specimen or to produce a spectroscopically visible response to a specific stimulus. Efficient fluorescent probes are synthesized with high quantum yield, high molar absorption coefficient, long lifetime and large Stokes shift. Both fluorescent molecular probes/organic dyes and nanoprobes are widely used in biomedical field. The main applications of fluorescent probes in biomedical field are bioimaging and biosensing for clinical diagnostics, pharmaceutical research, high-throughput screening, etc.

1.3. Fluorescent probes for biosensing

Fluorescence-based biosensors have been explored for a variety of applications including medical diagnostics, drug discovery, drug delivery, food safety and environmental monitoring. Fluorescence-based biosensing finds special attraction than any other methods of biosensing like colorimetric, radioactive tracing and electrochemical sensing, as the fluorescence-based sensor does not cause any damage to the surrounding of the analyte. A typical fluorescent biosensor is composed of three main parts: a sensing component called receptor, a linker/spacer molecule and one or more fluorophores (Figure 3). When the receptor reacts with the target analyte, the fluorescence property of fluorophore is altered through different mechanisms, i.e., either it is quenched or enhanced (Figure 3). The fluorescent biosensors are generally classified into four types: i) ON-OFF, ii) OFF-ON, iii) Ratiometric and iv) Chemodosimeter fluorescent biosensors (Figure 3). However, based on the mechanism of fluorescence alteration i.e., how the fluorescence is getting ON or OFF, the fluorescent biosensors are classified into four types: i) PET (Photo-induced Electron Transfer) based, ii) FRET (Fluorescence/Förster Resonance Energy Transfer) based, iii) ICT (Internal Charge Transfer) based and iv) ESIPT (Excited State Intramolecular Proton Transfer) based fluorescent biosensors, which is explained in section 1.3.1.

1.3.1. Mechanisms of fluorescent probes for sensing

The fluorescent probes developed so far used a variety of mechanism such as PET, FRET, ESIPT, ICT for biological ion sensing (Sreenath K *et al*., 2011, Sreejith S *et al*., 2010, Maruyama S *et al*., 2002, Xue L *et al*., 2009, Ajayaghosh A *et al*., 2005, Divya K *et al*., 2010). The mechanism of most widely used fluorescent sensors like PET, FRET and ICT are explained in this section.

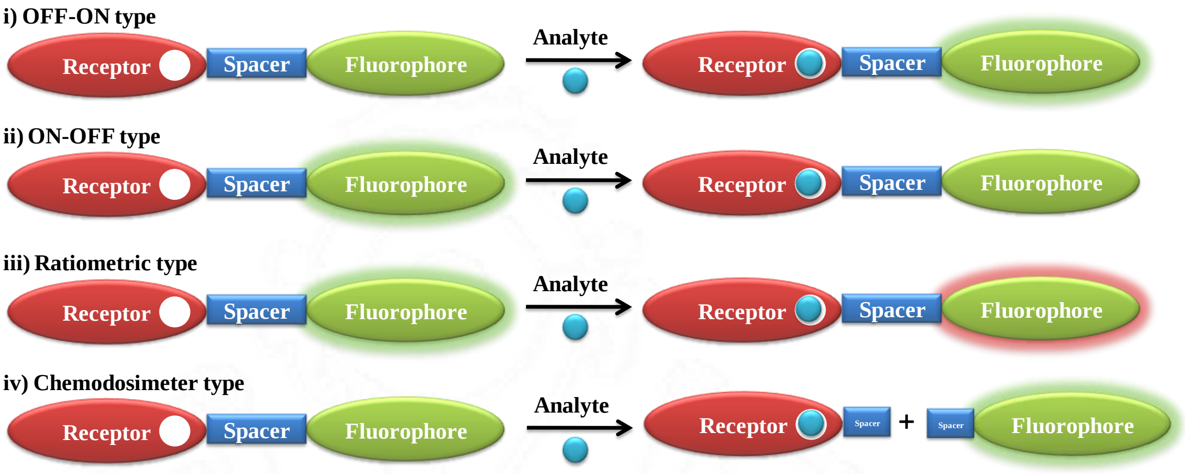

Figure 3: General mechanisms of a fluorescent biosensor.

PET based fluorescent sensors have a fluorophore connected to a receptor (contain high-energy non-bonding electron pair) via a spacer (Figure 4). In the absence of analyte, upon excitation, electron transfer occurs from receptor to fluorophore, thus quenching the fluorescence (Figure 4). But the binding of a cation to the receptor raises the redox potential of receptor (HOMO of receptor become lower in energy than the fluorophore) and thus blocking the electron transfer and consequently switching on the fluorescence of fluorophore (Figure 4). Most of the PET based fluorescent probes sense analyte resulting in increase or decrease of its absorption or emission spectral intensity (Zastrow M *et al.*, 2015).

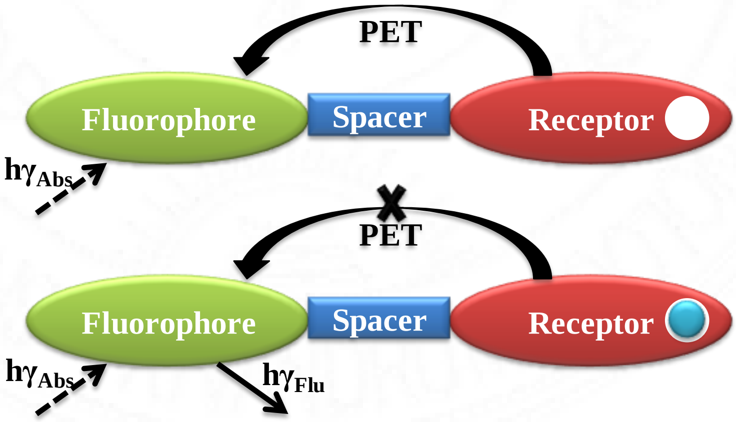

Figure 4: Mechanism of PET based fluorescent sensor.

FRET is a non-radiative process, which involves the transfer of energy from a donor fluorophore in an excited electronic state to a nearby acceptor fluorophore via dipole-dipole interactions (Figure 5b). In FRET mechanism, the emission spectrum of the donor fluorophore should overlap with the absorption spectrum of the acceptor fluorophore as shown in Figure 5a. Effective FRET results from larger overlap between the spectra. In addition to the spectral overlap, donor and acceptor fluorophores must be in close proximity (10–100 Å) for FRET to occur. Hence the efficiency of FRET varies in presence of analyte, as it controls the distance between two fluorophores (Figure 5b). FRET allows us to sense two different analytes at the same time.

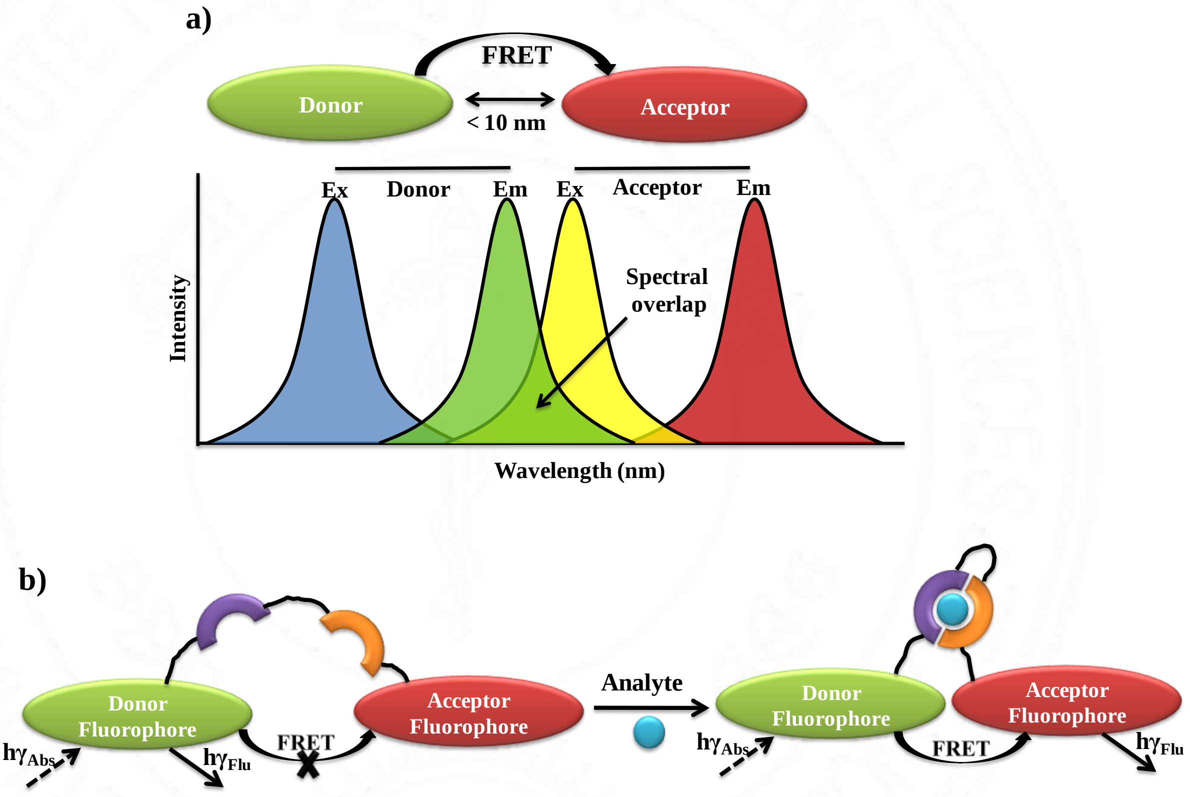

Figure 5: a) Spectral overlap of two fluorophores b) Mechanism of FRET based fluorescent sensor.

In contrast to PET based fluorescent sensors, ICT fluorescent sensors works on a different mechanism, i.e., the charge transfer from electron donor to electron acceptor occur within the fluorophores upon excitation by light. In ICT mechanism, electron donor group in the fluorophore is directly connected to an electron-acceptor group without spacer. Hence, the close interaction of analyte with donor or acceptor group changes the photophysical properties of the fluorophore. The binding of cation to the donor group decreases its electron donating character, resulting in the reduction of HOMO energy leading to blue shift of either absorption or fluorescence spectra (Figure 6). In contrast, the binding of cation to the acceptor group increases its electron accepting property, thus resulting in the red shift of either absorption or fluorescence spectra (Figure 6). In addition to these spectral shifts, changes in lifetime and quantum yield are also often observed. ICT probes show large stokes shift upon ion binding to its acceptor group. Therefore, ICT/FRET based fluorescent sensor probes are ideal for biological ion sensing, as it show spectral shift upon ion binding which causes fluorescence colour change and thus help in easy visualization.

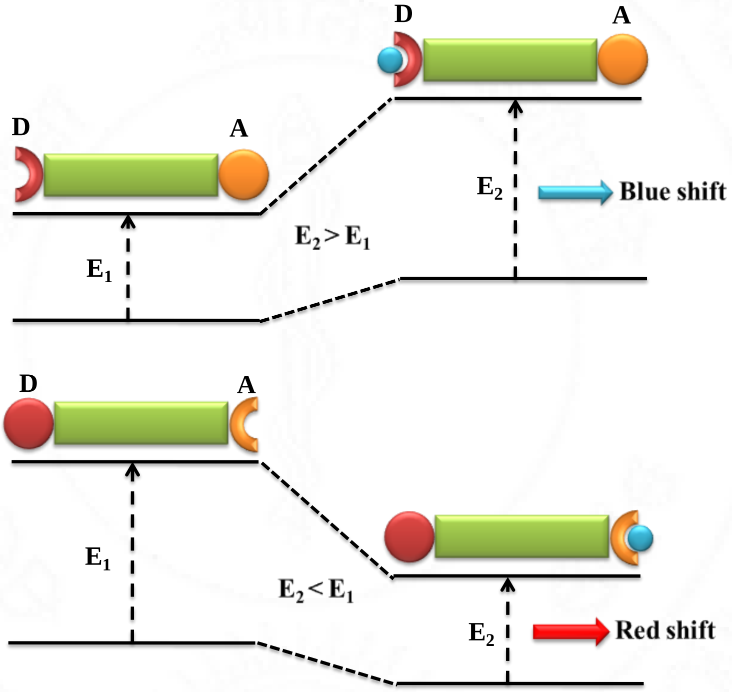

Figure 6: Schematic representation of ICT process.

Diseases such as neurodegenerative disorders, cancer and diabetes are often observed with abnormal homeostasis of metal ions. Fluorescent probes help us to understand the physiological and pathological functions of metal ions.

1.3.2. Fluorescent probes for ion sensing

Fluorescent probes for ion sensing must fulfil certain criteria for use in live biological specimens.

- Probes should be biocompatible and water-soluble.
- Probes must show a significant fluorescence change upon ion binding i.e., increase/decrease in emission intensity or shift in emission wavelength.
- The fluorescence response of probes upon ion binding should be fast enough to capture the biological event of interest.
- To minimize background autofluorescence from biological specimens and to minimize specimen damage, the probes should have visible light excitation or emission instead of UV-light excitation or emission.
- Probes should have high selectivity towards specific metal ion among other biologically abundant metal ions.

1.4. Fluorescent probes for bioimaging

Organic dyes/molecular probes are commonly used in fluorescence imaging as they are economical, easily available, and versatile. A number of natural and synthetic organic fluorophores are available commercially that can be chosen according to the requirements of chemical reactivity and spectroscopic properties. Cyanine structure or xanthene dyes are the most commonly used fluorescent probes. The first organic dyes used for fluorescent tagging are Fluorescein and rhodamine. In spite of many advantages, these fluorescent dyes suffer from some disadvantages like photo-bleaching, short fluorescence lifetime (1-5 ns), hydrophobicity/aggregation in aqueous solution, pH sensitivity, broad emission spectrum, etc. The discovery of fluorescent nanoparticles like semiconductor quantum dots, upconversion nanoparticles, polymeric nanoparticles and metal clusters overcame the obstacles faced by organic dyes/fluorescent molecular probes. Compared with organic dyes, these fluorescent nanoprobes can offer highly sensitive, selective and non-invasive bioimaging for visualization of cellular, sub-cellular and molecular events.

1.4.1. Fluorescent nanoprobes for bioimaging

Nanotechnology started with Professor Richard Feynman, who presented the idea of manipulating and controlling things on an extremely small scale by building and shaping matter one atom at a time. He stated nanotechnology as “There is plenty of room at the bottom”. Nanoparticles are defined as particles that have at least one dimension in the nanorange (1 to 100 nm). Nanoparticles bridge between bulk materials and atomic/molecular structures. The unique properties of nanoparticles are high surface to volume ratio, deep access to cells and organelles, better photostability than molecular probes and are virtually inert, so they neither interact with cellular proteins, nor their optical property affected by proteins outside (Wolfbeis O, 2015). The synthesis of nanoparticles for bioimaging application involves 3 main steps:

i) Preparation of optical core
ii) Surface modification
iii) Bioconjugation and targeting

The commonly used nanoparticles for bioimaging applications are mentioned in figure 7.

Of all these fluorescent nanoparticles, noble metal nanoparticles find special attraction in bioimaging application as it has excellent water-dispersibility, photostability, size-dependent colours, lack of swelling inside cells, sharp contrast for easy characterization in SEM or TEM and suitable surface functionalization with ligands for targeted imaging (Wolfbeis O, 2015). Among the metal nanoparticles, gold nanoparticles are especially attractive for biological studies as they show no surface oxidation and have biocompatibility even without any surface modification. The main difference of gold nanoparticles compared with its bulk material is its strong absorption in the optical spectrum @ 520 nm known as Surface Plasmon Resonance (SPR). SPR causes the intense colour of gold nanoparticles larger than 3 nm, which varies from blue to red as the size decreases.

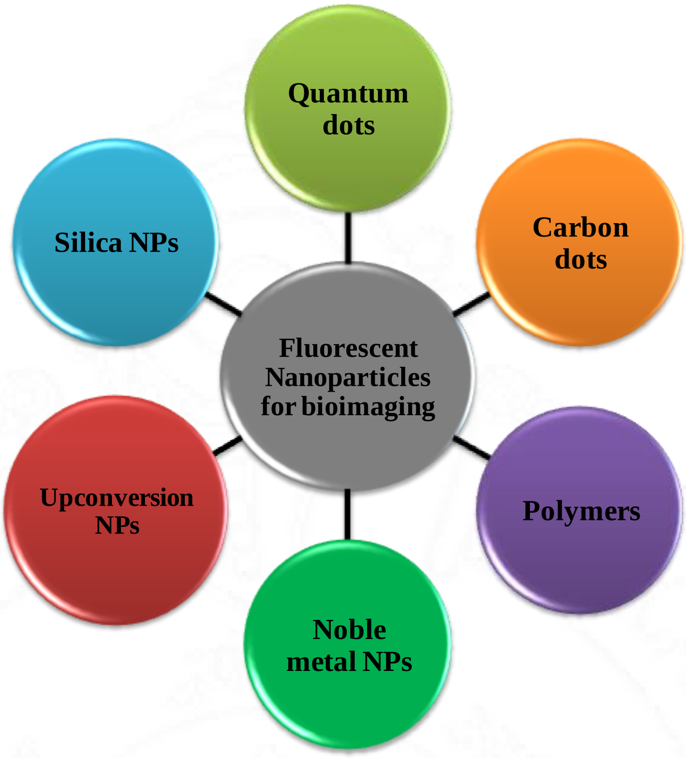

Figure 7: Different kinds of fluorescent nanoparticles used in bioimaging.

For the synthesis of nanoparticles and nanoclusters, top-down or bottom-up approaches are followed. In the top-down approach, the bulk material is subdivided into smaller pieces; while in bottom-up approach, defined building blocks are assembled into larger complexes. Generally, the synthesis of gold nanoparticles/nanoclusters is done by reducing its metal precursor to atoms and the metal clusters are then formed by subsequent nucleation process (Jin R *et al*., 2010). Then the particles are coated with a stabilizing layer to inhibit the aggregation of cluster core and to terminate further growth.

1.4.2. Fluorescent gold nanoclusters

Even though gold nanoparticles have well demonstrated optical properties and are well accepted in healthcare industry for sensing of biomolecules due to localized SPR, these spherical gold nanoparticles lack fluorescence property, which limits its usage in imaging applications. The discovery of gold nanoclusters overcame this limitation with its excellent fluorescent property. Gold nanoclusters are smaller than gold nanoparticles, but larger than the atom.

The term “clusters” refers to smaller structures with defined numbers of atoms. Unlike gold nanoparticles, ultra-small gold particles called nanoclusters (AuNCs) lack SPR band. This is due to the quantisation of energy levels of the cluster, and resulting fluorescence emission when its size is less than 3 nm. This unique feature provides several advantages to nanoclusters over large nanoparticles such as fluorescence (Luo Z *et al*., 2012), excellent catalytic activities (Zhang Y *et al*., 2020), two-photon absorptions (Han R *et al*., 2019), long lifetime (Yahia-Ammar A *et al*., 2016), etc. These properties make them well suitable for *in vitro* and *in vivo* imaging. Gold nanoclusters, in general are composed of tens to hundreds of gold atoms corresponding to a metal core smaller than 3 nm, stabilized by different biomolecules such as DNA, proteins or peptides (Figure 8). This ultrasmall size is extremely favourable for drug delivery and therapy applications due to low toxicity with high renal clearance and long blood circulation time. The fluorescence of the gold nanoclusters can be tuned by different core size and ligand functionalization (Figure 8) (Baral A *et al*., 2017, Yang T *et al*., 2020).

As mentioned in section 1.4.1, fluorescent gold nanoclusters are synthesized using either top-down or bottom-up strategies (Figure 8). In bottom-up strategy, small chemical molecules, amino acids, proteins and polymers are used as templates and protective ligands for the synthesis of gold nanoclusters. All these protective ligands have electron-rich heteroatoms such as nitrogen (N), oxygen (O), phosphorus (P), sulfur (S), etc., which play a main role in tuning the fluorescence of gold nanoclusters (Yang T *et al*., 2020). However, the exact role of the surface ligands and the kinetic of electron relax between core–shell structured gold nanoclusters are not clear.

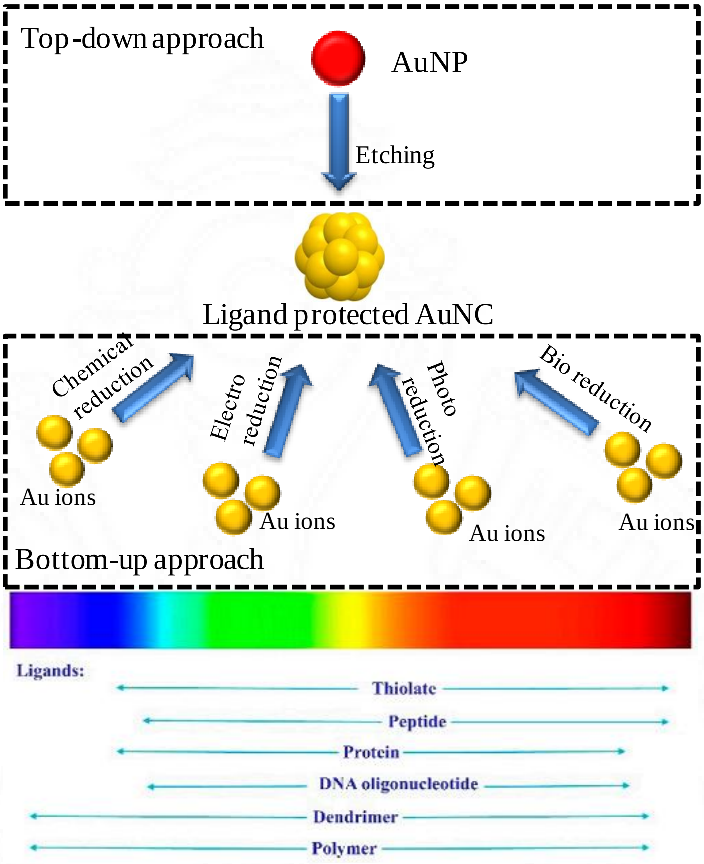

Figure 8: Synthetic approaches of fluorescent gold nanoclusters and effect of ligands on their fluorescence (Adapted from Yang T *et al.*, 2020).

1.4.3. Fluorescence mechanism of gold nanoclusters

Although the mechanism of fluorescence from metal nanoclusters is not fully understood, researchers have accepted two major explanations.

i) Metal quantum confinement effect – when the size of metal nanoclusters advance towards the Fermi wavelength of metals (< 3 nm), the continuous band of energy level break down to discrete energy levels, resulting in the emergence of molecule-like properties. The electron transfer from valence band to conduction band makes the nanoclusters fluorescent. Thus the fluorescence of metal nanoclusters originates from LUMO-HOMO transition (i.e., intraband (sp–sp) and interband (sp–d) transitions) (Yang T *et al.*, 2020, Qu X *et al.*, 2015). The fluorescence property may vary from visible to NIR region depending upon the size of clusters and corresponding electronic structure. Hence, addition or removal of one metal atom significantly changes the structure, electronic and optical property of nanoclusters.

ii) Ligand-to-metal charge transfer (LMCT) or ligand-to-metal−metal charge transfer (LMMCT) - the charge transfer on the shell of metal clusters due to the interaction between the metal core and the functional ligands. Surface ligands play major role in the formation of gold nanoclusters by preventing the aggregation of superatoms and maintain the size dependent fluorescence property. These ligands not only act as protecting agent but also largely affect the fluorescence of gold nanoclusters by transferring charge from surface ligand to the gold core (Qu X *et al.*, 2015).

1.5. Fluorescent nanoprobes for cancer therapy

1.5.1. Cancer and apoptosis

Cancer is one of the major life threatening diseases and it is the second leading cause of death worldwide. Recent cancer statistics reported 18.1 million new cancer cases each year and the mortality increases to 9.6 million across the world in the last ten years. Cancer is defined as the uncontrolled growth and spread of abnormal cells. Apoptosis plays an important role throughout life, from embryonic development to adult tissue homeostasis by balancing cell death with cell proliferation. Apoptosis can be initiated by three different pathways (Figure 9):

- Extrinsic pathway - triggered by death receptors and subsequent caspase-8 activation.
- Intrinsic pathway - initiated by cellular stress followed by activation of caspase-9
- Granzyme B pathway - cytotoxic cell protease granzyme B is delivered to sensitive target cells.

All these pathways converge to a common execution phase of apoptosis, which require proteolytic activation of caspases-3/7 from their inactive form. These caspases cause further DNA fragmentation and cellular protein degradation. The molecular mechanism of apoptosis is explained in figure 9.

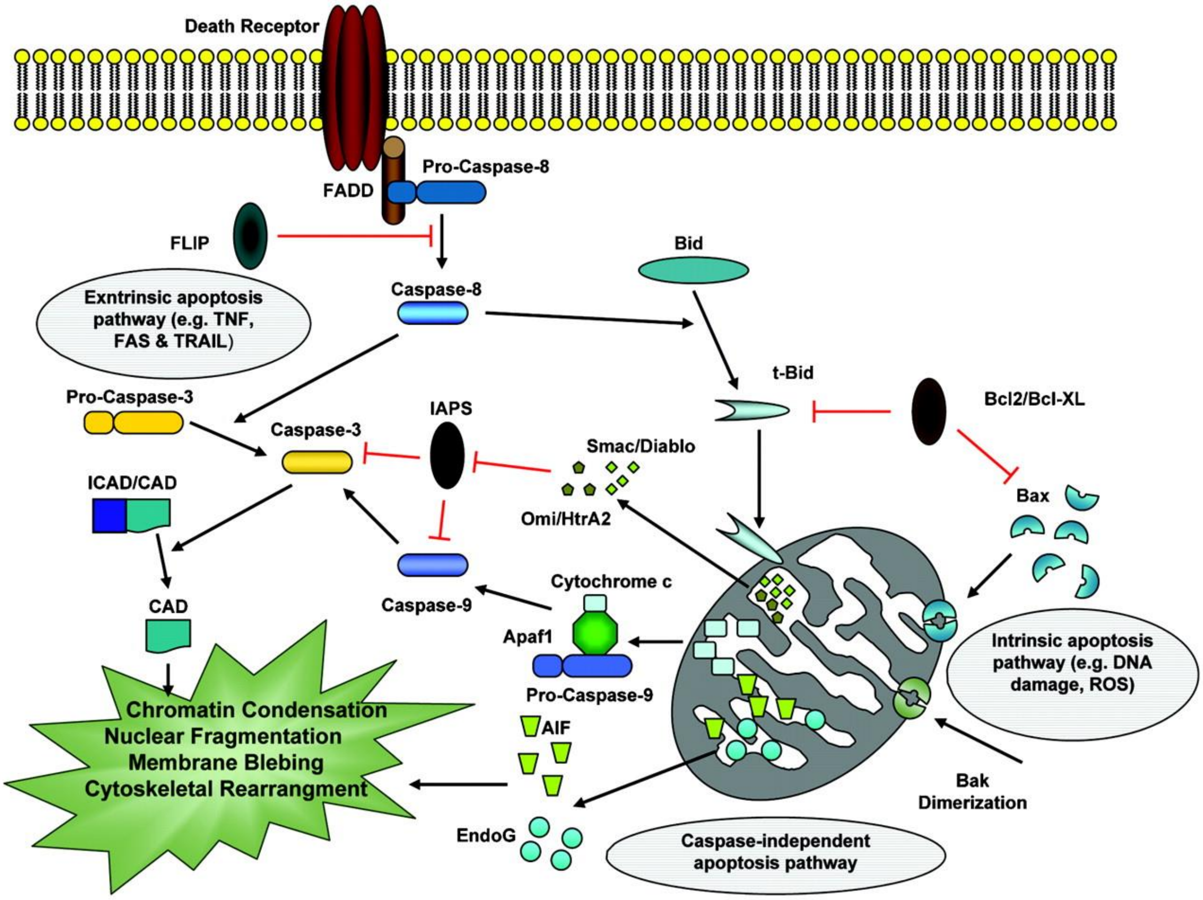

Figure 9: Molecular mechanisms of apoptosis (Adapted from Ghavami S *et al*., 2009)

Thus the failure of apoptosis may lead to cancer. Loss of apoptotic control allows cancer cells to survive longer and accumulate mutations, which further increase its invasiveness. Cancer cells evade apoptosis either by over expression of anti-apoptotic proteins/inhibitors of apoptotic proteins or by under expression of pro-apoptotic proteins/death signals/death receptors/p53 tumour suppressor protein/caspases (Figure 10). Hence, restoring a cell’s ability to undergo natural cell death by inducing apoptosis in any form may combat cancer.

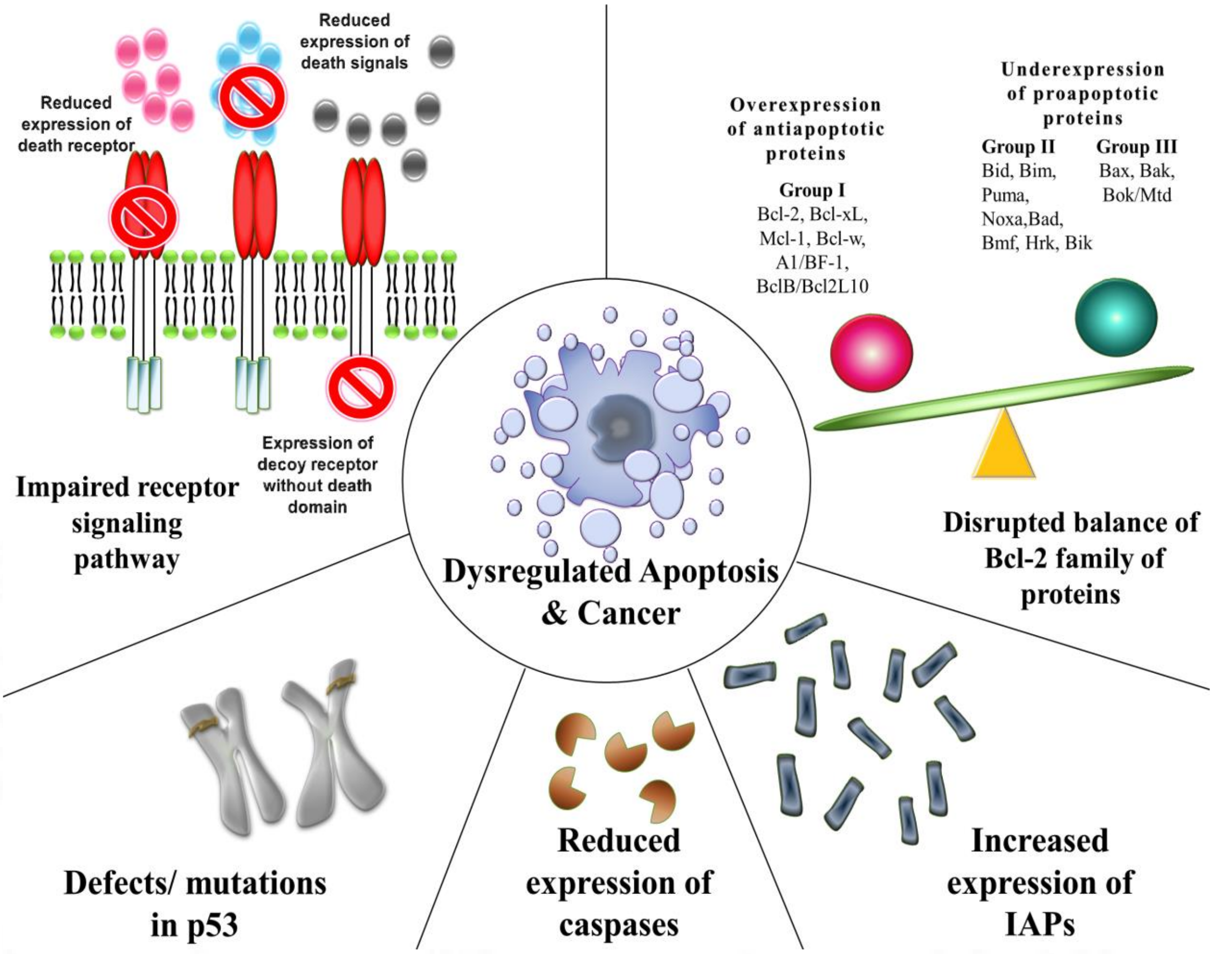

Figure 10: Evasion of apoptosis and carcinogenesis (Adapted from Wong R, 2011).

1.5.2. Photodynamic therapy

Photodynamic therapy (PDT) is a non-invasive, clinically approved therapeutic method for the treatment of cancer, which emerged as an alternative therapy for chemo- and radio-resistant cancer cells (Yang H *et al*., 2021). Also, PDT minimizes most of the unwanted side effects caused by these conventional therapies. PDT uses photosensitizers (PS) for their mechanism of action (Figure 11). Upon light absorption, these PS reaches an excited singlet state, which after intersystem crossing reaches excited triplet state (PS_{Et}). This PS_{Et} can react in two ways inside cells (Calixto G *et al*., 2016):

i) Type I reaction - PS_{Et} react with biomolecules by transferring a hydrogen atom (electron) to form radicals, which react with molecular oxygen to generate reactive oxygen species (ROS) like superoxide, hydroxyl radicals, and hydroperoxides (Figure 11)

ii) Type II reaction - PS_{Et} can react directly with oxygen through energy transfer, generating singlet oxygen (Figure 11)

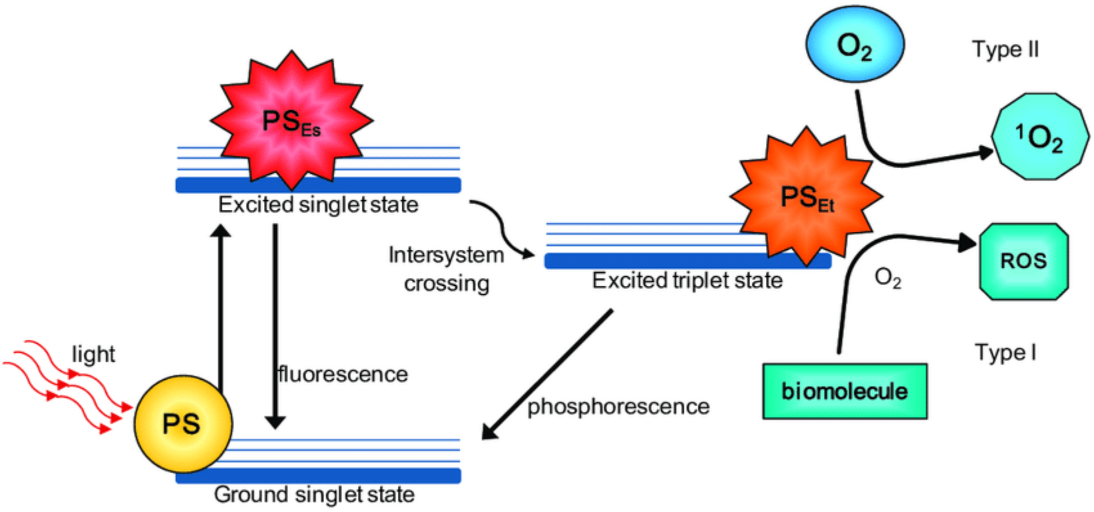

Figure 11: PDT mechanism of action (adapted from Calixto G *et al.*, 2016).

PDT works with the accumulation of photosensitizer (PS) in tumours, which upon light irradiation generate singlet oxygen ($^1O_2$) and other ROS (Figure 11). These ROS trigger intrinsic apoptotic pathways associated with mitochondrial oxidative damage. Hence, PDT can activate late stages of apoptosis bypassing many death signalling pathways and ultimately cause regression of targeted tumours. Structures and molecules that are proximal to the area of ROS generation (i.e., PS localized area) are alone affected by PDT. Also with the usage of localized light irradiation, only the malignant tissue with PS accumulation is affected by PDT. Hence the usage of PS can minimize the potential damage to vital tissues caused by conventional optical fiber insertion. Several Phase I/II clinical studies reported PDT as an effective and safe treatment for locally advanced cancer (DeWitt J *et al.*, 2019).

1.5.2.1. Nanoparticle based PDT

The usage of conventional PS such as porphyrins and other tetrapyrrole derivatives during clinical exploitation suffer from certain limitations. Poor water solubility, aggregation in physiological solution and thus quenching of $^1O_2$ yield, insufficient and lack of targeted delivery, tumour-oxygenation dependency (i.e., PS needs O_2 to generate ROS, but tumour has hypoxia condition), dark toxicity, etc. are some of the limitations of conventional PS. Nanoparticle (NP) based PDT can overcome these obstacles by encapsulating PS inside NP and improve its solubility and stability, thus increasing $^1O_2$ yield (Hong E *et al.*, 2016). Also, NP based PDT helps in active targeted delivery with specific ligands, which enhances PS entry and retention in tumour by EPR effect, relieving the tumour hypoxia by oxygen supplying, etc. The working mechanism of such NP based PDT is explained in figure 12.

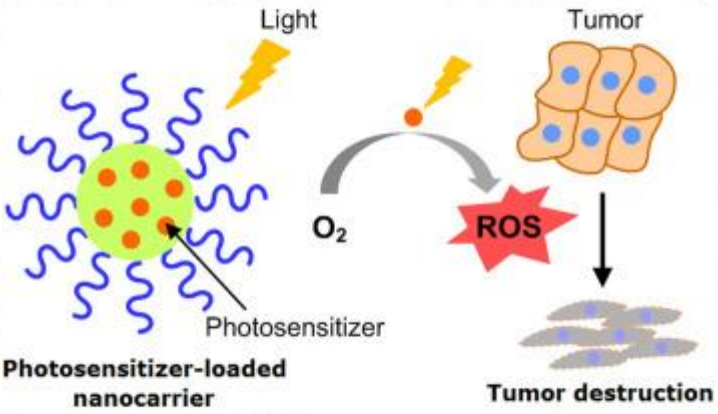

Figure 12: Nanoparticle based PDT to treat cancer (Adapted from Hong E *et al.*, 2016)

1.5.3. Gene therapy

Gene therapy is a future strategy to modulate gene expression level by introducing exogenous genetic materials into specific cells to treat human diseases, including cancer. Several techniques of gene therapy are gene augmentation/supplementation, gene replacement, gene inhibition and killing of specific cells. These different techniques focus on the usage of two genetic materials, DNA and RNA. DNA molecules are commonly used to achieve gain-of-function effects and RNA molecules are mostly used to achieve loss-of-function effects. In case of RNA, a subset of non-coding RNA like miRNA and siRNA (i.e., without protein coding potential) are used (Zhong X *et al.*, 2016).

Several pathological diseases appear as a consequence of abnormal activity of a particular protein. As mentioned in section 1.5.1, a large number of genes are upregulated in cancer and hence the increased expression of proteins, which are responsible for the pathology of disease. The treatments of these pathologies rely on the suppression of particular protein activity. Among the gene therapy techniques mentioned above, gene inhibition can play a main role in the management of these pathological conditions. The discovery of RNAi technology paved way for specific gene inhibition with the use of small RNA molecules. Andrew Fire and Craig Mello were awarded the Nobel Prize of Physiology and Medicine for the discovery of RNAi in 2006. Compared to other methods of gene therapy, RNAi therapy is cost-effective and can transmit silenced gene to next generation. Unlike chemotherapy, RNAi therapy is effective and specific towards cancer cells.

1.5.3.1. Mechanism of RNA interference

RNA interference (RNAi) is a fundamental pathway occurs in several eukaryotes, including animals. RNAi causes specific gene silencing via small double stranded molecules of RNA. Gene expression is the process, by which information stored in the genes of DNA is converted into a functional product called protein. In detail, the genetic information contained in the genes of DNA is transcribed into mRNA (messenger RNA) inside cell nucleus, and then the mRNA leaves the nucleus, interacts with ribosome in cytoplasm, which translates the mRNA into its corresponding protein. The blocking of this protein translation is what RNA interference does (Figure 13). This phenomenon of gene silencing occurs naturally in organism during embryonic development and defence against virus.

RNAi uses different types of RNA for gene silencing, which includes shRNA (short hairpin RNA), siRNA (short interfering RNA), miRNA (microRNA) and piRNA (piwi interacting RNA). siRNA is processed from shRNA, which is synthesized in the nucleus of cells. Both siRNA and miRNA is processed with Dicer enzyme for its function. Compared with miRNA, siRNA binds fully to the complementary mRNA, thus minimizing the off-target effects, while miRNA binds to only 3′ UTR region of mRNA. piRNA interact with piwi-proteins and is produced in a dicer independent manner. Among all these, siRNA finds special attraction for therapeutic purposes, as it has less off-target effects.

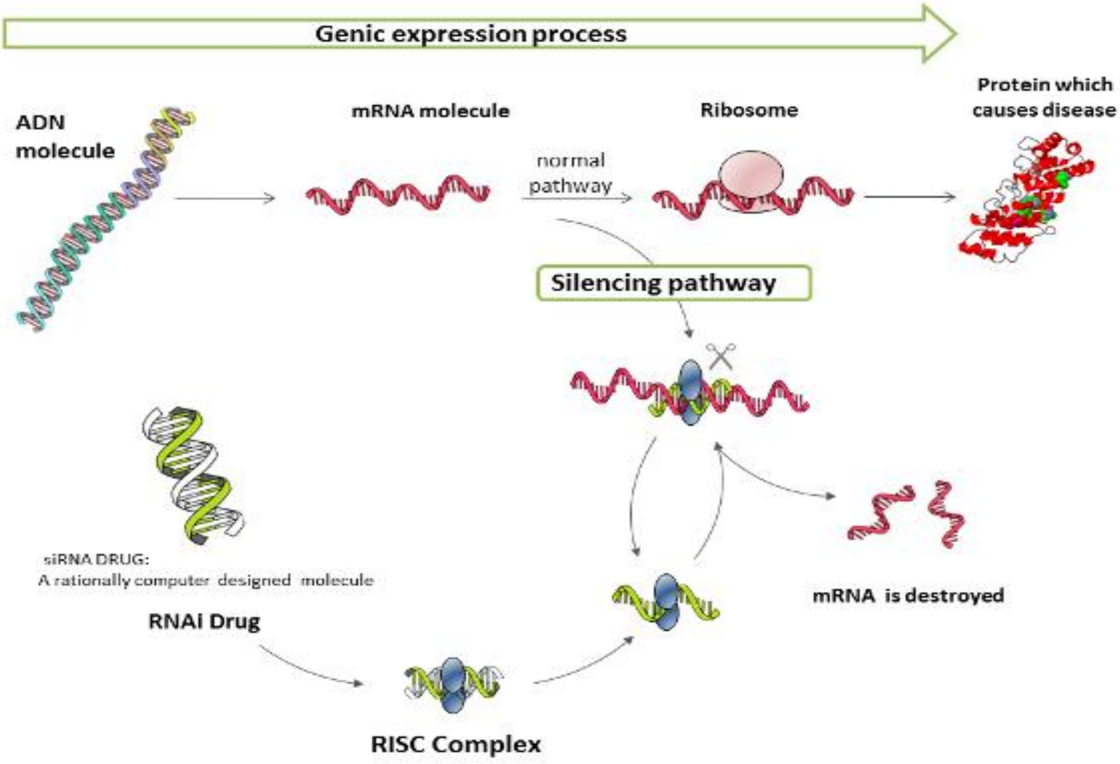

Figure 13: Gene expression and gene silencing.

The detailed mechanism of RNAi is explained in figure 14. RNAi is activated by long double-stranded RNA, which is cleaved into fragments called siRNA duplex by the endonuclease enzyme dicer. Generally, siRNA duplex is 21–27 nucleotides long which are loaded onto RISC (RNA-induced silencing complex). The Argonaute protein (Ago-2) present in RISC cleave and remove the passenger/sense strand of siRNA duplex. The single stranded guide RNA/antisense strand associated with RISC complex act as a guide to target the specific mRNA recognition through complementary base pairing and the Ago-2 protein in RISC degrade the mRNA (Ameres S *et al*., 2007). The endonucleolytic cleavage of mRNA occurs between bases 10 and 11 relative to the 5′ end of antisense siRNA strand, thereby causing mRNA degradation and gene silencing (Dykxhoorn D *et al*., 2006). Alternatively, siRNAs can be artificially introduced into cells to target a specific mRNA for the management of pathologies/genetic origin diseases.

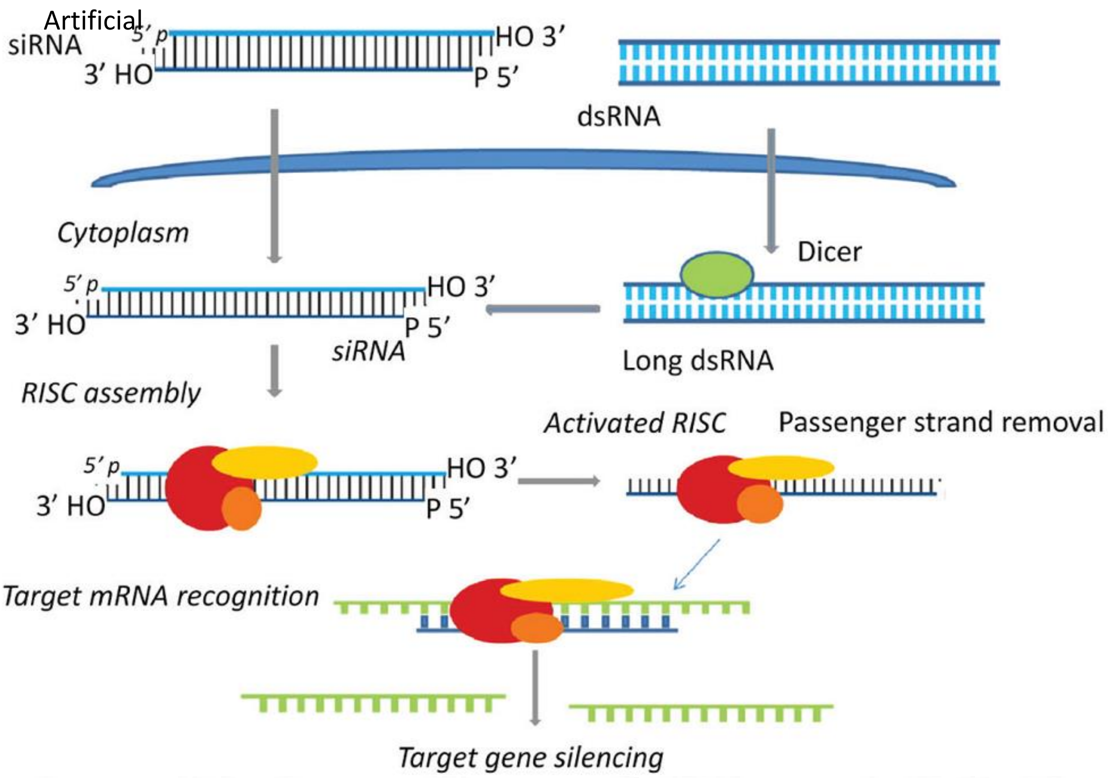

Figure 14: Detailed RNAi mechanism (Adapted from Singh A *et al.*, 2018).

1.5.3.2. Advantages of RNA interference

RNAi technology is a powerful tool for therapeutic purposes due to its two major advantages:

- All cells have biological machinery to implement RNAi.
- Every gene is a potential target, thus the number of “druggable” targets are considerably more.

Compared with traditional drugs, RNAi therapeutics has several advantages in terms of pharmaceutical development:

- RNAi therapeutic drugs can be designed to target almost any protein in human body knowing the target gene sequence.
- RNAi therapeutic drugs specifically silence one target gene.
- In contrast with traditional drugs, which target only existing/already expressed proteins, RNAi inhibit the synthesis/expression of target protein.

- Preclinical development timeline for RNAi therapeutics (1.5-2 years) is shorter than the traditional small molecules (3.5-5.5 years) and monoclonal antibodies (2.5-4 years).
- Compared with traditional drugs, RNAi therapeutic strategy has longer effect, hence reducing the drug administration frequency.

1.5.3.3. Barriers to siRNA delivery

Even though siRNA holds promise as therapeutic gene silencing, the clinical application of siRNA is limited because of some barriers which challenge effective *in vivo* delivery. The systemic application of siRNA drug has to cross certain barriers before reaching the cytoplasm of target cell.

- First, siRNA must cross extracellular barriers, i.e., must navigate the circulatory system of human body until it reaches the target cell/tissue, avoiding aggregation in presence of serum proteins, enzymatic degradation by endogenous nucleases, renal clearance and uptake by reticuloendothelial system (RES) (Figure 15). The maximum half-life of siRNA in serum is 1 h, as it is easily degraded by serum nucleases (Singh A *et al*., 2018). Also, several studies reported that the biodistribution of siRNA showed maximum uptake in kidney, spleen and liver (Singh A *et al*., 2018). Liver and spleen receive high blood flow with fenestrated vasculature and are rich with RES, i.e., they have numerous phagocytes like macrophages and monocytes which engulf foreign particles for elimination. This clearly indicates that these organs will accumulate high concentration of siRNA following systemic administration for rapid clearance from the body.
- Secondly, siRNA must cross intracellular barriers, i.e., it needs to be packaged in vesicles for successful entry inside cells, as it is anionic and hydrophilic. After cell entry, siRNA must escape to cytoplasm from endo or lysosomal compartments before degradation for its gene silencing action (Figure 15) (Xu C *et al*., 2015**).**

- Another most important barrier of siRNA therapy is immune stimulation. Recognition of siRNA by toll-like receptors will activate the innate immunity responses (Singh A *et al.*, 2018).

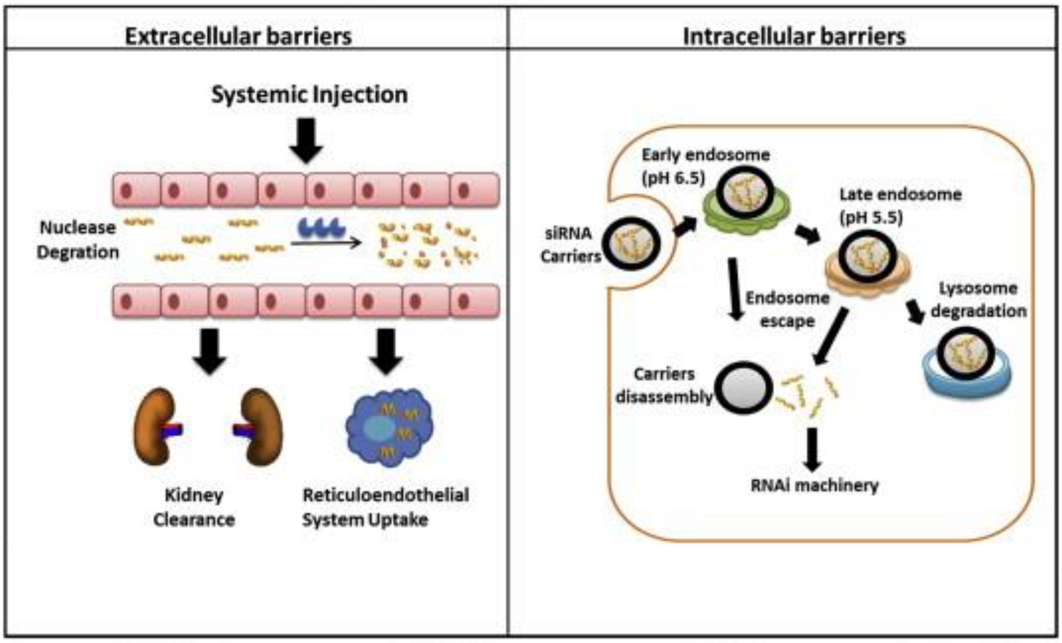

Figure 15: Extracellular and intracellular barriers encountered by siRNA following systemic administration (Adapted from Xu C *et al.*, 2015).

Hence, to achieve efficient delivery of siRNA, an ideal systemic delivery vehicle/vector/carrier must have certain characteristics:

- high loading capacity
- biocompatibility
- avoid serum nuclease degradation
- avoid rapid renal or hepatic clearance
- non-immunogenic
- biodegradable
- should target only necessary cells
- increased cellular uptake
- allow intracellular cytoplasmic release with endosomal escape

1.6. Hypothesis

Considering the importance of having a better platform to visualize and study the dynamics of Zn^{2+} under neuropathological conditions like epilepsy, a dual function fluorescent molecular probe will be worth exploring. Likewise, a bipyridine bridged bispyrrole - BP probe which has found to have high sensitivity and specificity towards Zn^{2+} is hypothesized to give good results for biological imaging and sensing under *in vivo* condition.

Similarly, considering the importance of nanotechnology and its significant advancement in the field of bioimaging and therapy, one of the inherently fluorescing nanoprobes, gold nanoclusters are expected to serve as an excellent bioimaging tool because of their photostability and tunable fluorescent property. It is proposed to use novel route of preparation of these gold nanoclusters using different tripeptides. It is hypothesized that these gold nanoclusters will be suitable for cancer imaging cum therapy.

Peptide stabilized gold nanoclusters are less explored for siRNA based cancer therapy. It is hypothesized that appropriated designed peptides and the gold nanoclusters stabilized with them can efficiently deliver siRNA to cancer cells, thereby providing a real time tracking of siRNA delivery.

1.7. Objectives

The following objectives are formulated based on the above hypothesis:

- To study the dynamics of Zn^{2+} under epileptic condition using a fluorescent ratiometric molecular probe.
- Design and development of fluorescent tripeptide stabilized gold nanoclusters for simultaneous imaging cum photodynamic therapy of cancer.
- Design and development of fluorescent nano gene downregulator for real-time tracking of siRNA based cancer therapy.

CHAPTER 2: LITERATURE REVIEW

2. LITERATURE REVIEW

2.1. Fluorescent molecular probe for zinc ion sensing

2.1.1. Importance of Zn^{2+} sensing

2.1.1.1. Zn^{2+} in human body

Zinc (Zn^{2+}) is a nutritionally essential trace element, which exist in human body as a free or bound form. The bound form of Zn^{2+} is closely associated with enzymes and proteins for their structural and functional role. For example, the structures of DNA, RNA and ribosome are stabilized by Zn^{2+} (Nakashima A *et al*., 2009, MacDonald R, 2000) and the catalytic role of many enzymes also depends on Zn^{2+} (Kim J et al., 2020). As a result, Zn^{2+} is involved in the regulation of various processes in human body such as DNA synthesis, cell proliferation, cell death, reproduction, fetal development, bone formation, brain development, behavioural response, wound healing, immunity, oxidative stress, etc (Roohani N *et al*., 2013, Franklin R *et al*., 2009, Murakami M *et al*., 2008).

The amount of Zn^{2+} in the blood of human body is very low i.e., 12-16 μM, which exist as free chelatable or protein-bound form (Rink L, 2000, Maret W, 2009). The concentration of cheatable zinc (Zn^{2+}) in various eukaryotic cells is in picomolar range (Frederickson C *et al*., 2005). But, some cells of brain, breast, gastro-intestinal tract, pancreas and prostate have high concentration of Zn^{2+} i.e., in millimolar (mM) range. For example, the secretory granules of β-cells in pancreas are packed with insulin and high concentration of Zn^{2+} around 10-20 mM. The epithelial cells of prostate gland and the prostate fluid have 3-4.5 and 10 mM of Zn^{2+} respectively. The mammary cells of breast produce 1-3 μg of Zn^{2+} during lactation. Compared to other organs in body, brain has the highest concentration of Zn^{2+} around 150 mM (De Leon-Rodriguez L *et al*., 2012).

2.1.1.2. Zn^{2+} in brain

Unlike all other essential trace elements, some trace elements such as zinc, iron and manganese are transported into the brain for several neural functions (Takeda A, 2000). 90% of total zinc in brain exists as zinc metalloproteins (Paoletti P *et al.*, 2009). The remaining 10% of total zinc in brain is chelatable zinc (Zn^{2+}). This chelatable zinc is accumulated mainly in the synaptic vesicles of glutamatergic neurons throughout the brain, but mostly in hippocampus (Sensi S *et al.*, 2009, Woodroofe C *et al.*, 2005). Zn^{2+} is co-localized with glutamate in the presynaptic vesicles of glutamatergic neurons. This co-localization leads to the hypothesis of vesicular Zn^{2+} involvement in synaptic neurotransmission (Frederickson C *et al.*, 2005). Some reports suggested that Zn^{2+} can function as a neuromodulator of NMDA (N-methyl-D-aspartate) and GABA (γ-amino butyric acid) receptors present in postsynaptic neurons of mammalian brain (Paoletti P *et al.*, 2009, Frederickson C *et al.*, 2005, Smart T *et al.*, 2004, Huang E, 1997). It is also reported that a little amount of Zn^{2+} can enter into the postsynaptic neurons through these NMDA and AMPA (α-amino-3-hydroxy-5-methyl-4-isoxazolepropionic acid) receptors or through Ca^{2+} channels and may control the activity of target proteins (Huang Y *et al.*, 2008, Grabrucker A *et al.*, 2011). Tamano H *et al.*, 2015 reported that low concentration (nM) of Zn^{2+} in ACSF is crucial for proper synaptic plasticity. The exact role of vesicular Zn^{2+} remains unclear, even though it is reported that these Zn^{2+} containing neuronal circuits are linked with episodic memory, behaviour, emotion and cognitive-mnemonic operations.

2.1.1.3. Zn^{2+} in diseases

In addition to playing roles in physiological condition, Zn^{2+} is involved in many pathological conditions/diseases. The deficiency and dyshomeostasis of Zn^{2+} is a risk factor for neurodegenerative diseases like Alzheimer's, Parkinson's, epilepsy, depression, etc. (Prakash A *et al.*, 2015, Szewczyk B, 2013). Lee E *et al.*, 2015 reported that the movement of Zn^{2+} from presynaptic to postsynaptic neurons can improve the social interaction in autism spectrum disorder. It is also reported that the movement of high concentration of Zn^{2+} to postsynaptic neurons or the excessive concentration of intracellular Zn^{2+} is a reason for neurodegeneration (Qian J *et al*., 2011). Recent reports suggested that the hippocampal neurogenesis is affected by cancer chemotherapy through disruption of vesicular Zn^{2+} in hippocampal mossy fibers. This chemotherapy-induced cognitive impairment can be restructured by a simple alternative treatment like Zn^{2+} supplement in diet (Lee B *et al*., 2017).

Even though Zn^{2+} appears to play an uncertain role in epilepsy till date, it has been reported that the entry of Zn^{2+} into postsynaptic neurons causes selective neuronal cell death during prolonged epileptic seizures (Choi D *et al*., 1998). The increase of Zn^{2+} level in brain is also noted following epileptic seizures in mice and rats (Dudek F, 2001). Zn^{2+} may attenuate GABA receptors in postsynaptic neurons and cause hyperexcitability which will trigger seizure. Dietary Zn^{2+} deficiency is reported to increase seizure but dietary Zn^{2+} supplementation in turn decrease seizure susceptibility, thus Zn^{2+} act as both proconvulsant and anticonvulsant (Fukahori M *et al*., 1990). However, systemic Zn^{2+} supplementation may increase brain Zn^{2+} level without control and may adversely affect the areas outside the seizure focus. Taken together, the connection between Zn^{2+} and epileptic seizure is much higher. However, the involvement of Zn^{2+} in the etiology and manifestation of epileptic seizures is still less clear. Thus Zn^{2+} sensing, its concentration determination and studying its dynamics under physiological and pathological conditions pose high demand. Therefore, better understanding of these Zn^{2+} factors can throw light on understanding the pathology of diseases, which in turn help to design better treatment. Hence with this background, a part of thesis is focussed to study the Zn^{2+} dynamics under neurodegenerative epileptic condition using a fluorescent ratiometric probe.

2.1.2. Fluorescent probes for Zn^{2+} sensing

2.1.2.1. Optical methods of Zn^{2+} sensing

Optical methods of ion sensing are well accepted among other techniques as it is highly sensitive, have wide dynamic range, chemical inertness and have user-friendly operative measures. The sensing of various metal ions in *in vitro*, *in vivo* and in environmental conditions are well established using optical imaging techniques (McRae R *et al.*, 2009). Earlier studies of Zn^{2+} sensing depend on histochemical method like Timm’s staining. Timm’s staining allows visualization of Zn^{2+} under microscope by precipitation with sulphide followed by silver development only in post-mortem specimens (Frederickson C *et al.*, 1990). Hence Timm’s staining cannot provide dynamic information of Zn^{2+} in live samples. Fluorescence based ion sensing methods/probes find special attraction among other optical imaging probes to image mobile Zn^{2+} in live cells/tissues as it is highly sensitive, minimal or non-invasive and have high spatial and temporal resolution (Nolan E *et al.*, 2009).

2.1.2.2. Fluorescent probes for Zn^{2+} sensing

Different fluorescent probes have been reported till date to sense Zn^{2+} in cells/tissues. The first reported fluorescent sensors for sensing cellular Zn^{2+} are TSQ (Frederickson C *et al.*, 1987) and Zinquin (Zalewski P *et al.*, 1993). Both of these probes bind with Zn^{2+} in 1:2 complexes and emit strong blue fluorescence (470 nm) on UV excitation. Following this, various kinds of fluorescent probes for Zn^{2+} sensing have been developed and studied.

Gee K *et al.*, 2002 reported the sensing of Zn^{2+} secretion from pancreatic β cells using a visible wavelength fluorescent probe, FluoZin-3, **9**. A range of similar fluorescent Zn^{2+} sensing probes with different affinities for Zn^{2+} (ZnAF-2, ZnAF-2M, ZnAF-2MM, ZnAF-3, ZnAF-4 and ZnAF-5) were reported by Komatsu K *et al.*, 2005 to study the synaptic release of Zn^{2+} in hippocampus (Figure 16). The disadvantage of these probes (FluoZin-3,**9**, ZnAFs) is its emission @ 515 nm, which is not more favourable for deep tissue imaging and it shows intensity change upon Zn^{2+} binding instead of spectral shift. More recently, two-photon fluorescent probes were developed to sense Zn^{2+}. One of them is ICT based TEO-MPVQ, which offer lower background fluorescence with high sensitivity and accuracy to track the dynamic changes of labile Zn^{2+} in zebra fish (Li W *et al.*, 2020).

Red emitting fluorescent probes for Zn^{2+} sensing is in high demand nowadays among other fluorescent probes, as their spectral window lies outside the autofluorescence range from biological specimens and hence these red emitting fluorescent probes are well suited for deep tissue endogenous Zn^{2+} sensing. A FRET based fluorescent probe conjugated with a mitochondrial targeting moiety (lipophilic triphenylphosphonium) was used to image the mitochondrial Zn^{2+} ratiometrically with its emission maximum @ 630 nm (Sreenath K *et al.*, 2011). Zastrow M *et al.*, 2015 modified some of the already existing PET based probes like blue coumarin-based sensor, benzoresorufin-based red-emitting probes and Zinpyr1 by acetylation, which significantly increased the sensitivity of respective probes and reduced their need for use from µM to nM concentration in live cells/tissues. The acetylation also reduced the background signal of metal-free probes effectively.

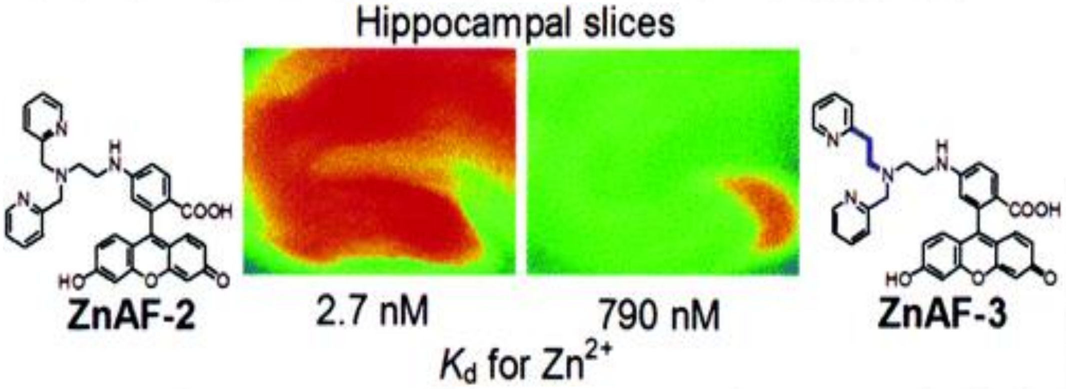

Figure 16: Fluorescence response of ZnAFs sensing extracellularly released Zn^{2+}, with varying affinity towards Zn^{2+}. The emission of ZnAFs is @ 515 nm, which is pseudo-coloured in the above image (Adapted from Komatsu K *et al.*, 2005).

2.1.3. Ratiometric probes and imaging

Among the fluorescent probes, ratiometric probes are of great interest as it has two different measurable signals in the presence and absence of ions (Divya K *et al.*, 2014, Zhang L *et al.*, 2014, Li D *et al.*, 2017). The advantage of using ratiometric probe for ion sensing among normal fluorescent probes is that they increase the sensitivity of ion sensing as well as reduce the artefacts caused by environmental factors like photobleaching, difference in probe concentration, fluctuation in excitation intensity and so on (Philips D *et al.*, 2016).

Woodroofe C *et al.*, 2005 prepared Zn^{2+} sensing ratiometric fluorescent probe based on FRET mechanism by using Zinpyr-1 and coumarin 343 fluorophores linked together by amido-ester or diester moiety, which works after intracellular esterase-catalyzed hydrolysis. Another ratiometric fluorescent probe, ZnIC developed by Komatsu K *et al.*, 2007 using iminocoumarin as a fluorophore and (ethylamino)-dipicolylamine as a Zn^{2+} chelator was highly selective and sensitive for the ratiometric sensing of changes in intracellular Zn^{2+} in cultured cells and in rat hippocampal slices (Figure 17). Even though both the probes mentioned above showed excellent ratiometric potential and fluorescence shift (from 543 to 558 nm) upon Zn^{2+} binding, the emission wavelength is not highly suitable for deep tissue imaging *in vivo*.

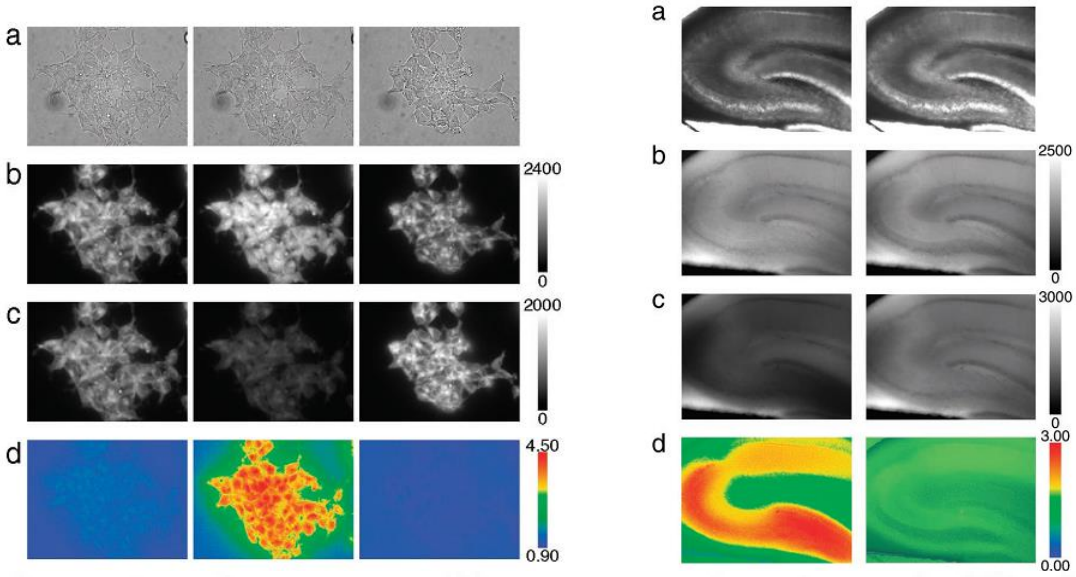

Figure 17: Fluorescence ratiometric imaging of intracellular Zn^{2+} (left) and Zn^{2+} in rat hippocampal slice (right) using ZnIC. HEK293 cells incubated with ZnIC (left 1st column), ZnIC-stained cells exposed to pyrithione and Zn^{2+} (left 2nd column) and after TPEN treatment (left 3rd column). Hippocampal slice incubated with ZnIC (right 1st column) and after TPEN treatment (right 2nd column) Fluorescence images were acquired with excitation @ 480-500 nm. (a) Bright-field images (b) Fluorescence images with emission @ 565-605 nm. (c) Fluorescence images with emission @ 510-550 nm. (d) Ratiometric images generated from (b) and (c). (Adapted from Komatsu K *et al.*, 2007).

An excitation based ratiometric fluorescent probe developed by Bozym R *et al.*, 2006 using carbonic anhydrase was successfully used to quantitatively image the picomolar concentration of intracellular Zn^{2+} in PC-12 cells. This probe uses FRET mechanism to ratiometrically measure Zn^{2+} with two different excitation wavelengths of 365 and 543 nm keeping the emission wavelength constant @ 613 nm. Even though the probe has red emission, ratiometric property and high sensitivity towards picomolar level Zn^{2+} sensing, the UV excitation may cause damage to live cells/tissues when used in time-lapse experiments.

ZnAF-R2 is a cell-permeable, fluorescent probe for ratiometric imaging of Zn^{2+} in cultured macrophages RAW 264.7 (Maruyama S *et al.*, 2002). Even though ZnAF-R2 has ratiometric imaging potential, the emission @ 495 nm is not favourable for *in vivo* imaging. An excellent fluorescent ratiometric probe with dual function i.e., colorimetric or fluorescence shift for visual sensing and ratiometric for quantification was reported earlier for endogenous H_2S sensing (NAP-1 by Zhang L *et al.*, 2014, Figure 18). But this NAP-1 probe shows emission shift from blue to green, which is not favourable for deep tissue imaging *in vivo* like red emitting probes.

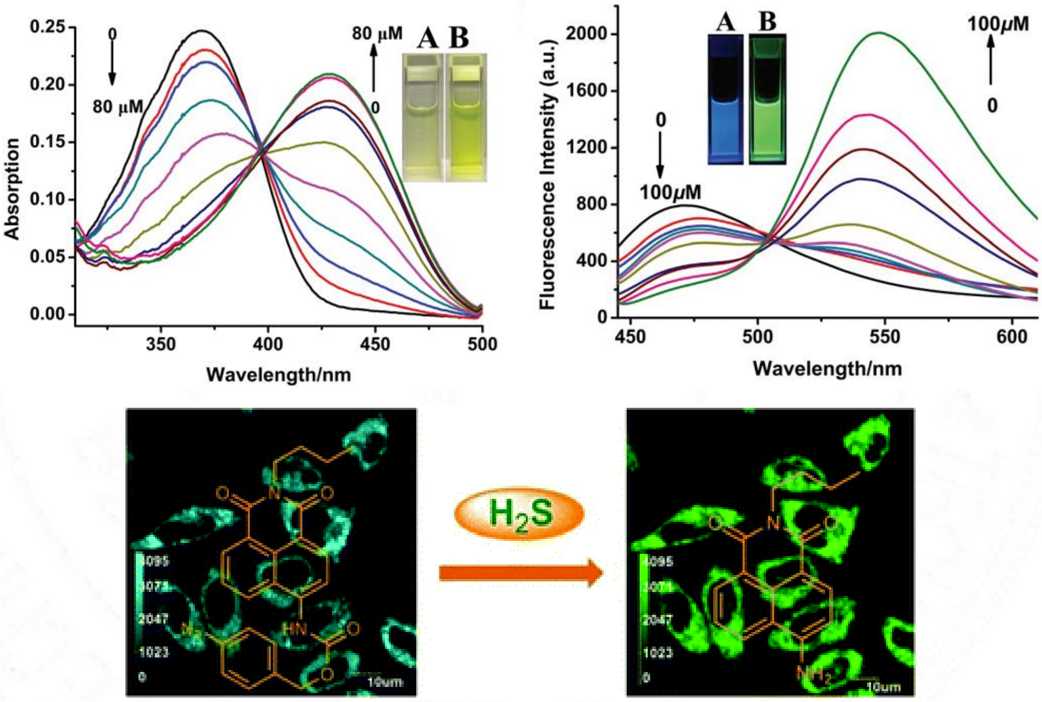

Figure 18: A naphthalimide-azide based colorimetric and ratiometric fluorescent probe, NAP-1, for selective and sensitive detection of hydrogen sulphide. Probe shows dual function property (colorimetric/fluorescence shift from blue to green upon H_2S binding and ratiometric). The top two graphs represent the absorption and emission property and the bottom image represents the cellular ratiometric imaging potential of NAP-1. (Adapted from Zhang L *et al.*, 2014).

In addition, several red emitting ratiometric fluorescent probes with change in intensity for endogenous Zn^{2+} sensing *in vivo* are reported till date (Guo Z *et al.*, 2012), but probes with dual function like fluorescence shift for easy visualization and ratiometric quantification of Zn^{2+} are very few. Ajayaghosh A *et al.*, 2005 reported a simple ratiometric probe based on vinylpyrrole end-capped bipyridine for the visual sensing of Zn^{2+} with red emission ideally suited for the imaging of biological specimens. The ratiometric fluorescent sensor FQ1, a furoquinoline based probe developed by Xue L *et al.*, 2009 for sensing Zn^{2+} in living cells. FQ1 exhibits large stokes shift of 199 nm and follows ICT mechanism for Zn^{2+} sensing with a red shift of 75 nm from 545 nm (Figure 19). FQ1 shows red emission (620 nm) upon binding with Zn^{2+} under visible light excitation, which is more favourable for deep tissue imaging without causing any tissue damage. Thus these dual function probes for Zn^{2+} sensing with red emission are highly demanding for visualization and accurate quantification of Zn^{2+} in complex biological tissues.

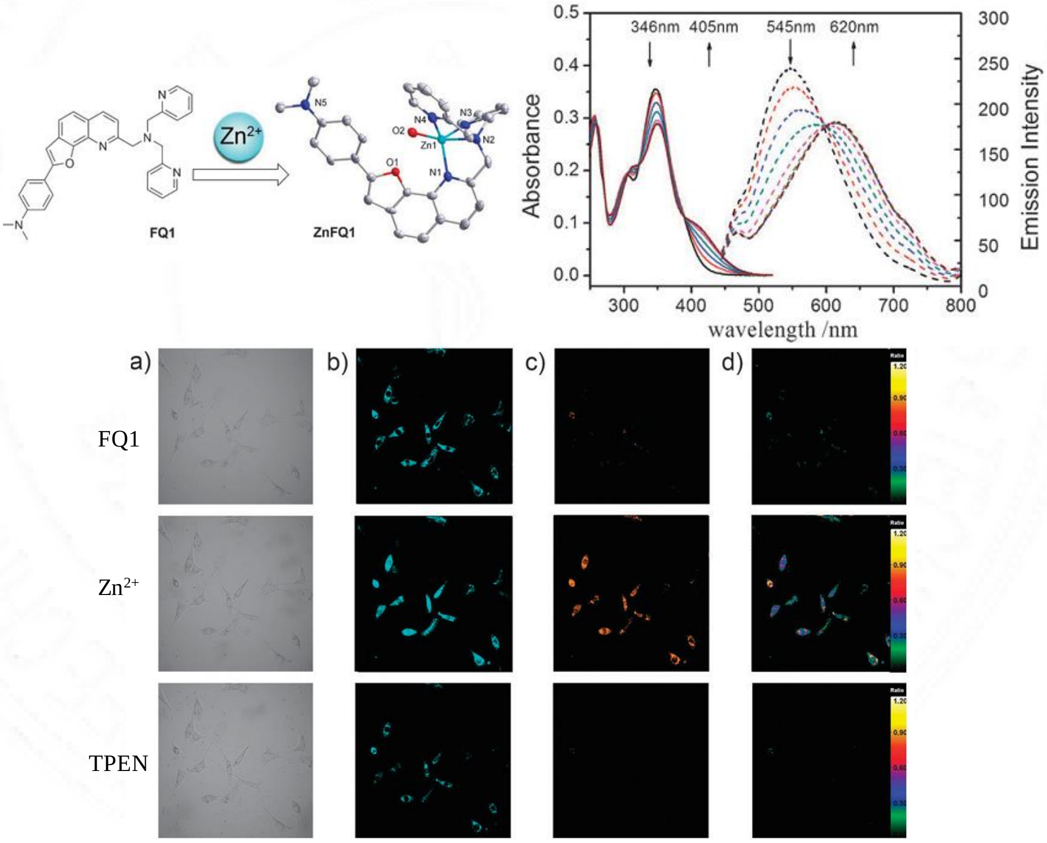

Figure 19: Schematic representation of FQ1 (top left), absorption and emission spectra of FQ1 with response to Zn^{2+} (top right) and confocal fluorescence images of intracellular Zn^{2+} in NIH 3T3 cells with FQ1 (bottom). (a) Bright-field transmission images (b and c) Fluorescence images with emission @ 510–550 and 600–650 nm respectively (d) Ratiometric images generated from (c) and (b) (Adapted from Xue L *et al.*, 2009).

Hence a part of thesis is mainly focussed on studying the dynamics of Zn^{2+} in hippocampus under a neurodegenerative condition like epilepsy using a bipyridine bridged bispyrrole (BP) dual function fluorescent molecular probe.

2.2. Fluorescent nanoprobe for cancer imaging and therapy

Fluorescent nanoparticles have obtained tremendous attention nowadays because of its application in light-emitting displays, optical sensors, biomedical imaging, etc. Among the fluorescent nanoparticles, semiconductor quantum dots were at focal point of research for these applications until recently, but the toxicity limited their application in biomedical field (Mancini M *et al.*, 2008). On the other hand, metal nanoprobes/nanoclusters finds special attraction compared to semiconductor quantum dots and organic dyes because of their low toxicity, ultrafine size, excellent photostability, etc (Luo Z *et al.*, 2008).

2.2.1. Gold based fluorescent nanoprobes

Ultra-small gold particles called nanoclusters (AuNCs) have several advantages over nanoparticles like fluorescence, catalytic activities, two-photon absorptions, etc. Different methods of gold nanocluster synthesis by top-down and bottom-up approaches have been extensively studied over the years. These include chemical reduction of Au(III) salts with suitable reducing agents in presence of stabilizing agents, core etching of large gold nanoparticles to small quantum clusters, biomacromolecule as reducing cum stabilizing ligand, etc (Baral A *et al.,* 2017). Template-assisted synthesis is considered as simple and efficient method to control the size and morphology of gold nanoclusters. Thiol stabilizing agents replaced phosphine stabilizing agents in recent times, owing to its high affinity towards gold atoms and biocompatibility nature. The size and emission profile of gold nanoclusters can be tuned by using different synthetic strategy.

Gold nanoclusters have been studied extensively for biomedical applications, such as biosensing (Zhang E *et al*., 2016), bioimaging (Han R *et al*., 2019), cancer therapy (Yang H *et al.*, 2021), antibacterial activity (Zhang E *et al.*, 2016), catalytic activity (Zhang Y *et al.*, 2020), etc.

2.2.2. Fluorescence enhancement in metal nanoclusters

Even though, gold nanoclusters showed excellent fluorescence stability against photobleaching, the low quantum yield clusters are not suitable for biological imaging. Hence, the enhancement of fluorescence quantum yield is necessary for using gold nanoclusters as successful biological imaging agent. Several studies reported different methods of fluorescence enhancement in gold nanoclusters which are explained in this section. Table 1 summarize the fluorescence quantum yield of gold nanoclusters obtained by different synthetic approaches.

Synthesis methods	**Fluorescence QY**	**Literatures**
Employing L-3,4-dihydroxyphenylalanine (L-DOPA) as a reducing/capping reagent	1.7%	Annie Ho J *et al.*, 2012
NIR-emitting AuCs capped with lipoic acid	< 2.5%	Nair L *et al.*, 2015
Protected by monolayers of glutathione	$(3.5\pm1.0)\times10^{-3}$	Link S *et al.*, 2002
DNA as template to prepare gold/silver nanoclusters from Au^{3+}, Ag^{+} and DNA (5′-CCCTTAATCCCC-3′)	4.5%	Chen W *et al.*, 2011
Bovine serum albumin molecules as templates and reductants	5.2%	Xie J *et al.*, 2009
11-Mercaptoundecanoic acid (11-MUA) as the protecting group to reduce Au^{3+} with $NaBH_4$ in methanol solutions	6.92%	Guo Y *et al.*, 2012
Employed poly(N-vinylpyrrolidone) (PVP) as stabilizer of the gold clusters	12.5%	Santiago González B *et al.*, 2010
N,N-dimethylformamide as a weak reducing agent as well as stabilizing ligand	14.28%	Liu X *et al.*, 2008
Aggregation induced emission of gold nanoclusters with glutathione	15%	Luo Z *et al.*, 2012
High photostability & enhanced fluorescence of gold nanoclusters by silver doping	16%	Le Guével X *et al.*, 2012
Poly(amidoamine) (PAMAM) dendrimers as stabilizer and capping agent	41±5%	Zheng J *et al.*, 2003

Table 1: Different synthetic approaches of gold nanoclusters and its fluorescence quantum yield

Luminescent gold nanoclusters ($Au_{22}(SG)_{18}$) based on glutathione (SG) with a quantum yield (QY) of 60% were synthesized by rigidifying its gold shell with bulky tetraoctylammonium (TOA) (Pyo K *et al.*, 2015). The carboxylate anions of glutathione were ion paired with bulky TOA cations in toluene phase (Figure 20). These TOA-paired Au_{22} clusters were stable in toluene and also soluble in many organic solvents like ethanol, methanol, DCM, acetonitrile, etc. In contrast, the TOA-unpaired plain $Au_{22}(SG)_{18}$ in water has only 7% QY calibrated with Rhodamine B. Thus the study reported an effective strategy to enhance the fluorescence of gold clusters by rigidifying the Au(I)−thiolate shell.

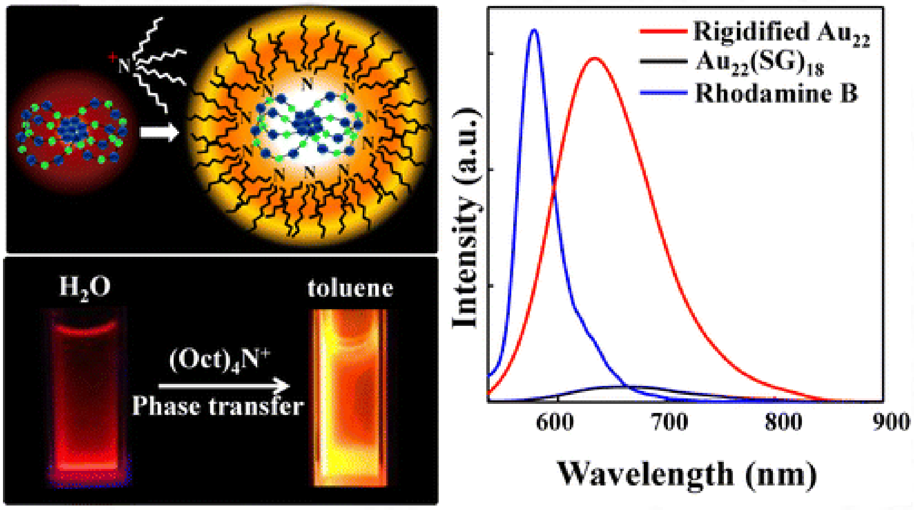

Figure 20: Schematic representation of binding of TOA to $Au_{22}(SG)_{18}$ clusters (top left) (Au-blue; S-green), photograph under UV lamp irradiation (bottom left) and fluorescence spectra (right) of $Au_{22}(SG)_{18}$ in water and TOA-Au_{22} clusters in toluene. (Adapted from Pyo K *et al.*, 2015).

A versatile and simple preparation of self-assembled gold nanoclusters with a 4-fold fluorescence enhancement (QY 25%) from free gold nanoclusters (QY 7%) was developed by Yahia-Ammar A *et al.*, 2016. Here, the gold nanoclusters synthesized with reduced glutathione were cross-linked into nanoparticles (120 nm size) using a cationic polymer PAH (poly(allyl amine hydrochloride)). The electrostatic interaction between PAH and surface ligand of gold nanoclusters causes the fluorescence enhancement due to aggregation induced emission phenomenon (AIE).

Luo Z *et al.*, 2012 reported a simple one pot synthesis of highly fluorescent Au-thiolate nanoclusters with glutathione as the reducing cum protecting agent. The controlled aggregation of non-luminescent oligomeric Au(I)-thiolate complexes by either solvent-induced or cation-induced method generated highly fluorescent Au-thiolate nanoclusters with a QY of 15% (Figure 21). This fluorescence enhancement is based on aggregation induced emission (AIE) mechanism.

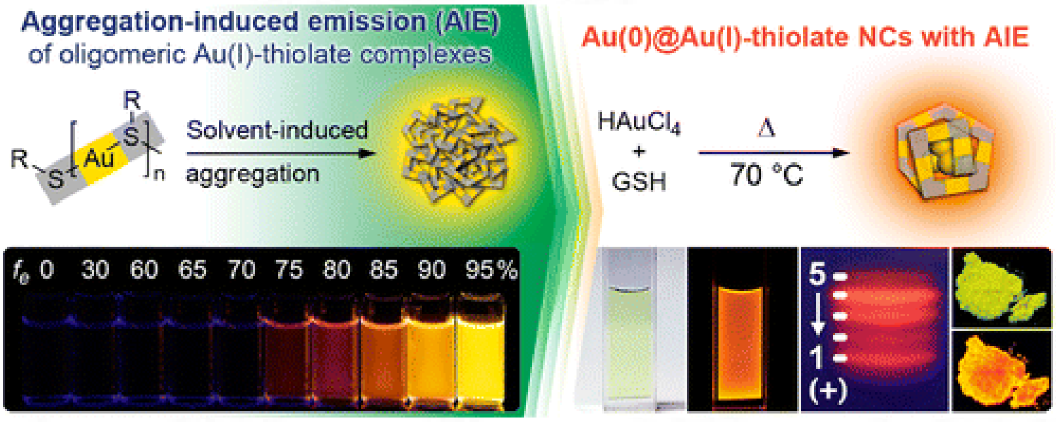

Figure 21: Aggregation induced emission of Au-thiolate nanoclusters. Solvent-induced aggregation of non-luminescent oligomeric Au(I)-thiolate complexes resulted in the fluorescence enhancement of Au-thiolate nanoclusters (Adapted from Luo Z *et al.*, 2012)

Few other studies reported that the fluorescence of gold nanoclusters can be enhanced by silver atom substitution in the gold core. Wang S *et al.*, 2014 reported a 200-fold fluorescent enhancement of gold nanoclusters with silver doping. The rod shaped Au_{25} nanocluster has a low QY (0.1%), which when substituted with silver atom for gold in the 13th atom drastically enhance the fluorescence with 40% QY. Le Guével X *et al.*, 2012 prepared gold nanoclusters with a controlled amount of Ag, which resulted in intense 5-fold fluorescence enhancement with 16% QY and long lifetime of >200 ns. Another metal enhanced fluorescence in gold nanoclusters was reported by Kim J *et al.*, 2017, in which Au_{25} clusters were adsorbed onto $Ag@SiO_2$core–shell nanoparticles resulted in 7-fold fluorescence enhancement than free Au_{25} clusters.

2.2.3. *Peptide stabilized Gold nanoclusters*

Different biosynthetic methods of gold nanocluster are reported earlier with proteins, enzymes and peptides. Among these, the peptide stabilized gold nanoclusters lack extensive studies. The advantages of peptide stabilized nanoclusters are that they are biocompatible; allow sequence specific tuning of fluorescence, possibility of different applications based on custom designed sequences.

A facile method for the synthesis of fluorescent gold nanocluster using peptide and mercaptoundecanoic acid as co-templating ligands was reported by Nguyen P *et al*., 2017. The as-synthesized gold nanoclusters were used for the preparation of gold nanocluster/graphene complex nanosensor for the sensing of enzyme matrix metalloproteinase-9 (MMP-9), abundantly secreted by cancer cells. Graphene quenches the fluorescence of gold nanoclusters. The peptide was designed to possess MMP-9 cleavage site, which get cleaved when encounter with MMP-9 in cancer environment, releasing gold nanoclusters from graphene, thus resulting in "turn-on" fluorescence (Figure 22). Even though, the study prepared red emitting gold nanoclusters with peptide as stabilizing agent, the use of MUA and $NaBH_4$ as strong reducing agent during synthesis may limit the usage of this complex in *in vivo* conditions.

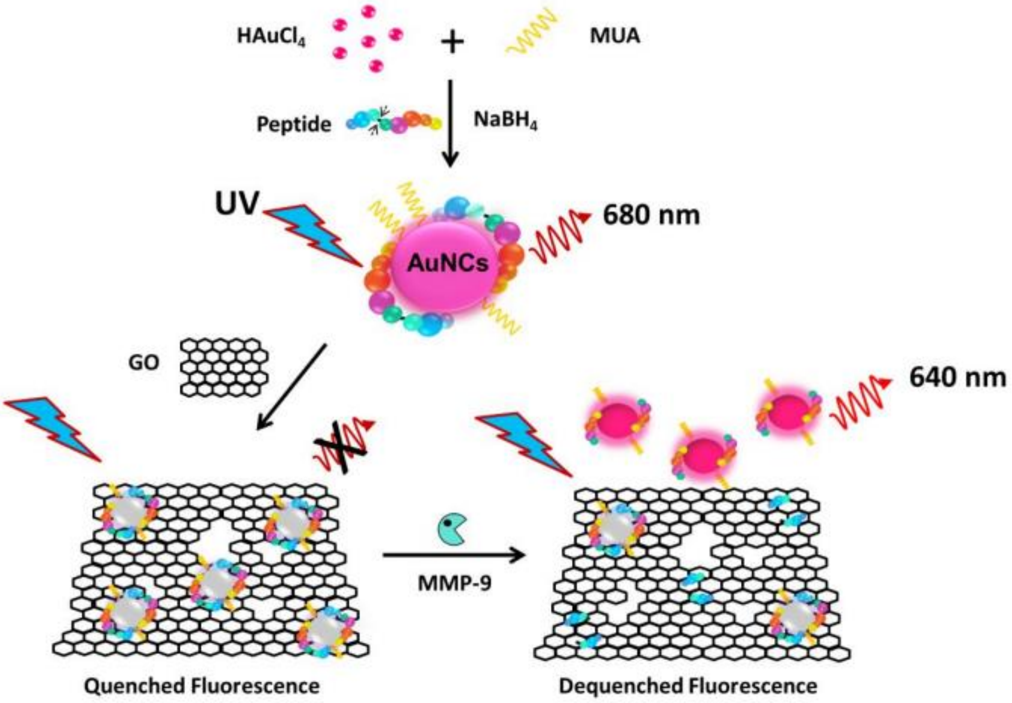

Figure 22: Schematic diagram showing the synthesis and application of fluorescent peptide-mercaptoundecanoic acid co-stabilized gold nanoclusters (peptide-MUA/AuNCs) for the sensing of metalloproteinase-9 (Adapted from Nguyen P *et al*., 2017).

Zhai J *et al.*, 2015 reported H_2N-CCYKKKKQAGDV-COOH peptide stabilized gold nanocluster for imaging and counting $\alpha_{IIb}\beta_3$ integrin on a single-cell. The first part of peptide CCY reduces and stabilizes Au cluster and the second part KQAGDV is specific for integrin. Even though the clusters have red emission, the quantum yield of these clusters was not mentioned. Zhang Y *et al.*, 2018 reported gold nanoclusters modified by a small peptide (H_2N–CGPDGRDGRDGPDGR–COOH) to target integrin $\alpha_v\beta_3$ rich U87-MG glioblastoma cells and to catalyze H_2O_2 to produce superoxide anion radicals in oxidative pressure-type cancer cells (Figure 23). These gold nanoclusters emit blue fluorescence (420 nm) and showed significant increase of ROS level in cancer cells, resulting in apoptosis.

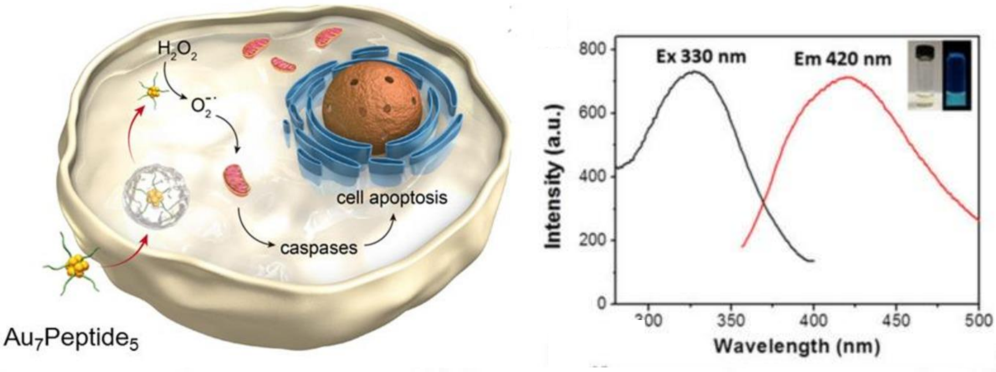

Figure 23: Schematic representation of peptide templated gold nanocluster inducing apoptosis through enzyme like catalysis (left), Absorbance and fluorescence spectra of gold nanocluster - Inset showing photographic images under visible and UV light (right), (Adapted from Zhang Y *et al.*, 2018).

Another simple, green one-step peptide biomineralization method was employed to prepare the peptide–AuNCs with 420 nm emission for the sensing of protein kinase activity (Song W *et al.*, 2015). The peptide H_2N–CCYLRRASLG–COOH was used both as reducing cum stabilizing agent for the synthesis of gold nanoclusters under alkaline conditions. CCY region can reduce Au^{3+} into peptide through phenolic group of Y (tyrosine) and stabilize the cluster through –SH group of C (cysteine). Though the above two peptide stabilized gold nanocluster is biocompatible due to green synthesis method, its emission is not suitable for biological imaging.

Three different types of gold nanoclusters emitting different fluorescence (blue, green and red) was developed using a thiol containing dipeptide (Leu-Cys) as stabilizing agent and sodium borohydride/trisodium citrate as reducing agent (Figure 24) (Baral A *et al*., 2017). Even though the study reported the size of red emitting gold nanoclusters, it failed to report the size of both blue and green emitting gold nanoclusters. But the study stated that the photoswitching property of green and red emitting clusters is due to variation of the cluster size. Also, it uses strong reducing agent for the synthesis, which is not favourable for *in vivo* imaging and the quantum yield of these dipeptide stabilized red emitting gold nanoclusters is very low (1.69 %) with respect to rhodamine B.

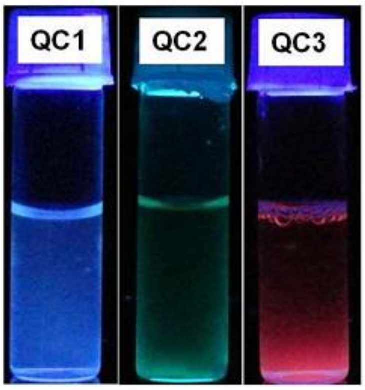

Figure 24: Different colour emitting gold quantum clusters (QC) under UV light developed by thiol containing dipeptide (Leu-Cys) as stabilizing agent and sodium borohydride/trisodium citrate as reducing agent (Adapted from Baral A *et al*., 2017)

Another study reported CCYLQLQAEER–NH_2 peptide stabilized gold nanocluster for tumour targeting and imaging (Bi F *et al*., 2016). In spite of its red emission, these clusters also have a low quantum yield (2.86%). Recently, Li Y *et al*., 2019 used $CCYR_6H_4$ peptide to synthesize gold nanoclusters with red emission (QY 12%) for mercury detection in both waste water and in intracellular condition. Thus, a simple and green one-step synthesis method to obtain peptide-stabilized gold nanoclusters with red emission and high quantum yield is in urgent demand.

2.2.4. Gold nanoclusters for bioimaging and cancer therapy

Gold nanocluster synthesis uses different surface modification methods for variety of application. Typical surface modification methods include ligand exchange, chemical conjugation, physical conjugation, and bioconjugation. These surface property or modification allows them to use for excellent bioimaging with cancer targeting, diagnosis and the simultaneous therapy.

BSA-conjugated gold nanoclusters with 640 nm red emission and 6% QY were applied for fluorescence imaging of gastric cancer cells (Zhang E *et al.*, 2016). Self-assembled gold nanoclusters using a cationic polymer based cross-linking were developed recently with a bright fluorescence and long lifetime for cellular imaging and enhanced drug delivery (Yahia-Ammar A *et al.*, 2016). Another good example of multifunctional tumour theranostic system composed of gold nanoclusters conjugated with pH-responsive poly(N-isopropyl acrylamide-co-acrylic acid) nanogels, chemotherapeutic drug doxorubicin and tumor targeting peptide iRGD were reported earlier for tumour targeting, imaging and therapy by controlled release of doxorubicin (Zhang E *et al.*, 2016, Su S *et al.*, 2013).

Recently, gold nanoclusters with several to tens of gold atoms and < 3 nm in diameter have emerged as a potential PS candidate for PDT, because of their chemically pure and known composition, minimal dark toxicity, long triplet-state lifetime (µs) favourable for excess ROS generation and rapid clearance to avoid potential systemic toxicity (Han R *et al.*, 2019). Numerous previous reports have illustrated the feasibility of using gold nanoclusters as PS agent for PDT.

Recently, Cui H *et al.*, 2017 developed a theranostic gold cluster nanoassembly (Au CNA) by self-assembly of gold nanoclusters (Au NC) based on protein cross-linking approach, which showed improved tumour targeting with NIR emission and ROS generating efficiency than Au NC under both *in vitro* and *in vivo*. Thus Au CNA can act as a diagnostic tool as well as photosensitizer for cancer PDT (Figure 25).

Another efficient *in vivo* PDT system namely AuNC@DHLA (dihydrolipoic acid coated gold nanocluster) was developed by Han R *et al.*, 2019. AuNC@DHLA has 620 nm emission @ 488 nm excitation. In addition, AuNC@DHLA showed large penetration depth in tissue (620 nm emission with 800 nm fs laser), high two-photon (TP) absorption cross section ($\sigma_2 \sim 10^6$ GM), strong ROS generation ability and tumour regression with negligible *in vivo* toxicity (Figure 26). This AuNC@DHLA follow type I mechanism of PDT. With all these properties, AuNC@DHLA served as an excellent photosensitizer for efficient PDT *in vivo*.

Figure 25: Gold clusters nanoassembly (Au CNA) for near-infrared fluorescent imaging and photodynamic therapy (PDT) *in vitro* and *vivo* (Adapted from Cui H *et al.*, 2017).

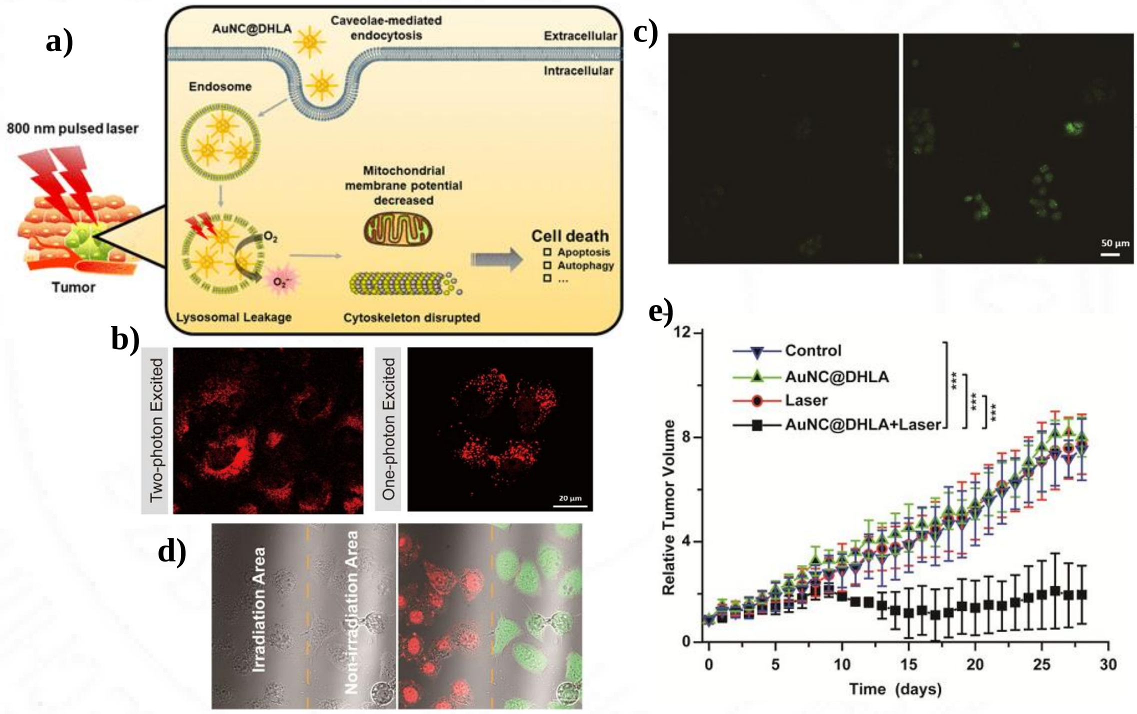

Figure 26: a) Schematic illustration of PDT of cancer by AuNC@DHLA, b) Two-Photon and One-Photon Exciatation images of HepG2 cells treated with AuNC@DHLA, c) ROS generation measured by DCFH-DA in control (left) and AuNC@DHLA (right) treated cells irradiated with laser, d) cell viability using Calcein-AM/Propidium Iodide in AuNC@DHLA treated laser irradiated cells, e) Tumor growth curve of HepG2-tumor-bearing nude mice in different treatment groups within 28 days (Adapted from Han R *et al.*, 2019).

Another simple protein stabilized gold nanoclusters (BSA-Au NCs) were examined for its ROS and singlet oxygen generation efficiency in breast cancer cells by Poderys V *et al.*, 2020. These BSA-Au NCs generate ROS upon light exposure and induce apoptosis in cancer cells with relative biocompatibility under non-irradiating condition. Thus, based on different ligand functionalization, gold nanoclusters can be used for cancer imaging cum therapy.

2.3. Fluorescent nano gene downregulator for cancer imaging cum therapy

2.3.1. Genes upregulated in cancer

As mentioned in section 1.5.1, apoptosis play a crucial role to maintain tissue homeostasis by balancing cell death with cell proliferation and hence prevent cancer. Cancer cells mainly evade apoptosis by over-expression of anti-apoptotic proteins like Bcl-2, Bcl-xL, Mcl-1, etc. or by over-expression of inhibitors of apoptotic proteins (IAPs) like survivin, livin, XIAP, c-IAP1, c-IAP2, NAIP, etc. It is reported that cancer cells express high level of Bcl-2, which blocks the release of cytochrome c from mitochondria by binding with pro-apoptotic protein Bax. The silencing of Bcl-2 initiated massive p53-dependent apoptosis even in the absence of genotoxic drugs to activate p53 (Jiang M, 2003). Trisciuoglio D *et al.*, 2017 reported that Bcl-xL promotes and maintain cancer stem cell phenotype and contributes to the aggressiveness of both melanoma and glioblastoma. The overexpression of Bcl-xL increases migration, invasiveness of tumour cells and suppressing the expression of Bcl-xL can inhibit proliferation in drug resistant cancer cells.

Overexpression of P-glycoprotein and IAP are the two common mechanisms of multidrug resistance in cancer cells. IAP family proteins are characterized by the presence of one or more baculovirus IAP repeat (BIR) domains. This class of proteins prevent caspase activation by interacting with caspases through BIR domain and inhibit apoptosis induced by various stimuli. Survivin, a member of IAP protein family has a single BIR domain. Survivin regulates cell division, promotes angiogenesis and suppresses apoptosis. Survivin is largely expressed in most of the cancers (90-97% in breast cancer), but undetectable in normal adult tissues (Li D *et al.*, 2018). This increased survivin expression in breast cancer patients is a prognostic marker associated with decreased overall survival. Hence, survivin serves as an attractive target for gene therapy in cancer (Jha K *et al.*, 2012). Hence downregulating these anti-apoptotic genes or IAPs can enhance apoptosis in cancer. The downregulation can be achieved by delivering siRNA against these genes.

2.3.2. siRNA delivery for cancer

The delivery of siRNA to down-regulate genes is turning into a remarkably attractive method for suppressing tumour cell growth and invasion. Figure 27 shows the timeline of milestones and discoveries in the field of siRNA. However, the effective gene silencing by naked siRNA is very low, as they are prone to degradation by nucleases in bloodstream. Also, the negative charge and large size hinder its entry across cell membrane. Thus, efficient delivery is a main issue for siRNA therapy. Best combination of anticancer siRNA and efficient delivery vector can pave way for successful clinical application of siRNA. Systemic siRNA can be delivered via three main approaches: chemical modification, viral and non-viral vectors. Non-viral vectors are preferred nowadays over viral vectors and chemical modification, because of their ease of synthesis and safety. The use of viral vectors can induce insertional mutagenesis and have undesired immune response.

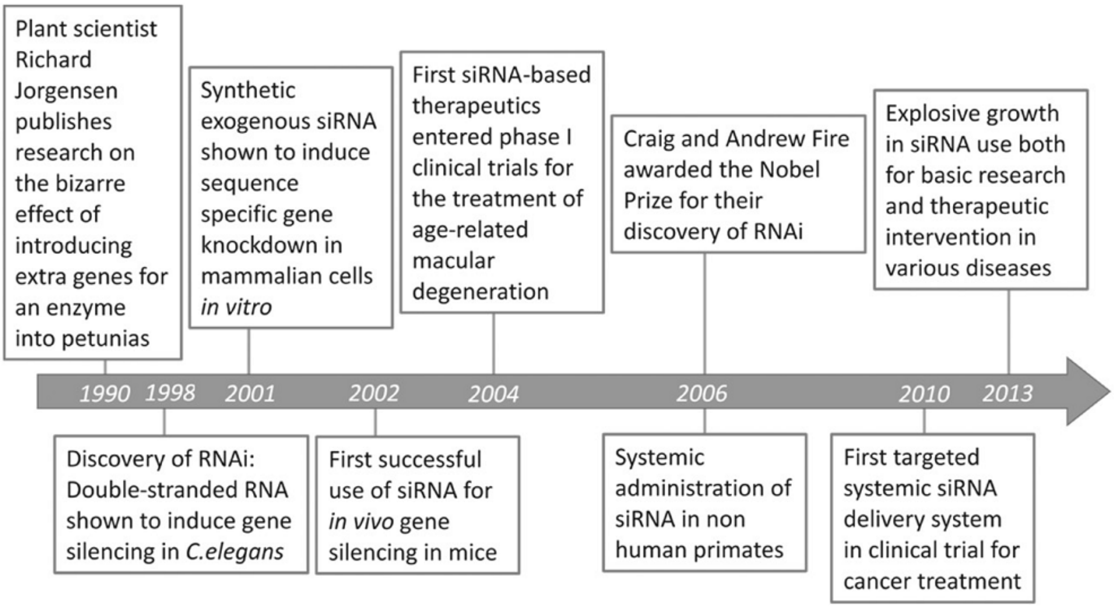

Figure 27: Timeline of discoveries in the field of siRNA (Adapted from Singh A *et al.*, 2018).

Also, conventional vectors for siRNA delivery suffer from the following limitations:

- Toxicity
- Non-traceability
- Inability to target cancer cells
- Instability in circulation
- Failure of endosomal escape

2.3.3. Nanoparticle based siRNA delivery

Nanotechnology has made significant advances in the development of efficient siRNA delivery vectors. Currently developed non-viral siRNA delivery vectors for cancer therapy are lipid based siRNA delivery vectors, polymer based siRNA delivery vectors, conjugate siRNA delivery vectors, co-delivery of siRNA and anticancer drugs, and inorganic nanoparticle (quantum dots, iron oxide, carbon nanotubes, and gold nanoparticles) based siRNA delivery vectors (Singh A *et al.*, 2018). The advantages of using nanoparticles for siRNA delivery are prolonged half-life of siRNA in blood, enhanced pharmacokinetics and targeting tumour tissues with Enhanced Permeation and Retention (EPR) effect.

Lipid based nanoparticles have been extensively used as drug delivery vectors. Among them, cationic liposomes are routinely used for siRNA delivery into mammalian cells *in vitro* (Taetz S *et al.*, 2009). However, many problems are reported with lipid-based delivery vectors *in vivo* because of rapid clearance by liver, lack of target tissue specificity and toxicity. Also, the surface interactions of cationic liposomes with cancer cells create an electrostatically derived binding site barrier effect, which inhibit further interaction of the delivery vector with tumour spheroids. Cationic polymers like polyethyleneimine (PEI), chitosan, hyaluronic acid are attractive delivery sources because of its association with negatively charged siRNAs. But all these polymers showed some toxicity towards cells.

A number of inorganic nanoparticles are emerging as potential siRNA delivery vectors for cancer imaging and therapy other than the above mentioned organic nanoparticles. Carbon nanotubes (CNTs) are one of the inorganic nanoparticles used for siRNA delivery. CNTs are classified as single-walled CNTs and multiwalled CNTs. Zhang *et al*., 2006 used positively charged single-walled CNTs functionalized with telomerase reverse transcriptase (TERT) siRNA for suppressing tumour growth. However, several studies reported the potential toxicity of CNTs. Medarova Z *et al*., 2007 reported an excellent dual-purpose probe with superparamagnetic iron oxide nanoparticle, Cy5.5 dye and myristoylated polyarginine peptide for simultaneous multimodal MRI, NIR imaging and delivery of siRNA against survivin, which significantly increased cancer cell apoptosis *in vitro* and in xenograft mouse models (Figure 28).

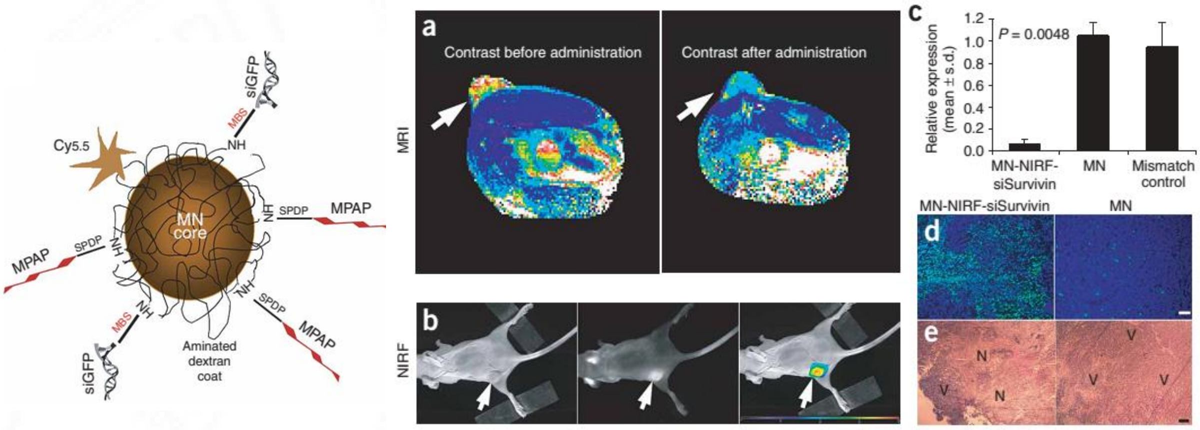

Figure 28: Schematic representation (left) of MN-NIRF-siGFP probe with magnetic nanoparticles labelled with NIR Cy5.5 dye linked to membrane translocation peptides (MPAP) and siRNA molecules targeting GFP (siGFP). MN-NIRF-siGFP probe for simultaneous MR imaging (a), NIR imaging (b) and siRNA mediated tumour therapy (c & d - RT-PCR analysis of survivin mRNA expression & apoptotic nuclei). (Adapted from Medarova Z *et al*., 2007).

Quantum dots (QDs) also have the potential to serve as a photostable vector for siRNA delivery and imaging. Yezhelyev M *et al*., 2008 reported proton-absorbing polymeric coated QDs for real-time tracking of siRNA delivery. But, the major problem of QD is toxicity because of highly toxic elements, such as cadmium, selenium, or tellurium. In contrast to QDs, gold nanoparticles have emerged as a promising siRNA delivery vector because of its excellent biocompatibility, ease of synthesis, high surface-to-volume ratio and easy surface functionalization. siRNAs can be conjugated onto the surface of gold by covalent interaction or electrostatic methods. Giljohann D *et al*., 2009 conjugated polyvalent siRNA molecules to the surface of gold nanoparticles via thiol groups, which increased the half-life and stability of siRNA and also caused significant knock down of targeted gene *in vitro* (Figure 29).

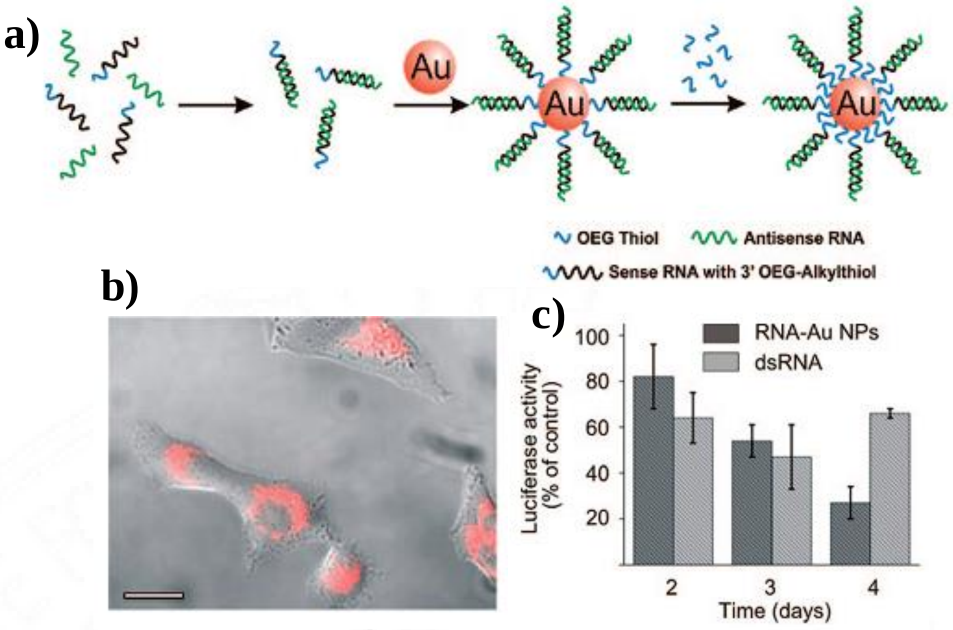

Figure 29: Preparation of Polyvalent RNA-AuNP Conjugates (a), cellular uptake of Cy5RNA-Au NPs (b) and knockdown of luciferase expression treated with RNA-AUNPs (c). (Adapted from Giljohann D *et al*., 2009).

Huschka R *et al*., 2012 used photothermal property of gold nanoparticles to deliver siRNA. In this, Poly-l-lysine peptide (PLL) covalently attached to the Silica-gold nanoshell surface was used to capture siRNA and NIR laser irradiation @ 800 nm was used for controlled release of fluorescent tagged siRNA inside cells (Figure 30). This light-triggered delivery caused ~47% and ~49% downregulation of targeted GFP expression in human lung cancer cells.

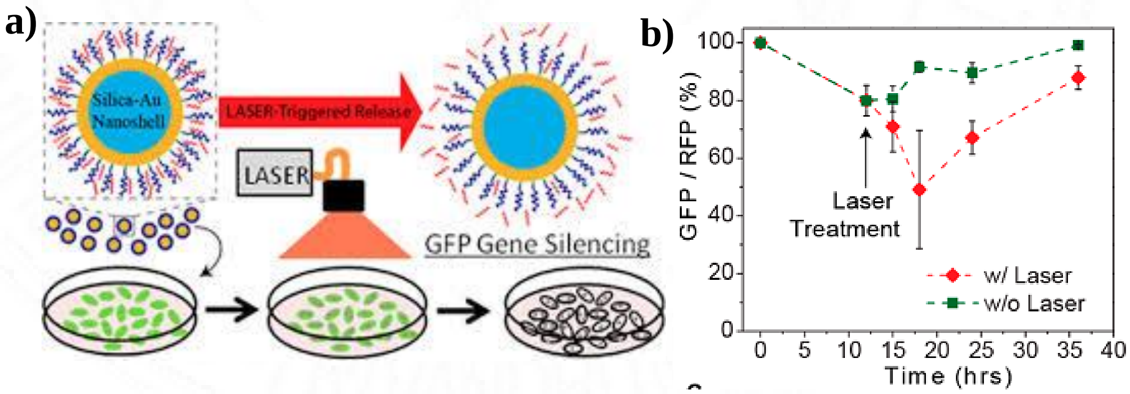

Figure 30: Schematic diagram of laser triggered release of siRNA from gold nanoshell (a) and downregulation of GFP in H1299 cells by siRNA using nanoshell poly-L-lysine (NS-PLL) delivery vectors (b). (Adapted from Huschka R *et al*., 2012).

Even though, these gold nanoparticles act as excellent siRNA delivery vectors among inorganic and organic nanoparticles, the lack of fluorescence property limits their usage for real-time tracking. Fluorescent dyes needs to be conjugated with gold nanoparticles for imaging purpose, but these dyes also lack photostability and hence cannot be used for long time imaging. Thus the discovery of gold nanoclusters with their excellent fluorescent property and photostability paved way for simultaneous imaging of siRNA delivery.

2.3.4. Gold nanoclusters for siRNA delivery

Very few reports are available with gold nanocluster mediated siRNA delivery for cancer therapy. The thiol modification of siRNA to conjugate with gold nanoparticle as mentioned by Giljohann D *et al.*, 2009 is complicated and hence electrostatic interaction is preferred. But in general, gold nanoclusters have negative surface charge which hinders the attachment of siRNA. Hence, few studies conjugated other positively charged molecules with gold nanoclusters for capturing siRNA. Fluorescent gold nanoclusters conjugated with chitosan, cationic polymers like polyethylenimine (PEI) and dendrimers like polyamidoamine (PAMAM) were used as a promising vector for gene delivery (Zhang E *et al.*, 2016). But all these nanoclusters exhibited toxicity towards cells because of the coating layer.

A simple co-caging strategy to overcome the limitations of dendrimer based siRNA transfection is reported by Chien C *et al.*, 2014. Embedding gold nanoclusters within dendrimer modify its structure by allowing irreversible back folding of exterior primary amines from branch to core. This structural change makes the dendrimer non-toxic. Gold nanoclusters also provide imaging potential to dendrimers. The partially tertiary amines were also transformed into quaternary ammonium ions to maximize the conjugation of siRNA. But this method mainly focuses on dendrimers to deliver siRNA.

Lei Y *et al.*, 2017 reported an effective NGF (nerve growth factor) siRNA delivery for pancreatic cancer treatment with gold nanoclusters. This gold nanocluster–siRNA complex prolonged the blood circulation lifetime, increased the serum stability and enhanced the cellular uptake and tumour accumulation of siRNA. The NGF expression in Panc-1 cells and pancreatic tumour was also effectively downregulated by gold nanocluster–siRNA complex (Figure 31). However, the study used far-red fluorescent dye Cy5 conjugated with siRNA for imaging rather than gold nanocluster fluorescence.

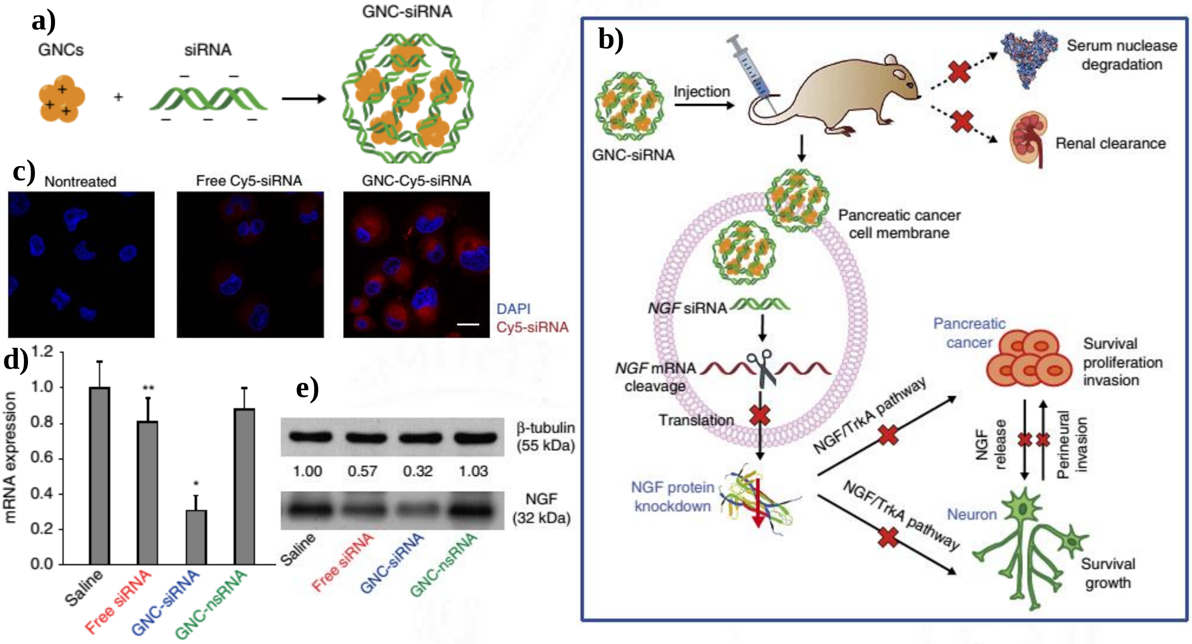

Figure 31: (a) Schematic diagram of the preparation of GNC–siRNA complex, (b) delivery mechanism of GNC–siRNA complex for NGF silencing and pancreatic cancer therapy, (c) Cellular uptake of free siRNA and GNC–siRNA into Panc-1 cells (siRNA labelled with Cy5 dye for visualization), (d) RT-PCR analysis of NGF mRNA expression after treatment and (e) western blot analysis of NGF protein expression after treatment (Adapted from Lei Y *et al*., 2017).

CHAPTER 3: MATERIALS AND METHODS

3. MATERIALS AND METHODS

3.1. Fluorescent molecular probe for zinc ion sensing

3.1.1. Chemicals

Fluorescent probes, TSQ (N-(6-Methoxy-8-Quinolyl)-p-Toluenesulfonamide) and FluoZin-3 AM were obtained from Molecular Probes, Invitrogen. TPEN (N,N,N′,N′-tetrakis(2-pyridylmethyl)ethylenediamine), CaEDTA (Ethylenediaminetetraaceticacid disodium calcium salt) and pyrithione (2-mercaptopyridine N-oxide) were purchased from Sigma-Aldrich. C6 Glioma cells were obtained from ATCC. Cell culture products like DMEM/F12 media, FBS, Streptomycin, Penicillin and Amphotericin B were purchased from HiMedia.

3.1.2. Imaging system and Instrumentation

UV-1800 Shimadzu UV-Vis spectrophotometer, FP-8200 Jasco spectrofluorometer, Carry 600 Fourier transform infrared spectrometer (Agilent Technologies) and alpha300R WITec Confocal Raman Microscope were used to record absorption, emission, FTIR and Raman spectra respectively. Cellular cytotoxicity assay measurements were done in Synergy H1 hybrid multi-mode microplate reader, Bio-Tek.

Hippocampal slicing was done using Vibroslice NVSL with manually advanced tissue bath. The microscopic imaging system consists of an inverted fluorescence microscope (IX51; Olympus, Tokyo, Japan) equipped with Rolera-XR Mono Fast 1394 Cooled digital camera (QImaging), mercury arc lamp and NIS Elements Advanced Research software (Nikon Instruments Inc.). Hippocampal slices were imaged with 4X/0.13 objective lens and mirror unit U-MWB2 WB (Excitation/Emission filter: 460–490/520). For ratiometric imaging, an inverted fluorescence microscope (IX83; Olympus, Tokyo, Japan) equipped with XM10 monochrome cooled CCD camera, metal halide lamp (X-Cite, series 120PC Q) and CellSens Imaging software was used. Cells and hippocampal slices were imaged with LUCPLFLN 40X PH/0.6 and PlanApoN 1.25X/0.04 objective lens respectively.

Images were acquired with 470–495 nm excitation filter, DM505 dichroic mirror and two emission filters (510–550 and 575–625 nm for green and red fluorescence respectively). Xenogen IVIS spectrum, a live animal optical imaging system was used for *in vivo* and *ex vivo* imaging of rat brain.

3.1.3. Synthesis and characterization of molecular probe

The preparation of Bipyridine bridged bispyrrole ratiometric probe (BP) was reported previously (Sreejith *et al.*, 2012). BP was synthesized by the slow addition of 12 mM sodium hydride suspension in dry THF to a THF solution containing 2 mM 2,2′-bipyridyldiphosphonate, 4 mM N-alkylpyrrole-2-carboxaldehyde and then the solution was refluxed for 12 h. A pasty residue was obtained after the reaction mixture was cooled and the THF was removed under reduced pressure. The residue was then suspended in water and extracted with DCM. The crude product was obtained by washing the organic layer with brine and dried over Na_2SO_4, which was then purified using column chromatography over silica gel (100-200 mesh) with petroleum ether/ethyl acetate mixture as eluent.

All spectroscopic measurements were conducted with 6 µM of BP @ RT in a biological buffer condition like Phosphate free saline (PFS, pH 7.4). The composition of PFS is mentioned in table 2. $ZnCl_2$ in PFS was used to test the Zn^{2+} sensing potential of BP. IR Spectra were recorded in transmission mode from 400 to 4000 cm^{-1} using KBr pellet method spanning over 32 scans.

3.1.4. In vitro studies

3.1.4.1. Cell culture

Rat glial tumour cell line, C6 glioma cells were cultured and maintained under humidified atmosphere with 5% CO_2 @ 37°C in DMEM/F12 media supplemented with FBS (10% (v/v)), sodium pyruvate (1 mM), antibiotics and antimycotics like penicillin (100 U/ml), streptomycin (100 µg/ml) and amphotericin B (2.5 µg/ml). Cells were harvested with trypsin-EDTA after 80-90% confluency and subcultured with a seeding density of $0.25x10^6$ cells/ml for all experiments.

3.1.4.2. Cytocompatibility study

The long term cellular cytocompatibility of BP was tested in C6 glioma cells. $1x10^4$ cells per well were seeded in 96-well plates and after 26 h of cell growth, different concentrations of BP in fresh media was added to cells. After 24 and 48 h of incubation, BP containing media was replaced with 100 µl of fresh media containing MTT (0.5 mg/ml). The insoluble formazan crystals formed after 4 h incubation of MTT were dissolved with 100 µl DMSO and the absorbance was measured @ 570 nm using a microplate reader. The percentage of cell viability at different concentrations related to the control well was then calculated.

3.1.4.3. Cellular imaging and Zn^{2+} sensing

To study the cellular imaging potential of BP, C6 glioma cells were incubated with 6 µM BP for 30 min. To study the Zn^{2+} sensing potential of BP, C6 glioma cells were pre-incubated with 50 µM $ZnCl_2$ and 25 µM pyrithione (2-mercaptopyridine N-oxide) for 15 min, washed with PBS and incubated with 6 µM BP for 30 min. Fluorescent microscopic images were acquired with 460–490 nm excitation, 510–550 and 575–625 nm emission filters.

3.1.4.4. Hippocampal slice preparation

Standard procedure with minor modification was adopted for the preparation of hippocampal slices (Buskila Y *et al*., 2014). Decapitation of Sprague-Dawley rats (adult male and female - 250-300 g) was done after anaesthesia by isoflurane inhalation. Brains of the decapitated rats were collected rapidly and placed in ice-cold artificial cerebrospinal fluid (ACSF). The composition of ACSF is mentioned in table 2. Vibroslice NVSL with manually advanced tissue bath was used to prepare 400 µm thick transverse brain slices. All the following experiments were carried out in PFS instead of ACSF. The presence of phosphate in ACSF can precipitate Zn^{2+} and limit the availability of free Zn^{2+} for sensing and hence PFS was used. It is reported that PFS has no negative effect on signal transmission at the Schaffer collateral CA1 synapse suggesting that the neurons have substantial reserves of phosphate for proper function (Frederickson C *et al.*, 2006 and Rumschik S *et al.*, 2009).

Composition (mM)	ACSF	PFS
NaCl	125	125
$NaHCO_3$	25	26
KCl	2.5	2.5
NaH_2PO_4	1.25	-
$MgCl_2$	1	-
$MgSO_4$	-	1.3
D-glucose	10	10
$CaCl_2$	2	2
pH 7.4, continuously bubbled with 95% O_2 and 5% CO_2 in all experiments		

Table 2: Composition of ACSF and PSF for hippocampal slice preparation

3.1.4.5. Zn^{2+} sensing in acute hippocampal slices

Acute hippocampal slices were prepared as mentioned in section 3.1.4.4. Hippocampal slices were incubated with BP (6 µM) for 30 min @ RT in PFS. Two commercially available cell permeable Zn^{2+} sensing probes, Fluozin-3 AM and TSQ (N-(6-Methoxy-8-Quinolyl)-p-Toluenesulfonamide) were used as positive controls for vesicular Zn^{2+} sensing. Fluozin-3 AM (Kd (Zn^{2+}) ~15 nM) can sense Zn^{2+} in the range of 1-100 nM. TSQ is also Zn^{2+} specific in the presence of physiological concentrations of Ca^{2+} and Mg^{2+}. Fluozin-3 AM and TSQ were added at a concentration of 2.5 µM and 90 µM for 15 and 20 min respectively. All the probe incubated slices were washed with PFS twice to remove excess probe and observed under IX51 Olympus inverted fluorescence microscope, except Fluozin-3 AM incubated slices which were imaged only after 30 min to allow the AM ester to cleave inside the cells to emit fluorescence. BP and Fluozin-3 AM incubated slices were imaged at an excitation/emission wavelength of 460–490/520 nm. TSQ incubated slices were imaged at an excitation/emission wavelength of 330–385/420 nm. The images were stitched manually.

To study whether BP can sense intracellular (endogenous vesicular) or extracellular Zn^{2+} in hippocampal slices, slices were separated into three groups (n=4) and pre-incubated with the following materials before the addition of BP:

Group I: Pre-incubated with PFS alone,

Group II: Pre-incubated with 50 µM of CaEDTA in PFS for 10-15 min

Group III: Pre-incubated with 50 µM of TPEN in PFS for 20 min @ 37°C

CaEDTA is a classic extracellular Zn^{2+} chelator and TPEN is an intracellular Zn^{2+} chelator. All the groups were further incubated with BP for 30 min and imaged under fluorescence microscope. Three regions of interest (ROI) from hippocampal slices such as hilus, CA3 and CA1 were chosen for Zn^{2+} quantification. Relative fluorescence intensity was measured from respective ROI using ImageJ and quantified by the following formula:

CTCF= Integrated Density - (Area of selection X Mean fluorescence of background)

3.1.4.6. Induction of epileptic condition *in vitro*

Many methods are available to stimulate the hippocampal slices for mimicking the epileptic condition *in vitro*. Here the hippocampal slices were stimulated with the addition of elevated exogenous potassium chloride in PFS (Frederickson C *et al.*, 2006, Jandova K *et al.*, 2006). Hippocampal slices were stimulated with KCl (50 mM) in PFS for 15 min under continuous purge of 95% O_2 and 5% CO_2. Then the slices were incubated with 6 µM BP for 30 min and imaged under fluorescence microscope. The images were stitched manually.

3.1.4.7. Zn^{2+} sensing in hippocampal slice using Raman Spectroscopy

Raman spectra were recorded from the hilar region of both unstimulated normal and stimulated epileptic hippocampal slices incubated with BP to study the molecular fingerprinting. All the slices were maintained in PFS with continuous bubbling of 95% O_2 and 5% CO_2 during the spectral recording.

3.1.4.8. Ratiometric imaging

To confirm the ratiometric imaging potential of BP, a time lapse imaging experiment was carried out in C6 glioma cells over a period of time with serial addition of BP, Zn^{2+} and TPEN. The cells cultured in 35 mm petridishes were kept immovable on the microscopic stage @ RT during the whole duration of ratiometric imaging. BP (6 µM), zinc (50 µM) as pyrithione complex and TPEN (50 µM) were subsequently added to the cells directly on the microscopic stage by bath application to the media @ 0, 30 and 45 min respectively. The excitation exposure time for image acquisition was kept constant throughout the experiment. Ratiometric imaging was carried out with single excitation (470–495 nm) and double emission (510–550 and 575–625 nm). The excitation filter and the dichroic mirror were changed accordingly. Ratiometric images were generated using CellSens imaging software (Olympus) from the ratio of red (575–625 nm) and green (510–550 nm) channel images. After every treatment, the average ratio of red and green channel images ($R=I_{575–625}/I_{510–550}$) were calculated from ROI of different cells (n=5). R represents ratio and I represents fluorescence intensity.

Similarly, the ratiometric imaging of endogenous Zn^{2+} in hippocampal slices and its dynamics under epileptic condition was also done. Epileptic condition was induced as mentioned in section 3.1.4.6. Ratiometric images were generated using CellSens imaging software (Olympus) from the ratio of red (575–625 nm) and green (510–550 nm) channel images. The average ratio of red and green channel images ($R=I_{575–625}/I_{510–550}$) was also calculated from ROI of different areas in hippocampus.

3.1.5. In vivo studies

All the animal experiments were done according to the principles set forth by CPCSEA (Committee for the Purpose of Control and Supervision of Experiments on Animals). The animal experiments were approved by the institutional animal ethics committee of Sree Chitra Tirunal Institute for Medical Sciences and Technology (B2982011 VIII).

3.1.5.1. Quantification of Zn^{2+} in rat brain

The whole brain was excised from the adult Sprague-Dawley rats weighing >300 g and incubated with 80 µM of BP for 1 h. Then the brain was sectioned equally into 22 parts. Each section was weighed separately and imaged along with different concentration of BP•Zn^{2+} complex as reference in a 96 well plate. First, a standard curve was plotted with the ratio of pixel intensity of different concentration of BP•Zn^{2+} complex (concentration of BP is kept constant) against pixel intensity of BP alone. The pixel intensity of each well was measured by drawing ROI using living image software of IVIS. The quantification of free Zn^{2+} in whole brain was done by measuring the fluorescence pixel intensity of a particular section of brain, assuming that the fluorescence from all brain sections are same. The concentration of Zn^{2+} in particular section was calculated using standard plot and the amount of Zn^{2+} in whole brain was calculated by multiplying the concentration of particular section with the total number of sections.

3.1.5.2. Establishing epilepsy rat model

All the animals used for inducing epilepsy were maintained under a 12/12h light/dark cycle @ RT. Adult Sprague-Dawley rats (female weighing 150 g) were chosen for this study. Epilepsy (n=6) was induced in rats by intra-peritoneal injection of pilocarpine hydrochloride (350mg/kg, Sigma), dissolved freshly in 0.9% sterile saline (Long J *et al*., 2009, Houser C *et al*., 2003). Control rats (n=3) were injected with equal volume of sterile saline. All the animals were monitored continuously for 24 h under video-recording with iBall Face2Face C8 (Rev.3.0) camera to note down the signs of seizure activity. The stages of seizure shown by animals were classified according to previous reports (Borges K, 2003, Klitgaard H *et al*., 2003) and Racine’s scale (1972). The epilepsy induced animals received an intra-peritoneal injection of midazolam (0.5 mg/kg) after 1 h of onset of status epilepticus (i.e., @ stage IV or V) or whenever severe seizure was observed after pilocarpine injection to increase the survival rate. The stages of seizure according to Racine scale were given in table 3.

Stages of seizure	**Activity of animal**
Stage 0	Normal activity
Stage I	Motionless stage for the first 10 min after pilocarpine injection
Stage II	Head nodding, stiffened tail and facial clonus
Stage III	Jerks in forelimb, whole body continuous clonic seizure
Stage IV	Severe whole body continuous clonic seizure, rearing
Stage V	Tonic-clonic seizure with falling or jumping due to loss of balance

Table 3: Stages of seizure activity according to Racine scale.

3.1.5.3. Intra-carotid artery infusion, Hyperosmolar BBB disruption

Slight modification of the protocol reported by Chertok B *et al.*, 2010 and Foley C *et al.*, 2014 was done for intra-carotid artery infusion and Hyperosmolar BBB disruption. Both control and epileptic rats were anesthetized by intra-peritoneal injection of xylazine (7mg/kg body weight) and ketamine (100mg/kg body weight). The anesthetised animals were taken for surgical procedure with aseptic precautions. Left common carotid artery was exposed by making a paramedian longitudinal incision in the jugular furrow. A 3-0 silk suture was passed underneath the exposed carotid artery to lift the blood vessel and to control bleeding. Then a direct puncture was made in the common carotid artery by a sterile 26G cannula, which was inserted into the lumen and directed towards the carotid bifurcation. Silk sutures were used to make ligature proximal to the cannula and to secure the cannula inside carotid artery. To prevent blood coagulation and to confirm the forward flow towards the carotid bifurcation, a small volume of heparinized sterile PFS was flushed into the cannula. PFS was purged continuously with 95% O_2 and 5% CO_2, warmed to 37°C and filtered through 0.22 µm membrane filter prior to infusion. To minimize the introduction of air in carotid artery, the hub of the cannula was filled with sterile pre-warmed PFS and 1.5 ml of PFS was infused through it for 1 min. Sterile 20% wt/vol mannitol was used to disturb the blood brain barrier (BBB). The mannitol pre-warmed to 37°C is injected through the cannula into the external carotid artery and the infusion was done for 30 s at a rate of 0.25 ml/kg/s. The particular concentration of mannitol is reported to cause a reversible BBB disruption without any neuronal damage.

3.1.5.4. *In vivo* Zn^{2+} imaging

The BBB of both control (n=3) and epileptic (n=6) Sprague-Dawley rats was disturbed with intra-carotid artery infusion of mannitol mentioned previously in section 3.1.5.3. For *in vivo* imaging, the anesthetised BBB disturbed control and epileptic rats were perfused with PFS and BP (80 µM) in PFS into the external carotid artery respectively. Then the animals were imaged using Xenogen IVIS live animal imaging system.

3.2. Fluorescent nano probe for cancer imaging and therapy

3.2.1. Chemicals and Reagents

DMF, DCM, piperidine, DIEA, HBTU, TFA, phenol, TIPS, glacial acetic acid, diethyl ether, Fmoc-Asp(OtBu)-OH, Fmoc-Cys(Trt)-OH, Fmoc-Gly-OH, Fmoc-Ser(tBu)-OH, Fmoc- His(Trt)-OH, Gold(III) chloride trihydrate, Silver nitrate, trypan blue, rhodamine 6G, hydrogen peroxide, acridine orange, ethidium bromide, DAPI, Hoechst, H_2DCF-DA and MTT were purchased from Sigma Aldrich. Poly-Prep® Chromatography Column and Fmoc-Rink Amide MBHA resin was obtained from Bio-Rad and AnaSpec respectively. Antibiotic (10,000 Uml^{-1} penicillin, 10 mgml^{-1} streptomycin) and antimycotic (25 µgml^{-1} amphotericin B) solution, FBS, DMEM and 0.25% trypsin-EDTA were obtained from Himedia laboratories. JC-10 was purchased from Enzo life sciences. All cell culture plastic wares were purchased from Nunc.

3.2.2. Synthesis and characterization of different tripeptides

The solid phase peptide synthesis protocol using Fmoc strategy was adopted from Coin I *et al.*, 2007 with necessary modifications and was done manually in polypropylene chromatography columns. The flowchart of synthesis is represented in figure 32. The synthesis was initiated with swelled Fmoc-Rink Amide MBHA resin (250 mg) in 2.5 ml DMF overnight and the Fmoc group was deprotected with 20% piperidine/DMF (v/v) followed by DMF and DCM wash. The incoming amino acid was activated with DIEA (2 M in DMF), HBTU (0.2 M) and was added to the deprotected resin for coupling and the reaction was continued with overnight shaking, followed by washing with DMF and DCM to remove the unreacted amino acids, HBTU and DIEA. The progress of the Fmoc deprotection and successful coupling reaction was monitored by UV spectral analysis (λ_{abs} = 300 nm) and Kaiser test respectively. The cycle was repeated for subsequent amino acids and the completed peptide was vacuum dried and stored at -18^{o} C. The cleavage of peptides from resin was done just before use with 2 ml of cleavage cocktail (TFA/H_2O/phenol/TIPS-8.5/0.5/0.5/0.5), dropped in 20 ml ice cold diethyl ether and the precipitate was isolated by centrifugation (2200 g, 10 min). The isolated precipitate was resuspended in 10% glacial acetic acid and lyophilized.

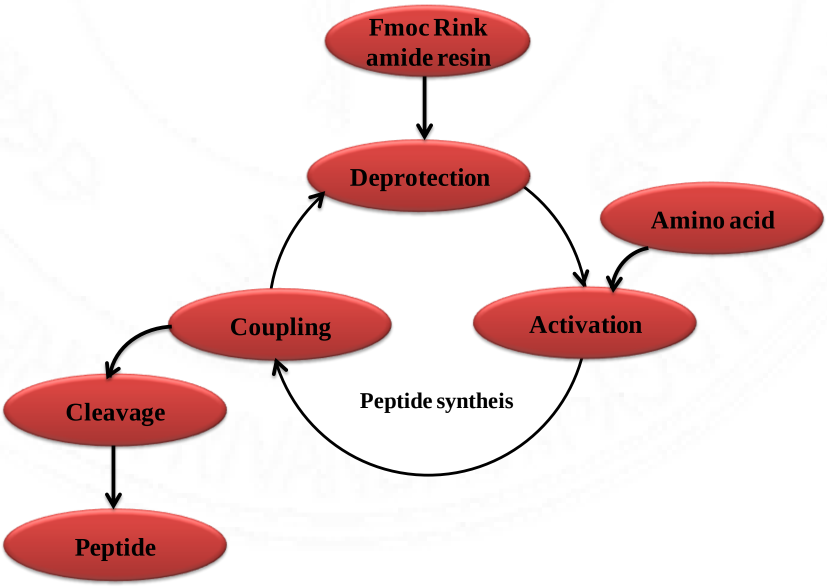

Figure 32: Flowchart of peptide synthesis.

The synthesis of six different tripeptides (Figure 33) namely, Asp-Cys-Gly (DCG), Asp-Cys-Ser (DCS), Asp-Cys-His (DCH), Ser-Cys-Gly (SCG), His-Cys-Ser (HCS) and His-Cys-Gly (HCG) was done by the above procedure with the following amino acids: Fmoc-Asp(OtBu)-OH (165 mg), Fmoc-Cys(Trt)-OH (265 mg), Fmoc-Gly-OH (110 mg), Fmoc-Ser(tBu)-OH (150 mg), Fmoc- His(Trt)-OH (250 mg). All the peptides were synthesized and mentioned as C-N terminal. The lyophilized peptides were analyzed with Liquid chromatography–mass spectrometry (LC-MS) to confirm the expected molecular weight. The analysis was done with electrospray ionization (negative ion mode).

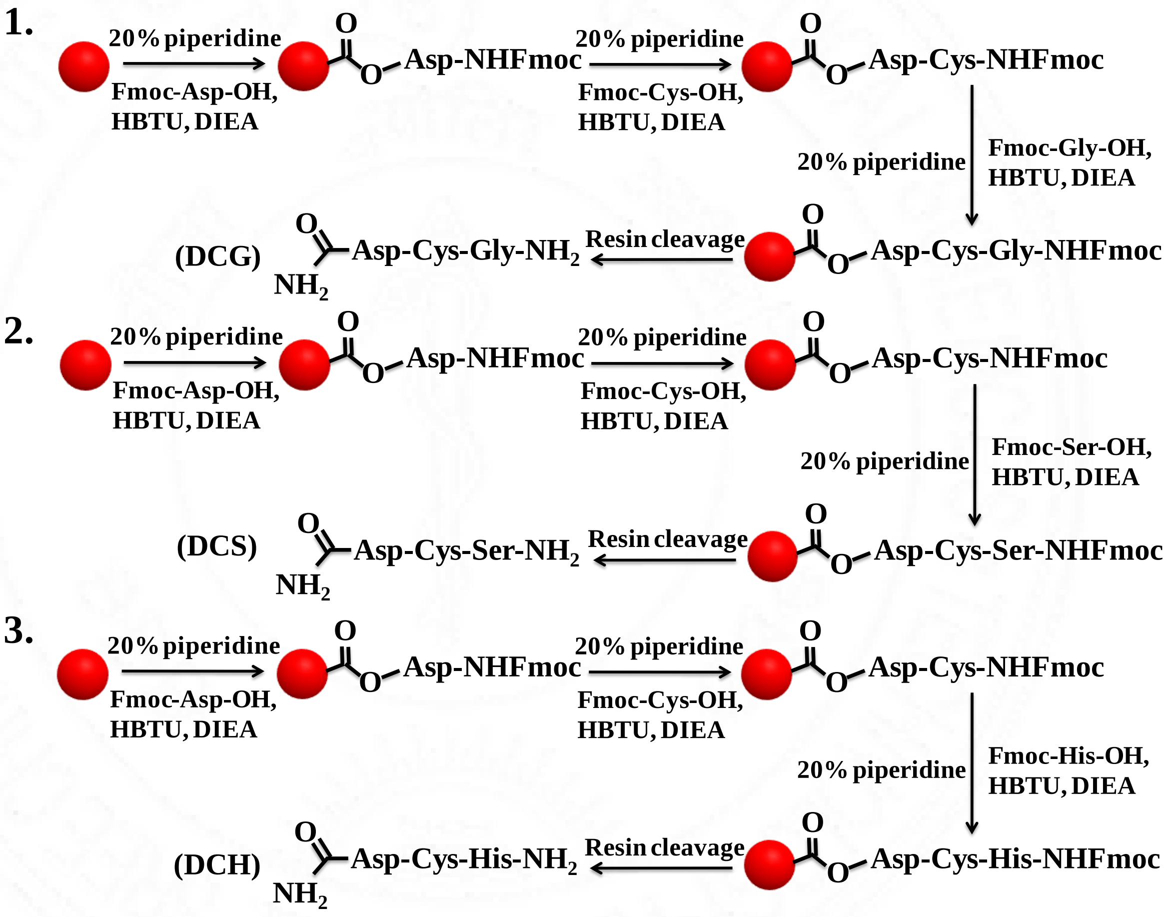

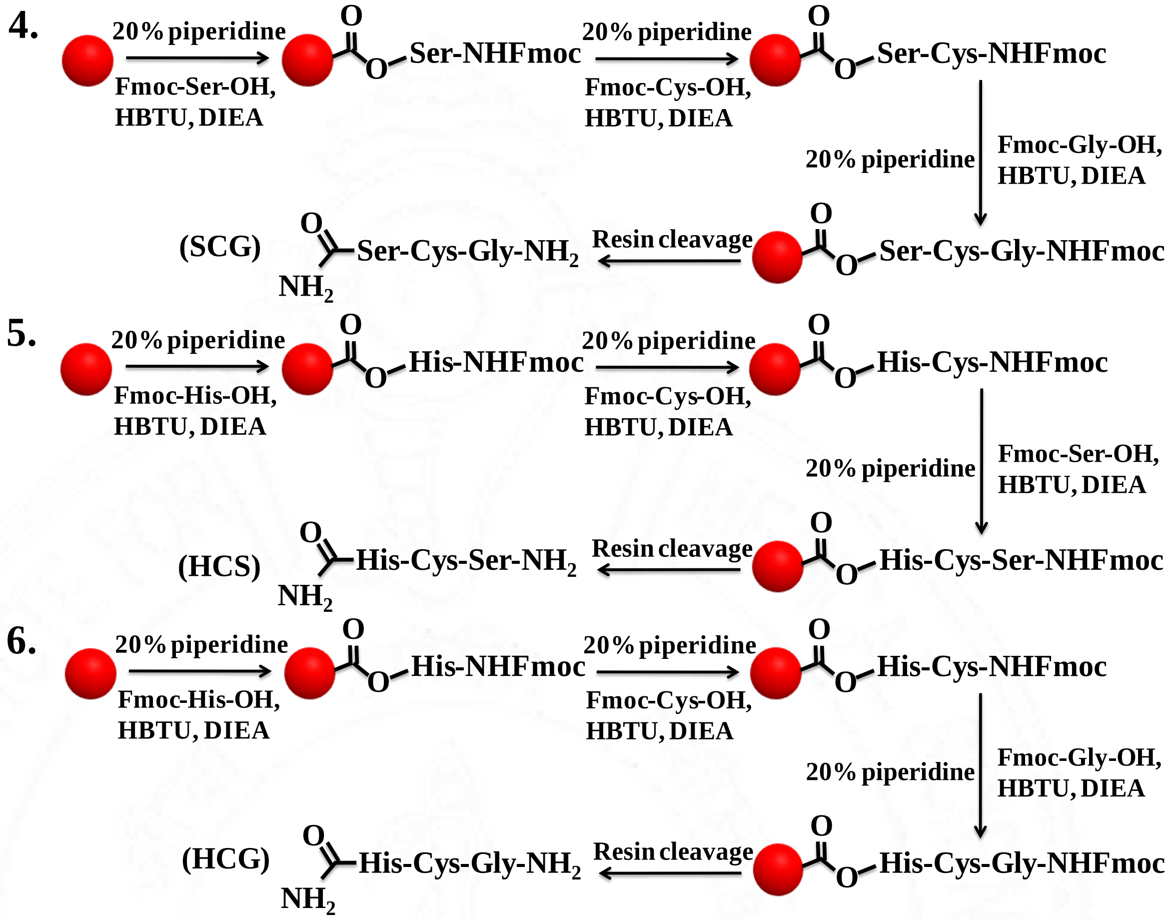

Figure 33: Synthesis of six different tripeptides (DCG, DCS, DCH, SCG, HCS, HCG).

3.2.3. Synthesis of tripeptide-gold nanoclusters

Six different tripeptide-gold nanoclusters (DCG-GNC, DCS-GNC, DCH-GNC, SCG-GNC, HCS-GNC and HCG-GNC) were synthesized by the following protocol. 20 mM of Gold (III) chloride trihydrate ($HAuCl_4 \cdot 3H_2O$) and 2.9 mM of silver nitrate stock solution was first prepared. The composition for the synthesis of six different tripeptide-gold nanoclusters is mentioned in table 4. All the components were mixed accordingly @ RT and the reaction mixture was heated to 72° C. The reaction was continued for 24 h with continuous stirring @ 900 rpm. The samples obtained afterwards were centrifuged @ 5000 rpm for 5 min to remove aggregates and the supernatant was precipitated with 1:1 mixture of acetone to remove impurities. The pellets obtained were resuspended in ultrapure water, lyophilized and stored @ 4° C.

Tripeptide-Gold nanoclusters	**$HAuCl_4 \cdot 3H_2O$ (20 mM)**	**Tripeptides (100 mM)**	**$AgNO_3$ (2.9 mM)**	**Ultrapure H_2O**
DCG-GNC	5 ml	DCG 43.6 mg in 1.5 ml	5 ml	43.5 ml
DCS-GNC	5 ml	DCS 48.1 mg in 1.5 ml	5 ml	43.5 ml
DCH-GNC	5 ml	DCH 55.6 mg in 1.5 ml	5 ml	43.5 ml
SCG-GNC	5 ml	SCG 39.4 mg in 1.5 ml	5 ml	43.5 ml
HCS-GNC	5 ml	HCS 51.4 mg in 1.5 ml	5 ml	43.5 ml
HCG-GNC	5 ml	HCG 46.9 mg in 1.5 ml	5 ml	43.5 ml

Table 4: Chemical composition for the synthesis of different tripeptide-gold nanoclusters.

3.2.4. Characterization of tripeptide-gold nanoclusters

The physico-chemical characterization of tripeptide-gold nanoclusters was done by below mentioned methods and instruments. UV-Vis absorption spectra and fluorescence spectra of the tripeptide-gold nanoclusters diluted in water were measured using Shimadzu UV spectrophotometer- UV 1800 in spectrometric mode and Fluorolog III spectrofluorometer (Jobin Yvon Horiba, USA) respectively. The photographic images of synthesized gold nanoclusters under white light and UV light (365 nm) was also obtained with hand held UV lamp. The quantum yield was calculated using comparative method with Rhodamine 6G as fluorescence standard (reference). The equation used for the calculation is mentioned below:

$$\phi_F \text{ or } QY_S = QY_R\,(A_R/A_S)\,(I_S/I_R)\,(\eta_S/\eta_R)^2$$

where, ϕ_F is the fluorescence quantum yield, QY_S and QY_R are the fluorescence quantum yield of sample and standard respectively, A_R and A_S are the integrated area under fluorescence excitation spectrum of standard and sample respectively, I_S and I_R are the integrated area under fluorescence emission spectrum of standard and sample respectively, η_S and η_R are the refractive index of respective solvents ($\eta_S = 1.33$ for water and $\eta_R = 1.36$ for ethanol). QY_R in ethanol was taken as 0.95.

Fluorescence life time measurements of tripeptide-gold nanoclusters were carried out using time-correlated single-photon counting (TCSPC) method with excitation wavelength of 375 nm using Fluoro Max-4C Spectrofluorometer (Horiba Instruments, USA). The size, size distribution and morphology of different tripeptide-gold nanoclusters were analyzed with TEM and HR-TEM (100 kv JEM-2010 HiTachi-JEOL, Tokyo, Japan and 300 kv FEI Tecnai G2 F30 S -Twin TEM). Samples were prepared by drop casting gold nanocluster samples dispersed in water on to the TEM 200 mesh Cu grid and kept for overnight drying and analyzed. The surface charge of the synthesized tripeptide-gold nanoclusters was analyzed using Malvern Zeta sizer Nano ZS 90.

FTIR spectroscopy was done using Carry 600 Fourier transform infrared spectrometer (Agilent Technologies) to study the surface chemistry and functionalization of synthesized tripeptide-gold nanoclusters. FTIR spectra were recorded in transmission mode with KBr pellet method from 500-4000 cm^{-1} range spanning over 32 scans. In addition with FTIR spectroscopy, the surface chemistry of tripeptide-gold nanoclusters were analyzed using X-ray photoelectron spectroscopy (XPS, PHI 5000 VersaProbe II, ULVAC-PHI Inc., USA) equipped with micro-focused (200 μm, 15 KV) monochromatic Al-Kα X-Ray source (hν = 1486.6 eV). High-resolution spectra of the major elements were recorded at 46.95 eV pass energy. XPS data were processed using PHI's Multipak software. The binding energy was referenced to the C 1s peak at 284.8 eV.

Fluorescence stability studies of tripeptide-gold nanoclusters at different pH and different time points were carried out using Fluorolog III spectrofluorometer. To study the photostability of tripeptide-gold nanoclusters against photodestruction, a simple photobleaching experiment was carried out and compared with rhodamine 6G as standard. Aqueous solutions of tripeptide-gold nanoclusters and rhodamine 6G (1 M in ethanol) were continuously illuminated with hand held UV lamp (365 nm) for 10 min. Fluorescence intensity of all samples was measured before and after UV illumination with Fluorolog III spectrofluorometer. The relative fluorescence intensity before and after UV illumination ($I-I_O$) is plotted in percentage.

3.2.5. In vitro cell studies

3.2.5.1. Cell culture

Six cancer cell lines and one normal cell line were used for the biological characterization of different tripeptide-gold nanoclusters: Human epithelial breast cancer cells (MCF-7, MDA-MB-231, SK-BR-3), Rat brain glial cancer cells (C6), Human brain glial cancer cells (U-87 MG), Human epithelial cervical cancer cells (HeLa) and Human lung fibroblast (WI-38). MCF-7, MDA-MB-231, SK-BR-3, U-87 MG and HeLa cells were routinely cultured in DMEM media supplemented with FBS (10%), antibiotics and antimycotics like penicillin (100 U/ml), streptomycin (100 µg/ml) and amphotericin B (2.5 µg/ml) under humidified atmosphere with 5% CO_2 @ 37°C. C6 cells were cultured in DMEM/F12 media supplemented with sodium pyruvate (1 mM) and all other components mentioned above. The cells were harvested using 0.25% trypsin-EDTA at 80-90% confluency, stained with trypan blue for cell counting using haemocytometer and subsequently used for all experiments. All the *in vitro* cellular studies of DCG-GNC and DCS-GNC were done in MCF-7 and MDA-MB-231 cells. Similarly all the *in vitro* cellular studies of DCH-GNC and SCG-GNC were done in C6 and U-87 MG cells. Likewise, all the *in vitro* cellular studies of HCS-GNC and HCG-GNC were done in SK-BR-3 and HeLa cells. The synthesized gold nanoclusters dissolved in sterile water was filtered through 0.22 µm syringe filter and used for all *in vitro* cellular studies.

3.2.5.2. Cytocompatibility study

The long term cytocompatibility of tripeptide-gold nanoclusters was tested in respective cancer cells mentioned above. The long term cytocompatibility of tripeptide-gold nanoclusters in normal cells were studied only for 24 h. Cells were seeded at a density of $1x10^4$ cells per well in tissue culture treated 96-well plates. After 24 h of cell growth, different concentrations (0.01, 0.05, 0.1, 0.5 and 1 mg/ml) of tripeptide-gold nanoclusters in fresh media was added to the respective cells.

DCG-GNC and DCS-GNC were added to MCF-7 and MDA-MB-231 cells. DCH-GNC and SCG-GNC were added to C6 and U-87 MG cells. HCS-GNC and HCG-GNC were added to SK-BR-3 and HeLa cells. In addition, all the tripeptide-gold nanoclusters were added to WI-38 cells for 24 h. After 24, 48 and 72 h of incubation, material containing media was replaced with 100 µl of fresh media containing MTT (0.5 mg/ml) and incubated for 4 h @ 37°C. The insoluble formazan crystals formed after 4 h incubation of MTT were dissolved with 100 µl DMSO and the absorbance was measured @ 570 nm using a Synergy H1 hybrid multi-mode microplate reader (Bio-Tek). The percentage of cell viability at each concentration related to the control cells was finally calculated and plotted.

3.2.5.3. Cellular uptake and accumulation study

To examine the cellular imaging potential of synthesized tripeptide-gold nanoclusters, the cellular uptake and accumulation of tripeptide-gold nanoclusters was studied at different time points. All the cells were seeded at a density of $5x10^4$ cells per well in 4-well plates and cultured for 24 h. After 24 h, the cells were incubated with 100 µg/ml of respective gold nanoclusters for 3, 6, 12 and 24 h. MCF-7 and MDA-MB-231 cells were incubated with DCG-GNC and DCS-GNC. C6 and U-87 MG cells were incubated with DCH-GNC and SCG-GNC. SK-BR-3 and HeLa cells were incubated with HCS-GNC and HCG-GNC. After material exposure, the cells were washed with sterile PBS, fixed with 4% paraformaldehyde for 10 min @ RT and counter stained with DAPI followed by PBS washing. The cells were imaged under IX83 inverted fluorescence microscope (Olympus) with 360-370 nm/420-460 nm for DAPI and 360-370 nm/575–625 nm excitation/emission for gold nanoclusters. Same exposure time was set during image acquisition for all the groups.

Followed by the accumulation study, the cellular uptake mechanism of these gold nanoclusters was studied simply by incubating the gold nanoclusters (100 µg/ml) in respective cells (seeded in 4-well plates at a density of $5x10^4$ cells/well) under normal (37°C) and low temperature (4°C) for 6 h and then observed under microscope after paraformaldehyde fixation and DAPI counterstaining. The quantification of gold nanoclusters uptake under both conditions was done using CellSens Imaging software analysis.

3.2.5.4. Analysis of intracellular ROS level

The synthesized gold nanoclusters were then tested for its efficacy to induce photodynamic therapy in cancer cells under laser irradiation. To detect the ROS generation, all the cells were seeded at a density of $5x10^4$ cells/well in 4-well plates for qualitative imaging and $1x10^4$ cells/well in 96-well plates for quantitative analysis. After 24 h of cell growth, respective gold nanoclusters (100 µg/ml) were added to cells and incubated for 6 h. MCF-7 and MDA-MB-231 cells were incubated with DCG-GNC and DCS-GNC. C6 and U-87 MG cells were incubated with DCH-GNC and SCG-GNC. SK-BR-3 and HeLa cells were incubated with HCS-GNC and HCG-GNC. Cells without material addition were taken as negative control group and cells incubated with 0.3% H_2O_2 for 30 min were taken as positive control group. Then the cells were replaced with fresh media and irradiated with 532 nm laser (0.5 W/cm^2) for 30 sec except positive control group. All the cell groups were loaded with 10 µM of H_2-DCFDA and incubated for 30 min @ 37°C. The cells were then washed with PBS to remove excess H_2-DCFDA and replaced with fresh media. For microscopic qualitative imaging, the live cells were counterstained with Hoechst and observed under IX83 inverted fluorescence microscope (Olympus) using 470–495 nm/510–550 nm excitation/emission filters. Same exposure time was set during image acquisition for all the groups. For quantitative measurements, the fluorescence was measured using a Synergy H1 hybrid multi-mode microplate reader (Bio-Tek) with 485 nm excitation and 530 nm emission.

3.2.5.5. Mitochondrial membrane potential ($\Delta\Psi m$) analysis

The change in the mitochondrial membrane potential ($\Delta\Psi m$) of gold nanocluster treated cells irradiated with laser was analyzed with JC-10 probe, which can be used as an indicator for early apoptosis. All the cells were seeded onto 4-well plates with a seeding density of $5x10^4$ cells per well. After 24 h of cell growth, cells were incubated with respective gold nanoclusters (100 µg/ml) for 6 h. MCF-7 and

MDA-MB-231 cells were incubated with DCG-GNC and DCS-GNC. C6 and U-87 MG cells were incubated with DCH-GNC and SCG-GNC. SK-BR-3 and HeLa cells were incubated with HCS-GNC and HCG-GNC. Cells without material addition were taken as control group. Then the cells were replaced with fresh media and irradiated with 532 nm laser (0.5 W/cm^2) for 30 sec. All the cells including control, laser irradiated and non-irradiated cells were loaded with 10 µM of JC-10 probe and incubated for 30 min @ 37°C. The cells were then washed with PBS to remove excess JC-10 and replaced with fresh media and observed under IX83 inverted fluorescence microscope (Olympus) with 470–495 nm/510–550 nm excitation/emission for JC-10 monomers and 540-550 nm/575–625 nm excitation/emission for JC-10 aggregates. Same exposure time was set during image acquisition for all the groups.

3.2.5.6. Analysis of cell death

For the cell death analysis, cells were seeded onto 96-well plates with a seeding density of 1x10^4 cells per well. After 24 h of cell growth, the cells were treated with respective gold nanoclusters (100 µg/ml) and incubated for 6 h. MCF-7 and MDA-MB-231 cells were incubated with DCG-GNC and DCS-GNC. C6 and U-87 MG cells were incubated with DCH-GNC and SCG-GNC. SK-BR-3 and HeLa cells were incubated with HCS-GNC and HCG-GNC. Cells without material addition were taken as control group. The existing material containing media was replaced with 100 µl of fresh media and the cells were irradiated with 532 nm laser (0.5 W/cm^2) for 30 sec. After laser irradiation, the cells were further incubated @ 37°C for 4 h. For qualitative imaging of cell death, live dead assay was performed with acridine orange and ethidium bromide double staining. The cells were stained with 1:1 mixture of acridine orange (5 mg/ml) and ethidium bromide (3 mg/ml) for 2 min and immediately observed under microscope with 470–495 nm/510–550 nm excitation/emission and 540-550 nm/575–625 nm excitation/emission filters. For quantitative measurement of cell death, MTT assay was carried out. All the cells were incubated with 10 µl of MTT (5 mg/ml) and incubated for another 4 h @ 37°C. The insoluble formazan crystals formed after 4 h incubation of MTT were dissolved with 100 µl DMSO and the absorbance was measured @ 570 nm using a Synergy

H1 hybrid multi-mode microplate reader (Bio-Tek). The percentage of cell viability at each concentration related to the control cells was finally calculated and plotted.

3.2.6. Statistical analysis

All the data results were expressed as Mean values ± Standard deviation. The statistical differences were analyzed by two-tailed, Student's t-test with a significance level of $p < 0.01$. In all the results, $p < 0.01$ was considered as statistically significant (i.e., significantly different).

3.3. Fluorescent nano gene downregulator for cancer imaging cum therapy

3.3.1. Chemicals and Reagents

DMF, DCM, piperidine, DIEA, HBTU, TFA, phenol, TIPS, glacial acetic acid, diethyl ether, Fmoc-Cys(Trt)-OH, Fmoc-His(Trt)-OH, Fmoc-Arg(Pbf)-OH, Fmoc-Lys(Boc)-OH, Gold(III) chloride trihydrate, Silver nitrate, trypan blue, rhodamine 6G, acridine orange, ethidium bromide, DAPI, Hoechst, Chloroform, Isopropanol and MTT were purchased from Sigma Aldrich. Poly-Prep® Chromatography Column was obtained from Bio-Rad. Fmoc-Rink Amide MBHA resin and Sensolyte Homogenous RH110 Caspase-3/7 assay kit were purchased from AnaSpec. Antibiotic (10,000 Uml^{-1} penicillin, 10 $mgml^{-1}$ streptomycin) and antimycotic (25 μgml^{-1} amphotericin B) solution, FBS, DMEM and 0.25% trypsin-EDTA were obtained from Himedia laboratories. Non-specific siRNA (NSsiRNA), Survivin siRNA (SURsiRNA) Control-siRNA-FITC conjugate A (NSsiRNA-FITC) and Survivin antibody were purchased from Santa Cruz Biotechnology. Rabbit monoclonal to ERBB2/Her2 and Goat anti-rabbit IGG H&L (Alexa Fluor® 488) antibodies were obtained from Abcam. Celllight early endosomes-GFP, Lysotracker-green DND-26, Lipofectamine2000 transfection reagent, TRIzol reagent and Dead Cell Apoptosis Kit with Annexin V Alexa Fluor® 488 & Propidium Iodide (PI) were purchased from Invitrogen. Reverse Transcriptase core kit and Takyon No ROX SYBR MMX DTTP BLUE were purchased from Eurogentec. Primers were purchased from Sigma. All cell culture plastic wares were purchased from Nunc. All the siRNA experiments were carried out using RNase free water inside PCR workstation (UVT-B-AR cabinet, Biosan, UK).

3.3.2. Construction of fluorescent nano gene downregulator and its characterization

The nano gene downregulator for targeted cancer imaging cum siRNA delivery was constructed with oligopeptide stabilized gold nanoclusters, complexed with siRNA and conjugated with Her2.

3.3.3. Synthesis and characterization of oligopeptides

The solid phase peptide synthesis protocol using Fmoc strategy was adopted from Coin I *et al.*, 2007 with necessary modifications and was done manually in polypropylene chromatography columns. The flowchart of peptide synthesis is represented in figure 32. The synthesis was initiated with swelled Fmoc-Rink Amide MBHA resin (250 mg) in 2.5 ml DMF overnight and the Fmoc group was deprotected with 20% piperidine/DMF (v/v) followed by DMF and DCM wash. The incoming amino acid was activated with DIEA (2 M in DMF), HBTU (0.2 M) and was added to the deprotected resin for coupling and the reaction was continued with overnight shaking, followed by washing with DMF and DCM to remove the unreacted amino acids, HBTU and DIEA. The progress of the Fmoc deprotection and successful coupling reaction was monitored by UV spectral analysis ($\lambda_{abs} = 300$ nm) and Kaiser test respectively. The cycle was repeated for subsequent amino acids and the completed peptide was vacuum dried and stored at -18° C. The cleavage of peptides from resin was done just before use with 2 ml of cleavage cocktail (TFA/H_2O/phenol/TIPS-8.5/0.5/0.5/0.5), dropped in 20 ml ice cold diethyl ether and the precipitate was isolated by centrifugation (2200 g, 10 min). The isolated precipitate was resuspended in 10% glacial acetic acid and lyophilized.

The synthesis of three different oligopeptides (Figure 34) namely, HRHRHRCHRHRHR ($(HR)_3C(HR)_3$), HKHKHKCHKHKHK ($(HK)_3C(HK)_3$) and

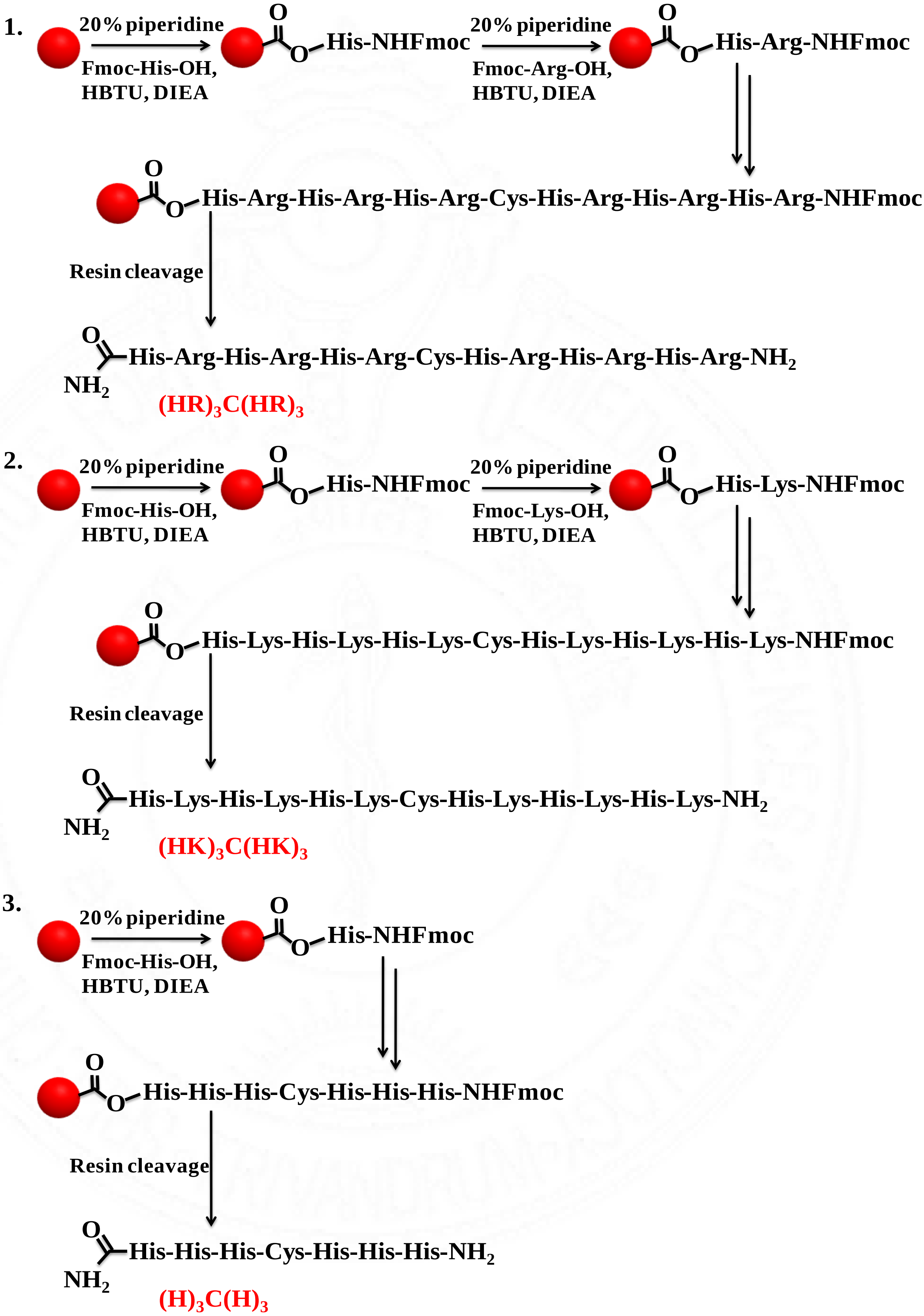

Figure 34: Synthesis of three different oligopeptides (HR)$_3$C(HR)$_3$, (HK)$_3$C(HK)$_3$ and (H)$_3$C(H)$_3$.

HHHCHHH ($(H)_3C(H)_3$) was done using the above procedure with the following amino acids: Fmoc- His(Trt)-OH (250 mg), Fmoc-Cys(Trt)-OH (265 mg), Fmoc-Arg(Pbf)-OH and Fmoc-Lys(Boc)-OH. His (H), Arg (R), Lys (K) and Cys (C) in peptides represent histidine, arginine, lysine and cysteine amino acids respectively. All the peptides were synthesized and mentioned as C-N terminal. The lyophilized peptides were analyzed with Matrix assisted laser desorption and ionization–mass spectrometry (MALDI-MS) to confirm the expected molecular mass.

3.3.4. Synthesis of oligopeptide -gold nanoclusters

Three different oligopeptide-gold nanoclusters $(HR)_3C(HR)_3$-GNC, $(HK)_3C(HK)_3$-GNC and $(H)_3C(H)_3$-GNC were synthesized by the following protocol. 20 mM of Gold (III) chloride trihydrate ($HAuCl_4{\cdot}3H_2O$) and 2.9 mM of silver nitrate stock solution was first prepared in RNase free water. The composition for the synthesis of three different oligopeptide-gold nanoclusters is mentioned in table 5. All the components were mixed accordingly @ RT and the reaction mixture was heated to 72° C. The reaction was continued for 24 h with continuous stirring @ 900 rpm. The samples obtained afterwards were centrifuged @ 5000 rpm for 5 min to remove aggregates and the supernatant was precipitated with 1:1 mixture of acetone to remove impurities. The pellets obtained were resuspended in RNase free water, lyophilized and stored @ 4° C.

Oligopeptide-Gold nanoclusters	**$HAuCl_4{\bullet}3H_2O$ (20 mM)**	**Oligopeptides (100 mM)**	**$AgNO_3$ (2.9 mM)**	**RNase free H_2O**
$(HR)_3C(HR)_3$-GNC	5 ml	$(HR)_3C(HR)_3$ 282 mg in 1.5 ml	5 ml	43.5 ml
$(HK)_3C(HK)_3$-GNC	5 ml	$(HK)_3C(HK)_3$ 257 mg in 1.5 ml	5 ml	43.5 ml
$(H)_3C(H)_3$-GNC	5 ml	$(H)_3C(H)_3$ 142 mg in 1.5 ml	5 ml	43.5 ml

Table 5: Chemical composition for the synthesis of different oligopeptide-gold nanoclusters.

3.3.5. Characterization of oligopeptide-gold nanoclusters

The physico-chemical characterization of oligopeptide-gold nanoclusters was done by below mentioned methods and instruments. UV-Vis absorption spectra and Fluorescence spectra of the oligopeptide-gold nanoclusters diluted in water were measured using Shimadzu UV spectrophotometer- UV 1800 in spectrometric mode and Fluorolog III spectrofluorometer (Jobin Yvon Horiba, USA) respectively. The photographic images of synthesized gold nanoclusters under white light and UV light (365 nm) was also obtained with hand held UV lamp. The quantum yield was calculated using comparative method with Rhodamine 6G as fluorescence standard (reference). The equation used for the calculation is mentioned below:

$$\phi_F \text{ or } QY_S = QY_R\ (A_R/A_S)\ (I_S/I_R)\ (\eta_S/\eta_R)^2$$

where, ϕ_F is the fluorescence quantum yield, QY_S and QY_R are the fluorescence quantum yield of sample and standard respectively, A_R and A_S are the integrated area under fluorescence excitation spectrum of standard and sample respectively, I_S and I_R are the integrated area under fluorescence emission spectrum of standard and sample respectively, η_S and η_R are the refractive index of respective solvents ($\eta_S = 1.33$ for water and $\eta_R = 1.36$ for ethanol). QY_R in ethanol was taken as 0.95.

Fluorescence life time measurements of oligopeptide-gold nanoclusters were carried out using time-correlated single-photon counting (TCSPC) method with excitation wavelength of 375 nm using Fluoro Max-4C Spectrofluorometer (Horiba Instruments, USA). The size, size distribution and morphology of different oligopeptide-gold nanoclusters were analyzed with HR-TEM (300 kv FEI Tecnai G2 F30 S -Twin TEM). Samples were prepared by drop casting gold nanocluster samples dispersed in water on to the TEM 200 mesh Cu grid and kept for overnight drying and analyzed. The surface charge of the synthesized oligopeptide-gold nanoclusters was analyzed using Malvern Zeta sizer Nano ZS 90.

FTIR spectroscopy was done using Carry 600 Fourier transform infrared spectrometer (Agilent Technologies) to study the surface chemistry and functionalization of synthesized oligopeptide-gold nanoclusters. FTIR spectra were recorded in transmission mode with KBr pellet method from 500-4000 cm^{-1} range spanning over 32 scans. In addition with FTIR spectroscopy, the surface chemistry of oligopeptide-gold nanoclusters were analyzed using X-ray photoelectron spectroscopy (XPS, PHI 5000 VersaProbe II, ULVAC-PHI Inc., USA) equipped with micro-focused (200 µm, 15 KV) monochromatic Al-Kα X-Ray source (hν = 1486.6 eV). High-resolution spectra of the major elements were recorded at 46.95 eV pass energy. XPS data were processed using PHI's Multipak software. The binding energy was referenced to the C 1s peak at 284.8 eV.

Fluorescence stability studies of oligopeptide-gold nanoclusters at different pH and different time points were carried out using Fluorolog III spectrofluorometer. To study the photostability of oligopeptide-gold nanoclusters against photodestruction, a simple photobleaching experiment was carried out and compared with rhodamine 6G as standard. Aqueous solutions of oligopeptide-gold nanoclusters and rhodamine 6G (1 M in ethanol) were continuously illuminated with hand held UV lamp (365 nm) for 10 min. Fluorescence intensity of all samples was measured before and after UV illumination with Fluorolog III spectrofluorometer. The relative fluorescence intensity before and after UV illumination ($I-I_O$) is plotted in percentage.

3.3.6. In vitro cell studies

3.2.6.1. Cell culture

One cancer cell line and one normal cell line were used for the biological characterization of different oligopeptide-gold nanoclusters: Human epithelial breast cancer cells (SK-BR-3) and Human lung fibroblast (WI-38). Both the cells were routinely cultured in DMEM media supplemented with FBS (10%), antibiotics and antimycotics such as penicillin (100 U/ml), streptomycin (100 µg/ml) and amphotericin B (2.5 µg/ml) under humidified atmosphere with 5% CO_2 @ 37°C.

The cells were harvested using 0.25% trypsin-EDTA at 80-90% confluency, stained with trypan blue for cell counting using haemocytometer and subsequently used for all experiments. The synthesized oligopeptide-gold nanoclusters were dissolved in sterile water and were filtered through 0.22 µm syringe filter for all *in vitro* cellular studies.

3.2.6.2. *In vitro* cytocompatibility study

The long term cytocompatibility of oligopeptide-gold nanoclusters $(HR)_3C(HR)_3$-GNC, $(HK)_3C(HK)_3$-GNC and $(H)_3C(H)_3$-GNC was tested in SK-BR-3 cells for 24, 48 and 72 h. Cells were seeded at a density of $1x10^4$ cells per well in tissue culture treated 96-well plates. After 24 h of cell growth, different concentrations (0.001, 0.0025, 0.005, 0.01, 0.025, 0.05, 0.1, 0.25, 0.5 and 1 mg/ml) of oligopeptide-gold nanoclusters in fresh media was added to the cells. After 24, 48 and 72 h of incubation, material containing media was replaced with 100 µl of fresh media containing MTT (0.5 mg/ml) and incubated for 4 h @ 37°C. The insoluble formazan crystals formed after 4 h incubation of MTT were dissolved with 100 µl DMSO and the absorbance was measured @ 570 nm using a Synergy H1 hybrid multi-mode microplate reader (Bio-Tek). The percentage of cell viability at each concentration related to the control cells was finally calculated and plotted.

3.2.6.3. Cellular uptake study

To examine the cellular imaging potential of synthesized oligopeptide-gold nanoclusters, the cellular internalization of oligopeptide-gold nanoclusters $(HR)_3C(HR)_3$-GNC, $(HK)_3C(HK)_3$-GNC and $(H)_3C(H)_3$-GNC was studied in SK-BR-3 cells. All the cells were seeded at a density of $5x10^4$ cells per well in 4-well plates and cultured for 24 h. After 24 h, the cells were incubated with 100 µg/ml of respective gold nanoclusters. After material exposure for 3 h, the cells were washed with sterile PBS and counter stained with Hoechst. The cells were imaged under IX83 inverted fluorescence microscope (Olympus) with 360-370 nm/420-460 nm for Hoechst and 360-370 nm/610 nm excitation/emission for gold nanoclusters. Same exposure time was set during image acquisition for all the groups.

3.3.7. siRNA complexation to oligopeptide-gold nanoclusters

The complexation of siRNA with different oligopeptide-gold nanoclusters $(HR)_3C(HR)_3$-GNC, $(HK)_3C(HK)_3$-GNC and $(H)_3C(H)_3$-GNC was done through electrostatic interaction between the positively charged oligopeptide-gold nanoclusters and negatively charged siRNA in RNase free water. Respective gold nanoclusters were mixed with different weight ratio of siRNA (1:0, 1:0.5, 1:1, 1:1.5, 1:2, 1:4, 1:8, 1:16) and allowed to bind in a low speed vortex mixer for 1 h. The prepared samples were mentioned as $(HR)_3C(HR)_3$-GNC-siRNA, $(HK)_3C(HK)_3$-GNC-siRNA and $(H)_3C(H)_3$-GNC-siRNA.

3.3.7.1. Characterization of oligopeptide gold nanocluster-siRNA complex

The complexation of siRNA with different gold nanoclusters and the maximum loading capacity was analyzed by charge reversal study using Malvern Zeta sizer Nano ZS 90. The different weight ratio of siRNA complexed with respective gold nanoclusters was analyzed for its surface charge and charge reversal due to the binding of siRNA to gold nanoclusters. Carry 600 Fourier transform infrared spectrometer (Agilent Technologies) was used to study the complex formation and surface chemistry of oligopeptide-GNC-siRNA complex. FTIR spectra were recorded in transmission mode with KBr pellet method from 500-4000 cm^{-1} range spanning over 32 scans.

In addition with FTIR spectroscopy, the surface chemistry and the elemental composition of oligopeptide-GNC-siRNA complex were also analyzed using X-ray photoelectron spectroscopy (XPS, PHI 5000 VersaProbe II, ULVAC-PHI Inc., USA) equipped with micro-focused (200 μm, 15 KV) monochromatic Al-Kα X-Ray source (hν = 1486.6 eV). High-resolution spectra of the major elements were recorded at 46.95 eV pass energy. XPS data were processed using PHI's Multipak software. The binding energy was referenced to the C 1s peak at 284.8 eV.

3.3.8. In vitro cell studies

3.3.8.1. siRNA transfection

The siRNA delivery or transfection by oligopeptide-gold nanoclusters were studied by monitoring the cellular uptake of siRNA complexed with oligopeptide-gold nanoclusters. For this, FITC-labelled control siRNA (NSsiRNA-FITC) were complexed with oligopeptide-gold nanoclusters and used. For siRNA transfection, SK-BR-3 cells were seeded at a density of $5x10^4$ cells per well in 4-well plates and cultured for 24 h. After 24 h, the cells were incubated with free siRNA, Lipo2000-siRNA, $(HR)_3C(HR)_3$-GNC-siRNA and $(HK)_3C(HK)_3$-GNC-siRNA with a siRNA concentration of about 100 nM. Lipofectamine mediated siRNA transfection (Lipo2000-siRNA) was done according to the manufacturer’s protocol. After 4 h of siRNA transfection, the cells were washed with PBS, counterstained with Hoechst and observed under IX83 Olympus inverted fluorescence microscope. The excitation/emission filters for DAPI, NSsiRNA and oligopeptide-gold nanoclusters were set as 360-370/420-460 nm, 470-495/510-550 nm and 360-370 nm/610 nm respectively. Same exposure time was set during image acquisition for all the groups. The quantification of siRNA uptake under different transfection methods was done using measuring MFI per cell.

3.3.8.2. Cytocompatability of different siRNA transfection methods

To evaluate the cytocompatibility of oligopepide-gold nanoclusters mediated siRNA transfection, NSsiRNA is complexed to $(HR)_3C(HR)_3$-GNC, $(HK)_3C(HK)_3$-GNC and lipo2000 with different concentrations of siRNA (1, 5, 10, 20, 50, 100, 200, 300, 400 and 500 nM) and were used for transfection. SK-BR-3 cells were seeded in 96-well plates with a seeding density of $1x10^4$ cells per well. After 24 h of cell growth, the cells were treated with the above mentioned GNC-siRNA complexes and lipo2000-siRNA complex. After 48 h of incubation, the treated cells were tested for its percentage viability using MTT assay. The material containing media was replaced with 100 µl of fresh media containing MTT (0.5 mg/ml) and incubated for 4 h @ 37°C. The insoluble formazan crystals formed after 4 h incubation of MTT were dissolved with 100 µl DMSO and the absorbance was measured @ 570 nm using a Synergy H1 hybrid multi-mode microplate reader (Bio-Tek). The percentage of cell viability at each concentration related to the control cells was finally calculated and plotted.

3.3.8.3. Endosomal/lysosomal escape of oligopeptide-GNC-siRNA complex

To study the endosomal/lysosomal escape effect of $(HR)_3C(HR)_3$-GNC-siRNA complex and $(HK)_3C(HK)_3$-GNC-siRNA complex, SK-BR-3 cells were seeded in 4-well plates with a density of $5x10^4$ cells per well. After 24 h of cell growth, the cells were transfected with Celllight early endosomes-GFP BacMam reagent (30 particles/cell) and incubated overnight @ 37°C for labelling early endosomes. For labelling lysosomes, the cells were stained with 75 nM of LysoTracker Green (Invitrogen) for 1 h. Then the cells were transfected with respective oligopeptide-GNC-siRNA complex for 1 h. The cells were washed with PBS and incubated in phenol red free fresh DMEM. The cells co-transfected with GNC-siRNA complex and early endosome-GFP were counterstained with Hoechst and imaged @ 1 h and the cells co-transfected with GNC-siRNA complex and LysoTracker Green were counterstained with Hoechst and imaged @ 1 and 4 h using inverted fluorescence microscope. The excitation and emission filters for Hoechst and early endosome-GFP/LysoTracker Green were set as 360-370 nm/420-460 nm and 470-495 nm/510-550 nm respectively and 360-370 nm/610 nm for oligopeptide-gold nanoclusters.

3.3.8.4. Immunocytochemistry

Immunocytochemistry (ICC) was done to evaluate the expression of survivin and Her2 in SK-BR-3 cancer cells and WI-38 normal cells. Both the cells were seeded in 4-well plates with a density of $5x10^4$ cells per well and grown for 24 h. The cells were fixed with 3.7% paraformaldehyde for 15 min @ RT and washed with PBS thrice for 10 min. For survivin ICC, the fixed cells were permeabilized with 0.25% Triton X-100 for 10 min and washed with PBS thrice (10 min). Then the cells were blocked with 1% BSA for 1 h and incubated with Mouse monoclonal to

Survivin and Rabbit monoclonal to ERBB2/Her2 primary antibodies in 3% BSA for overnight @ 4°C. The cells were then washed with PBS thrice (10 min each) and incubated with anti-mouse and anti-rabbit secondary antibody conjugated with fluorescent tag for survivin and Her2 respectively for 1 h @ RT. The dilution of the antibodies was prepared according to manufacturer's protocol. Then the cells were washed with PBS thrice (10 min each), counterstained with DAPI and imaged under fluorescence microscope with 360-370/420-460 nm and 470-495/510-550 nm for DAPI and antibodies respectively.

3.3.8.5. Quantitative RT-PCR

SK-BR-3 cells were seeded with a density of 5x10^4 cells per well in 24-well plates and grown for 24 h. The cells were transfected with free SURsiRNA, Lipo2000-SURsiRNA, $(HR)_3C(HR)_3$-GNC-SURsiRNA, $(HK)_3C(HK)_3$-GNC-SURsiRNA, $(HR)_3C(HR)_3$-GNC-NSsiRNA and $(HK)_3C(HK)_3$-GNC-NSsiRNA with siRNA concentration of 100 nM. Cells without any treatment were used as untreated control group. After 48 h of transfection, total RNA was isolated from SK-BR-3 cells using TRIzol reagent (Invitrogen) according to manufacturer's protocol and the RNA was converted to cDNA (complementary DNA) using Reverse Transcriptase core kit (Eurogentec) and the qPCR amplication was performed with Takyon No ROX SYBR MasterMix DTTP BLUE (Eurogentec) in 7900 HT Fast Real-Time PCR system (Applied Biosystems, CA) under standard cycling conditions. The relative expression of survivin was calculated using $2^{-\Delta\Delta Ct}$ method (Ct – Threshold cycle) with GAPDH as endogenous control. Melting curves were examined to verify the product specificity. The primers used for qRT-PCR analysis are listed in table 6.

Primers	**Sequence**
Survivin forward	5' –TCCACTGCCCCACTGAGAAC‑3'
Survivin reverse	5' –TGGCTCCCAGCCTCCA‑ 3'
GAPDH forward	5' ‑GAGTCAACGGATTTGGTCGT‑ 3'
GAPDH reverse	5'‑TTGATTTTGGAGGGATCTCG‑3'

Table 6: Sequences of primers used for qRT-PCR.

3.3.8.6. Wound healing assay

SK-BR-3 cells were seeded with a density of $5x10^4$ cells per well in 24-well plates. After 24 h of cell growth, the cells were scraped with the aid of sterile tips to create a linear scratch wound. Then the cells were washed carefully with sterile PBS twice and were transfected with free SURsiRNA, $(HR)_3C(HR)_3$-GNC-SURsiRNA and $(HK)_3C(HK)_3$-GNC-SURsiRNA with siRNA concentration of 100 nM. Cells without any treatment were used as untreated control group. The migration of cells into the wound area was observed and imaged @ 1, 24 and 48 h under IX83 Olympus inverted microscope. The gap closure percentage was quantified using CellSens Imaging software (Olympus) and plotted for each treatment group.

3.3.8.7. Apoptosis assay

To evaluate the apoptosis induced in cells treated with oligopeptide-GNC-siRNA complex, SK-BR-3 cells were seeded with a density of $5x10^4$ cells per well in 4-well plates and incubated for 24 h. Then the cells were transfected with free SURsiRNA, $(HR)_3C(HR)_3$-GNC-SURsiRNA and $(HK)_3C(HK)_3$-GNC-SURsiRNA with siRNA concentration of 100 nM. Cells without any treatment were used as untreated control group. After 48 h of transfection, the cells were washed with 1X annexin binding buffer and stained with Dead Cell Apoptosis Kit with Annexin V Alexa Fluor® 488 & Propidium Iodide (PI) (Invitrogen). 5 µl of Annexin V Alexa Fluor® 488 and 5 µl of PI were mixed with 300 µl of 1X annexin binding buffer and incubated in cells for 15 min @ RT in dark. The cells were then viewed under inverted fluorescence microscope to identify the live, early apoptotic and necrotic cells. The excitation/emission filters used for Annexin V Alexa Fluor® 488 and PI were set as 470-495/510-550 nm and 540-550/575–625 nm respectively.

3.3.8.8. Live dead assay

To evaluate the cell death induced in cells treated with oligopeptide-GNC-siRNA complex, SK-BR-3 cells were seeded with a density of $5x10^4$ cells per well in 4-well plates and incubated for 24 h. Then the cells were transfected with free SURsiRNA, $(HR)_3C(HR)_3$-GNC-SURsiRNA and $(HK)_3C(HK)_3$-GNC-SURsiRNA with siRNA concentration of 100 nM. Cells without any treatment were used as untreated control group. After 48 h of transfection, the cells were washed with sterile PBS and dual stained with Acridine orange and ethidium bromide for 2 min. The cells were stained with 1:1 mixture of acridine orange (5 mg/ml) and ethidium bromide (3 mg/ml) in PBS. The cells were then viewed under inverted fluorescence microscope to identify the live, apoptotic, late apoptotic and necrotic cells. The excitation/emission filters for Acridine orange and Ethidium bromide were set as 470-495/510-550 nm and 540-550/575–625 nm respectively.

The quantification of cell death under each treatment was done using MTT assay. SK-BR-3 cells were seeded with a density of $1x10^4$ cells per well in 96-well plates and incubated for 24 h. Then the cells were transfected with free SURsiRNA, $(HR)_3C(HR)_3$-GNC-SURsiRNA and $(HK)_3C(HK)_3$-GNC-SURsiRNA with siRNA concentration of 20 nM. Cells without any treatment were used as untreated control group. After 48 h of transfection, the cells were washed with sterile PBS and incubated with 100 µl of fresh media containing MTT (0.5 mg/ml) for 4 h @ 37°C. The insoluble formazan crystals formed after 4 h incubation of MTT were dissolved with 100 µl DMSO and the absorbance was measured @ 570 nm using a Synergy H1 hybrid multi-mode microplate reader (Bio-Tek). The percentage of cell viability at each concentration related to the control cells was finally calculated and plotted.

3.3.8.9. Caspase assay

For caspase 3/7 activity assay, SK-BR-3 cells were seeded with a density of $1x10^4$ cells per well in 96-well plates and incubated for 24 h. Then the cells were transfected with free SURsiRNA, $(HR)_3C(HR)_3$-GNC-SURsiRNA and $(HK)_3C(HK)_3$-GNC-SURsiRNA with siRNA concentration of 20 nM. Cells without any treatment were used as untreated control group. After 24 h of transfection, the cells were examined for activation of caspase using Sensolyte Homogenous RH110 Caspase-3/7 assay kit (AnaSpec). The protocol was followed as per manufacturer’s instructions. Caspase substrate solution (50 µl) was added to the cells and incubated @ 37ºC in dark for 1 h with intermittent shaking. Then the plates were read using a fluorescent plate reader with excitation/emission of 496/520 nm. The results were expressed in relative fluorescent units (RFU).

3.3.9. Her2 conjugation to oligopeptide-GNC-siRNA complex

Further to target oligopeptide-GNC-siRNA complex specifically to cancer cells, the oligopeptide-gold nanocluster $(HR)_3C(HR)_3$-GNC was first conjugated with Her2 antibody using EDC/NHS chemistry. For this, 2 mg of $(HR)_3C(HR)_3$-GNC was dispersed in 5 ml of RNase free water. 250 µl of EDC (50 mM) in RNase free water was added to $(HR)_3C(HR)_3$-GNC and the pH was adjusted to 4 and the mixture was stirred for 2 h @ RT. After 2 h, 250 µl of NHS (50 mM) in RNase free water was added to the above mixture and 2 ml of primary antibody Her2 with 1:100 dilution was added. The pH of the solution was adjusted to 9 and the reaction was continued overnight. Then the solution was centrifuged with 1:1 acetone mixture at 10,000 rpm for 15 min to remove the unreacted Her2 and chemicals. The obtained $(HR)_3C(HR)_3$-GNC-Her2 conjugate was then complexed with NSsiRNA for 1 h and characterized with UV-Vis and FTIR spectroscopy.

3.3.9.1. Evaluation of uptake of oligopeptide-GNC-Her2-siRNA complex in co-culture model

A simple co-culture model of Her2 overexpressed SK-BR-3 breast cancer cells and Her2 negative WI-38 normal fibroblast cells was established with optimization of different ratio of both cell lines. SK-BR-3 and WI-38 cells were mixed at different ratio (1:1, 1:2, 1:3, 1:4, 1:5) and allowed to grow for 3 days and observed under microscope for morphological characterization. 1:3 ratio were optimized as a good heterotypic culture model based on the morphological observation under microscope. Then the cells were treated with 100 µl of $(HR)_3C(HR)_3$-GNC-Her2-siRNA complex and incubated for 3 h @ 37ºC. The cells were then washed with sterile PBS twice, counterstained with Hoechst and observed under inverted fluorescence microscope. The excitation and emission filters for Hoechst and $(HR)_3C(HR)_3$-GNC-Her2-siRNA complex were set as 360-370/420-460 nm and 360-370/610 nm respectively.

3.3.10. Statistical analysis

All the data results were expressed as Mean values ± Standard deviation. The statistical differences between mean values were analyzed by two-tailed, Student's t-test with a significance level of $p < 0.05$ represented as *, $p < 0.01$ represented as ** and $p < 0.001$ represented as ***. In all the results, $p < 0.05$ is considered as statistically significant, and $p < 0.001$ is considered as statistically highly significant.

CHAPTER 4: RESULTS AND DISCUSSIONS

4. RESULTS AND DISCUSSION

4.1. Fluorescent molecular probe for zinc ion sensing

Due to the importance of Zn^{2+} sensing in neurobiology, fluorescent molecular probes that can sense Zn^{2+} with a considerable change in fluorescence emission have special attraction in recent years. A fluorescent molecular probe (BP) for Zn^{2+} sensing was previously designed and reported by Sreejith *et al.,* 2012. The probe was studied for its optical properties in organic buffer (1:4 HEPES (0.1 M) buffered aqueous acetonitrile). The current study uses BP probe for studying the dynamics of Zn^{2+} under neurodegenerative condition and to prove the sensing and imaging potential of BP *in vitro* and *in vivo*.

4.1.1. Design of molecular probe for Zn^{2+} sensing

BP probe was designed with 2,2′-bipyridine as acceptor moiety, which is connected to pyrrole donor groups through a π-bridge (Figure 35). The bipyridine group in BP probe act as metal chelating centre for selective binding of Zn^{2+}. A partial positive charge is generated in the molecule when cationic Zn^{2+} binds to the bipyridine acceptor moiety. Upon subsequent excitation, the charge is transferred from acceptor to donor moiety as the π-bridge connects the two moieties. Also the conformational change of molecule from non-planar to planar conformation upon Zn^{2+} binding enhances the intramolecular charge transfer (Figure 35). This intramolecular charge transfer is the result of change in both excitation and emission spectra of BP. The binding constant of BP•Zn^{2+} complex was calculated as 3.6×10^5/M. The complexation of Zn^{2+} with BP induces a decrease in HOMO-LUMO energy gap which is responsible for the observed red shift in the emission of BP (Figure 36).

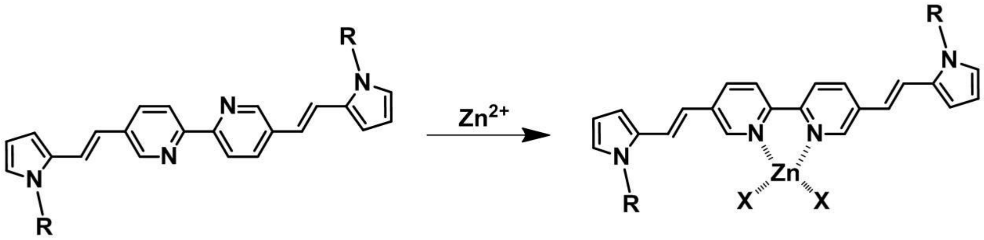

Figure 35: Structure of BP and BP•Zn^{2+} complex (Santhakumar H *et al*., 2018).

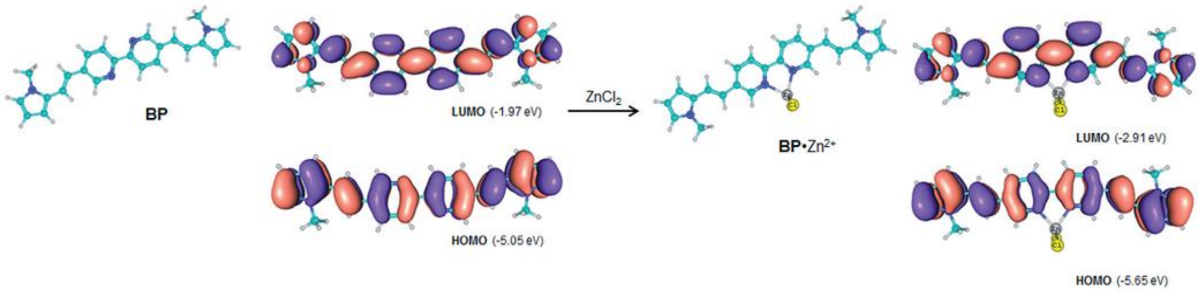

Figure 36: Frontier orbitals of models of BP and BP•Zn^{2+} complex (Adapted from Sreejith *et al.*, 2012).

4.1.2. Characterization of molecular probe towards Zn^{2+} sensing

The properties of BP in biological buffer condition (Phosphate free saline, PFS) are studied here against the original report where organic buffer is used (Sreejith *et al.*, 2012). BP•Zn^{2+} complex formation in PFS is confirmed by Surface Enhanced Raman Scattering (SERS) and Fourier Transform Infrared (FTIR) spectroscopic techniques. A well defined peak @ 678 cm^{-1} in the SERS spectra of BP•Zn^{2+} complex in contrast with BP alone indicates the metal-nitrogen vibration peak, confirming the BP•Zn^{2+} complex formation (Figure 37). FTIR spectra also showed a metal-nitrogen stretching @ 450 cm^{-1} which confirms the BP•Zn^{2+} complex formation (Figure 38). Both SERS and FTIR spectra confirmed the binding of metallic Zn^{2+} to the nitrogen group of bipyridine moiety in BP.

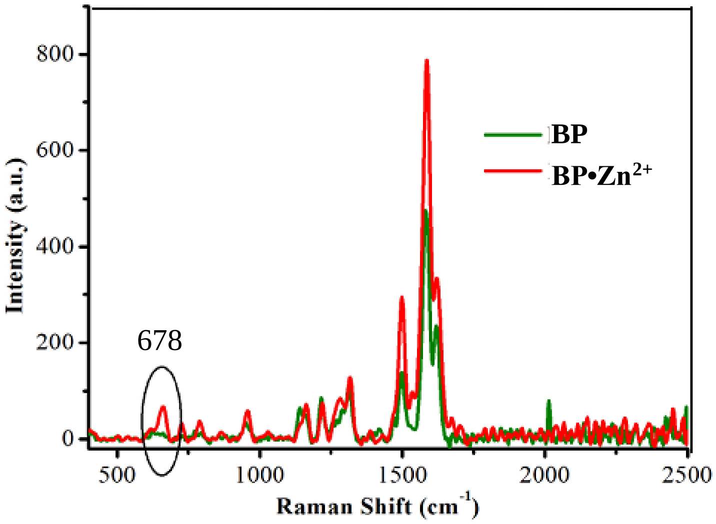

Figure 37: SERS spectra of BP and BP•Zn^{2+} complex (Santhakumar H *et al.*, 2018).

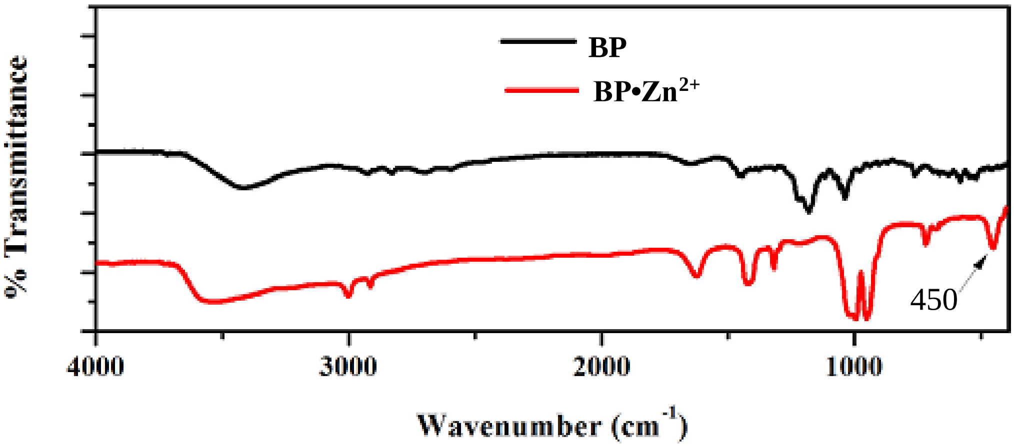

Figure 38: FTIR spectra of BP and BP•Zn^{2+} complex (Santhakumar H *et al.*, 2018).

BP has an absorption maximum @ 410 nm in PFS, which shifts to 421 nm upon Zn^{2+} binding (Figure 39a). The emission maximum of BP alone is @ 565 nm. Upon addition of Zn^{2+} in increasing concentration, the emission profile also showed a concentration dependent red shift from 565 nm (Figure 39b). To confirm whether the emission shift is due to BP•Zn^{2+} complex formation, a Zn^{2+} chelator CaEDTA was added to the BP•Zn^{2+} complex. Addition of CaEDTA (50 µM) reverted the emission peak of BP to 565 nm (Figure 39b). CaEDTA de-complexed Zn^{2+} from BP by competitive binding with Zn^{2+}, allowing BP to emit its original fluorescence, hence confirming the red shift of BP is due to BP•Zn^{2+} complex formation. Remarkable differences in the optical behaviour of BP were observed in physiological buffer condition, compared to that in the organic buffer (Sreejith *et al.*, 2012). BP is highly favourable for biological imaging with its red emission and large stoke shift (155 nm) in PFS, thereby reducing the interference from spectral overlap and autofluorescence.

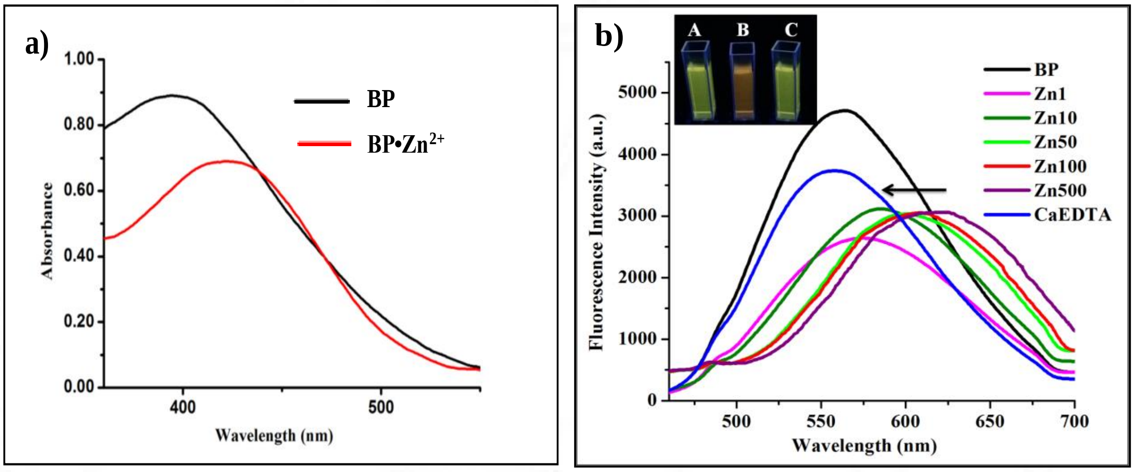

Figure 39: a) Absorption spectra of BP and BP•Zn^{2+} complex, b) Fluorescence spectra of BP and BP•Zn^{2+} complex with $ZnCl_2$ @ different conc. (µM), CaEDTA (50 µM). Arrow indicates the reversal of fluorescence shift on addition with CaEDTA. Inset shows the visual fluorescence colour change of BP (A), after the addition of $ZnCl_2$ (B) and after the addition of CaEDTA (C). (Santhakumar H *et al*., 2018).

4.1.3. In vitro studies

4.1.3.1. Cytocompatibility

The suitability of BP to use in live cell imaging was first assessed by studying the long-term cellular cytocompatibility in C6 glioma cells using standard MTT assay. Results showed that 6.25 µM concentration of BP retain more than 85 and 70% cell viability in 24 and 48 h of incubation period respectively (Figure 40). The long term cellular cytotoxicity study of BP in C6 glioma cells showed that 6 µM of BP is non-toxic over a period of 48 h incubation. Hence this concentration is considered to be safe and used in further experiments. Also it is proved that this concentration can be used for Zn^{2+} sensing in complex physiological environment that require prolonged probe treatment.

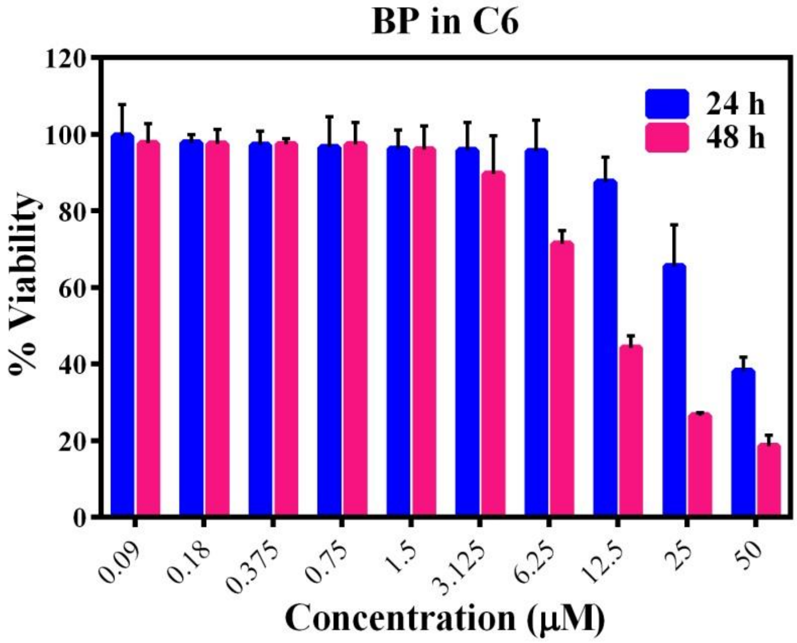

Figure 40: Cell viability (%) of C6 glioma with different concentration of BP. Mean±s.d. (n=4) (Santhakumar H *et al*., 2018).

4.1.3.2. Fluorescence imaging and Zn^{2+} sensing

4.1.3.2.1. Imaging and Zn^{2+} sensing in C6 glioma cells

The intracellular Zn^{2+} sensing potential of BP was then studied in C6 glioma cells. Green fluorescence in figure 41 B of C6 glioma cells clearly indicates the cell permeability of BP. The excellent intracellular distribution showed by BP in just 30 min incubation period proved that BP requires very short period of time for cellular permeabilization. Further to investigate the intracellular Zn^{2+} sensing potential of BP, C6 glioma cells were pre-incubated with Zn^{2+} and pyrithione. Pyrithione is a Zn^{2+} specific ionophore used to transport Zn^{2+} efficiently into cells. These ionophores can act as passive shuttle for specific ions to move across cell membranes and are extensively used in experimental biology (Nydegger I *et al*., 2012). The addition of BP to the Zn^{2+} and pyrithione pre-loaded cells resulted in red fluorescence, whereas the cells incubated with BP alone showed green fluorescence (Figure 41 B,E). This confirms BP can sense Zn^{2+} intracellularly with the change in fluorescence from green to red.

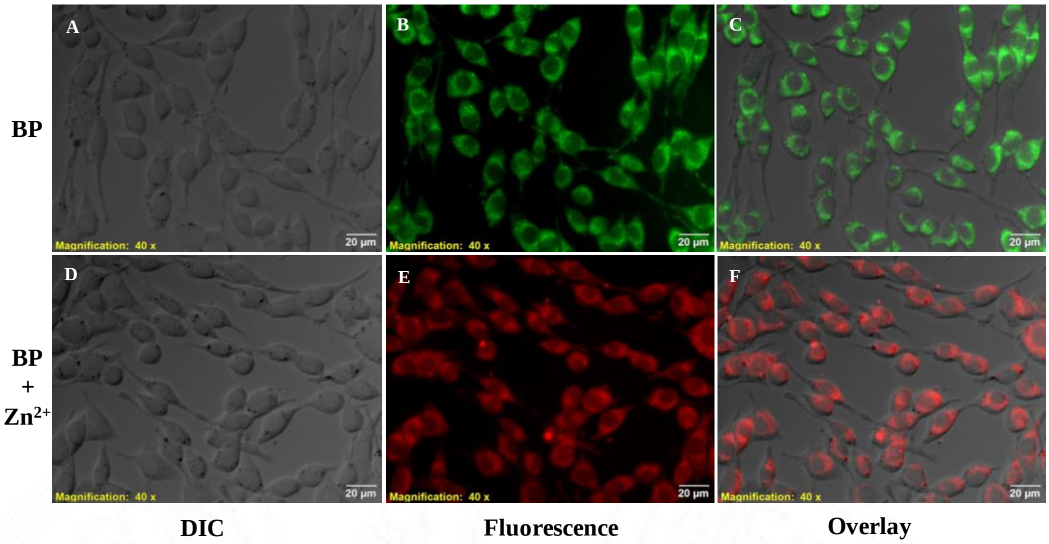

Figure 41: Imaging and Zn^{2+} sensing in C6 Glioma cells using BP. Scale bar = 20 µm. (Santhakumar H *et al*., 2018).

4.1.3.2.2. Imaging and Zn^{2+} sensing in hippocampal slice

Inspired by the results of externally supplied Zn^{2+} sensing in C6 glioma cells, BP was further tested for its efficiency to sense endogenous Zn^{2+} in hippocampus. The anatomy of 400 µm thick hippocampal slice prepared according to section 3.1.4.4 can be seen in figure 42. H, DG, CA1, CA2, CA3, ML, GCL, SL and SP represents the region of hilus, dentate gyrus, cornu ammonis 1, 2, 3, molecular layer, granular cell layer, stratum lucidum and stratum pyramidale respectively.

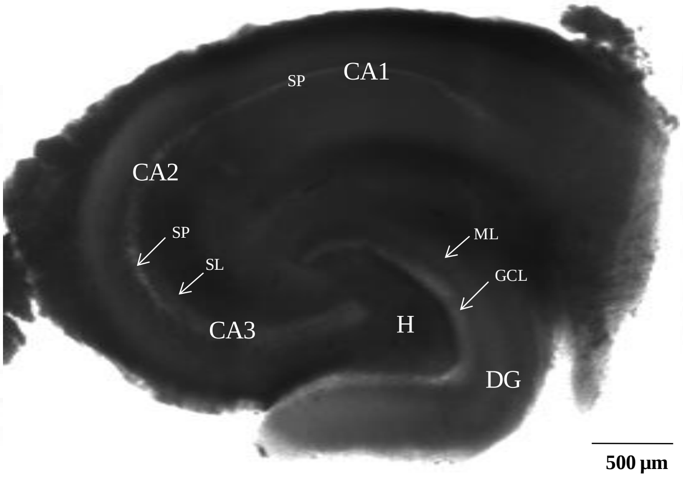

Figure 42: Detailed lamellar anatomy of hippocampal slice sectioned perpendicular to the septo-temporal axis. Scale bar = 500 µm. (Santhakumar H *et al*., 2018)

The hippocampal slices incubated with BP showed intense red fluorescence in hilar region of dentate gyrus (H) as well as in SL of CA2 and CA3 (Figure 43a). This validates the presence of large number of Zn^{2+} containing synaptic vesicles in these two regions as reported previously (Tóth K, 2011). Hence, BP can efficiently sense endogenous vesicular Zn^{2+} in neurons. The result was further checked with commercially available cell-permeable Zn^{2+} sensors, Fluozin-3 AM and TSQ. The binding of Zn^{2+} to these sensors causes an increase in the intensity of respective green and blue fluorescence (Figure 43b,c). Thus, compared to the intensity change by these commercial Zn^{2+} sensors, a visible fluorescence shift of BP upon Zn^{2+} binding is much appreciable.

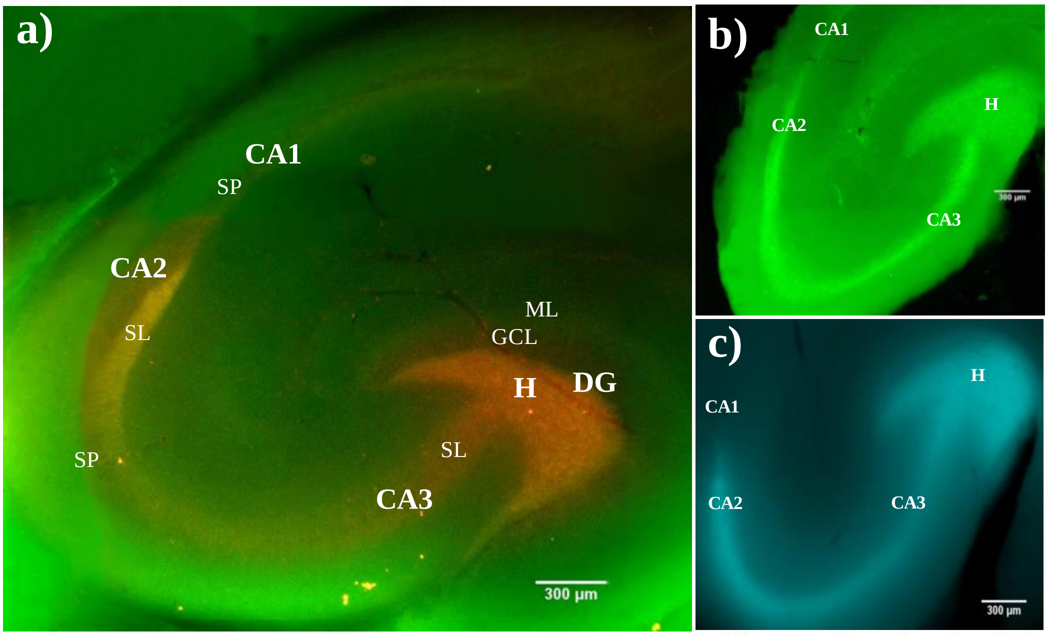

Figure 43: Imaging and sensing endogenous Zn^{2+} in hippocampal slice. Slices incubated with a) BP, b) Fluozin-3 AM and c) TSQ. Scale bar = 300 µm. (Santhakumar H *et al*., 2018)

A membrane impermeant Zn^{2+} chelator CaEDTA and a membrane permeant Zn^{2+} chelator TPEN were added separately to different groups of hippocampal slices to check whether BP senses intracellular (vesicular) Zn^{2+} inside neuronal cells or extracellular Zn^{2+} in between neurons as mentioned in section 3.1.4.5. Compared to Group I control slices, both Group II CaEDTA and Group III TPEN slices showed an immediate depletion of red fluorescence of BP in hilus, mossy fiber terminals of CA3, radiatum and oriens of CA1 (Figure 44). This confirms both CaEDTA and

TPEN chelated Zn^{2+} in these regions rich with Zn^{2+} containing innervations. But Group III slices showed a drastic decrease of red fluorescence than Group II slices (Figure 44 inset), hence confirmed that BP is efficient in sensing intracellular (vesicular) Zn^{2+}.

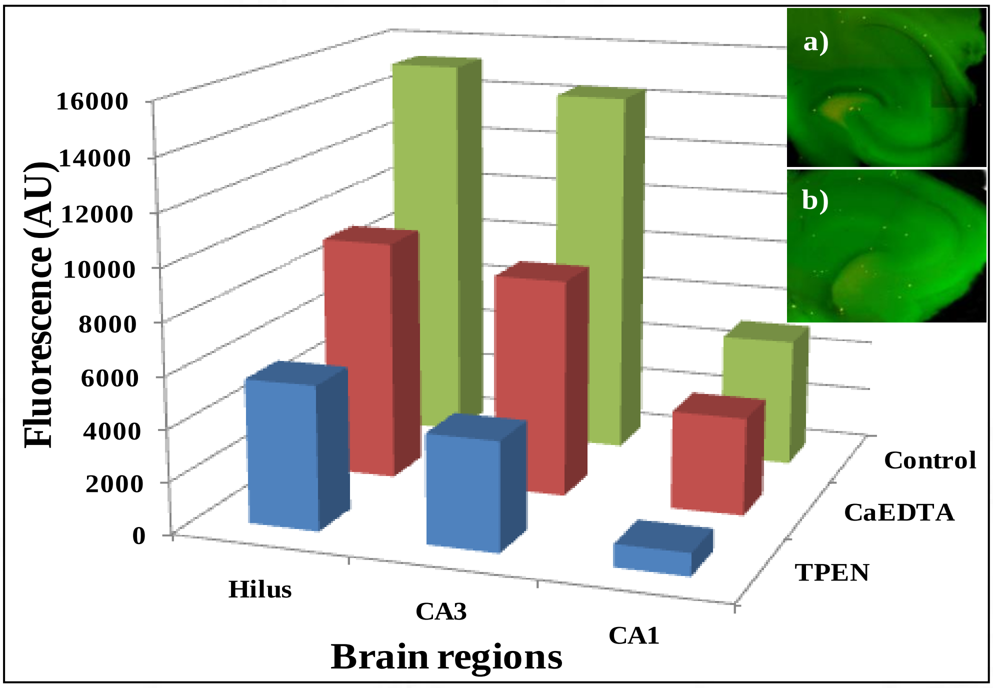

Figure 44: Effect of CaEDTA and TPEN on vesicular Zn^{2+}, imaged with BP. Inset shows fluorescence images of group II (a) and III slices (b). (Santhakumar H *et al*., 2018)

4.1.3.2.3. Imaging Zn^{2+} dynamics under in vitro epileptic condition

To evaluate whether BP can be used to study the dynamics of Zn^{2+} during a pathological condition, BP was tested in a clinically relevant neuropathological condition like epilepsy. It is known that the depolarization of neuronal membrane causes the release of neurotransmitters from the synaptic vesicles into the synaptic cleft for signal transduction. Similar to neurotransmitters, Zn^{2+} is also released into the synaptic cleft from presynaptic vesicles under normal physiological condition (Takeda A, 2000). Whereas under neuropathological condition like epilepsy, it is reported that higher concentration of Zn^{2+} is released into the synaptic cleft (Qian J *et al*., 2011). Therefore, studying the Zn^{2+} dynamics is essential to understand the aetiology and manifestation of epilepsy.

Here, to study the dynamics of Zn^{2+}, stimulation of hippocampal slice was done to mimic epileptic condition *in vitro*. One of the common techniques to induce *in vitro* epileptiform activity is using elevated exogenous potassium stimulation (K^+) (Jandova K *et al.*, 2006, Malinska D *et al.*, 2010). This exogenous addition of elevated potassium causes the nerve terminals in the hippocampus to depolarize. Compared with the unstimulated control slice incubated with BP (Figure 43a), K^+ stimulated slices incubated with BP showed a drastic reduction of red fluorescence in H, SL of CA3 and CA2 (Figure 45a). This confirms the release of highly concentrated histochemically active zinc ions from the presynaptic neuronal vesicles of mossy fiber boutons into the synapse by extracellular K^+ stimulation (Frederickson C *et al*., 2006, Ketterman J *et al*., 2008).

In addition to the synaptic release of Zn^{2+}, an interesting phenomenon of Zn^{2+} translocation was observed using BP during K^+ stimulation. Interestingly, red fluorescence was observed in GCL, SP of CA2 and CA3 (Figure 45a). This confirms that the Zn^{2+} released from the vesicles of presynaptic neurons in hilus and SP is translocated into the GCL of DG and SP of CA3 and CA2. Red fluorescence was also visible in the postsynaptic pyramidal neurons of CA1, confirming the translocation of Zn^{2+} (Figure 45a), which was absent in unstimulated control slice (Figure 43a). Low level of Zn^{2+} is translocated to CA1 pyramidal neurons than CA2 stratum pyramidale neurons. On the basis of these results, a connectome was mapped for the Zn^{2+} translocation during epileptic condition in hippocampus as DG→CA3→CA2→CA1. Eventhough there are a few studies that reported the translocation of Zn^{2+} in single neuronal cells (Ketterman J *et al*., 2008, Suh S, 2009), the imaging of Zn^{2+} translocation in whole hippocampal slice was reported by Santhakumar H *et al.*, 2018. Similar translocation pattern was shown by commercially available Fluozin-3 AM sensor, but with less efficiency than BP (Figure 45b).

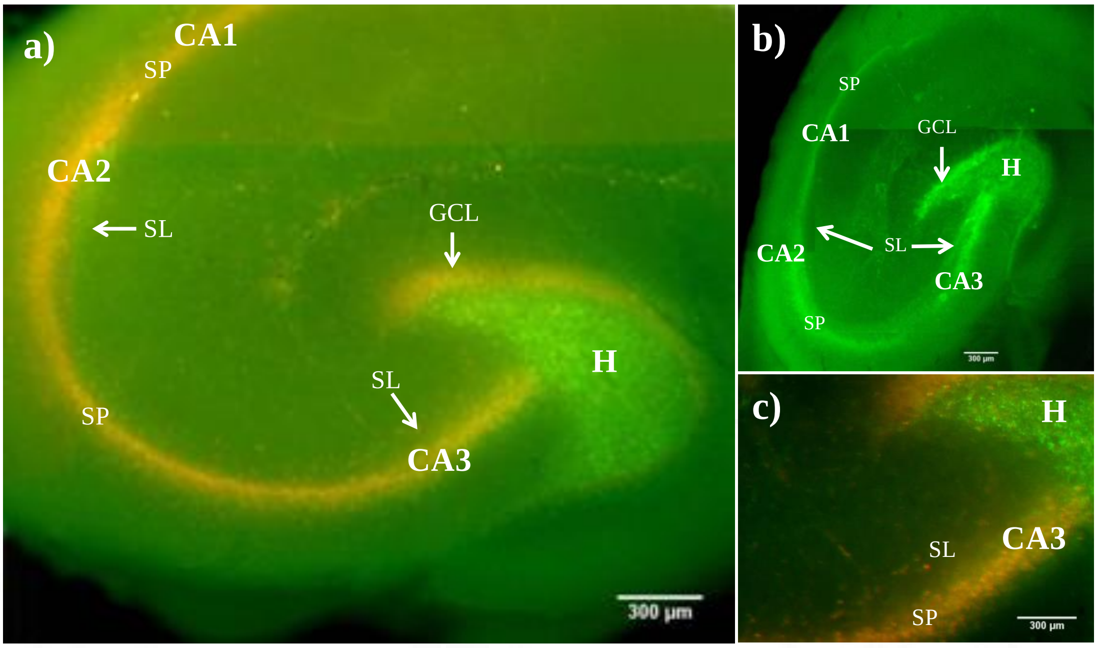

Figure 45: Imaging Zn^{2+} dynamics under *in vitro* epileptic condition using BP (a) and Fluozin-3 AM (b). (c) Higher magnification of a part of (a). Scale bar = 300 µm. (Santhakumar H *et al*., 2018)

Kodirov S *et al.*, 2006 reported that the vesicular Zn^{2+} released into the synaptic junction under physiological condition would bind to NMDA and glycine receptors on postsynaptic neurons to play a role in synaptic plasticity or modulate the function of these receptors. However, under pathological conditions like epilepsy, the function of synaptically released Zn^{2+} is mostly unclear. The conventional concept of neurotransmitters relies on the fact that the neurotransmitters once released into the synapse upon depolarization will bind with specific receptors in the postsynaptic neuronal cells to activate/inhibit the membrane channels for signal transduction. But the translocation exhibited by Zn^{2+} from synaptic cleft into post-synaptic neurons under stimulating epileptic condition poses a high demand for re-evaluating the conventional concept of neurotransmitters. Unlike conventional neurotransmitters, the entry of Zn^{2+} into postsynaptic neuronal cytosol would allow it to interact with many cytosolic macromolecules (Lengyel I *et al*., 2000) and this unique feature of Zn^{2+} translocation might be a cause of neurodegenerative diseases, like epilepsy (Kim J *et al*., 2012).

Hence, this study provides a clear visual picture of Zn^{2+} dynamics under epileptic condition and confirms that BP can efficiently study the dynamics of Zn^{2+} under neuropathological conditions. Therefore the development of probes like BP will largely help to visualize and study the dynamics of important ions under neurodegenerative disorders.

4.1.3.3. Studying Zn^{2+} dynamics using Raman spectroscopy

As BP showed excellent Raman peaks to understand the Zn^{2+} sensing in solution (section 4.1.2. Figure 37), BP was further tested through Raman spectroscopy to understand the dynamics of Zn^{2+} during epileptic condition in hippocampal slices. Raman spectra were recorded from the hilar region of all slices as this region is rich with Zn^{2+} containing synaptic vesicles. All the slices showed characteristic vibrational peaks of aliphatic amines, tryptophan, tyrosine, phospholipids, etc. of hippocampal slices (Figure 46). The complete Raman peak assignments in unstimulated control and stimulated epileptic slices are mentioned in Table 7. In case of unstimulated control slice, the metal–nitrogen bond formed in $BP•Zn^{2+}$ complex is prominent in 678 cm^{-1} vibrational peak (Figure 46). But in case of stimulated epileptic slice, the intensity of metal–nitrogen vibrational peak is decreased, thus confirming the release of vesicular Zn^{2+} from the hilar region presynaptic neurons. The results are in good agreement with the SERS spectra of material characterization study (Figure 37) and fluorescence imaging (Figure 43, 45). Hence BP can be used both as a fluorescent probe and Raman probe to study the dynamics of Zn^{2+} under various neuropathological conditions.

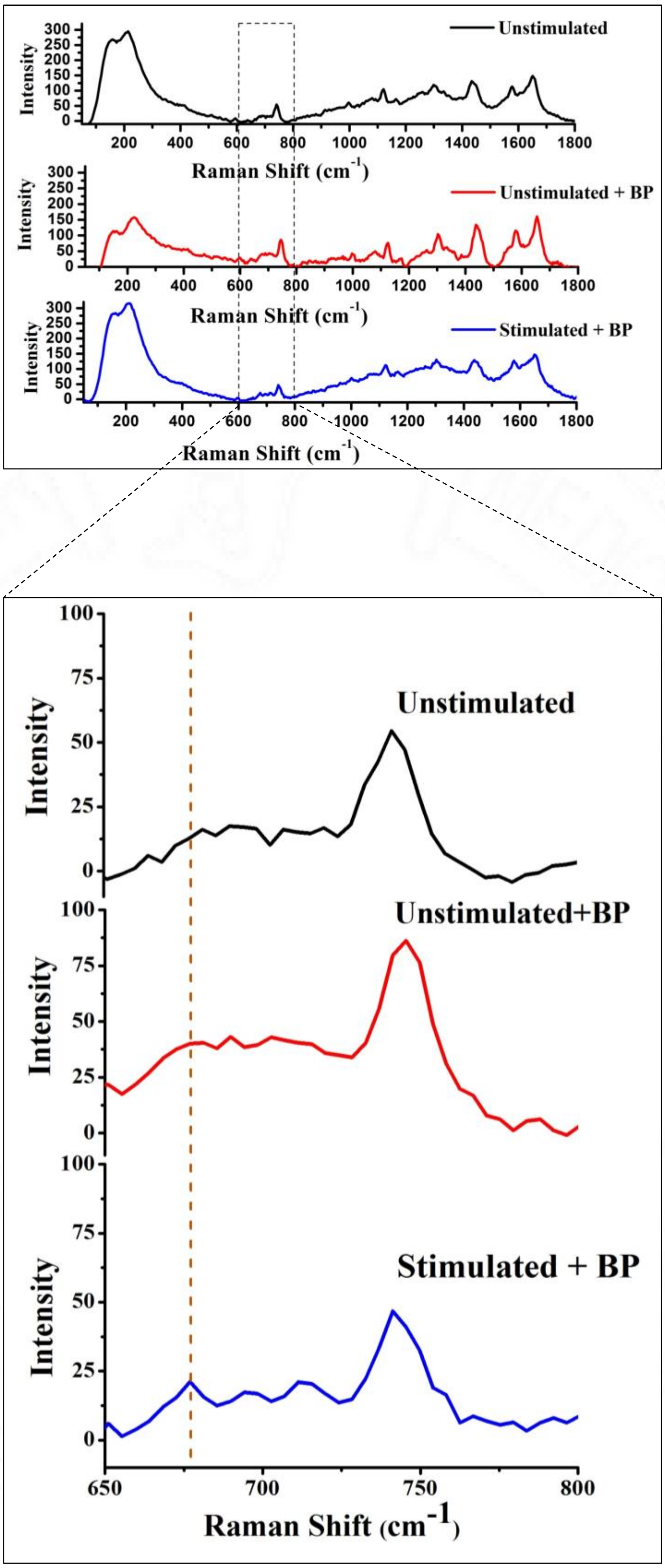

Figure 46: Raman Spectra from the hilar region of unstimulated (control) and stimulated (epileptic) hippocampal slices incubated with BP. (Santhakumar H *et al.*, 2018)

Raman Shift (cm^{-1})				Assignments
BP	Unstimulated Slice	Unstimulated slice+BP	Stimulated slice+BP	
	157-267	148-114	162-284	
	211-295	223-156	209-319	
	350-69	347-66	341-71	
	415-51	418-56	402-54	
		471-37		
	510-21	516-34		S-S Stretch
	542-12	545-29		
	563-8	572-25		
	596-11	599-30	597-6	Tyrosine
	637-3	640-23		
670-930				C-S stretch
→		678-41	678-25	Metal-nitrogen bond
710-867	714-16		709-21	Phospholipids such as phosphatidylethanolamine/phosphatidylcholine
	741-56	741-88	740-46	Tryptophan
		821-16		
		848-18	863-29	Tyrosine
			889-33	
949-913		966-33	958-55	C-C of peptide backbone and BP, and PO$_2^-$ stretching
	996-60	996-43	1001-70	Ring breathing-phenylalanine, PO$_2^-$ stretch
1017-950	1022-51		1027-68	
			1057-83	
1070-962	1085-75	1079-51		Aliphatic side chain
	1120-102	1126-76	1122-111	Aliphatic side chain C-C stretch
	1165-75	1171-25	1161-91	
		1230-32	1230-102	
	1254-95	1263-55	1260-108	Amide III (alpha helix) & lipids
	1301-119	1304-102	1301-131	
	1340-97	1337-65		Tryptophan
	1358-83	1360-45	1352-102	
	1393-75	1390-38		
1415-1114	1435-131	1438-135	1438-130	CH$_2$ deformation
			1494-75	
1529-1109		1541-49		
	1574-52	1577-114	1577-131	Tryptophan
	1603-95		1609-112	Phenylalanine
	1654-147	1654-158	1652-148	Amide I alpha helix

Table 7: Raman peak assignments of control and epileptic hippocampal slices incubated with BP (Santhakumar H *et al*., 2018)

4.1.3.4. Ratiometric imaging

4.1.3.4.1. Ratiometric imaging of Zn^{2+} in C6 glioma cells

To prove the ratiometric imaging potential of BP, time lapse imaging was carried out in C6 glioma cells serially treated with BP (30 min), Zn^{2+} (15 min) and Zn^{2+} chelator TPEN (20 min). Images were acquired with two emission filters (510–550 nm as green channel and 575–625 nm as red channel) excited with a single excitation filter (470–495 nm). Time lapse images were acquired @ 30, 45 and 65 min for BP, Zn^{2+} and TPEN addition respectively. Cells imaged @ 30 min with the incubation of BP showed increased fluorescence intensity in green channel (Figure 47A2) but with reduced fluorescence intensity in red channel (Figure 47A3). At 45 min with the subsequent addition of Zn^{2+} to the cells, the fluorescence intensity in green channel is reduced with a marked elevation of fluorescence intensity in the red channel (Figure 47B3), confirming the sensing of Zn^{2+} by BP. At 65 min with the subsequent addition of TPEN, cells again showed reduced fluorescence intensity in red channel (Figure 47C3) due to the reversible Zn^{2+} chelation effect of TPEN. In all the cases, ratiometric images were generated based on the ratio of intensity in red and green channels (I_{620}/I_{570}).

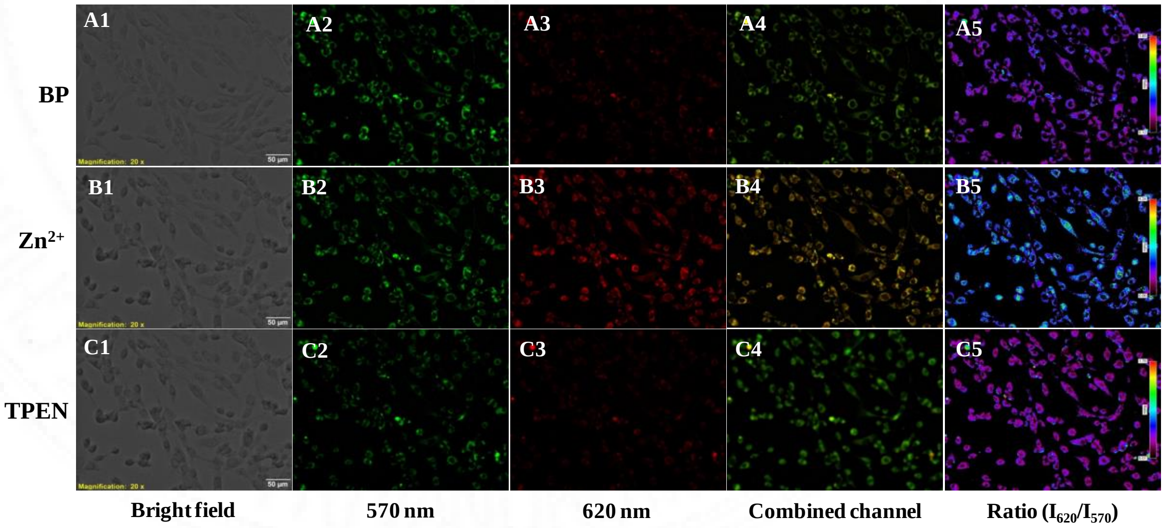

Figure 47: Ratiometric time lapse imaging of Zn^{2+} in C6 Glioma cells using BP. Scale bar = 50 µm. Ratio bar from 0.12 to 1.85 in a5, 0.06 to 4.24 in b5, 0.01 to 1.76 in c5. (Santhakumar H *et al.*, 2018)

The average ratio of emission intensities (R= I_{620}/I_{570}) in each treatment was calculated. On addition of Zn^{2+}, the emission intensity ratio of BP treated cells increased from 0.48 to 2.86 (Figure 48), hence confirming the enhancement of red intensity is due to BP•Zn^{2+} complex. Thus BP ruled out the influence of factors in fluorescence like autofluorescence, light scattering, proton flux into the cells or probe photo activation due to overexposure mentioned in section 2.1.3. Hence BP is qualified to monitor intracellular Zn^{2+} concentration under biological conditions in real time.

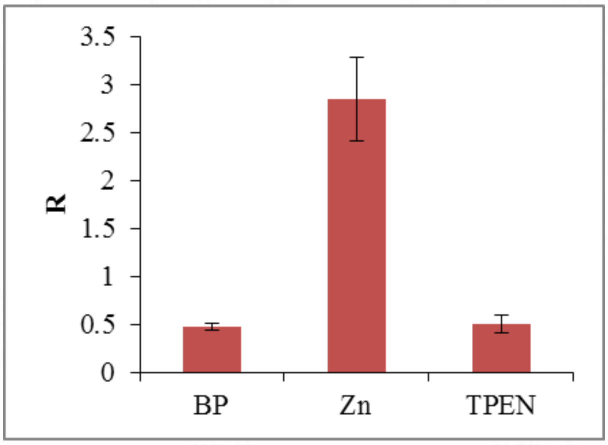

Figure 48: Average emission intensity ratio (R=I_{620}/I_{570}) according to the corresponding ratiometric images of cells in Figure 47. Mean±s.d. (n=5). (Santhakumar H *et al*., 2018)

4.1.3.4.2. Ratiometric imaging of Zn^{2+} dynamics in epileptic hippocampal slice

In addition to the ratiometric imaging of Zn^{2+} in cells, the endogenous Zn^{2+} in hippocampal slices and its dynamics were also ratiometrically measured under normal and epileptic condition (Figure 49). The ratiometric images generated from the red and green channel images provide an indication about the quantity of Zn^{2+} in each area of hippocampal slices and its dynamics under epileptic stimulation.

The average ratio of emission intensities from different areas of hippocampal slices were also calculated (Figure 50). Compared to the normal slice, the epileptic slice showed a reduced ratio in the hilar, SL region and an increased ratio in GCL of DG, SP of CA3 and CA1. Hence the release and translocation of Zn^{2+} from presynaptic vesicles to postsynaptic neurons during epilepsy is again confirmed and the results are in good agreement with section 4.1.3.2.3 and section 4.1.3.3.

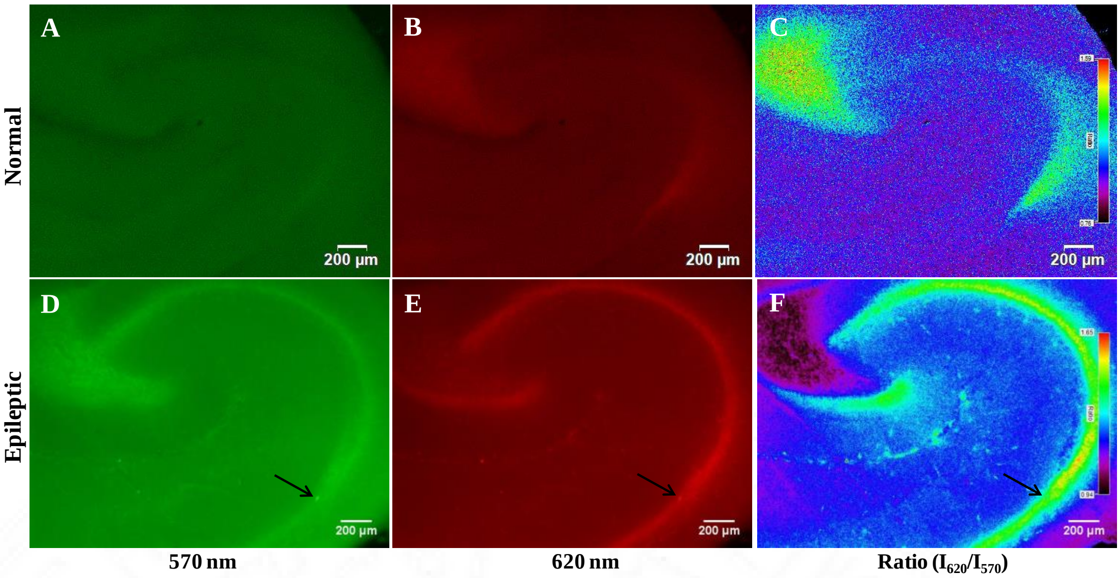

Figure 49: Ratiometric imaging of endogenous Zn^{2+} and its dynamics in hippocampal slices. Scale bar = 200 µm. Ratio bar represents Zn^{2+} concentration from low (black) to high (red). Arrows in (D,E) indicates the intense fluorescence due to artefact which is cancelled out in (F). (Santhakumar H *et al.*, 2018).

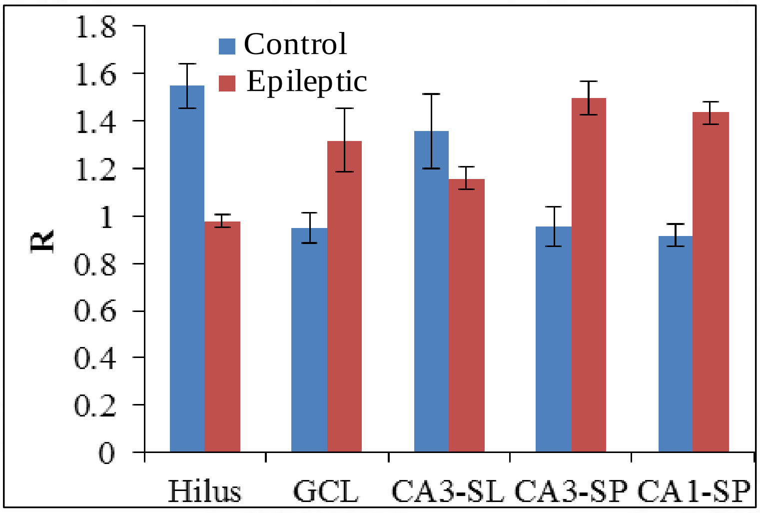

Figure 50: Average emission intensity ratio ($R=I_{620}/I_{570}$) according to corresponding ratiometric images of slices in figure 49. Mean±s.d. (n=4)

In general, factors like non-uniformity of the slice thickness, excitation exposure time variation and artefacts associated with probe concentration can affect the fluorescence intensity of tissue slices. On the other hand, ratiometric imaging is expected to overcome these problems, by taking the ratio between the two fluorescence intensities, which is independent of such factors. For example, the strong fluorescence of a point at the end of CA3 in figure 49D and E is due to artefact, which was cancelled out in the ratiometric image (Figure 49F). The development of ratiometric probes like BP can solve the challenges faced by neurobiologists to understand the concentration of vesicular Zn^{2+} and its dynamics under neuropathological conditions like epilepsy conditions in greater depth, thereby would pave a way for successive treatment.

4.1.4. In vivo studies

4.1.4.1. Zn^{2+} quantification in rat brain

The total amount of free Zn^{2+} in rat brain was quantified using an *in vivo* optical imaging system. Quantification was done by measuring the pixel intensity of Zn^{2+} in brain sections incubated with BP compared with a standard plot generated with different concentration of BP•Zn^{2+} complex (Figure 51). The total amount of free Zn^{2+} estimated was 0.4356 M (~2.85 mg) for a brain weighing 2.4 g.

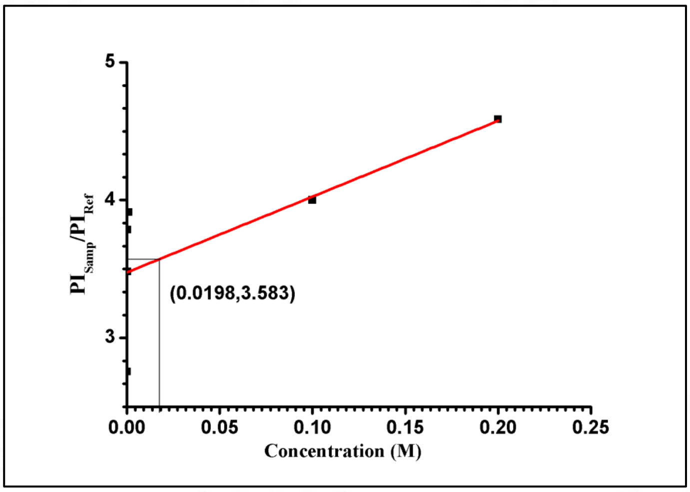

Figure 51: Quantification of total free Zn^{2+} in rat brain weighing 2.4 g. The standard plot shows the pixel intensity ratio with reference to different concentration of BP•Zn^{2+} complex.

4.1.4.2. Epileptic behavioural changes

The epileptic behavioural changes observed in pilocarpine injected animals are given in the table 8 below. After 1 h, all the rats were injected with an anticonvulsant, midozolam (McMullan J *et al.*, 2010, Reddy S *et al.*, 2015). With the injection of midozolam, one of the rats experienced a slight sedation and the severity of seizure is decreased. After 1 h, stage III seizure was observed in rat, which was again controlled with another dose of midazolam injection. 4 out of 6 rats showed stage IV/V status epilepticus that lasted for about 3 to 4 h and the seizures stopped after 5 to 6 h. All the animals survived after epileptic seizures. After 24 h of video recording, both control and epileptic animals were anesthetized for intra-carotid artery cannulation and BBB disruption.

Observed activity in animal	**Time**	**Stages of epilepsy**
Normal activity	0-5 min	Stage 0
Reduced mobility	5-10 min	Stage I
Intense salivation, mouth and facial movements	10-20 min	Stage II
Head nodding, jerk in forelimb	20-30 min	Stage III
Rearing, whole body continuous clonic seizure	30-40 min	Stage IV
Falling due to loss of balance, tonic-clonic seizure	40 -60 min	Stage V

Table 8: Stages of epileptic seizures observed under video recording.

4.1.4.3. *In vivo* Zn^{2+} imaging in epileptic rat brain

The efficiency of BP to image Zn^{2+} *in vivo* during epileptic condition was then studied. The epilepsy rat model obtained by pilocarpine injection and infused with BP (80 µM) through external carotid artery and the control rats infused with PFS through external carotid artery were used for *in vivo* imaging. The presence of BBB is expected to prevent the access of BP into the brain and hence mannitol was used to disturb the BBB temporarily through intra-carotid artery infusion to ensure the easy access of BP into brain. Throughout the imaging procedure, all the animals were kept stable under anesthesia with normal respiration under IVIS live animal imaging system and hence the imaging is not interfered with any motion artefacts due to seizure. The animals were imaged @ Excitation/Emission = 430/620 nm. Compared with the PFS infused control rats, BP infused epileptic rats showed an intense fluorescence in left hemisphere of brain (Figure 52), as BP is infused through left carotid artery. This confirms the sensing of concentrated Zn^{2+} present in hippocampus by BP. Hence it is proved that BP has deep tissue imaging potential and can be used for real time imaging of Zn^{2+} in epileptic and other neurodegenerative conditions, *in vivo*.

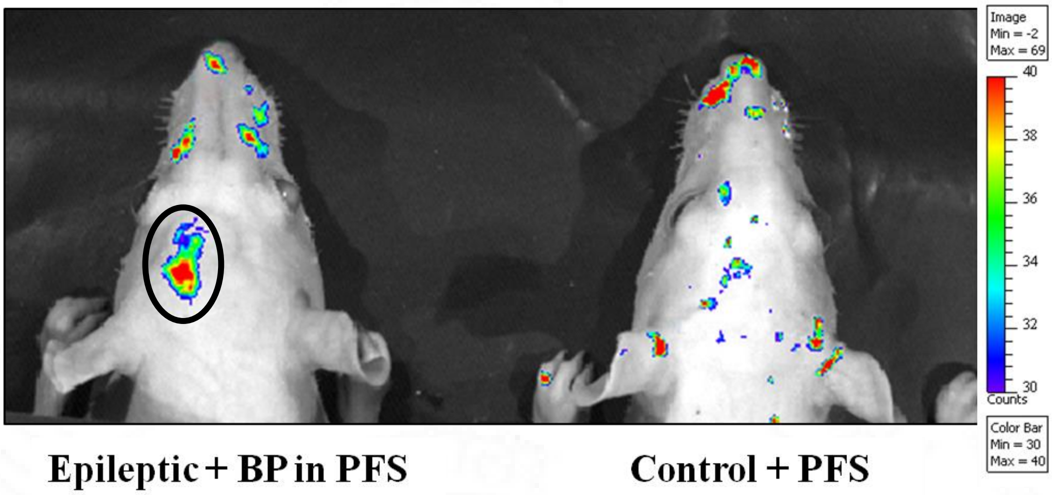

Figure 52: *In vivo* imaging of brain Zn^{2+} in epileptic rat using BP @ 430 nm excitation.

4.2. Fluorescent nano probe for cancer imaging and therapy

Gold nanoclusters are considered as an ideal candidate for imaging because of its exceptional fluorescent properties. However, the synthesis of highly fluorescent gold nanoclusters requires multiple steps and use of harsh chemicals that causes severe side effects in biological applications. Thus, a green, simple, one-step synthesis method to obtain biocompatible metal clusters is in urgent demand. Proteins or peptides protected metal clusters offers a great advantages owing to their biocompatibility and can be used for a variety of biomedical applications, such as biosensing, biolabeling, and bioimaging. The use of customized peptide sequences will also allow the fabrication of peptide-protected metal clusters with desirable structure, size, charge and targeting capability. In the present study, different tripeptide-stabilized gold nanoclusters were synthesized using a simple one-step green method and the cellular interaction of these tripeptide- gold nanoclusters were also studied.

4.2.1. Synthesis and characterization of tripeptides

The details of the synthetic procedure of six different tripeptides are explained in section 3.2.2. The progress of the successful coupling of each amino acid was monitored by Kaiser test. Complete coupling of each amino acid is confirmed with the colourless/very faint blue colour beads using Kasier test, while incomplete coupling shows blue colour beads in Kasier test (Figure 53). In case of incomplete coupling, recoupling was done with increased incubation time until the Kaiser test results shows complete coupling. The verification of complete coupling thus reflects in the preparation of proper sequence of peptides without any change. The chemical structure and the respective ball and stick model of the synthesized tripeptides (DCG, DCS, DCH, SCG, HCS and HCG) is shown in figure 54. All the tripeptides were designed and grafted with cysteine (C) amino acid to interact with gold during gold nanocluster synthesis. All the peptides were synthesized and mentioned as C-N terminal. As the peptides were synthesized using rink amide mbha resin, the final peptide product is believed to contain amide group at the C-terminal end. Hence all the peptides have C-terminal amide group and N-terminal amine group. LC-MS analysis was done to characterize all tripeptides. The mass of tripeptides calculated theoretically, correlated with the mass obtained from LC-MS analysis (Figure 55). The final mass of the tripeptides obtained from LC-MS analysis are 290.63 (DCG), 320.70 (DCS), 370.67 (DCH), 262.73 (SCG), 342.72 (HCS) and 312.68 (HCG).

Figure 53: Kaiser test results of peptide synthesis: R represents reference and S represents sample, In R - resin beads after Fmoc deprotection showed blue colour indicating the exposure of amino groups reacting with ninhydrin in Kaiser test. In S – resin beads showing white colour upon reaction with ninhydrin indicates the complete coupling of incoming amino acids with the deprotected previous amino groups.

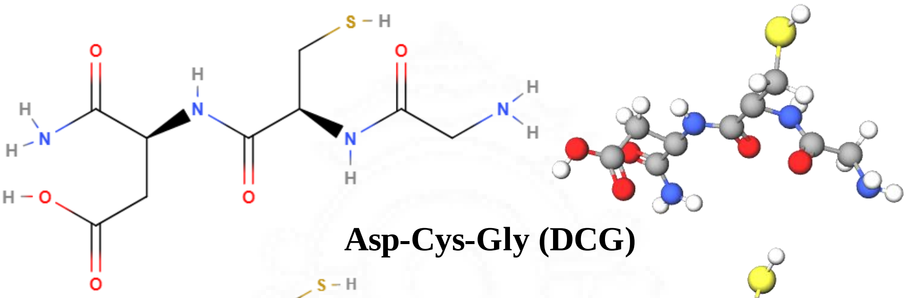

Asp-Cys-Gly (DCG)

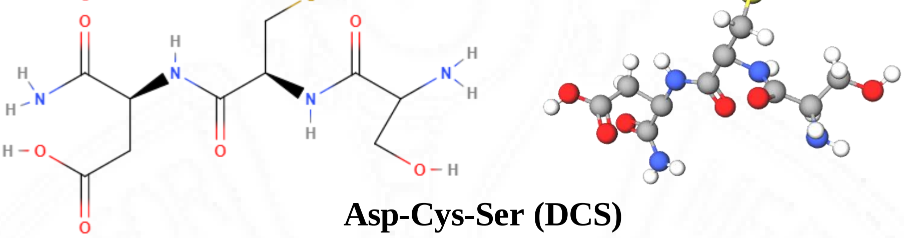

Asp-Cys-Ser (DCS)

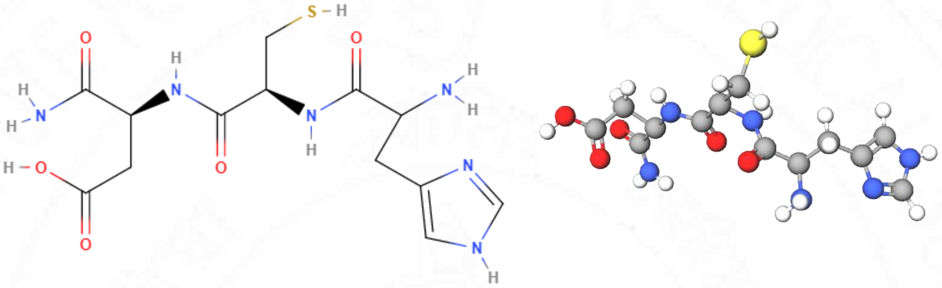

Asp-Cys-His (DCH)

● - C

● - S

● - O

● - N

● - H

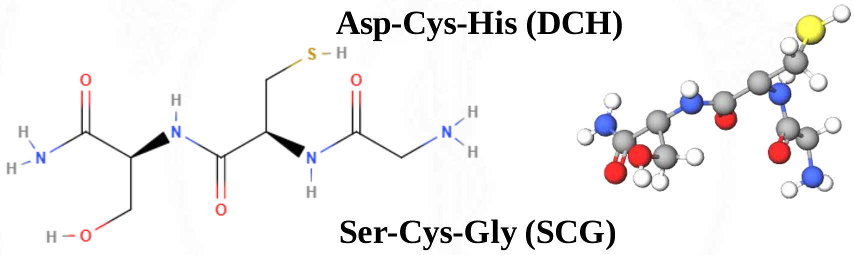

Ser-Cys-Gly (SCG)

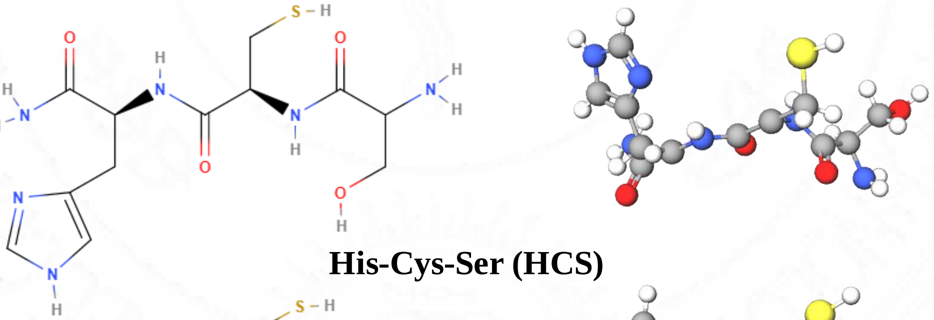

His-Cys-Ser (HCS)

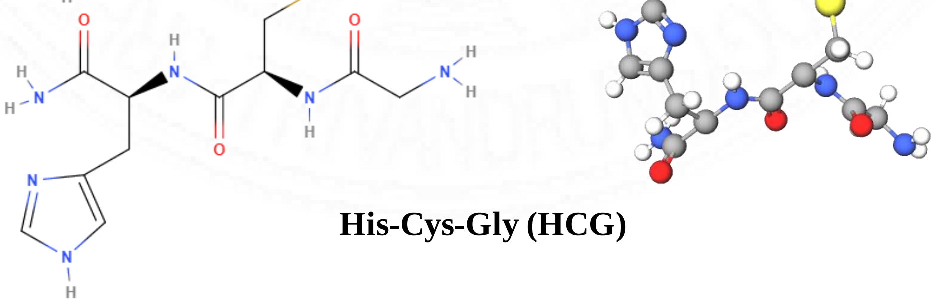

His-Cys-Gly (HCG)

Figure 54: Chemical structure of tripeptides with Ball and stick model.

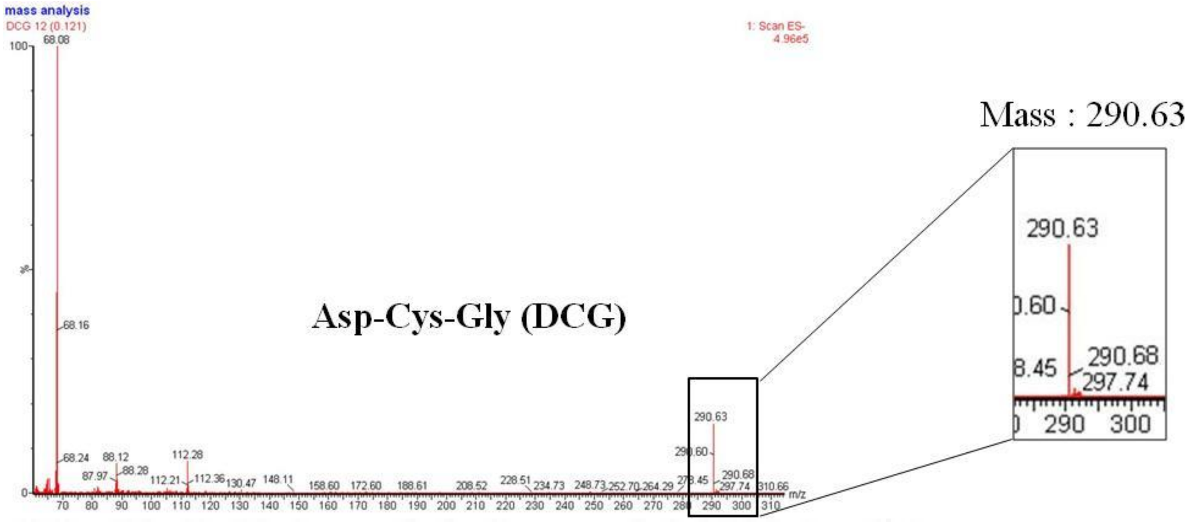
mass analysis
DCG 12 (0.121)
1: Scan ES-
4.96e5
Asp-Cys-Gly (DCG)
Mass : 290.63
68.08
68.16
68.24
88.12
87.97
88.28
112.28
112.21
112.36
130.47
148.11
158.60
172.60
188.61
208.52
228.51
234.73
248.73
252.70
264.29
278.45
290.60
290.63
290.68
297.74
310.66
100
%
0
m/z

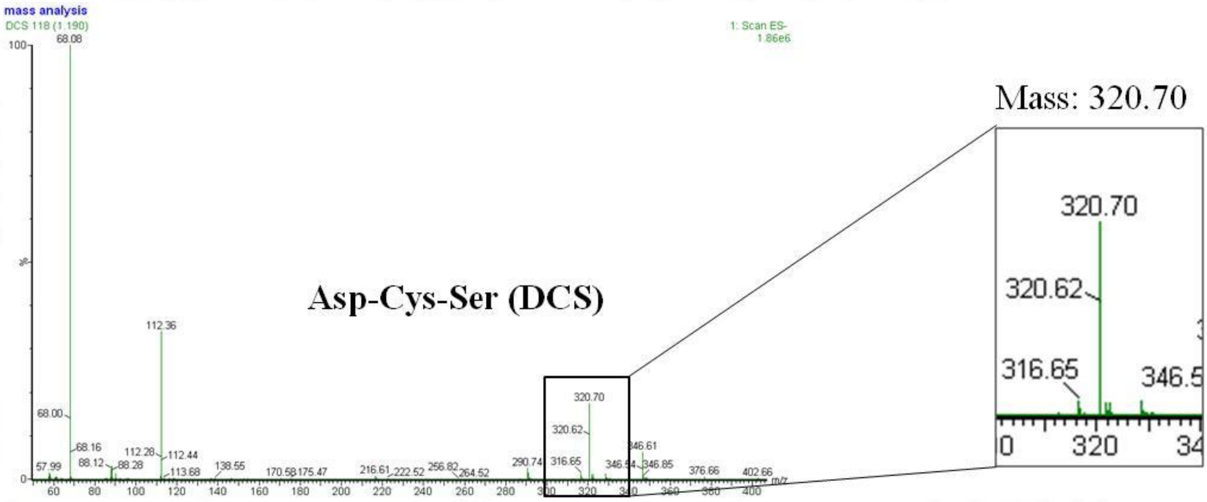
mass analysis
DCS 118 (1.190)
1: Scan ES-
1.86e6
Asp-Cys-Ser (DCS)
Mass: 320.70
68.08
68.00
68.16
57.99
88.12
88.28
112.36
112.28
112.44
113.68
138.55
170.58
175.47
216.61
222.52
256.82
264.52
290.74
316.65
320.62
320.70
346.54
346.61
346.85
376.66
402.66
100
%
0
m/z

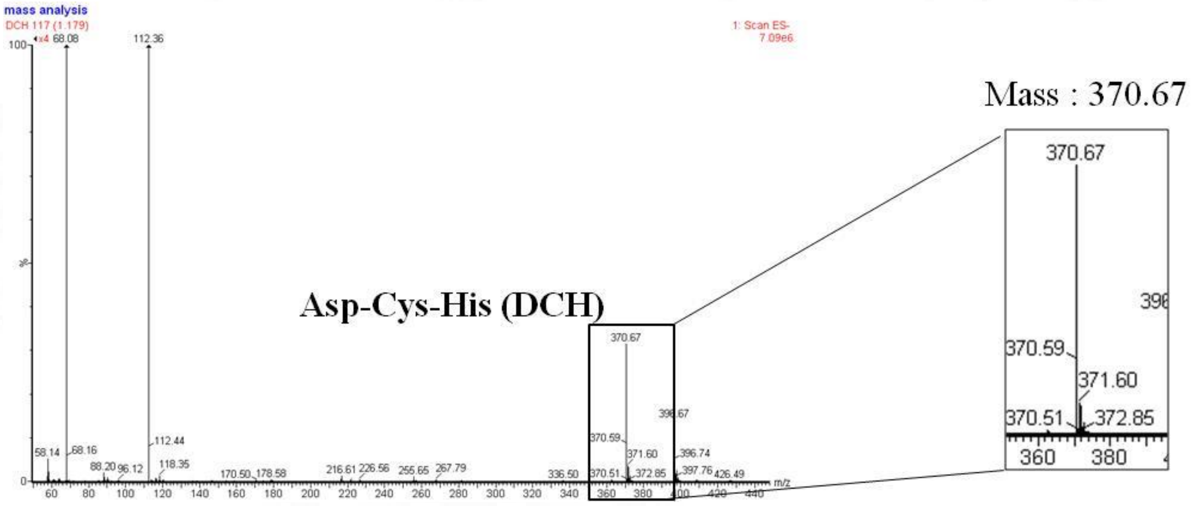
mass analysis
DCH 117 (1.179)
1: Scan ES-
7.09e6
x4
Asp-Cys-His (DCH)
Mass : 370.67
68.08
112.36
58.14
68.16
88.20
96.12
112.44
118.35
170.50
178.58
216.61
226.56
255.65
267.79
336.50
370.51
370.59
370.67
371.60
372.85
396.67
396.74
397.76
426.49
100
%
0
m/z

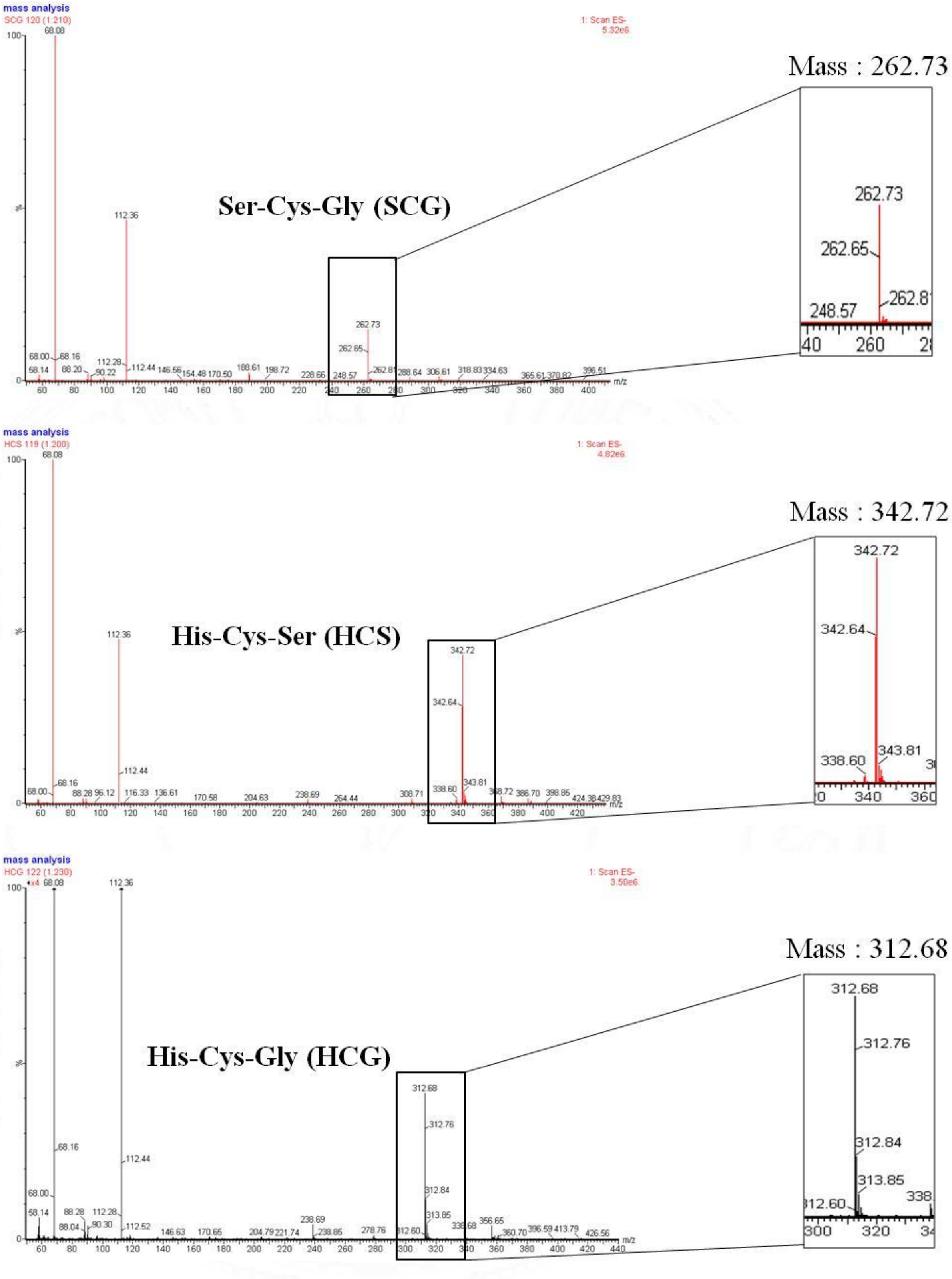

Figure 55: LC-MS of synthesized tripeptides with its respective mass shown in the magnified box

4.2.2. Synthesis of tripeptide-gold nanoclusters

The synthesis of different gold nanoclusters (GNCs) namely, DCG-GNC, DCS-GNC, DCH-GNC, SCG-GNC, HCS-GNC and HCG-GNC was done using the above custom synthesized six different tripeptides DCG, DCS, DCH, SCG, HCS and HCG respectively (Figure 56). Herein, the tripeptides were used as reducing cum stabilizing agents and hence this is a simple one-step, green method to obtain the peptide– GNCs. The thiol (–SH) group of the amino acid cysteine in peptides participate in the reduction of Au^{3+} into peptide-AuNCs (GNCs) without requiring additional strong reducing agents. The thiol (–SH) groups in the peptides also capture the clusters and stabilize it based on the unique metal-sulphur chemistry and form a strong Au-S bond. The other groups in the peptides such as carboxyl and amino groups may also contribute to the structural stabilization of metal clusters. It is also reported that the imidazole group in histidine play a crucial role as reducing cum stabilizing agent for the formation of gold nanoclusters (Yang X *et al*., 2011). Hence, in the three gold nanoclusters (DCH-GNC, HCS-GNC and HCG-GNC), histidine along with cysteine might be responsible for the reduction of Au atom and stabilization of gold nanoclusters. Reports have suggested that the doping of silver atoms to gold nanoclusters can contribute to the fluorescence enhancement of gold nanoclusters (Le Guével X *et al*., 2012, Wang S *et al*., 2014). Hence the addition of silver during the gold nanocluster synthesis was attempted to influence the fluorescence enhancement of pure gold nanoclusters. In addition, the synthetic procedure of gold nanoclusters in water medium is easy and provides biocompatibility to these nanoclusters. The pictorial representation of the synthesis of different tripeptide-gold nanoclusters, along with their excitation and emission details is given in figure 56.

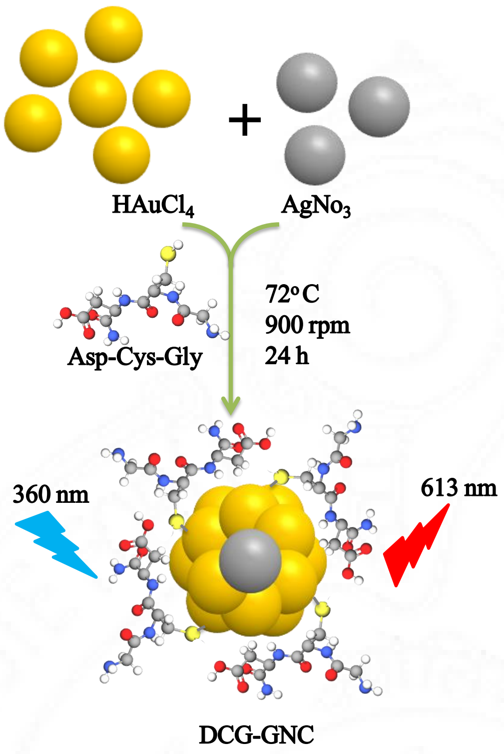
$HAuCl_4$
+
$AgNo_3$
Asp-Cys-Gly
72°C
900 rpm
24 h
360 nm
613 nm
DCG-GNC

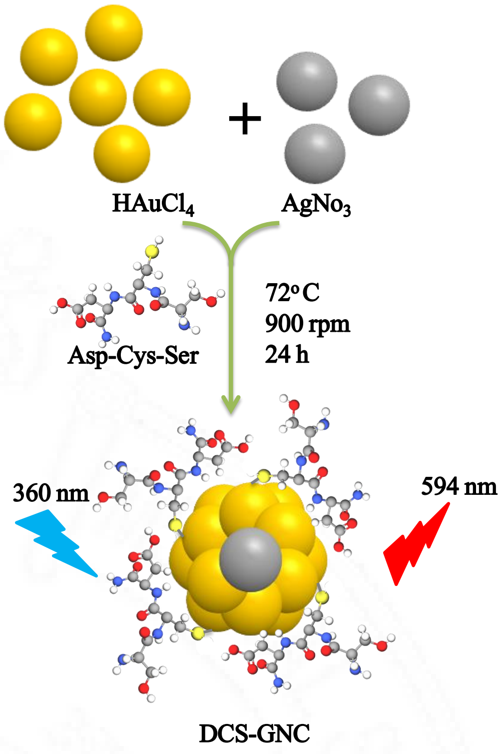
$HAuCl_4$
+
$AgNo_3$
Asp-Cys-Ser
72°C
900 rpm
24 h
360 nm
594 nm
DCS-GNC

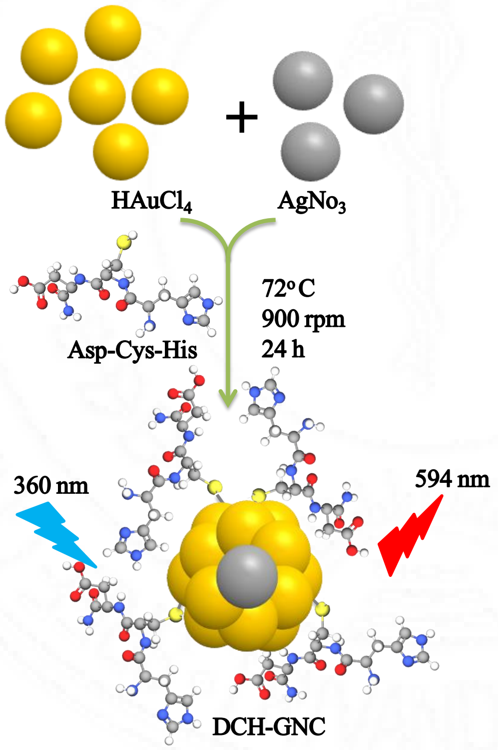
$HAuCl_4$
+
$AgNo_3$
Asp-Cys-His
72°C
900 rpm
24 h
360 nm
594 nm
DCH-GNC

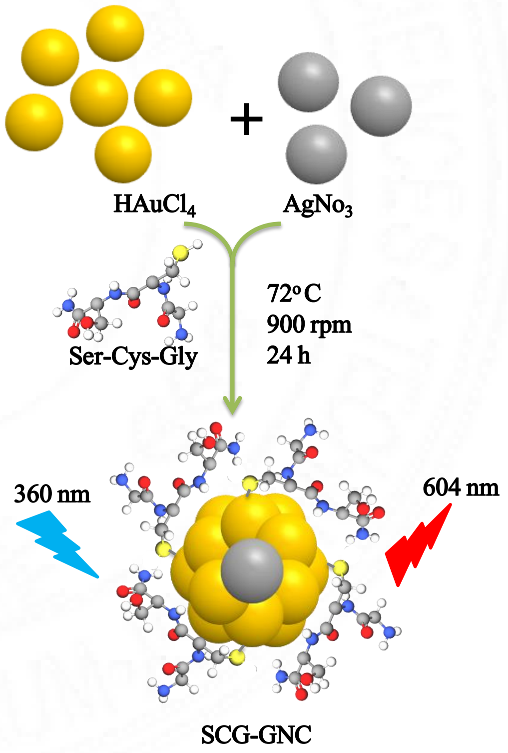
$HAuCl_4$
+
$AgNo_3$
Ser-Cys-Gly
72°C
900 rpm
24 h
360 nm
604 nm
SCG-GNC

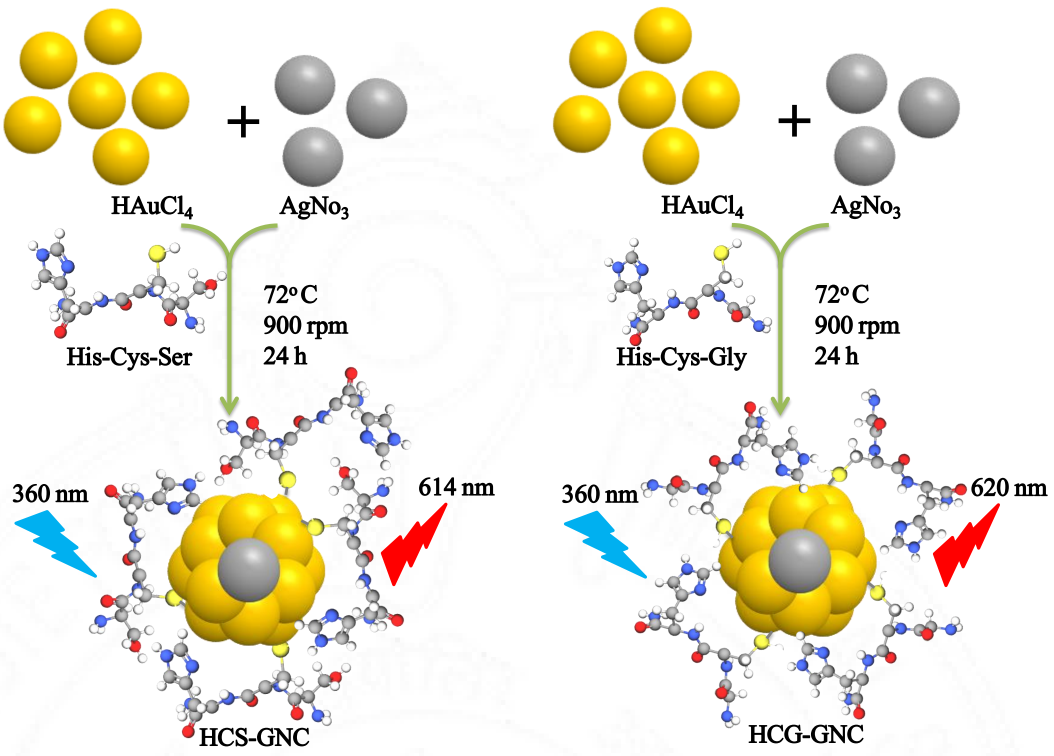

Figure 56: Pictorial representation of the synthesis of six tripeptide-gold nanoclusters (DCG-GNC, DCS-GNC, DCH-GNC, SCG-GNC, HCS-GNC and HCG-GNC).

4.2.3. Physico-chemical characterization of tripeptide-gold nanoclusters

4.2.3.1. Optical properties

The absorption, emission and excitation spectra of six tripeptide-gold nanoclusters are shown in figure 57. Insets in figure 57 show the photographic image of gold nanoclusters under white light and UV light illumination (365 nm). The absorption spectra of different tripeptide-gold nanoclusters were recorded with UV-Vis spectrophotometer, which shows the characteristic spectra of gold nanoclusters. The absence of surface plasmon resonance (SPR) peak @ ~520 nm indicates the absence of larger size gold nanoparticles and confirms the presence of small size nanoclusters. Due to the molecular-like property, the absorption spectra of all the tripeptide-gold nanoclusters rise sharply below 300 nm with a band edge of 450 nm. These gold nanoclusters emit strong fluorescence from yellow to red depending on the different tripeptides used for synthesis. This emission range is highly advantageous for bioimaging, since it avoids the hindrance from autofluorescence.

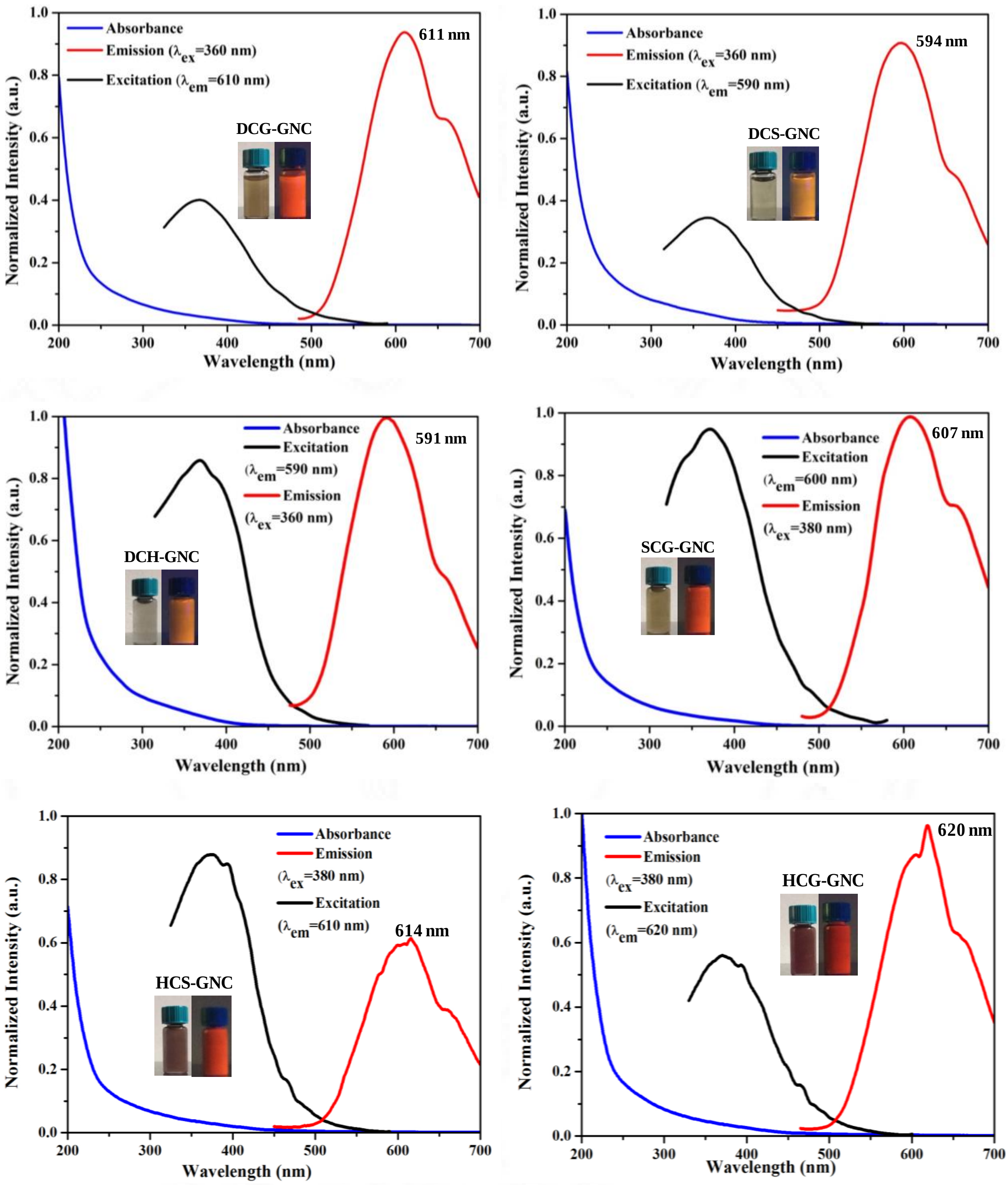

Figure 57: UV-Vis Absorption, Emission & Excitation spectra of different tripeptide-gold nanoclusters. Insets in every graph shows the photographic image of gold nanoclusters under visible and UV light illumination.

The maximum emission and excitation peak of gold nanoclusters are mentioned in table 9 and the emission spectra upon different excitation wavelength are shown in figure 58. The excitation of gold nanoclusters at different wavelength did not shift the emission spectra, indicates the high optical stability of these tripeptide-gold nanoclusters. These gold nanoclusters also exhibited very large stokes shift (>220 nm), which avoids the interference from spectral overlap and autofluorescence and therefore highly beneficial for biological imaging.

Gold nanoclusters	Excitation maximum	Emission maximum
DCG-GNC	367 nm	611 nm
DCS-GNC	367 nm	594 nm
DCH-GNC	369 nm	591 nm
SCG-GNC	371 nm	607 nm
HCS-GNC	374 nm	614 nm
HCG-GNC	371 nm	620 nm

Table 9: Excitation and emission maximum of different tripeptide-gold nanoclusters.

The fluorescence quantum yield of these tripeptide-gold nanoclusters was estimated using the comparative method with an organic dye Rhodamine 6G as reference standard. The experimentally determined fluorescence quantum yield of six gold nanoclusters is mentioned in table 10. All the tripeptide-gold nanoclusters exhibited more than 12 % quantum yield confirming the high brightness of gold nanoclusters in water. DCG-GNC and HCS-GNC showed highest quantum yield (18 %) than other clusters, which is significantly higher than most of the gold nanoclusters reported in the literature. This high quantum yield or fluorescence enhancement may be due to the presence of silver atom in the gold nanoclusters. It has been reported that Ag^+ influence the fluorescence enhancement of Au clusters by ligand-to metal charge transfer (LMCT) or ligand-to metal-metal charge transfer (LMMCT) (Li B *et al*., 2016, Le Guével X *et al*., 2012, Wang S *et al*., 2014).

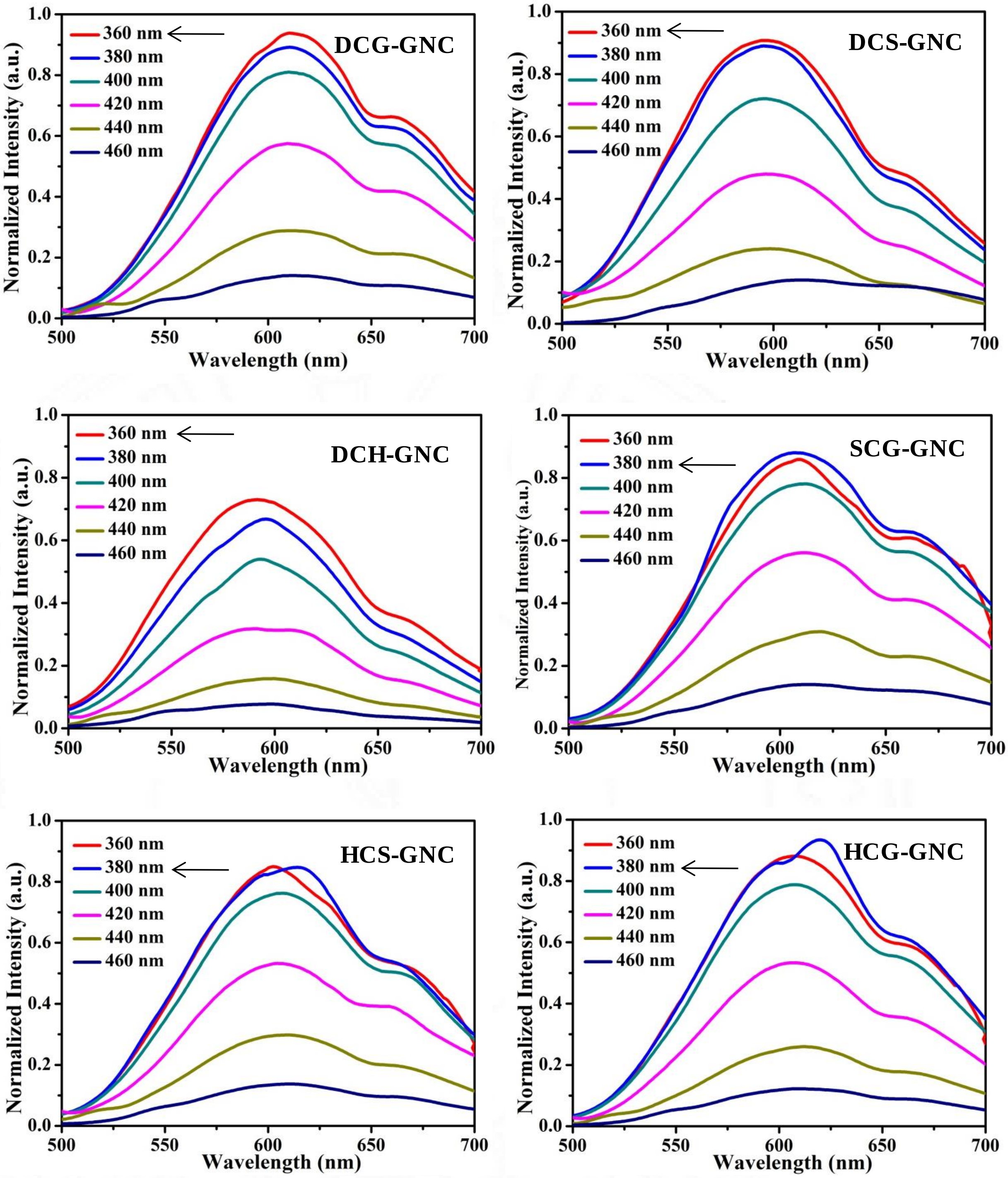

Figure 58: Emission spectra of different tripeptide-gold nanoclusters upon different excitation.

Sample	**Quantum Yield with reference to Rhodamine 6G (Φ_F)**	**Φ_F (%)**
DCG-GNC	0.18	18
DCS-GNC	0.16	16
DCH-GNC	0.13	13
SCG-GNC	0.14	14
HCS-GNC	0.18	18
HCG-GNC	0.15	15

Table 10: Quantum yield of six different tripeptide-gold nanoclusters.

Many noble metal nanoclusters have long fluorescence lifetime with one or two magnitudes higher than quantum dots and organic dyes (Le Guével X *et al.*, 2011). These metal nanoclusters commonly have multiple lifetime components depending on the excitation wavelength. The fluorescence lifetime of different nanoclusters is shown in figure 59. All the synthesized tripeptide-gold nanoclusters exhibit remarkably long fluorescence lifetime with biexponential decay: one short component (τ_1) and one long component (τ_2) (table 11). DCG-GNC, HCS-GNC and HCG-GNC exhibited longer lifetime (> 250 ns) than DCS-GNC, DCH-GNC and SCG-GNC. The abundance of the long lifetime component τ_2 expressed in percentage is plotted in figure 60. Patel S et al., 2009 reported that the long lifetime component of metal nanoclusters is related to the electron transfer from the clusters to the ligand during the reduction process.

Sample	**λ_{em}**	**τ_1 (ns)**	**A_1 (%)**	**τ_2 (ns)**	**A_2 (%)**	**χ^2**
DCG-GNC	611	18.2	5.14	307.5	94.86	1.2
DCS-GNC	594	2.5	7.69	43.5	92.31	1.0
DCH-GNC	591	1.3	7.53	39.1	92.47	1.0
SCG-GNC	607	3.8	7.05	54.3	92.95	1.0
HCS-GNC	614	31.1	5.72	362.6	94.28	1.1
HCG-GNC	620	17.6	5.45	294.8	94.55	1.2

Table 11: Summary of lifetimes of tripeptide-gold nanoclusters @ λ_{ex} = 375 nm with their respective emission maximum. τ_1 and τ_2 represents short and long lifetime of gold nanoclusters in nanoseconds (ns), A1 and A2 represents relative amplitude in %, χ^2 represents Chi square value.

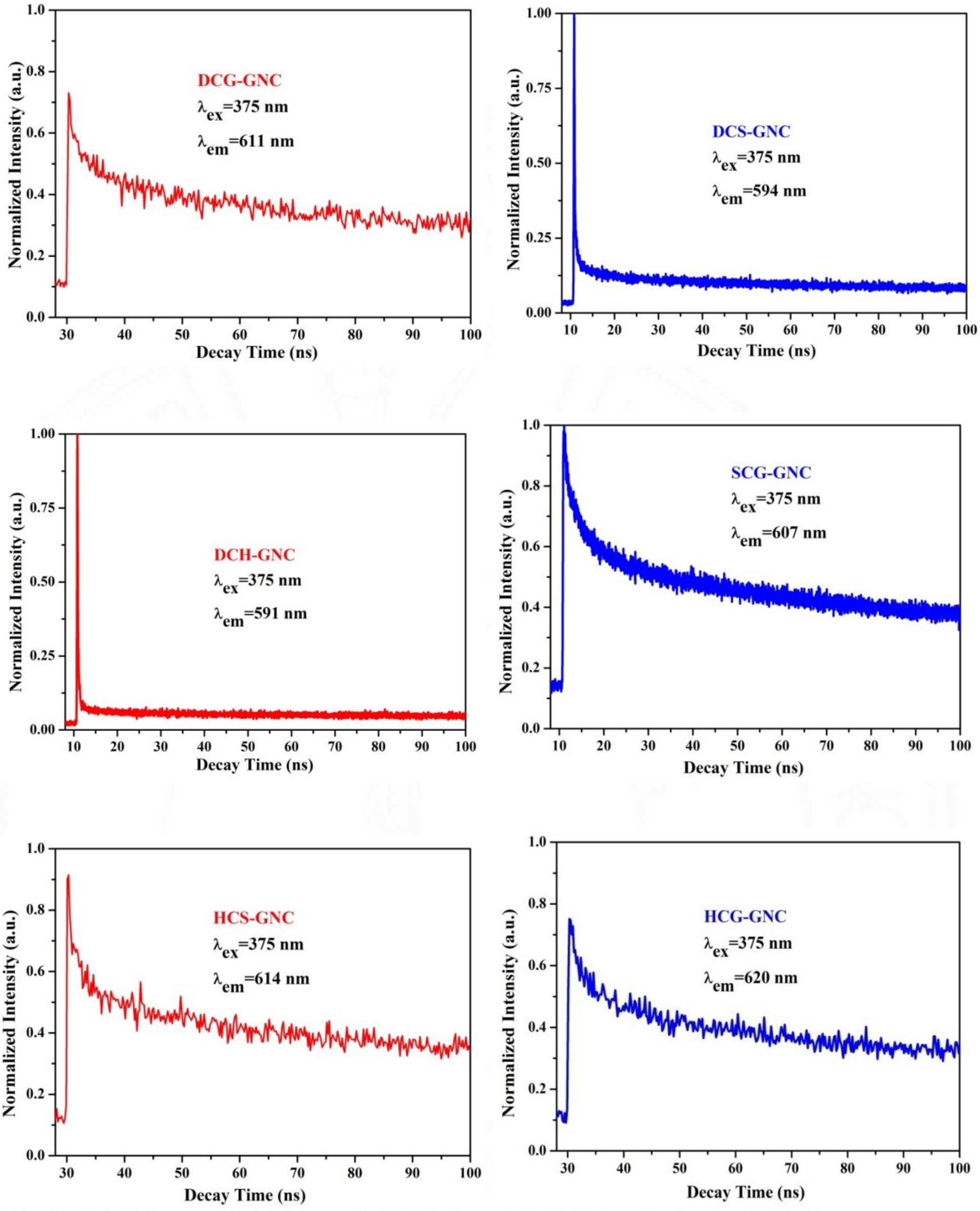

Figure 59: Fluorescence lifetime of tripeptide-gold nanoclusters at their respective emission maximum and @ 375 nm excitation.

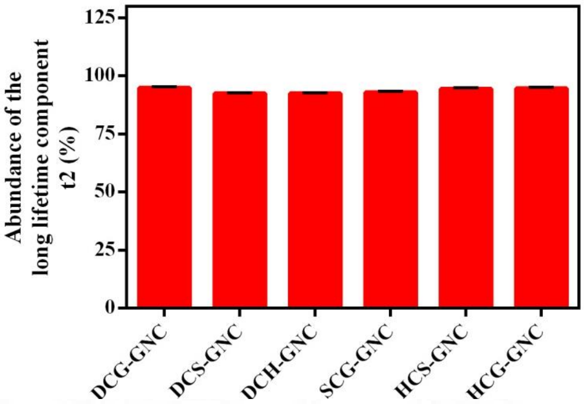

Figure 60: Relative amplitude of long lifetime component (τ_2) for different tripeptide-gold nanoclusters with λ_{ex} = 375 nm with their respective emission maximum.

4.2.3.2. Size, surface charge and surface chemistry

The size, size distribution and shape of tripeptide-gold nanoclusters were analyzed by HR-TEM. All the tripeptide-gold nanoclusters have spherical shape and narrow size distribution with an average diameter below 3 nm. Figure 61 shows the HR-TEM image and size distribution of different tripeptide-gold nanoclusters. HR-TEM image clearly illustrated the size as 2.5±0.2 nm, 2.9±0.25, 2.8±0.17 nm, 2.7±0.28 nm, 2.3±0.24 and 1.8±0.19 nm for DCG-GNC, DCS-GNC, DCH-GNC, SCG-GNC, HCS-GNC and HCG-GNC respectively. These ultra-small sizes strongly support the metal quantum confinement effect as mentioned in section 1.4.3, i.e., the emergence of attractive fluorescent property in tripeptide-gold nanoclusters is due to the ultra-small size of gold nanoclusters. All the tripeptide-gold nanoclusters showed aggregation in TEM image, which also strongly support the aggregation-induced emission phenomenon (AIE) of gold nanoclusters.

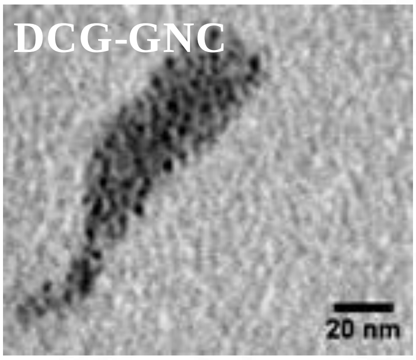
DCG-GNC
20 nm

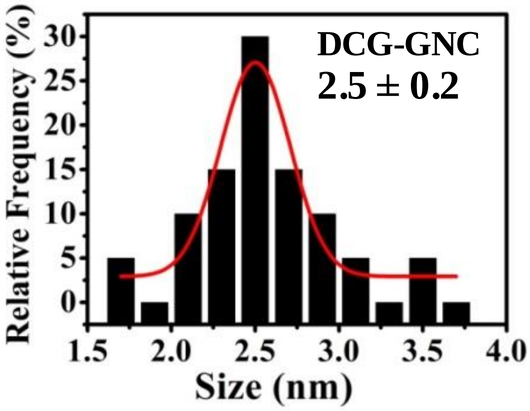
DCG-GNC
2.5 ± 0.2
Relative Frequency (%)
30
25
20
15
10
5
0
1.5
2.0
2.5
3.0
3.5
4.0
Size (nm)

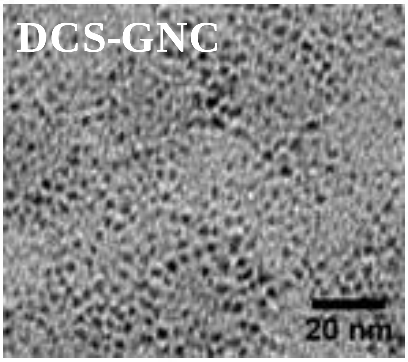
DCS-GNC
20 nm

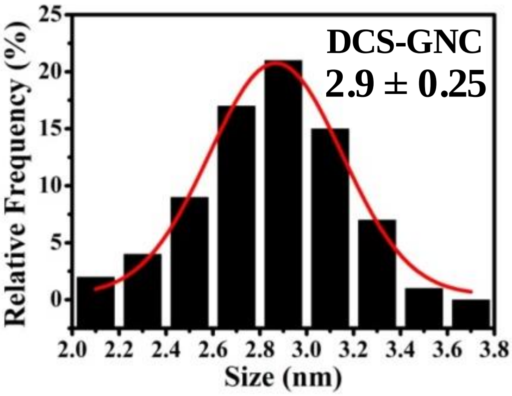
DCS-GNC
2.9 ± 0.25
Relative Frequency (%)
25
20
15
10
5
0
2.0
2.2
2.4
2.6
2.8
3.0
3.2
3.4
3.6
3.8
Size (nm)

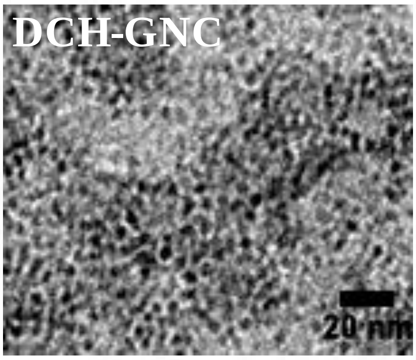
DCH-GNC
20 nm

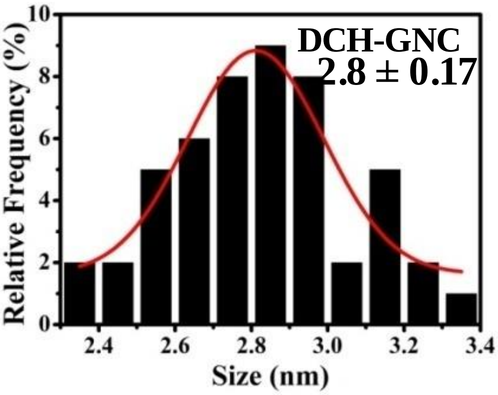
DCH-GNC
2.8 ± 0.17
Relative Frequency (%)
10
8
6
4
2
0
2.4
2.6
2.8
3.0
3.2
3.4
Size (nm)

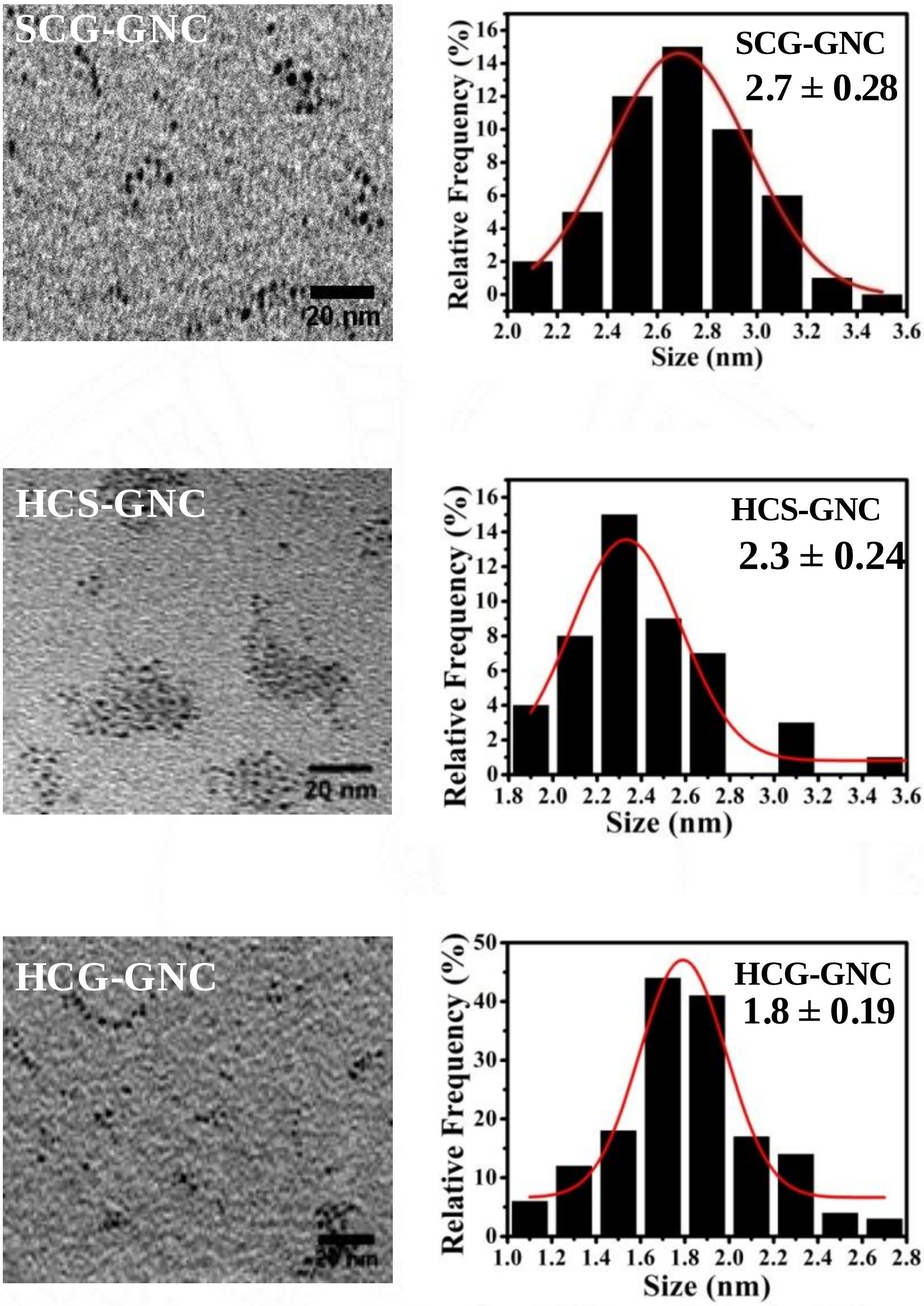

Figure 61: HR-TEM image (left) and size distribution (right) of tripeptide-gold nanoclusters (Scale bar = 20 nm).

The surface charge or zeta potential of the as-prepared tripeptide-gold nanoclusters were then analyzed by Malvern zeta sizer. The zeta potential of tripeptide-gold nanoclusters is shown in figure 62. From the results, the surface charge of DCG-GNC, DCS-GNC, DCH-GNC, SCG-GNC, HCS-GNC and HCG-GNC was found to be -7.4 mV, -10.25 mV, -2.59 mV, -4.62 mV, +1.67 mV and +2.33 mV respectively. The aspartic acid (Asp or D) in the peptide of DCG-GNC, DCS-GNC and DCH-GNC are negatively charged under physiological conditions and hence the surface charge of these nanoclusters is negative in as-prepared condition (pH 7). In contrast, histidine (His or H) in the peptide of HCS-GNC, HCG-GNC was positively charged under physiological conditions and hence the surface charge of these nanoclusters was positive in as-prepared condition (pH 7).

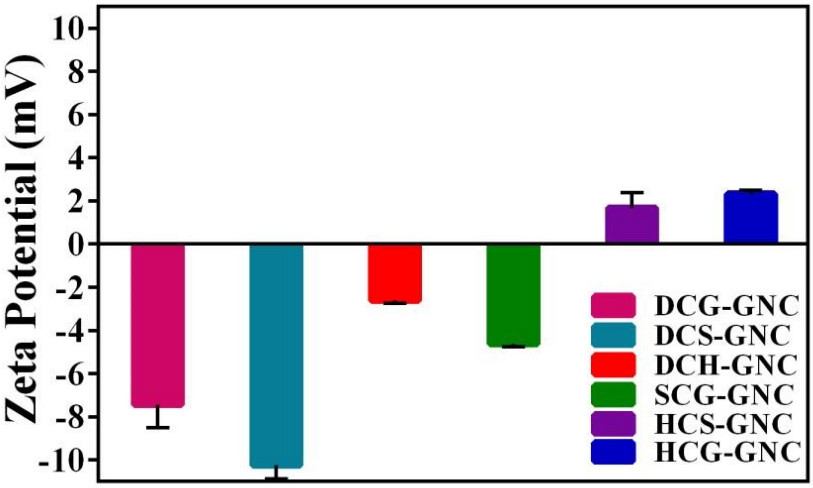

Figure 62: Surface charge of tripeptide-gold nanoclusters. Mean±s.d. (n=3)

FTIR spectral analysis was done to understand the nature of ligand-metal interaction, surface chemistry and functional properties of tripeptide-gold nanoclusters. Figure 63 shows the FTIR spectra of different tripeptides and its respective gold nanoclusters. The characteristic peak @ 2524 cm^{-1} in all the tripeptides attributes to the –SH group present in cysteine. The infrared measurements confirmed the covalent binding of tripeptides to the metal nanoclusters by the disappearance of peak @ 2524 cm^{-1} in gold nanoclusters and hence confirming the formation of Au-S bond in gold nanoclusters. In addition to the –SH peak, the broadening of band between 1750 to 1030 cm^{-1} in gold nanoclusters compared to the tripeptides also confirmed the covalent binding between tripeptides and metal clusters. In addition, the typical IR peaks @ 1640 cm^{-1} and 1535 cm^{-1} was observed for amide I band (C=O) and amide II band (N-H) respectively in all gold nanoclusters. The wide absoption band @ 3450 cm^{-1} corresponds to –NH_2, -C-NH and –COOH groups in the peptide at the surface of gold nanoclusters. The peak @ 2921 cm^{-1} and 1409 cm^{-1} are assigned to C-H stretching and O-H bending respectively.

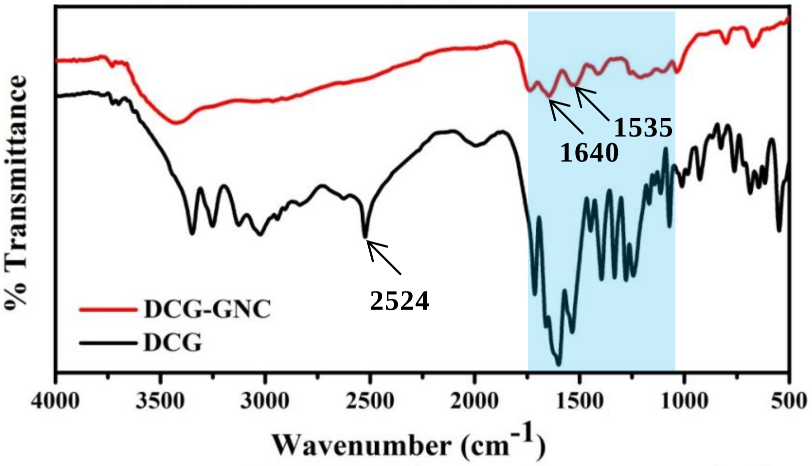

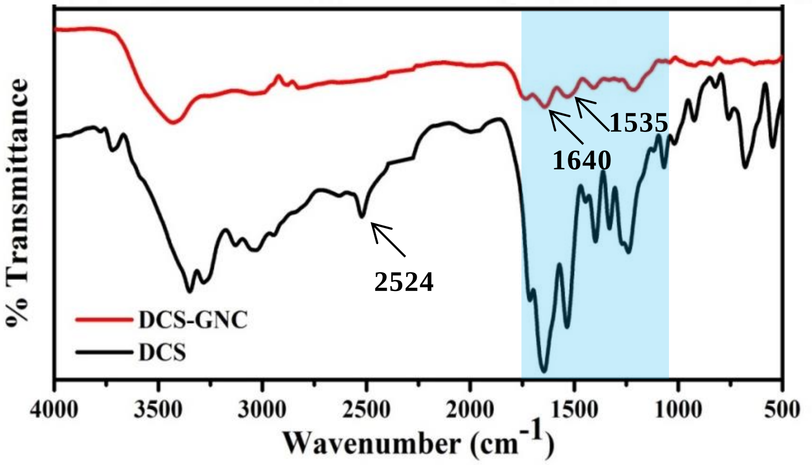

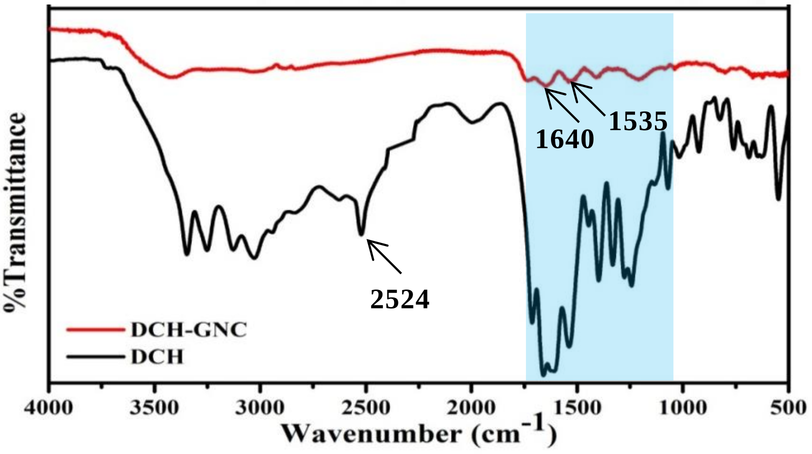

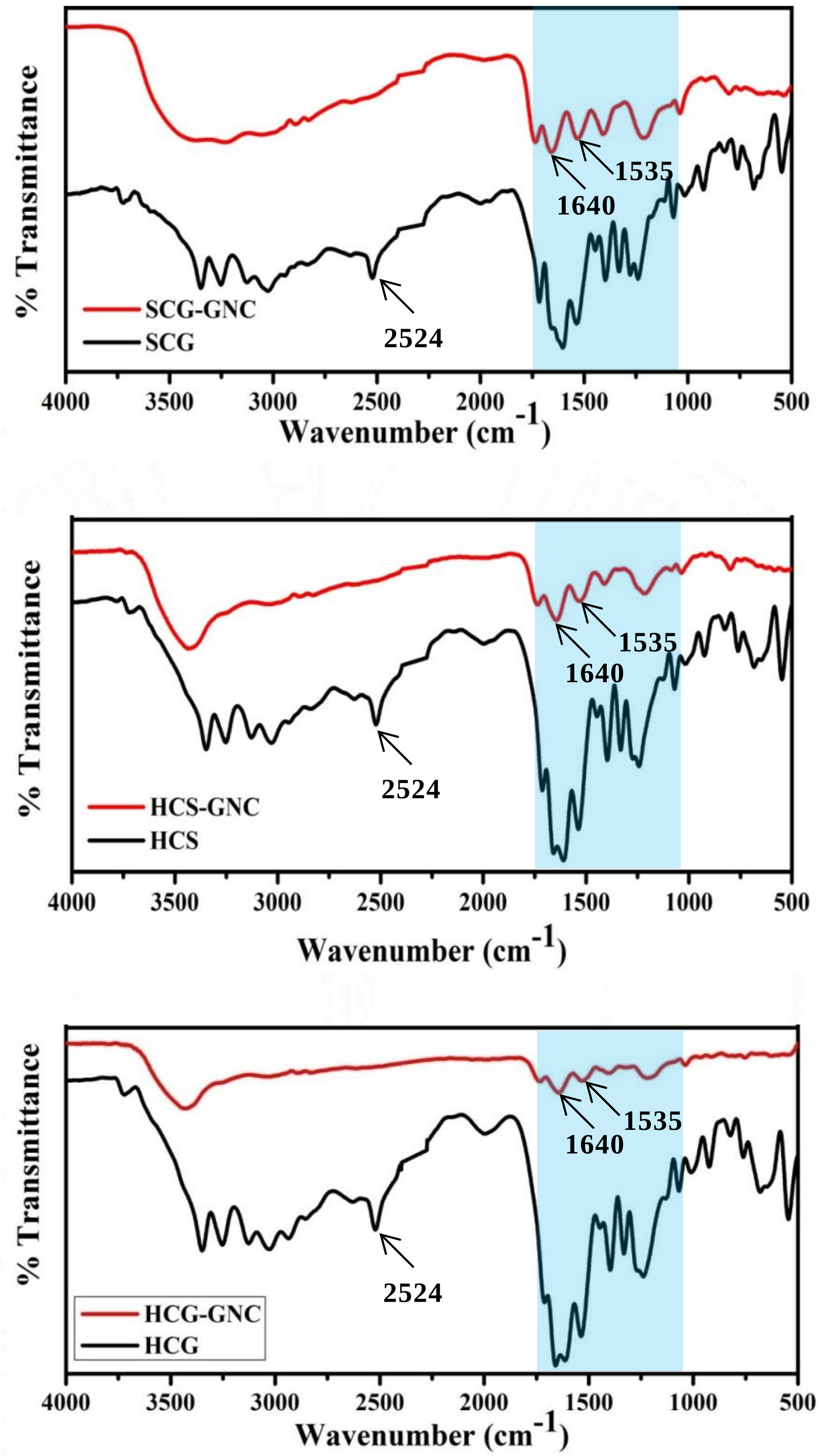

Figure 63: FTIR spectra of tripeptides and its respective gold nanoclusters.

Followed by FTIR analysis to study the nature of ligand-metal interaction, XPS analysis was done to understand the oxidation state of metals in the tripeptide-gold nanoclusters. The high resolution XPS core-level spectra in figure 64 shows the binding energy of gold (Au $4f_{7/2}$ and Au $4f_{5/2}$) and silver (Ag $3d_{5/2}$ and Ag $3d_{3/2}$) in all tripeptide-gold nanoclusters. The maximum peak values of the binding energies are given in table 12. All the tripeptide-gold nanoclusters showed the presence of both gold and silver with its characteristic binding energies, which is in good agreement with the silver-doped gold nanoclusters reported by Le Guével X *et al.*, 2012. The binding energy value obtained for Au $4f_{7/2}$ is ~84 eV for all tripeptide-gold nanoclusters corresponds to Au(0) state, which clearly indicates the complete reduction of gold salt by tripeptides. These results are in good agreement with the previous reported peptide capped gold quantum clusters (Baral A *et al.*, 2017) and thiol/protein directed synthesized gold nanoclusters (Shibu E *et al.*, 2009, Xie J *et al.*, 2009). The binding energy value obtained for Ag $3d_{5/2}$ is ~368 eV for all tripeptide-gold nanoclusters corresponds to Ag(0) state, correlated with silver-doped gold nanoclusters reported by Le Guével X *et al.*, 2012. The doublet separation energy between high-resolution elemental spectra of Au $4f_{7/2}$ and $4f_{5/2}$ is ~3.8 eV and the doublet separation energy between Ag $3d_{5/2}$ and $3d_{3/2}$ is around ~5 eV. The observed peak values and the doublet separation energies are consistent with Au(0) and Ag(0) oxidation states. The electronic transistion between metal core and the peptide caused the minor shift observed in the binding energy of both Au and Ag. These observations also confirm that these tripeptide-gold nanoclusters are bimetallic in nature because of the silver doping to gold nanoclusters. Unfortunately, DCH-GNC doesn’t show visible peak of Ag binding energy, which corresponds to its low quantum yield (table 10). Hence, it is clear that silver doping influenced the fluorescence enhancement in these tripeptide-gold nanoclusters, in addition with the variation of peptide sequences.

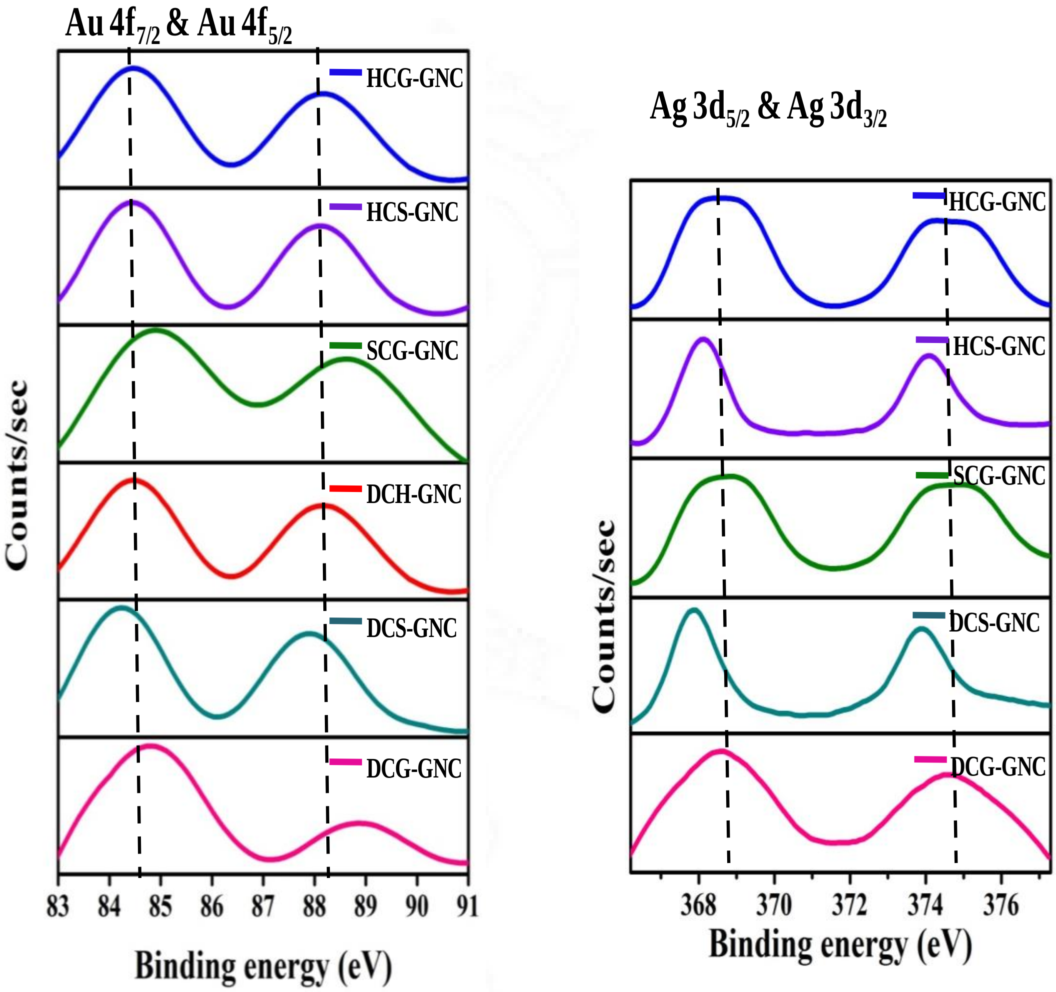

Figure 64: High resolution XPS spectra of tripeptide-gold nanoclusters showing the binding energies of Au 4f and Ag 3d.

Sample	**Au 4f$_{7/2}$**	**Au 4f$_{5/2}$**	**Ag 3d$_{5/2}$**	**Ag 3d$_{3/2}$**
DCG-GNC	84.81	88.91	368.65	374.65
DCS-GNC	84.23	87.93	367.43	373.93
DCH-GNC	84.44	88.14	-	-
SCG-GNC	84.95	88.65	368.85	374.95
HCS-GNC	84.44	88.14	368.14	374.04
HCG-GNC	84.44	88.14	368.55	374.25

Table 12: The binding energies of Au 4f$_{7/2}$, Au 4f$_{5/2}$, Ag 3d$_{5/2}$ and Ag 3d$_{3/2}$ in respective tripeptide-gold nanoclusters.

4.2.3.3. Stability of tripeptide-gold nanoclusters

To study the fluorescence stability of tripeptide-gold nanoclusters at different pH, the respective emission maximum of tripeptide-gold nanoclusters at pH 4, 5, 6, 7, 8 and 9 was measured. As shown in figure 65, significant difference was observed between the emission maximum at different pH for all the nanoclusters. DCG-GNC, DCS-GNC, DCH-GNC and SCG-GNC showed similar pattern from pH 4 to pH 9 (Figure 65). The fluorescent intensity of DCG-GNC, DCS-GNC, DCH-GNC and SCG-GNC at acidic pH (pH 4 and pH 5) is very low. When the pH is increased to 6, the fluorescent intensity of all these nanoclusters drastically increased and at pH 7, the fluorescent intensity reached its peak. However, the fluorescence intensity decreased on increasing the pH from 7 to 9. HCS-GNC and HCG-GNC showed different pattern of fluorescent intensity from pH 4 to pH 9 (Figure 65) compared with the other nanoclusters. At pH 9, HCS-GNC and HCG-GNC exhibited very low fluorescent intensity. Both these nanoclusters showed increase in fluorescent intensity upon decreasing the pH from 9 to 8 and at pH 7, the fluorescent intensity reached its peak. The decrease in pH from 7 to 4 again resulted in decrease of fluorescent intensity. The results also correlated with the zeta potential study. Even though different pH influences the fluorescent stability, all the tripeptide-gold nanoclusters retain maximum fluorescence intensity at pH 7 and hence are highly favourable for bioimaging.

Further to evaluate the stability of tripeptide-gold nanoclusters against photodestruction, a simple photobleaching experiment was carried out by illuminating the aqueous solution of tripeptide-gold nanoclusters with the hand-held UV lamp (λ_{ex} = 365 nm) for 10 min. The fluorescence intensity at their respective emission maximum was measured before and after UV illumination. Rhodamine 6G, an organic dye was used as reference. The stability of fluorescence was plotted in percentage by dividing the intensity after illumination with initial intensity (I/I_O). The results showed that all the tripeptide-gold nanoclusters have a strong resistance to photobleaching (Figure 66), while the fluorescence intensity of Rhodamine 6G drastically decreased after continuous UV illumination. DCG-GNC, SCG-GNC and HCG-GNC retained maximum fluorescence stability (> 85 %) after UV illumination compared with other tripeptide-gold nanoclusters. Thus these tripeptide-gold nanoclusters are highly photostable and can be used for long term biological time lapse imaging with continuous excitation.

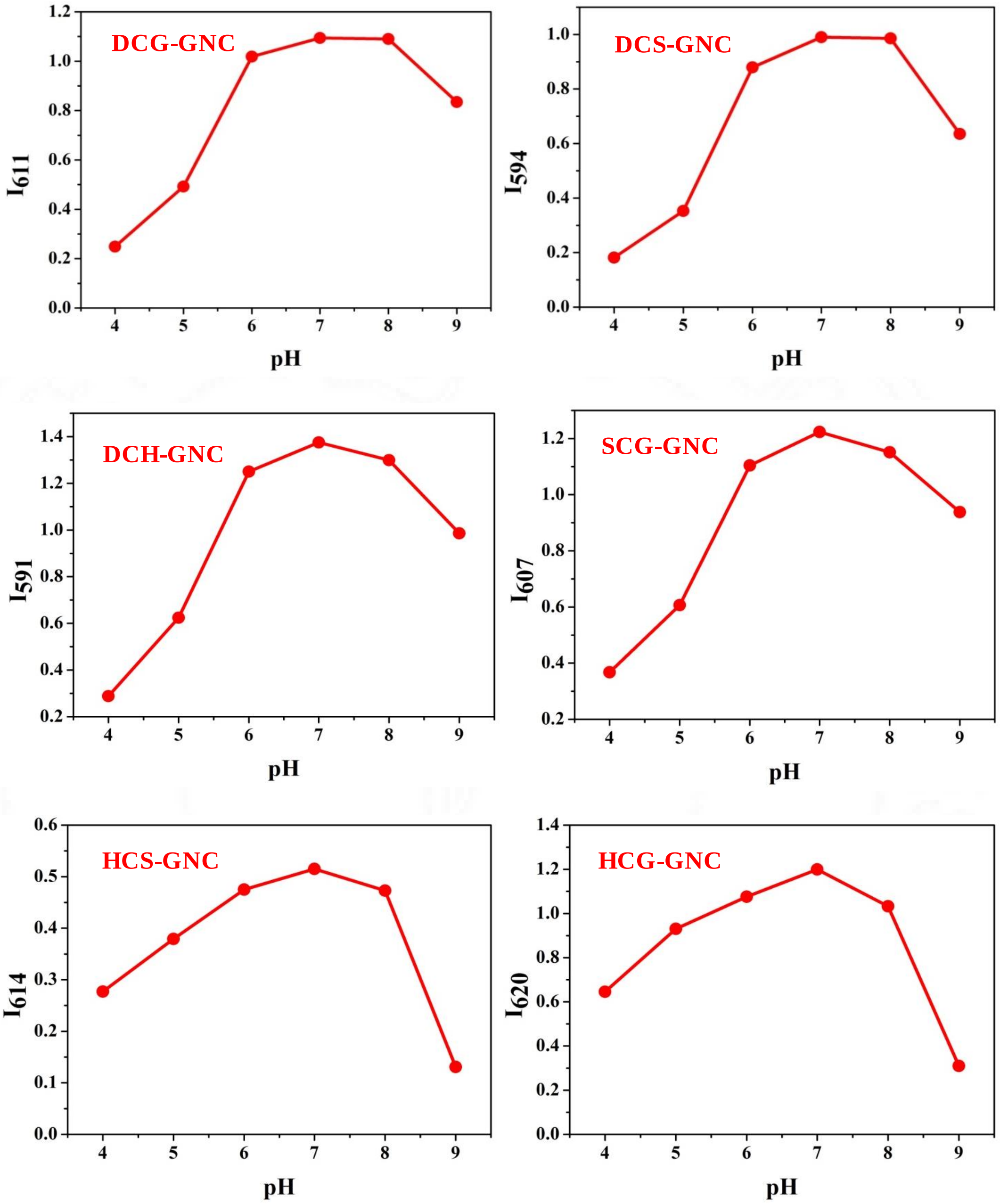

Figure 65: Influence of different pH on the fluorescent stability of tripeptide-gold nanoclusters.

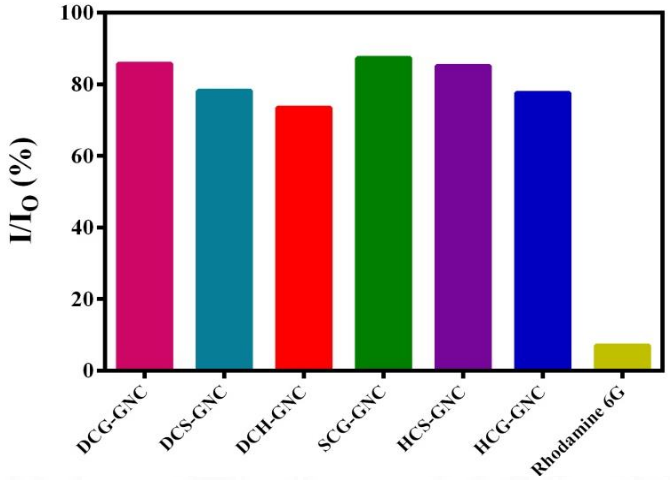

Figure 66: Photobleaching measurements of tripeptide-gold nanoclusters and Rhodamine 6G after continuous UV illumination.

The fluorescence stability is one of the important factors that limit the practical use of nanoparticles. Hence, to evaluate the fluorescent stability of tripeptide-gold nanoclusters during long period storage, the synthesized tripeptide-gold nanoclusters were redissolved in distilled water and stored @ 4°C. The respective emission maximum of all tripeptide-gold nanoclusters stored @ 4°C for different time points (1, 10, 30, 60, 120, 180 days) was measured. The fluorescence of all the tripeptide-gold nanoclusters was stable even after 6 months with only a slight change in fluorescent intensity (Figure 67). Thus these tripeptide-gold nanoclusters are favourable for utilization and further exploitation.

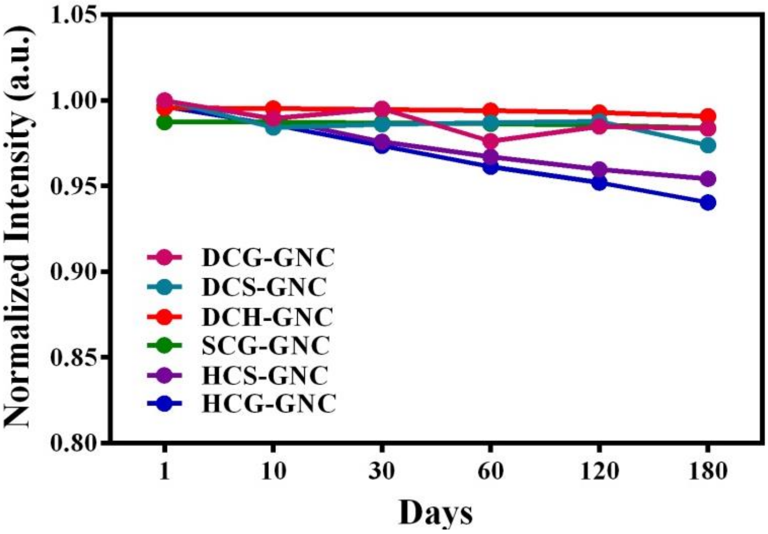

Figure 67: Effect of storage time on the fluorescence stability of tripeptide-gold nanoclusters.

4.2.4. Biological evaluation of tripeptide-gold nanoclusters

Encouraged by the fluorescent property and photostability of tripeptide-gold nanoclusters, the biological interaction of these tripeptide-gold nanoclusters was then studied for use in bioimaging application. It is reported that not only the size or shape or surface charge of nanoclusters, but also the different cell type influences the cellular uptake of nanoclusters (Behzadi S *et al*., 2017). Hence, in this study different cancer cell lines (MCF-7, MDA-MB-231, C6, U-87 MG, SK-BR-3 and HeLa) were used to study the biological interaction of gold nanoclusters. Six tripeptide-gold nanoclusters were separated into 3 groups (Group I: DCG-GNC and DCS-GNC, Group II: DCH-GNC and SCG-GNC, Group III: HCS-GNC and HCG-GNC) (Figure 68). The cellular interaction of Group I nanoclusters was studied in breast cancer cells MCF-7 and MDA-MB-231. Similarly, the cellular interaction of Group II nanoclusters was studied in brain cancer cells C6 and U-87 MG. Likewise, the cellular interaction of Group III nanoclusters was studied in breast and cervical cancer cells SK-BR-3 and HeLa respectively.

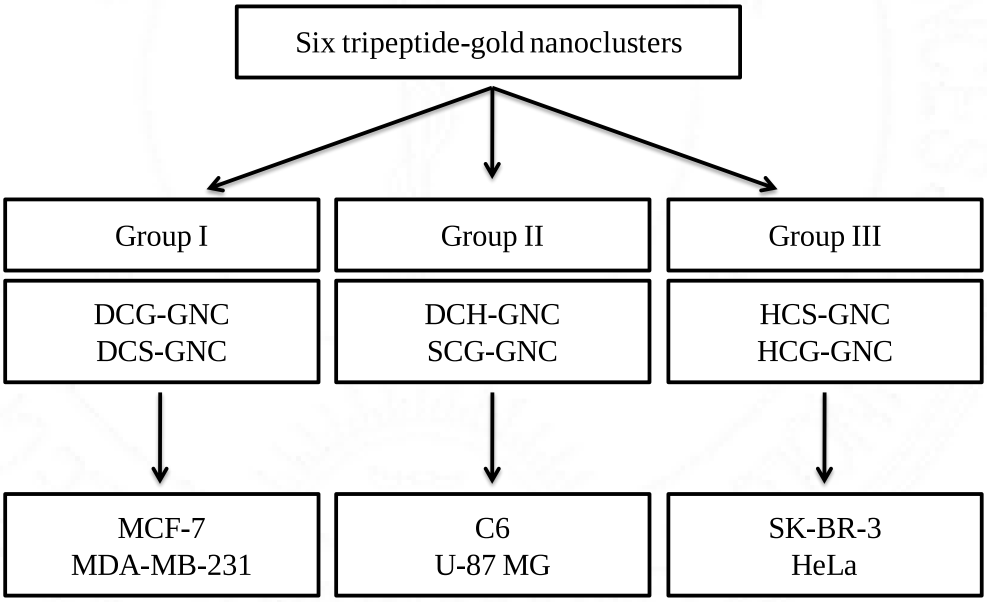

Figure 68: Group separation for the **c**ellular interaction studies of tripeptide-gold nanoclusters.

4.2.4.1. *In vitro* cytocompatibility of tripeptide-gold nanoclusters

Toxicity or low biocompatibility limits the practical application of nanomaterials for bioimaging. In order to use tripeptide-gold nanoclusters for bioimaging application, the long term cytocompatibility of these gold nanoclusters in different cancer cells was first studied using MTT assay. Metabolically active cells reduce the soluble MTT into insoluble coloured formazan crystals by mitochondrial dehydrogenase. The absorbance of these formazan crystals dissolved in respective solvent indicates the total cell viability after material treatment. The long term cytocompatibility of DCG-GNC and DCS-GNC were tested in MCF-7 and MDA-MB-231 cells. Similarly, the long term cytocompatibility of DCH-GNC and SCG-GNC were tested in C6 and U-87 MG cells. The long term cytocompatibility of HCS-GNC and HCG-GNC were tested in SK-BR-3 and HeLa cells. The cytocompatibility of all tripeptide-gold nanoclusters were also tested in WI-38 normal lung fibroblast cells for 24 h.

Figure 69 shows the percentage of cell viability after respective tripeptide-gold nanoclusters treatment. All the tripeptide-gold nanoclusters showed a concentration dependent decrease in cell viability @ 24, 48 and 72 h. All the cells retained more than 70 % viability upon material treatment for 24 h even at high concentration (1 mg/ml) except DCH-GNC in C6, which showed only 46 % viability. Each cell line maintained its pattern of concentration dependent viability upon material treatment irrespective of material type. 100 µg/ml (0.1 mg/ml) concentration was chosen for further cell studies as all the cells retained more than 50% viability at this concentration even after long term (72 h) treatment. WI-38 cells also retained more than 75 % cell viability upon all tripeptide-gold nanoclusters treatment even at high concentration (1 mg/ml). Hence the results of cytocompatibility evaluation proved the low cytotoxicity of all tripeptide-gold nanoclusters at 0.1 mg/ml and the feasibility of these nanoclusters at this concentration to be safely exploited for bioimaging applications.

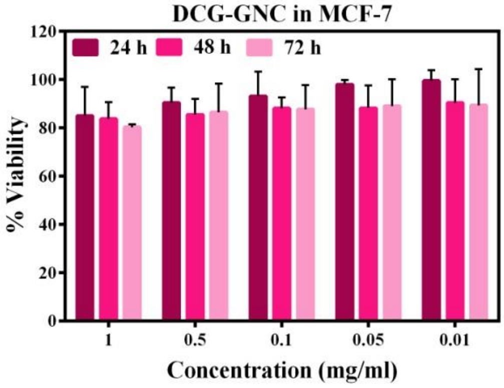
DCG-GNC in MCF-7

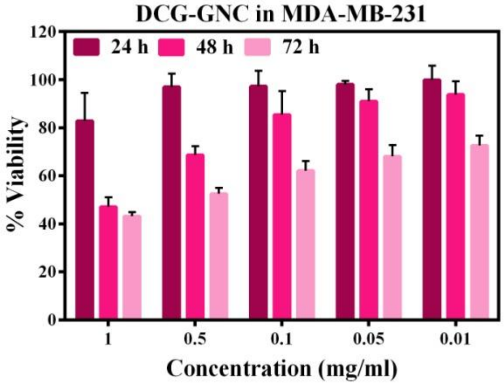
DCG-GNC in MDA-MB-231

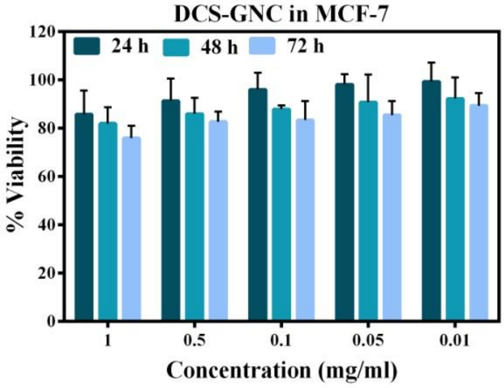
DCS-GNC in MCF-7

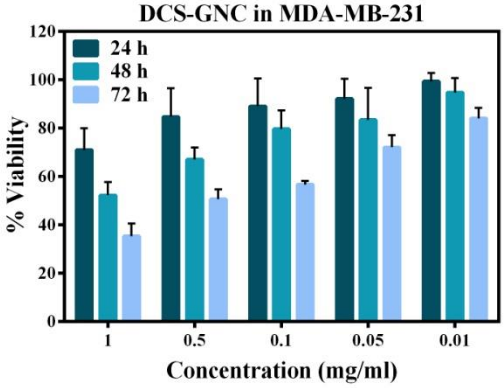
DCS-GNC in MDA-MB-231

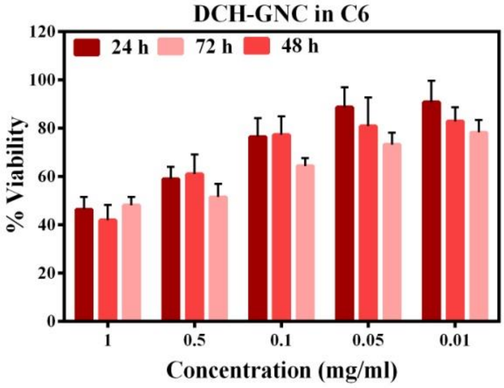
DCH-GNC in C6

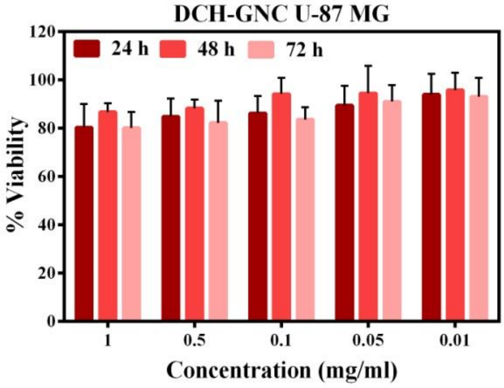
DCH-GNC U-87 MG

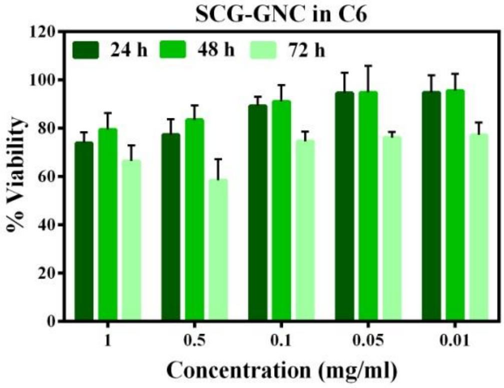
SCG-GNC in C6

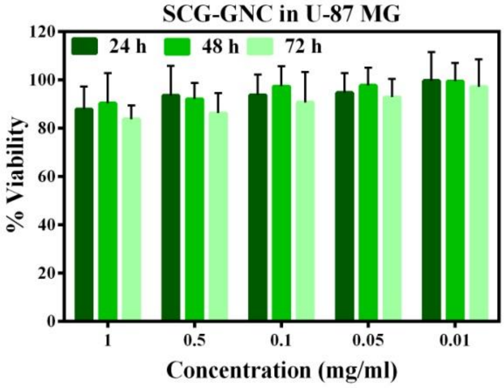
SCG-GNC in U-87 MG

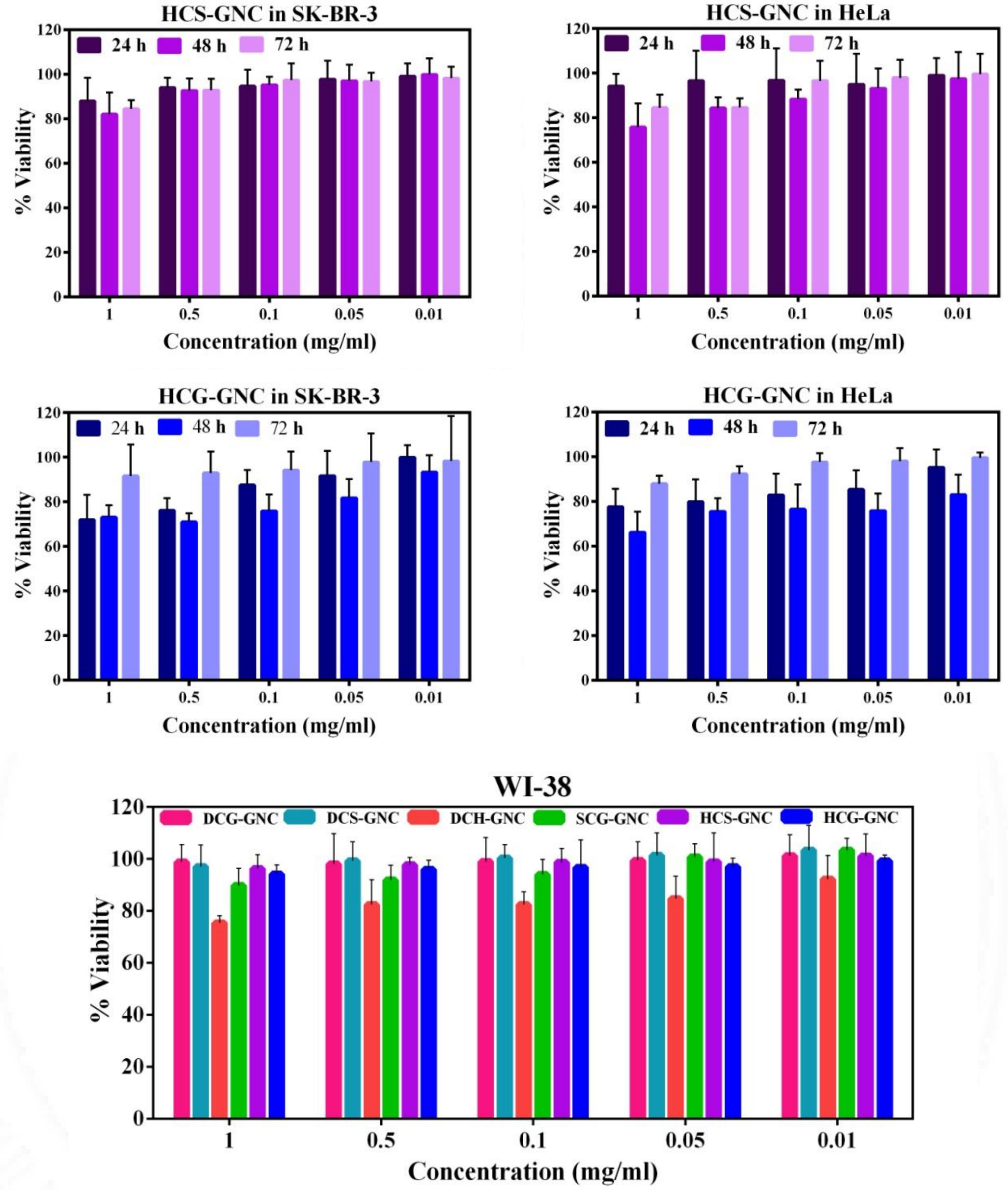

Figure 69: *In vitro* cytocomapatibility study of tripeptide-gold nanoclusters in cancer and normal cells showing the percentage of cell viability at different concentrations. Mean±s.d. (n=5).

4.2.4.2. Cellular uptake and accumulation of tripeptide-gold nanoclusters

In order to use the tripeptide-gold nanoclusters for bioimaging application, the cellular internalization of these nanoclusters in cancer cells was first studied. The fluorescence emission of each tripeptide-gold nanoclusters was employed to assess the cellular uptake by incubating 100 µg/ml of gold nanoclusters in respective cells for different time points (3, 6, 12 and 24 h). As grouped (figure 68), the cellular internalization of DCG-GNC and DCS-GNC was studied in both MCF-7 and MDA-MB-231 cells. Similarly, the cellular internalization of DCH-GNC and SCG-GNC was tested in both C6 and U-87 MG cells. Likewise, HCS-GNC and HCG-GNC was investigated in both SK-BR-3 and HeLa cells.

As shown in figure, all tripeptide-gold nanoclusters were found in the cytoplasm of respective cells with a little uptake after 3 h of incubation. Nucleus of the cells was differentially visualized with DAPI stain. Time dependent accumulation of gold nanoclusters was observed in all cases, i.e., the increase in incubation time resulted in increased accumulation of gold nanoclusters inside cells (Figure 70). It is noted that these gold nanoclusters were not accumulated uniformly inside cells, but were found as aggregates inside cells.

It has been reported that gold nanoclusters are internalized either by passive diffusion across cell membrane due to ultra-small size or by active transport through endocytosis pathway (Kapara A *et al*., 2020, Chen H *et al*., 2013). Hence to evaluate the mechanism of cellular uptake of these tripeptide-gold nanoclusters, a low-temperature (4° C) cellular uptake assay was done (Figure 71). For this, tripeptide-gold nanoclusters were incubated in respective cells for 6 h in low temperature (4° C) and normal temperature (37° C). The cells incubated at 4° C retained their cell morphology and continued to grow with no dead cells detected. The microscopic images in figure 71 clearly shows that the internalization of all tripeptide-gold nanoclusters at 37° C, which is much higher than 4° C, where a little or no uptake was observed. The quantification of tripeptide-gold nanoclusters uptake at both temperatures was done by measuring the mean fluorescence intensity (MFI) of nanoclusters.

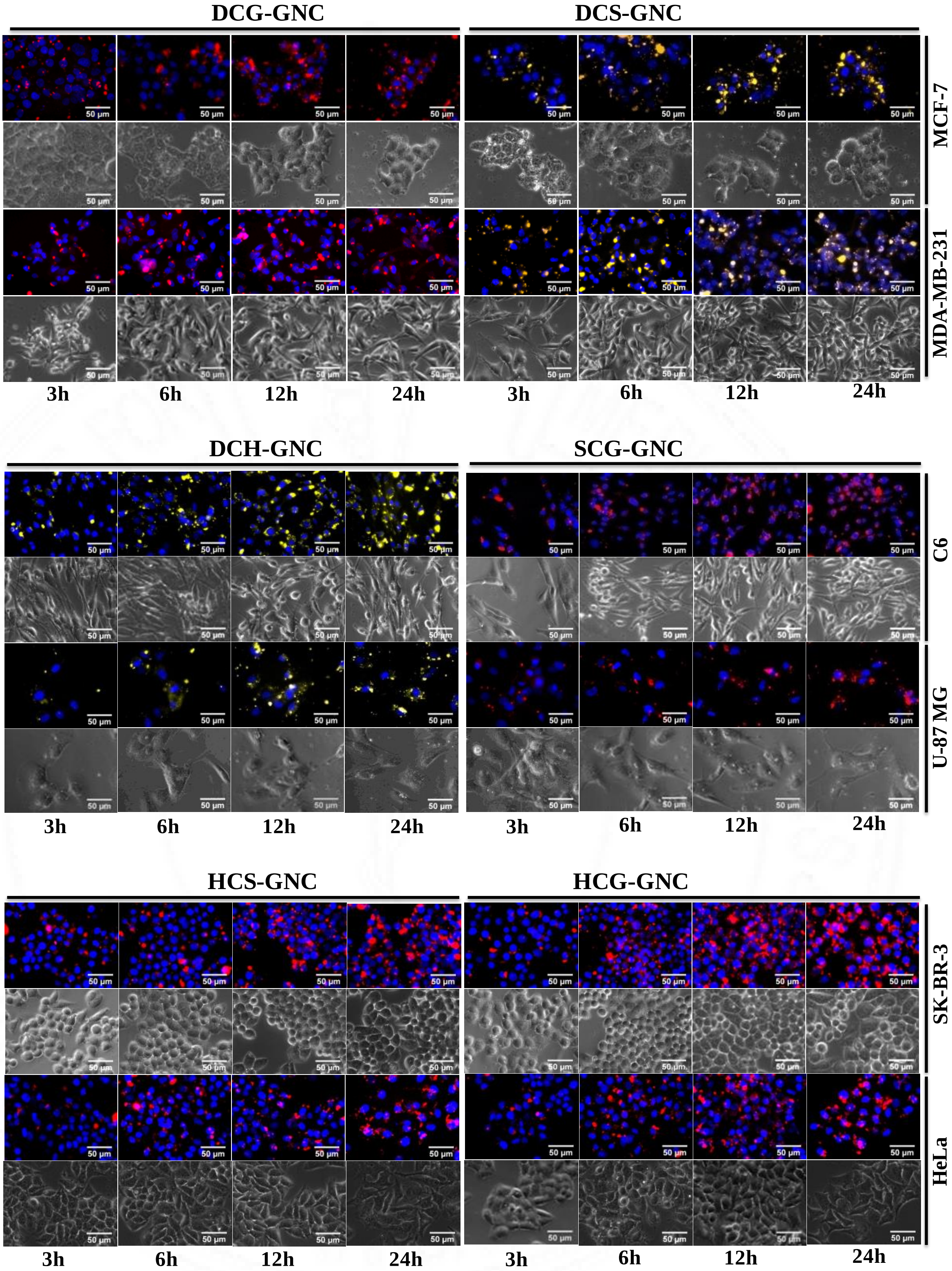

Figure 70: Cellular uptake and accumulation of tripeptide-gold nanoclusters in respective cells after 3,6, 12 and 24 h incubation. The top row in each cell line is the fluorescent images of DAPI and gold nanoclusters. Red and yellow fluorescence represents the emission of gold nanoclusters; Blue fluorescence represents the DAPI staining of nuclei. Corresponding Phase contrast images are also shown. Scale bar = 50 µm.

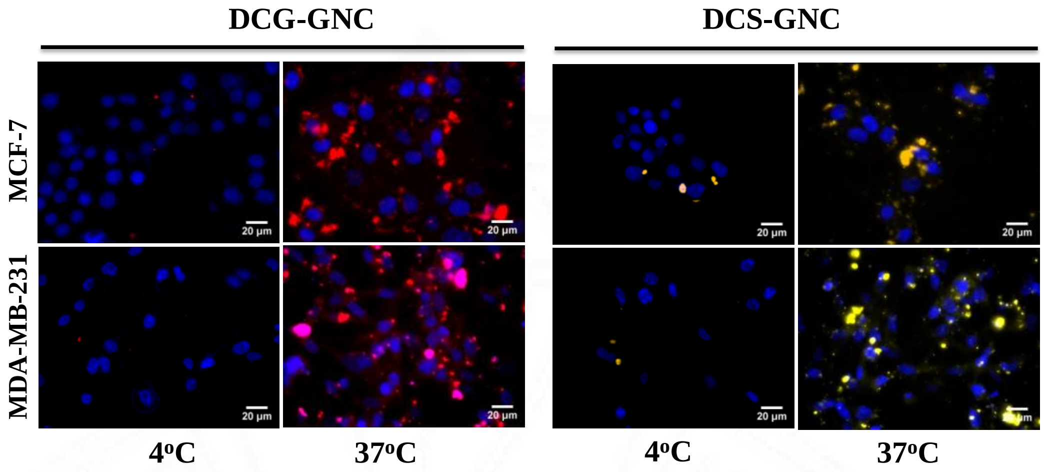
DCG-GNC
DCS-GNC
MCF-7
MDA-MB-231
20 μm
4ºC
37ºC
4ºC
37ºC

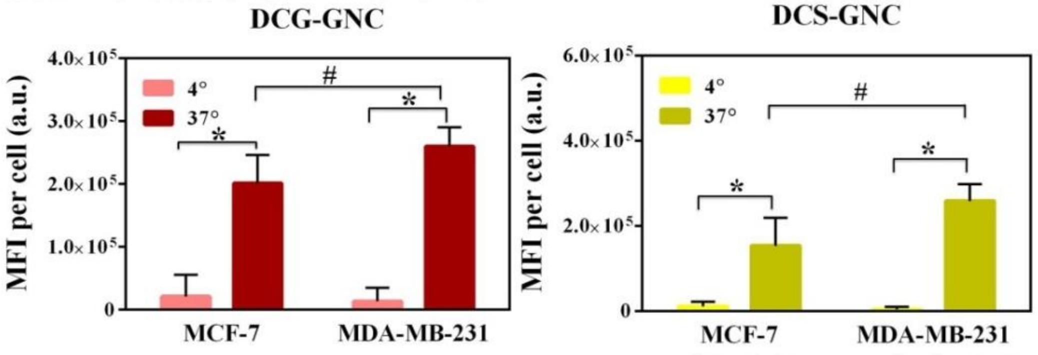
DCG-GNC
MFI per cell (a.u.)
4.0×10⁵
3.0×10⁵
2.0×10⁵
1.0×10⁵
0
4°
37°
*
#
*
MCF-7
MDA-MB-231
DCS-GNC
MFI per cell (a.u.)
6.0×10⁵
4.0×10⁵
2.0×10⁵
0
4°
37°
#
*
*
MCF-7
MDA-MB-231

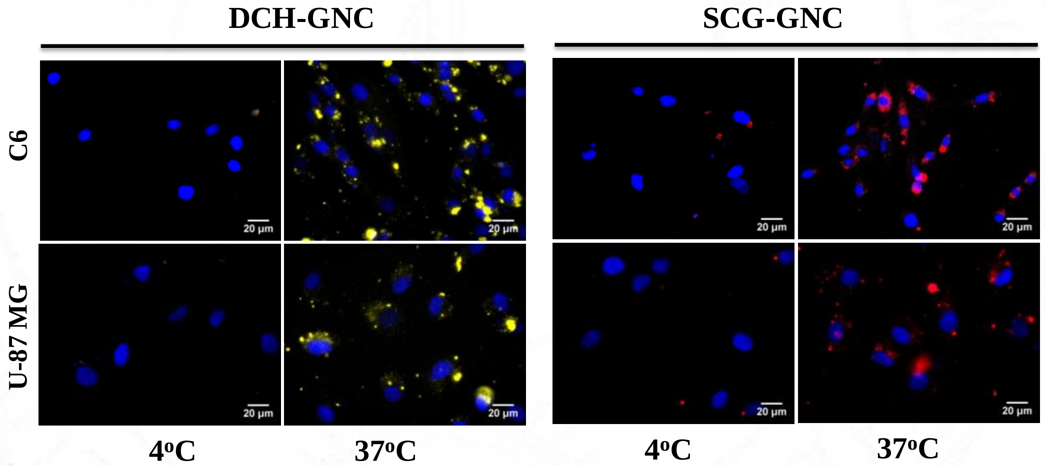
DCH-GNC
SCG-GNC
C6
U-87 MG
20 μm
4ºC
37ºC
4ºC
37ºC

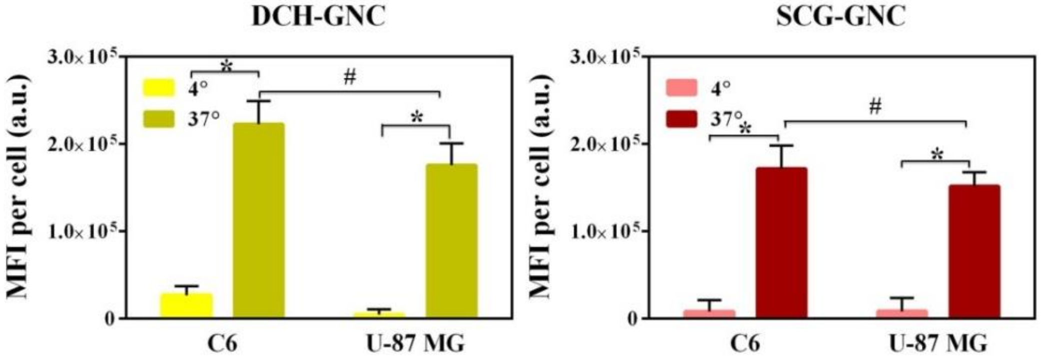
DCH-GNC
MFI per cell (a.u.)
3.0×10⁵
2.0×10⁵
1.0×10⁵
0
4°
37°
*
#
*
C6
U-87 MG
SCG-GNC
MFI per cell (a.u.)
3.0×10⁵
2.0×10⁵
1.0×10⁵
0
4°
37°
*
#
*
C6
U-87 MG

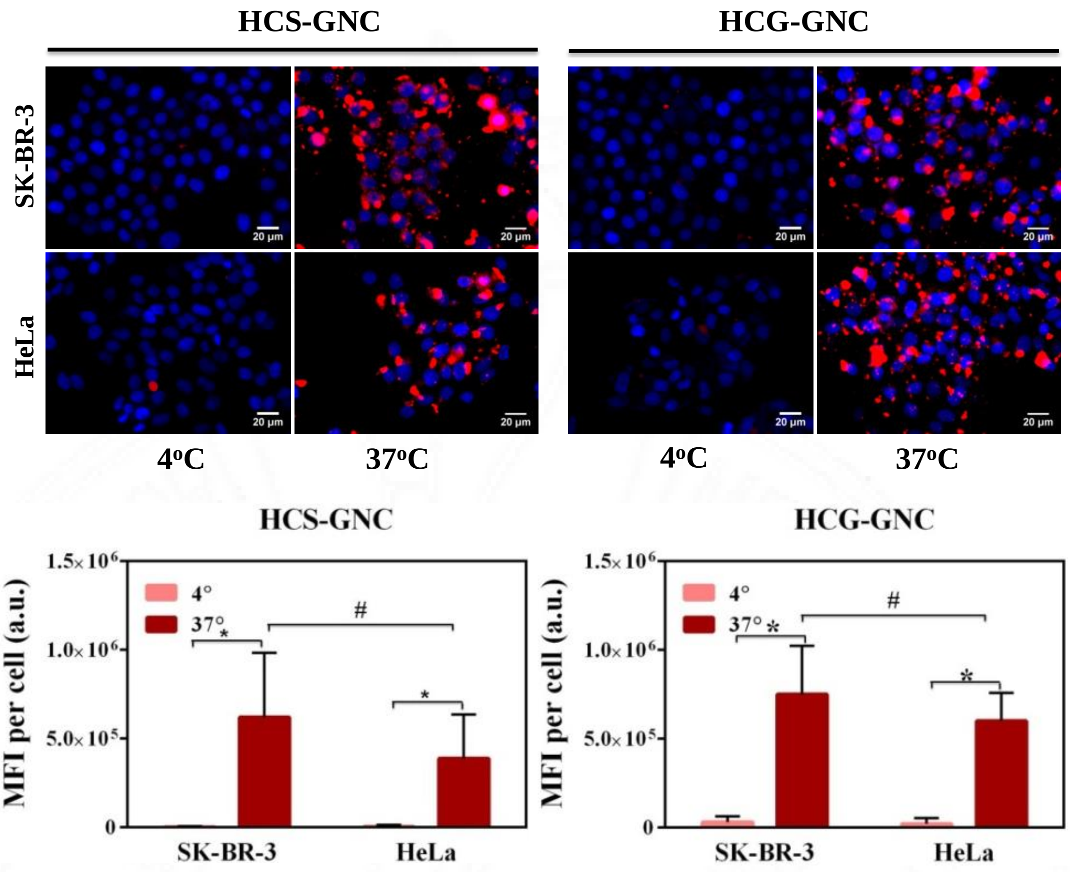

Figure 71: Cellular uptake mechanism of tripeptide-gold nanoclusters evaluated at different temperature. Red and yellow fluorescence in microscopic images represents the emission from gold nanoclusters. Blue fluorescence in microscopic images represents the emission from DAPI staining of nucleus. Scale bar = 20µm. Graph represents the mean fluorescence intensity of tripeptide-gold nanoclusters per cell. Mean±s.d. (n = 10). * indicates significant difference in accumulation of gold nanoclusters between 4 and 37° C ($p < 0.01$), # indicates significant difference in accumulation of gold nanoclusters between different cells @ 37° C ($p < 0.01$).

The mean fluorescence intensity (MFI) per cell is directly proportional to the accumulation of tripeptide-gold nanoclusters per cell. The results clearly showed that DCG-GNC showed a 2-fold and 2.6 fold increase of mean fluorescence intensity (MFI) @ 37° C than 4° C in MCF-7 and MDA-MB-231 cells respectively (figure 71). Similarly, DCS-GNC showed a 1.8-fold and 2.3 fold increase of MFI @ 37° C than 4° C in MCF-7 and MDA-MB-231 cells respectively (figure 71). DCH-GNC showed a 2.3-fold and 1.9 fold increase of MFI @ 37° C than 4° C in C6 and U-87 MG cells respectively (figure 71). SCG-GNC showed a 1.7-fold and 1.5 fold increase of MFI @ 37° C than 4° C in C6 and U-87 MG cells respectively (figure 71). HCS-GNC showed a 6-fold and 3.8 fold increase of MFI @ 37° C than 4° C in SK-BR-3 and HeLa cells respectively (figure 71). HCG-GNC showed a 7.5-fold and

6 fold increase of MFI @ 37° C than 4° C in SK-BR-3 and HeLa cells respectively (figure 71). The low signal observed @ 4° C in all the cases was likely due to passive diffusion of a significantly lower number of nanoclusters into cells. Thus the internalization of these tripeptide-gold nanoclusters is highly temperature- and energy-dependent, which implies that the mechanism of tripeptide-gold nanoclusters internalization is an energy dependent active endocytic process. These results correlate with the previous literature reports, which suggested that at lower temperature, decrease in cellular uptake happens if the nanoparticles enter the cells through endocytosis (Kapara A *et al.*, 2020).

It has been proposed that the cellular internalization rate and internalization mechanism of nanoparticles is influenced by nanoparticles size, charge and surface properties as well as the cell type (Behzadi S *et al.*, 2017). It is known that the cell membrane has negative charge and hence positive charged nanoparticles penetrates cell membrane easily. But as mentioned above, even though these tripeptide-gold nanoclusters are small, they prefer active endocytic mechanism for cellular internalization than passive diffusion. However, the surface charge of these tripeptide-gold nanoclusters greatly influences the nanoparticles attraction towards cell entry and thereby influences uptake, accumulation and cell viability percentage upon treatment. As shown in the results of figure 62, the surface charge of DCS-GNC is more negative than DCG-GNC and hence the latter accumulated more in both MCF-7 and MDA-MB-231 cells. Both DCG-GNC and DCS-GNC accumulated more in MDA-MB-231 than in MCF-7 (Figure 70, 71). Similarly, the surface charge of SCG-GNC is more negative than DCH-GNC and hence the latter accumulated more in both C6 and U-87 MG cells. Both DCH-GNC and SCG-GNC accumulated more in C6 than in U-87 MG (Figure 70, 71). Likewise, the surface charge of HCS-GNC is more negative than HCG-GNC and hence the latter accumulated more in both SK-BR-3 and HeLa cells. Both HCS-GNC and HCG-GNC accumulated more in SK-BR-3 than in HeLa (Figure 70, 71). In this study, both the surface charge of gold nanoclusters and cell type influence the uptake percentage of nanoparticle inside cells. Irrespective of cell type, the accumulation percentage of nanoclusters was found to be HCG-GNC>HCS-GNC>DCH-GNC>SCG-GNC>DCG-GNC>DCS-

GNC, which greatly support the zeta potential results. Also, these results correlates with the findings reported in previous literatures which states that the uptake of nanoparticles by endocytosis resulted in accumulation of nanoparticles inside cells in the form of large aggregates (Chen H *et al*., 2013).

4.2.4.3. *In vitro* PDT of tripeptide-gold nanoclusters: Photoinduced ROS generation

As mentioned in section 1.5.2., photodynamic therapy (PDT) works with the accumulation of photosensitizer (PS) in tumours, which upon light irradiation generate singlet oxygen ($^1O_2$) and other reactive oxygen species (ROS) to induce cell death. ROS, a specific type of oxygen-containing reactive molecules play important roles in different cellular processes, including cell proliferation at basal level, but at high concentration, ROS can be cytotoxic and induce apoptosis/necrosis (Matés J *et al*., 2008). To evaluate whether the tripeptide-gold nanoclusters can act as a photosensitizer or induce ROS generation under laser irradiation, H_2-DCFDA staining method was performed. H_2-DCFDA is a non-fluorescent cell-permeable dye, which is activated by intracellular esterases through cleavage of acetate groups and becomes fluorescent (λ_{em} = 525 nm) upon oxidation by ROS (Zhang C *et al*., 2015). As mentioned in section 4.2.4. figure 68, the ROS generation potential of DCG-GNC and DCS-GNC under laser irradiation was evaluated in both MCF-7 and MDA-MB-231 cells. Similarly, the ROS generation potential of DCH-GNC and SCG-GNC under laser irradiation was tested in both C6 and U-87 MG cells. Likewise, the ROS generation potential of HCS-GNC and HCG-GNC under laser irradiation was investigated in both SK-BR-3 and HeLa cells. All the tripeptide-gold nanoclusters were incubated at a concentration of 100 µg/ml for 6 h and irradiated with 532 nm laser (0.5 W/cm^2) for 30 sec and stained with H_2-DCFDA.

As shown in figure 72, the entire laser irradiated cells treated with tripeptide-gold nanoclusters observed under microscope showed an intense green fluorescence, while the non-irradiated cells treated with tripeptide-gold nanoclusters showed a little green fluorescence, thus confirming the photoinduced ROS generation potential of these nanoclusters. The low fluorescence signal in non-irradiated cells might be due to the overlapping of material emission in the DCFDA emission range. Control cells with and without laser irradiation showed negligible green fluorescence in all cases (Figure 72). Cells treated with H_2O_2 also showed intense green fluorescence (Figure 72). Morphological differences were also observed between the laser irradiated and non-irradiated group of tripeptide-gold nanoclusters treated cells. The quantitative measurement of photoinduced ROS production was also measured by a microplate reader assay (figure 73), which correlates with the microscopic imaging studies. The increase in fluorescence intensity is proportional to the oxidation of the fluorescent probe and thereby indicate the relative ROS concentration.

Significant differences were observed in the amount of photoinduced ROS production between different tripeptide-gold nanoclusters and cell lines. Compared with DCS-GNC, DCG-GNC showed increased photoinduced ROS production in both cell lines. Both DCG-GNC and DCS-GNC showed high photoinduced ROS production in MDA-MB-231 than in MCF-7 (figure 73). Compared with SCG-GNC, DCH-GNC showed increased photoinduced ROS production in both cell lines. Also, both DCH-GNC and SCG-GNC showed high photoinduced ROS production in C6 than in U-87 MG (figure 73). Similarly, compared with HCS-GNC, HCG-GNC showed increased photoinduced ROS production in both cell lines (figure 73). From the results of quantitative measurements, it is proved that the amount of photoinduced ROS generation is directly proportional to the accumulation of different tripeptide-gold nanoclusters in respective cells (Figure 70, 71).

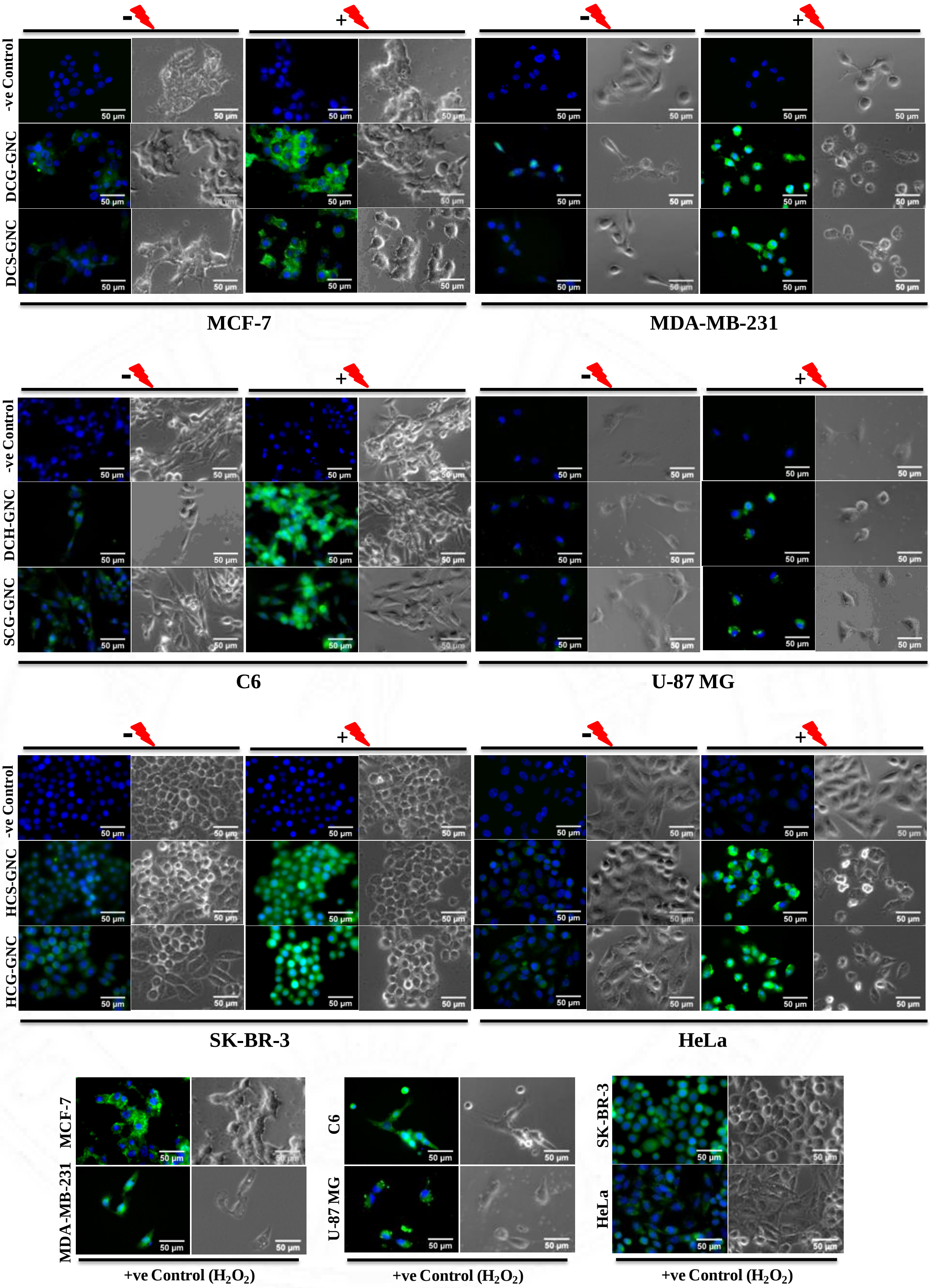

Figure 72: Microscopic images of ROS generation in tripeptide-gold nanocluster treated cancer cells with and without laser irradiation. Green and Blue colour in fluorescent images (1st and 3rd column in each cell) represents DCFDA and Hoechst staining respectively. Corresponding phase contrast images are also shown. Scale bar = 50 μm.

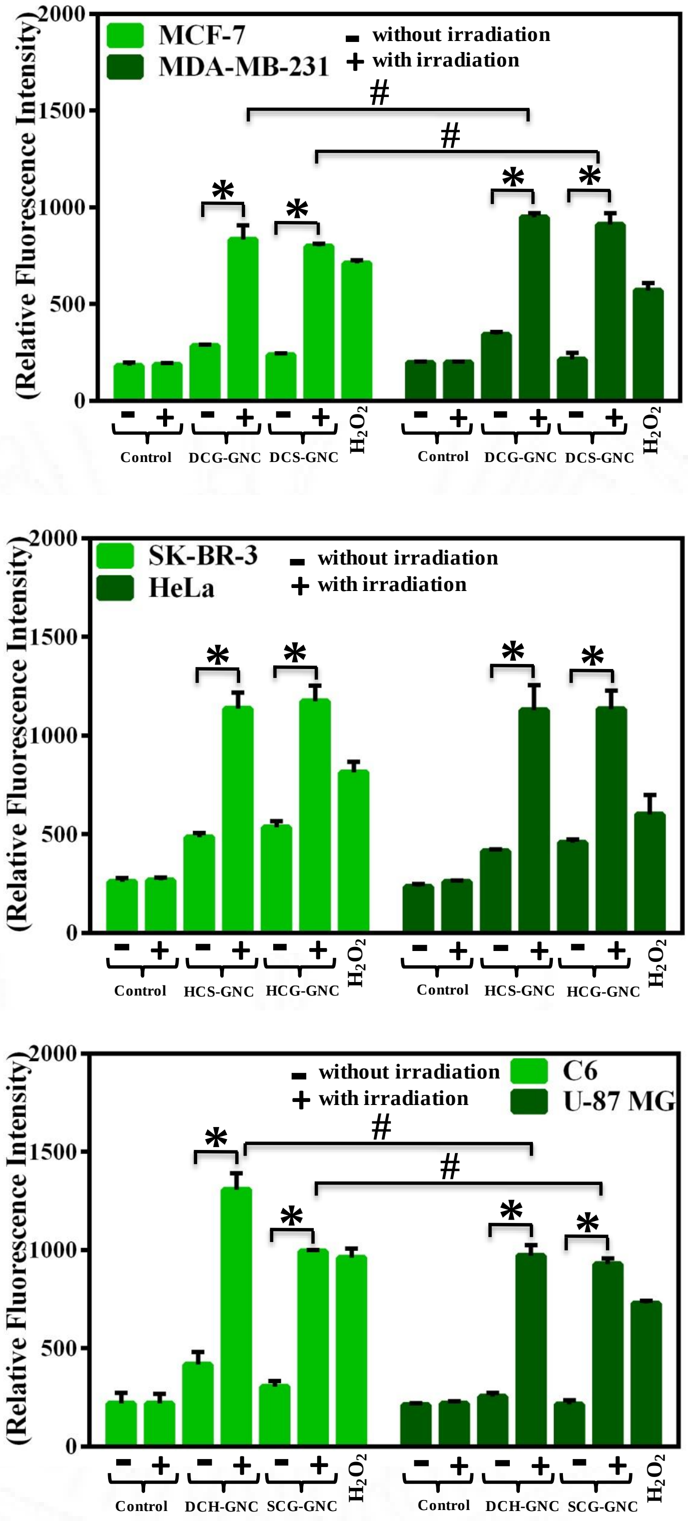

Figure 73: Quantitative measurement of ROS generation by tripeptide-gold nanoclusters in respective cancer cells with and without laser irradiation. Mean±s.d. (n = 5). * indicates significant difference in ROS production between laser irradiated and non-irradiated cells ($p < 0.01$), # indicates significant difference in ROS production between two cancer cells ($p < 0.01$).

4.2.4.4. *In vitro* PDT of tripeptide-gold nanoclusters: Photoinduced change in mitochondrial membrane potential (ΔΨm)

Mitochondria play a crucial role in determining the cell fate, as these organelles are the major site of energy and ROS production. As mentioned in section 1.5.2., ROS trigger intrinsic apoptotic pathways associated with mitochondrial oxidative damage. Excessive ROS cause damage to mitochondria, resulting in the loss of mitochondrial membrane potential (Ψm), a distinctive feature of apoptosis. To evaluate whether the photoinduced ROS generation by tripeptide-gold nanoclusters causes change in mitochondrial membrane potential, JC-10 staining was done. JC-10 is a membrane permeable dye that accumulates within the healthy mitochondria as JC-10 aggregates, which has red emission. Whereas, the disintegrated mitochondria do not accumulate JC-10, hence the dye exists in cytoplasm as monomeric form and emits green fluorescence. Therefore, the decrease in red fluorescence is an indicative of mitochondrial membrane potential loss.

As shown in figure 74, untreated control cells with polarized mitochondria appear as red punctuate staining, whereas tripeptide-gold nanocluster treated cells irradiated with laser showed progressive loss of red fluorescence and appearance of diffused green fluorescence in cytoplasm clearly indicating the significant loss or change of mitochondrial membrane potential (ΔΨm). Cells incubated with tripeptide-gold nanocluster without laser irradiation showed a slight ΔΨm. Morphological differences were also observed between the laser irradiated and non-irradiated group of tripeptide-gold nanoclusters treated cells. These results correlate with the above photoinduced ROS generation analysis. Literatures reported that the loss of mitochondrial membrane potential is an early event in apoptotic process (Ly J *et al*., 2003).

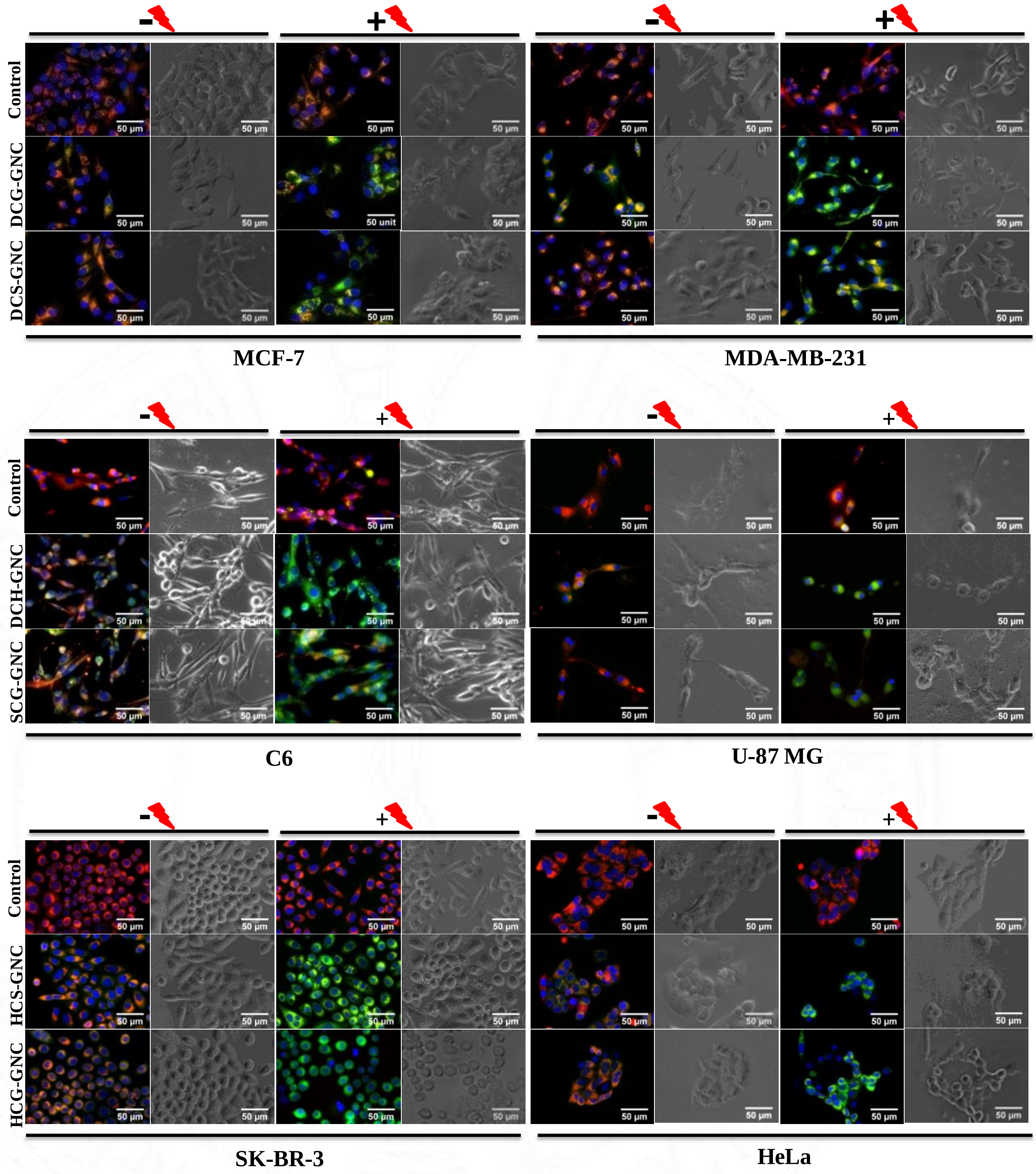

Figure 74: Microscopic images of mitochondrial membrane potential change in tripeptide-gold nanoclusters treated cancer cells with and without laser irradiation. Fluorescence images showing the red dots, diffused green signal and blue fluorescence in cells for JC-10 aggregates, JC-10 monomers and Hoechst respectively. Corresponding phase contrast images are also shown. Scale bar = 50 µm.

4.2.4.5. *In vitro* PDT of tripeptide-gold nanoclusters: Photoinduced cell death

As mentioned in section 1.5.2., PDT can activate late stages of apoptosis bypassing many death signalling pathways. To evaluate the secondary effects of elevated ROS generation and loss of mitochondrial membrane potential caused by photoinduced tripeptide-gold nanoclusters observed in figure 72 and 74, live dead/apoptotic analysis was done by dual staining with acridine orange and ethidium bromide. Acridine orange stains both live and dead cells, while ethidium bromide stains only dead cells which lost membrane integrity. Thus with this dual staining, live cells appear uniformly green, early apoptotic cells show green fluorescence with bright green dots in nucleus due to chromatin condensation, late apoptotic cells appear orange by ethidium bromide incorporation with condensed chromatin and necrotic cells appear uniformly orange with no chromatin condensation.

Microscopic images in figure 75 clearly show the appearance of late apoptotic as well as necrotic cells in tripeptide-gold nanocluster treated cells irradiated with laser, whereas small number of cells is early apoptotic in cells without laser irradiation. A minimum number of early apoptotic cells are also noted in control cells without any treatment. Quantitative measurement of photoinduced cell death was measured using a microplate reader with MTT assay. The percentage viability of cells in figure indicates the viable number of cells after each treatment. The dark toxicity of these tripeptide-gold nanoclusters (i.e., without laser irradiation) is low which correlates with the results in section 4.2.4.1. Laser irradiation in all gold nanoclusters treated cells caused high percentage of cell death compared with non-irradiated cells, thereby confirming the efficiency of these tripeptide-gold nanoclusters to cause photoinduced cell death.

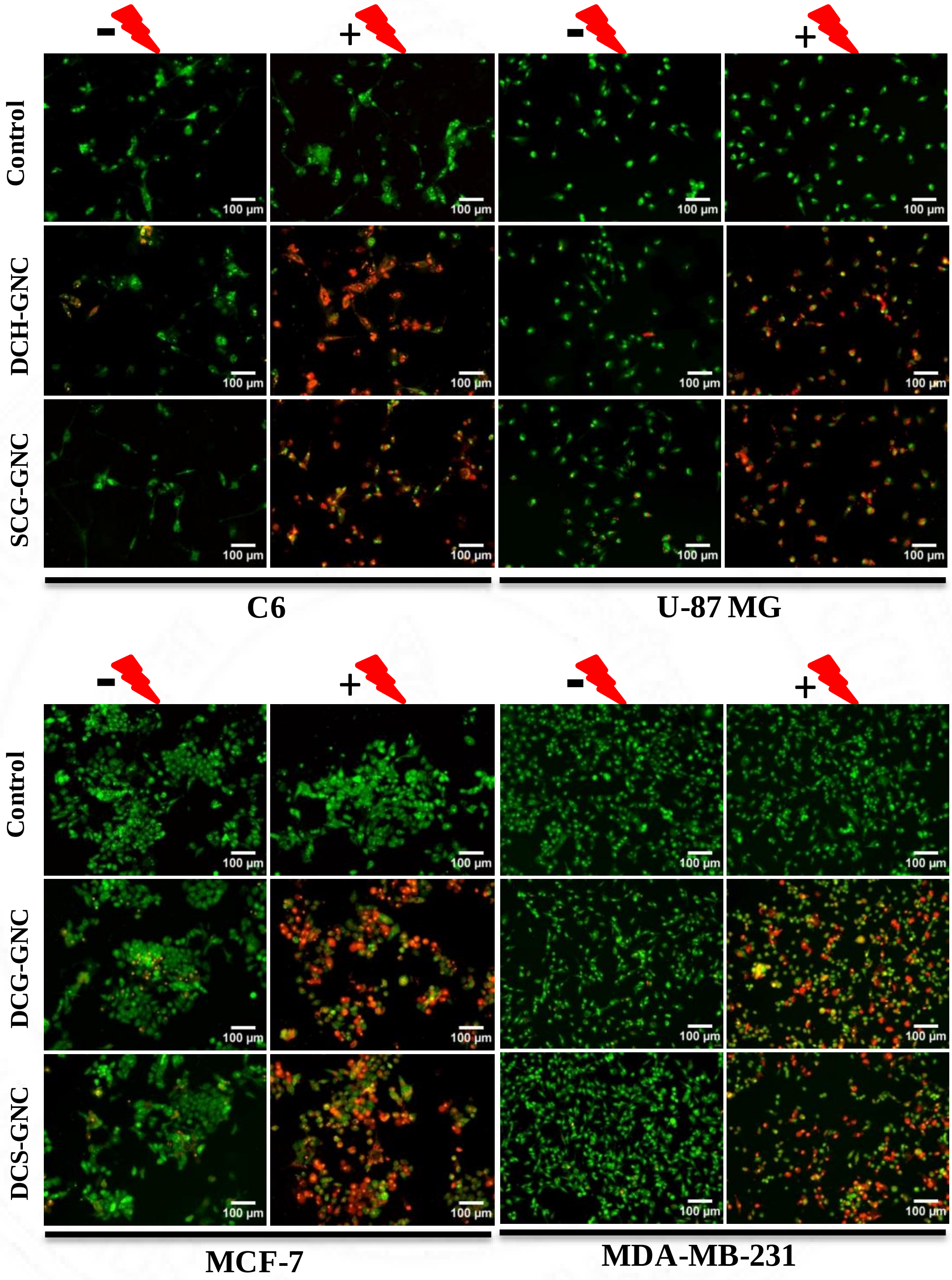
-
+
-
+
Control
DCH-GNC
SCG-GNC
100 µm
C6
U-87 MG
-
+
-
+
Control
DCG-GNC
DCS-GNC
100 µm
MCF-7
MDA-MB-231

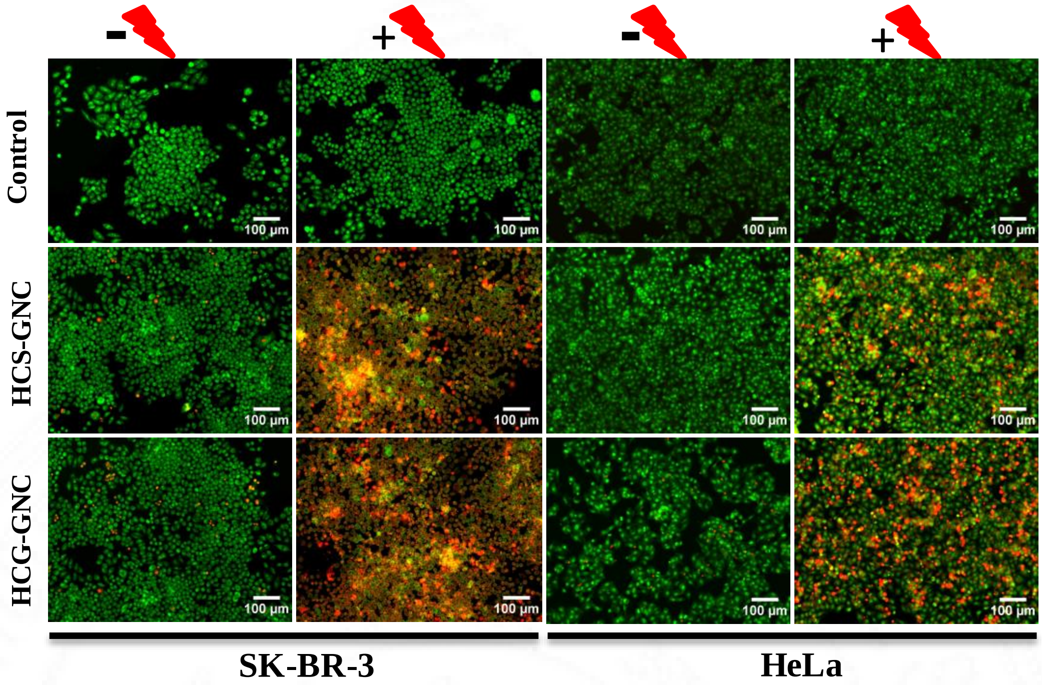

Figure 75: Live dead imaging of tripeptide-gold nanocluster treated cancer cells with and without laser irradiation. Red fluorescence indicates apoptotic/dead cells and green fluorescence indicates live cells. Scale bar = 100 µm.

The quantitative measurement of cell death in all these conditions are also analyzed using MTT assay. Significant differences were observed between different gold nanoclusters and cell types as seen in section 4.2.4.3 and 4.2.4.4. DCG-GNC with laser irradiation caused more cell death in both MCF-7 and MDA-MB-231 cells than DCS-GNC with laser irradiation (Figure 76). Both material with laser irradiation caused significantly higher percentage of cell death in MDA-MB-231 than MCF-7. Similarly, DCH-GNC with laser irradiation caused more cell death in both C6 and U-87 MG than SCG-GNC with laser irradiation. Both material with laser irradiation caused significantly higher percentage of cell death in C6 than U-87 MG (Figure 76). HCG-GNC with laser irradiation caused more cell death in both SK-BR-3 and HeLa than HCS-GNC with laser irradiation. Both material with laser irradiation caused significantly higher percentage of cell death in SK-BR-3 than HeLa (Figure 76). Thus these results correlated well with the above accumulation study, ROS generation and mitochondrial membrane potential study.

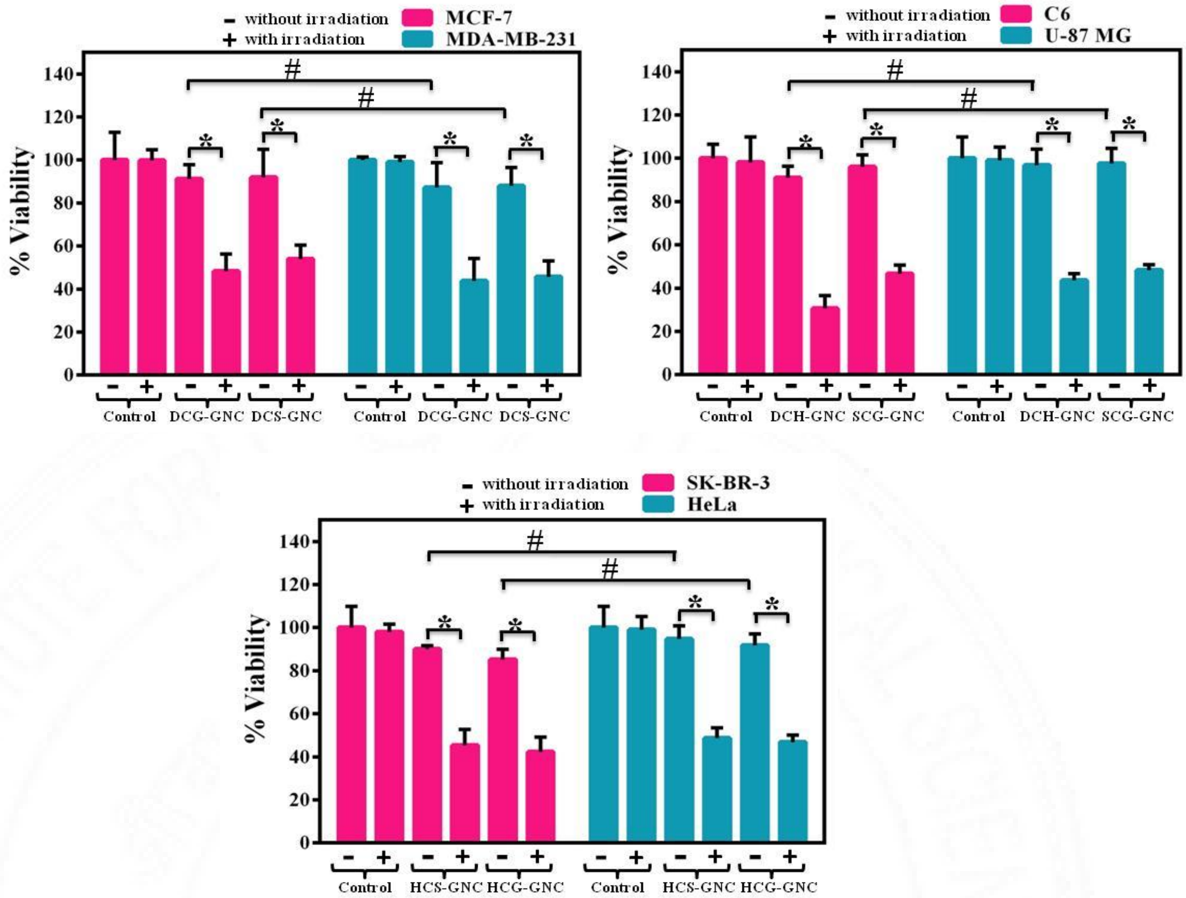

Figure 76: Quantitative measurement of cell death in tripeptide-gold nanocluster treated cells with and without laser irradiation using MTT assay. % viability plotted as Mean ± SD, indicates the percentage of viable cells after each treatment with respect to control. Mean±s.d. (n=4). * indicates significant difference in % viability between laser irradiated and non-irradiated cells ($p < 0.01$), # indicates significant difference in % viability between two cancer cells ($p < 0.01$).

Therefore, it is confirmed that the photoinduced ROS generation potential of tripeptide-gold nanoclusters caused mitochondrial membrane damage, which may have facilitated the release of cytochrome c from mitochondria to cause apoptotic cell death. These tripetide-gold nanoclusters can act as a bioimaging agent as well as a photosensitizer. Hence, the image guided PDT efficiency of tripeptide-gold nanoclusters is confirmed *in vitro*.

4.3. Fluorescent nano gene downregulator for cancer imaging cum therapy

Cancer cells evade apoptosis either by over expression of anti-apoptotic proteins/inhibitors of apoptotic proteins or by under expression of pro-apoptotic proteins/death signals/death receptors/p53 tumour suppressor protein/caspases (Figure 10). Hence, restoring a cell’s ability to undergo natural cell death by inducing apoptosis in any form may combat cancer. One form of inducing apoptosis is downregulation of anti-apoptotic or IAP (inhibitor of apoptosis) genes. This can be achieved by gene therapy, which is a future strategy to modulate gene expression level by introducing exogenous genetic materials into specific cells to treat human diseases, including cancer. Implementing gene therapy with RNA interference (RNAi) can downregulate the targeted gene like IAPs in cancer to induce apoptosis. This RNAi therapy is cost effective than other gene therapy methods and is more specific than chemotherapy, hence is expected to have more impact in personalized treatment in future.

RNAi therapy can be achieved by delivering siRNA against overexpressed IAPs in cancer. As mentioned in section 1.5.3.3., a novel siRNA delivery vector with properties to overcome the limitations of conventional vectors is essential. Cytocompatible carriers which can specifically target cancer cells with efficient endosomal escape and in-built fluorescent property to track siRNA delivery will be an efficient siRNA delivery vector.

4.3.1. Construction of fluorescent nano gene downregulator

As discussed in section 4.2., gold nanoclusters are considered as an ideal candidate for imaging because of its exceptional fluorescent properties and the synthesis of gold nanoclusters with custom designed peptides offers not only biocompatibility but also provides the desired surface properties for fabrication of variety of biomolecules. In this part of study, different positively charged oligopeptides were custom designed and used for the preparation of gold nanoclusters. These oligopeptide-gold nanoclusters were synthesized using the same simple one-step green method adopted for tripeptide-gold nanoclusters in previous section 4.2. Here, the construction of a fluorescent nano gene downregulator performed with positively charged oligopeptide-gold nanoclusters, siRNA against IAPs, cancer targeting ligand and their *in vitro* application for simultaneous imaging cum siRNA delivery for cancer therapy is explained. The pictorial representation of fluorescent nano gene downregulator is shown in the figure 77.

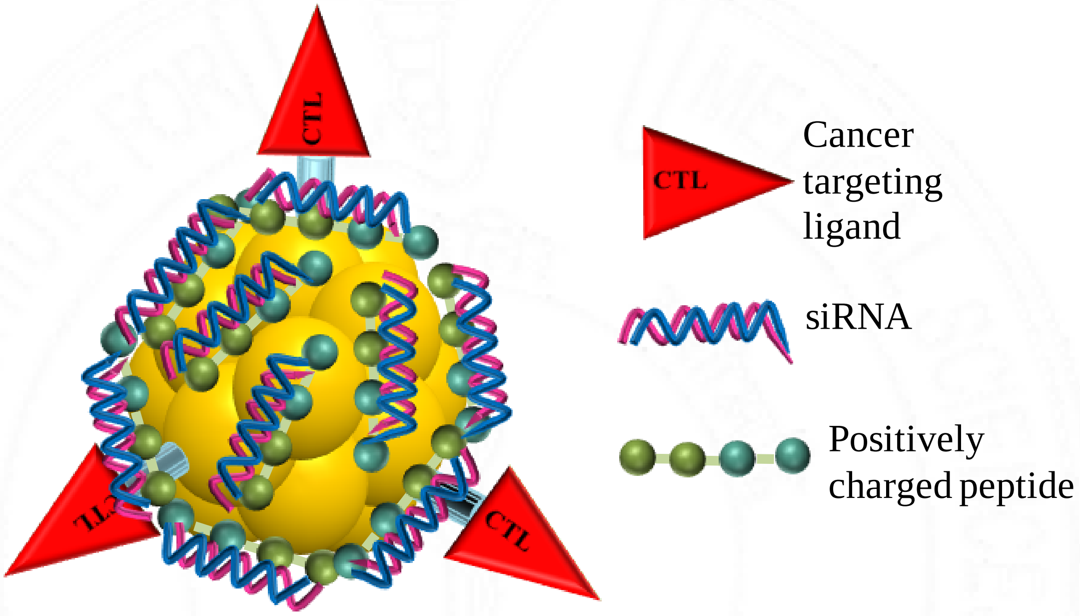

Figure 77: Pictorial representation of fluorescent nano gene downregulator.

4.3.2. Synthesis and characterization of oligopeptides

The details of the synthetic procedure for three different oligopeptides are explained in section 3.3.3. The progress of the successful coupling of each amino acid was monitored by Kaiser test. Complete coupling of each amino acid is confirmed with the colourless/very faint blue colour beads using Kasier test, while incomplete coupling shows blue colour beads in Kasier test (figure 78). In case of incomplete coupling, recoupling was done with increased incubation time until the Kaiser test results shows complete coupling. The verification of complete coupling thus reflects in the preparation of proper sequence of peptides without any change.

Figure 78: Kaiser test results of peptide synthesis: R represents reference and S represents sample, In R - resin beads after Fmoc deprotection showed blue colour indicating the exposure of amino groups reacting with ninhydrin in Kaiser test. In S – resin beads showing white colour upon reaction with ninhydrin indicates the complete coupling of incoming amino acids with the deprotected previous amino groups.

The chemical structure and the respective ball and stick model of the synthesized oligopeptides $(HR)_3C(HR)_3$, $(HK)_3C(HK)_3$ and $(H)_3C(H)_3$ are shown in figure 79. H, R, K and C in peptides represent histidine, arginine, lysine and cysteine amino acids respectively. All the oligopeptides were designed and grafted with cysteine (C) amino acid to interact with gold during gold nanocluster synthesis. The rationale behind choosing other amino acids including histidine (H), arginine (R) and lysine (K) is to provide buffering capacity and to provide sufficient positive charge for the peptides for siRNA complexation. All the peptides were synthesized and mentioned as C-N terminal. As the peptides were synthesized using rink amide MBHA resin, the final peptide product is believed to contain amide group at the C-terminal end. Hence all the peptides have C-terminal amide group and N-terminal amine group. MALDI-MS analysis was done to characterize all oligopeptides. The mass of oligopeptides calculated theoretically correlated with the mass obtained from MALDI-MS analysis (Figure 80). The final mass of the oligopeptides obtained from MALDI-MS analysis are 1880.192 and 1712.158 for $(HR)_3C(HR)_3$ and $(HK)_3C(HK)_3$ respectively. Unfortunately, the acquisition of MALDI-MS of $(H)_3C(H)_3$ was unsuccessful even after repeated trials and hence it is not included in the results.

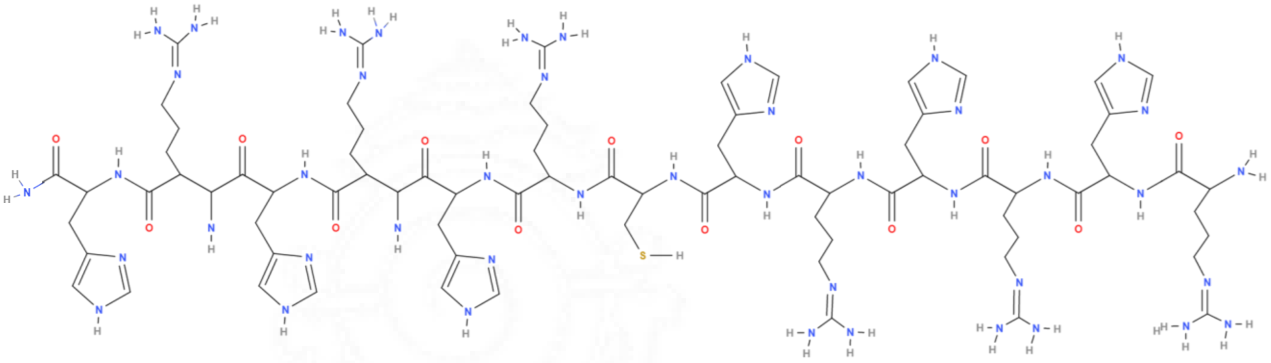

$(HR)_3C(HR)_3$

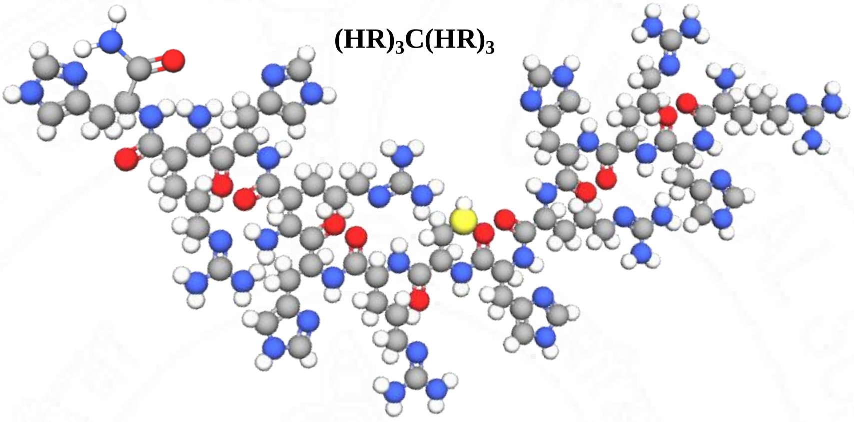

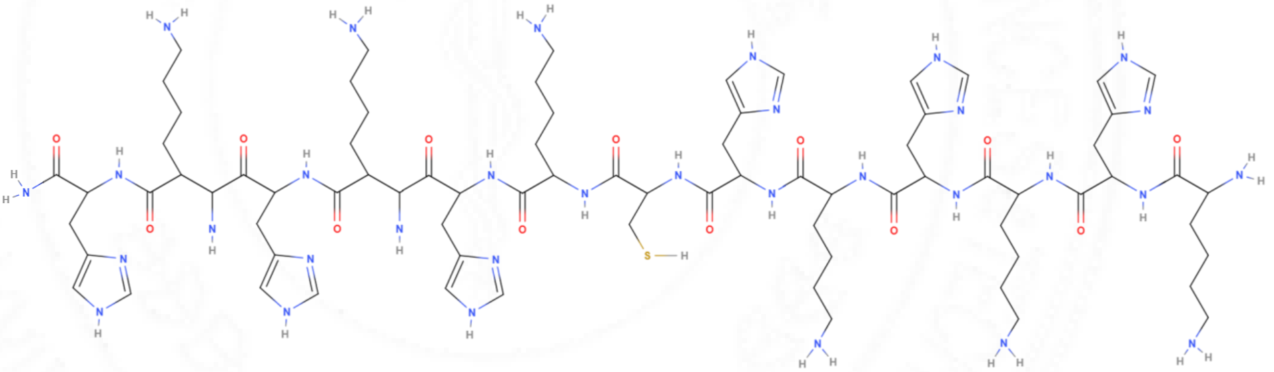

$(HK)_3C(HK)_3$

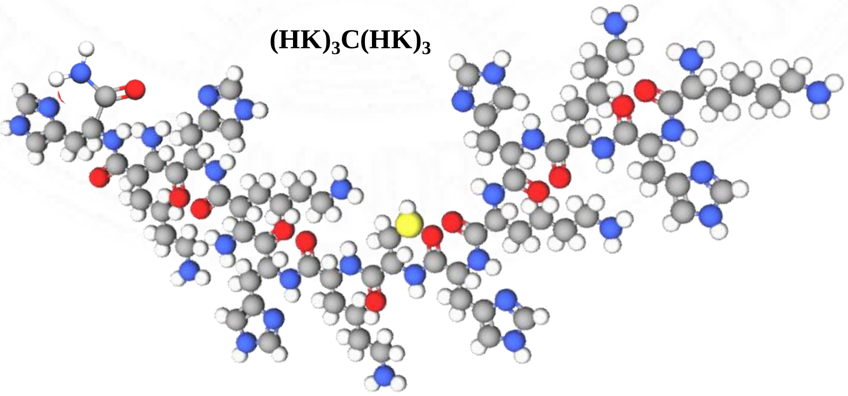

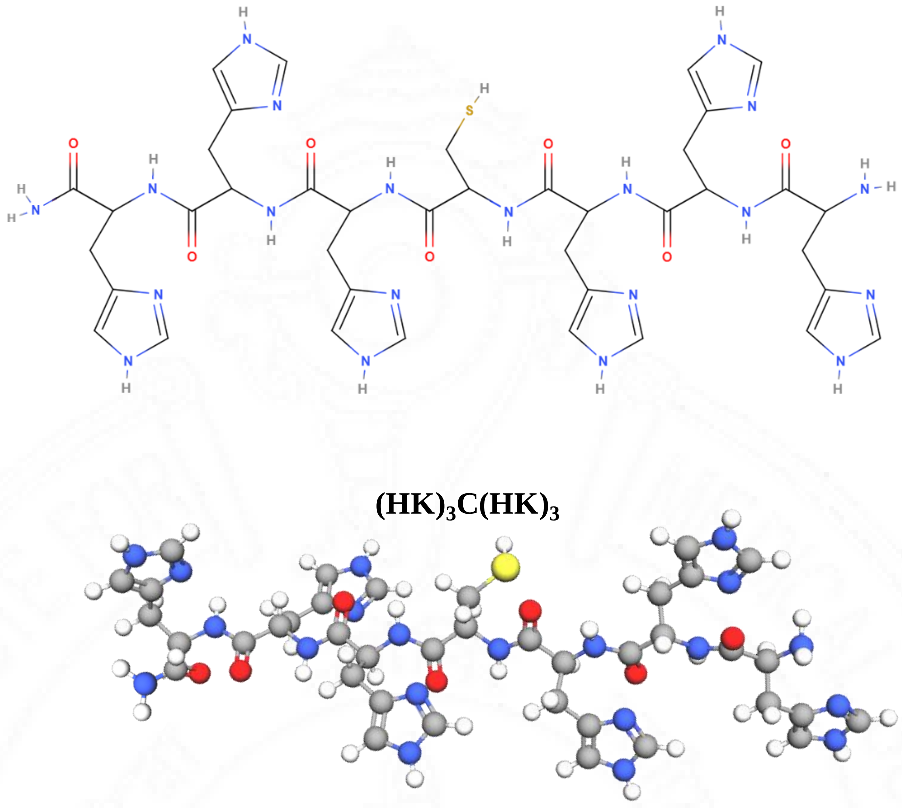

$(HK)_3C(HK)_3$

Figure 79: Chemical structure of oligopeptides with Ball and stick model.

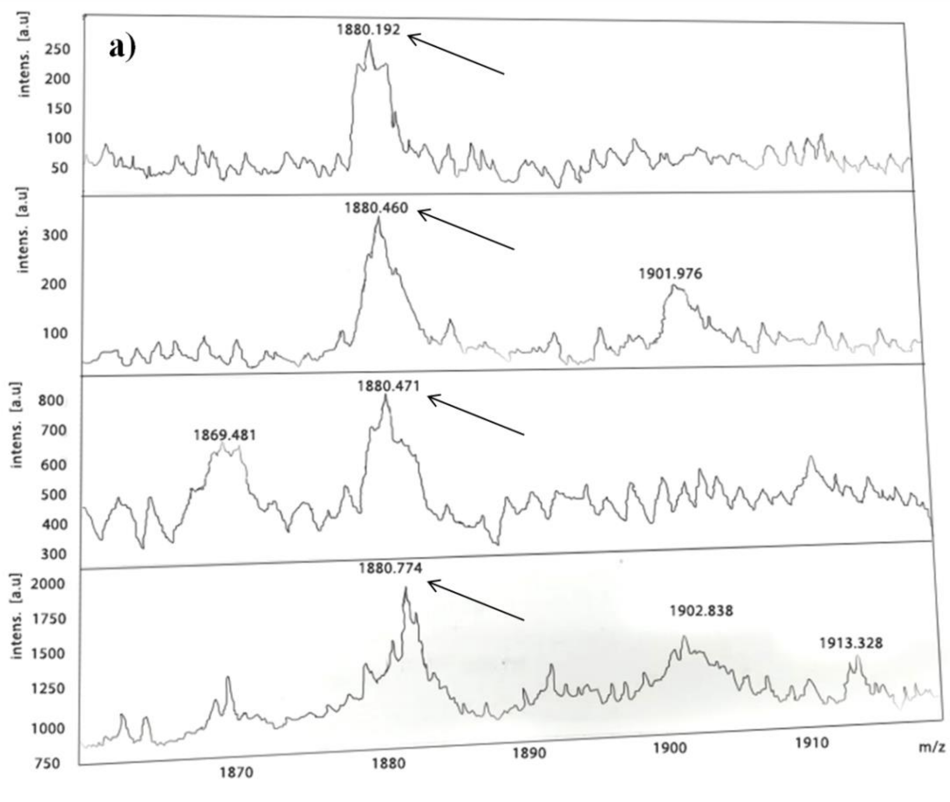

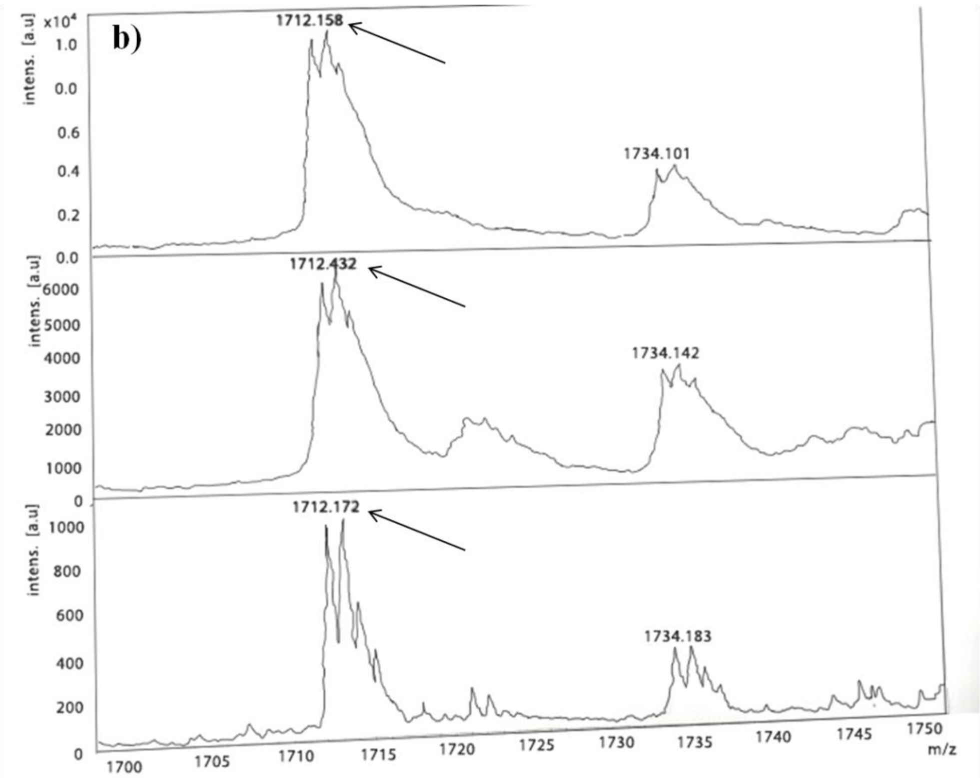

Figure 80: MALDI-MS of synthesized oligopeptides showing the respective mass, indicated by arrows $(HR)_3C(HR)_3$ (a) and $(HK)_3C(HK)_3$ (b)

4.3.3. Synthesis of oligopeptide-gold nanoclusters

The synthesis of different oligopeptide-gold nanoclusters (GNCs) namely, $(HR)_3C(HR)_3$-GNC, $(HK)_3C(HK)_3$-GNC and $(H)_3C(H)_3$-GNC was performed using custom synthesized three different oligopeptides $(HR)_3C(HR)_3$, $(HK)_3C(HK)_3$ and $(H)_3C(H)_3$ respectively (Figure 34). Similar to the tripeptide stabilized gold nanoclusters in section 4.2., here the oligopeptides were used as reducing cum stabilizing agents for the preparation of oligopeptide-gold nanoclusters and hence this is a simple one-step, green method to obtain the peptide–GNCs. The thiol (–SH) group of the amino acid cysteine present in the oligopeptides participate in the reduction of Au^{3+} into oligopeptide-AuNCs (GNCs) without requiring additional strong reducing agents. The thiol (–SH) groups in the peptides also capture the clusters and stabilize it based on the unique metal-sulphur chemistry and form a strong Au-S bond. The other groups in the peptides such as carboxyl and amino groups may also contribute to the structural stabilization of metal clusters. It is also reported that the imidazole group in histidine play a crucial role as reducing cum stabilizing agent for the formation of gold nanoclusters (Yang X *et al.*, 2011). Hence, in all the three oligopeptide-gold nanoclusters (HR)$_3$C(HR)$_3$-GNC, (HK)$_3$C(HK)$_3$-GNC and (H)$_3$C(H)$_3$-GNC, histidine along with cysteine is expected to play key role for the reduction of Au atom and stabilization of gold nanoclusters. Also, histidine is reported to have buffering capacity under acidic conditions, which provides controlled release efficiency for the drug delivery systems (Bilalis P *et al.*, 2016, P Sun *et al.*, 2017) Here, the fabrication of gold nanoclusters with many histidine amino acids provide them high buffering capacity to induce “proton-sponge” effect inside the endosomes of cells. This feature allows the gold nanoclusters to escape from the endosomes for successful delivery of siRNA inside cytoplasm for its mechanism of action. Similar to the tripeptide-gold nanocluster synthesis in section 4.2., silver doping was done to enhance the fluorescence of pure gold nanoclusters. It is reported that the doping of silver atoms to gold nanoclusters can contribute to the fluorescence enhancement of gold nanoclusters (Le Guével X *et al.*, 2012, Wang S *et al.*, 2014). In addition, the synthetic procedure of these oligopeptide-gold nanoclusters was performed in water medium is not only easy but also provides biocompatibility to these nanoclusters. The pictorial representation of the synthesis of the three oligopeptide-gold nanoclusters, along with their excitation and emission details is given in figure 81.

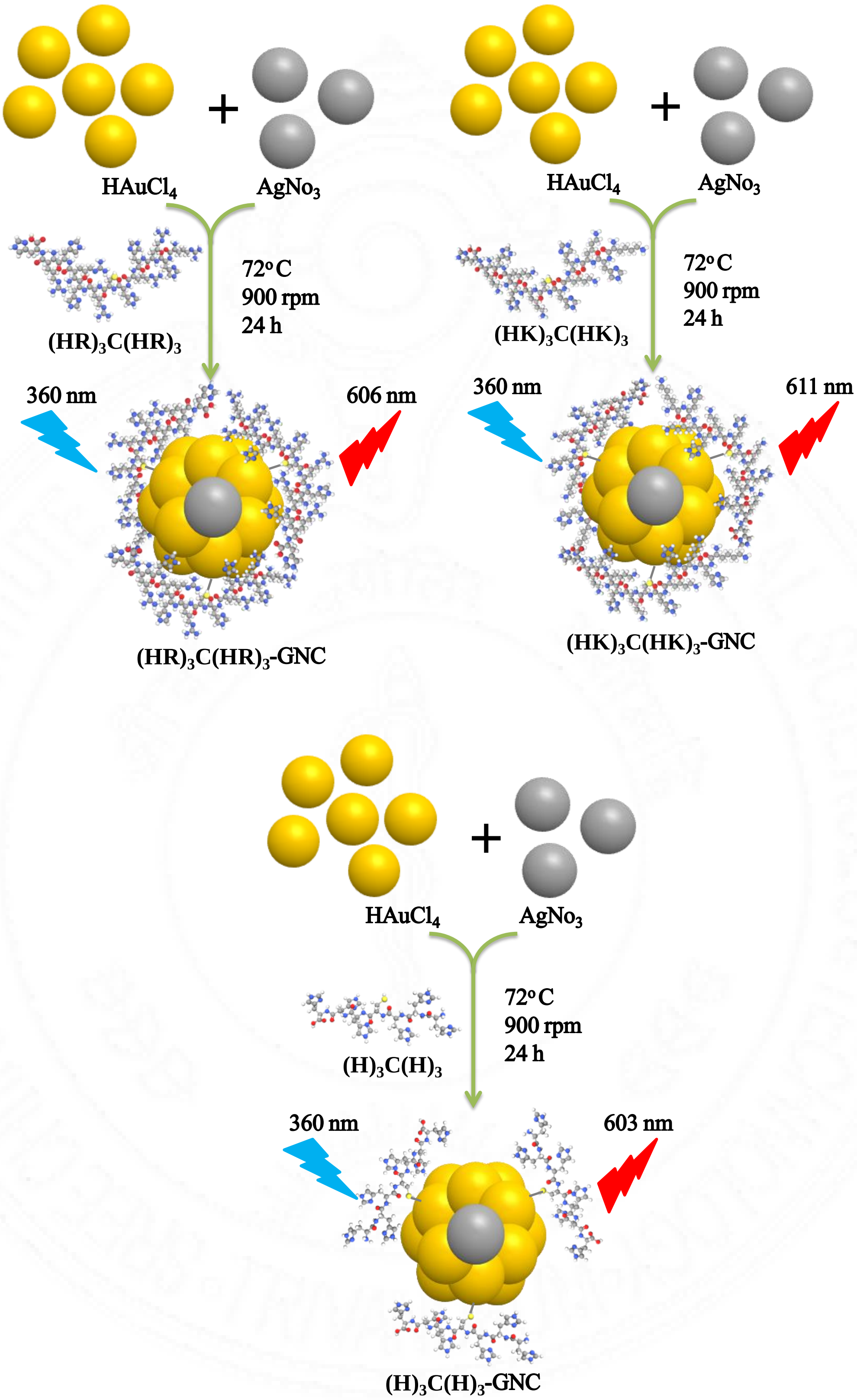

Figure 81: Pictorial representation of the synthesis of three oligopeptide-gold nanoclusters: (HR)$_3$C(HR)$_3$-GNC, (HK)$_3$C(HK)$_3$-GNC and (H)$_3$C(H)$_3$-GNC.

4.3.4. Physico-chemical characterization of oligopeptide-gold nanoclusters

4.3.4.1. Optical properties

The absorption and emission spectra of three oligopeptide-gold nanoclusters, $(HR)_3C(HR)_3$-GNC, $(HK)_3C(HK)_3$-GNC and $(H)_3C(H)_3$-GNC are shown in figure 82. Insets in figure 82 show the photographic image of oligopeptide-gold nanoclusters under white light and UV light illumination (365 nm). The absorption spectra of the three oligopeptide-gold nanoclusters were recorded with UV-Vis spectrophotometer, which shows the characteristic spectra of gold nanoclusters. The absence of surface plasmon resonance (SPR) peak @ ~520 nm indicates the absence of larger gold nanoparticles and also confirms the presence of smaller nanoclusters, with the characteristic absorption peak of the same. This result validates the purity of the gold nanoclusters by the above synthesis method. The absorption spectra of all the oligopeptide-gold nanoclusters rise sharply below 300 nm with maximum wavelength @ 260 nm and have a band edge of 400 nm. The molecular-like absorption bands @ 260 and 300 nm confirms the gold nanocluster formation with the presence of more number of histidine in the surface, similar to the histidine mediated Au and Ag nanoclusters reported by Guo Y *et al.*, 2015 and Pal N *et al.*, 2015.

$(HR)_3C(HR)_3$-GNC, $(HK)_3C(HK)_3$-GNC and $(H)_3C(H)_3$-GNC emit strong fluorescence in red region with maximum wavelength @ 606, 611 and 603 nm respectively with 360 nm excitation. This emission range is highly advantageous for bioimaging, since it avoids the hindrance from autofluorescence. Qu X *et al.*, 2015 reported that ligands not only act as protecting agent but also largely affect the fluorescence of gold nanoclusters by transferring charge from surface ligand to the gold core. Thus, the use of different sequences of peptides $(HR)_3C(HR)_3$, $(HK)_3C(HK)_3$ and $(H)_3C(H)_3$ for the preparation of gold nanocluster resulted in the slight variation of emission maximum in respective gold nanoclusters as supported by ligand-to-metal−metal charge transfer (LMMCT) theory explained in section 1.4.3.

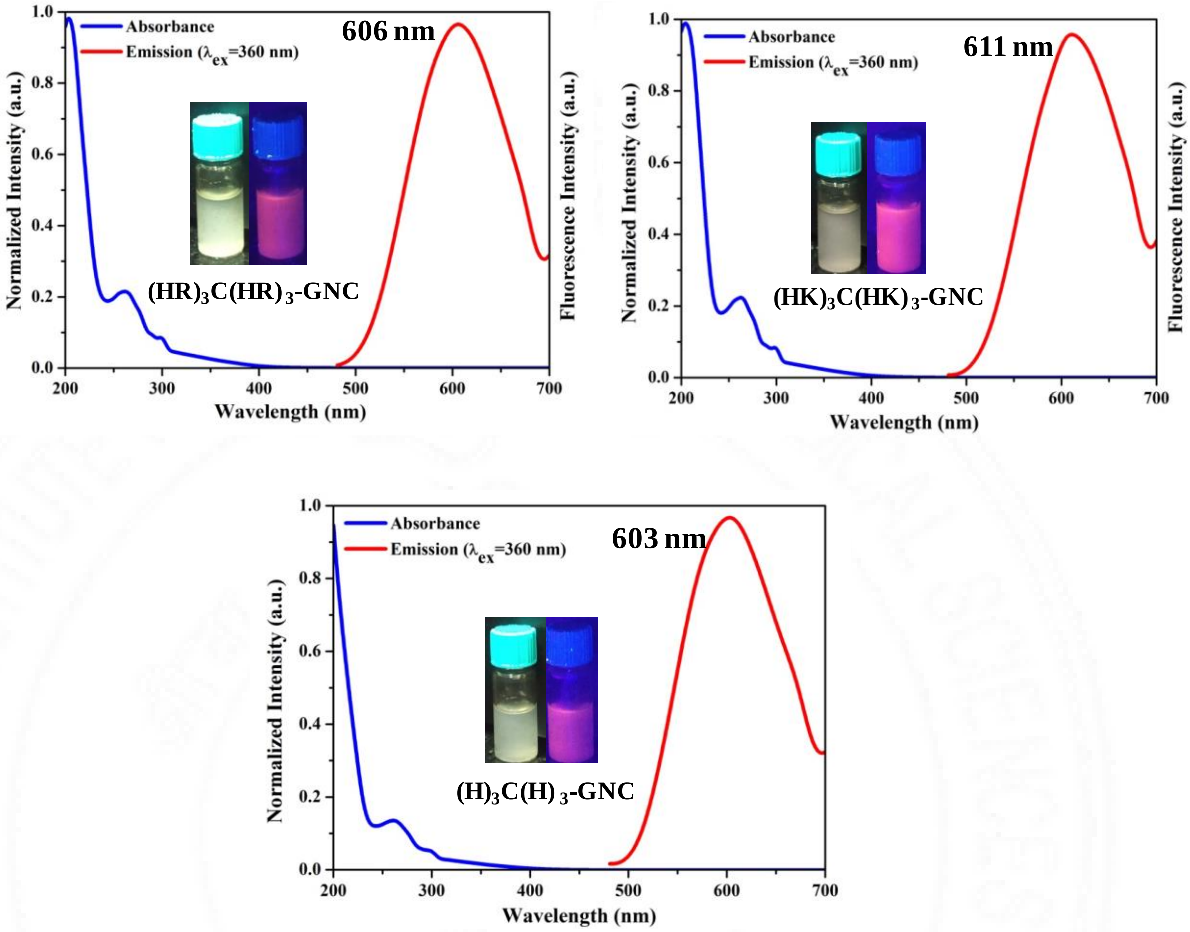

Figure 82: UV-Vis absorption and emission spectra of different oligopeptide-gold nanoclusters, $(HR)_3C(HR)_3$-GNC, $(HK)_3C(HK)_3$-GNC and $(H)_3C(H)_3$-GNC. Insets in every graph shows the photographic image of gold nanoclusters under visible and UV light illumination.

The emission spectra of all the oligopeptide-gold nanoclusters upon different excitation wavelength are shown in figure 83. All the oligopeptide-gold nanoclusters exhibited maximum emission @ 365 nm excitation. The excitation of these gold nanoclusters at different wavelength did not shift the emission spectra, indicating the high optical stability of these oligopeptide-gold nanoclusters. These gold nanoclusters also exhibited very large stokes shift (>220 nm), which avoids the interference from spectral overlap and autofluorescence and therefore highly beneficial for biological imaging.

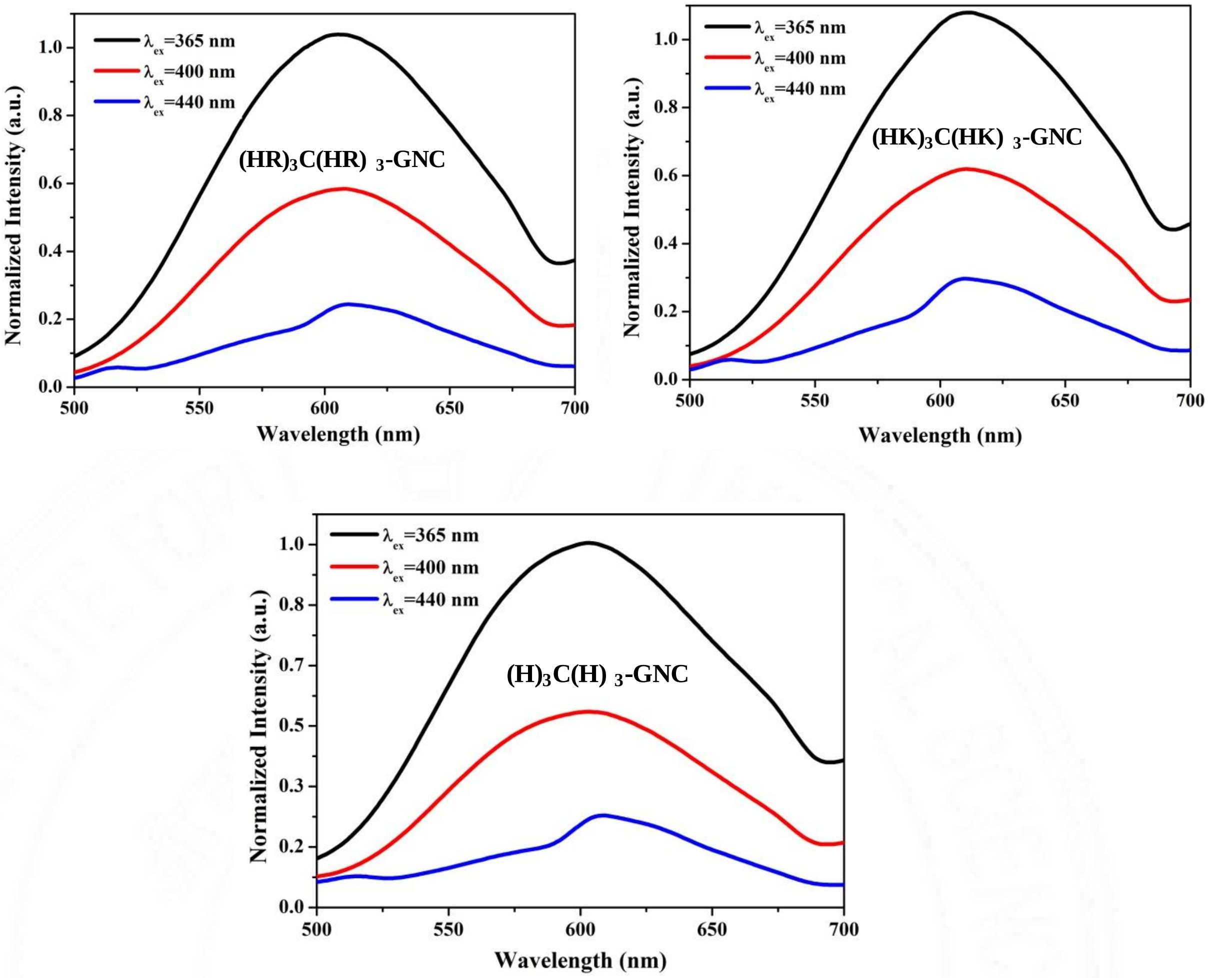

Figure 83: Emission spectra of different oligopeptide-gold nanoclusters $(HR)_3C(HR)_3$-GNC, $(HK)_3C(HK)_3$-GNC and $(H)_3C(H)_3$-GNC upon different excitation.

The fluorescence quantum yield of these oligopeptide-gold nanoclusters was estimated using the comparative method with an organic dye Rhodamine 6G as reference standard. The experimentally determined fluorescence quantum yield of three oligopeptide-gold nanoclusters is mentioned in table 13. All the oligopeptide-gold nanoclusters exhibited more than 9 % quantum yield confirming the high brightness of gold nanoclusters in water. $(HK)_3C(HK)_3$-GNC showed highest quantum yield (14 %) than other nanoclusters, which is significantly higher than most of the gold nanoclusters reported in the literature. The high quantum yield or fluorescence enhancement is due to the presence of silver atoms in the gold nanoclusters. It is clear from the results that the usage of different ligands along with silver doping influences the fluorescence enhancement or the quantum yield of gold nanoclusters. These results validated the findings reported by Li B *et al.*, 2016, Le Guével X *et al.*, 2012 and Wang S *et al.*, 2014, where Ag^+ influence the fluorescence enhancement of gold nanoclusters by ligand-to metal-metal charge transfer (LMMCT).

Sample	**Quantum Yield with reference to Rhodamine 6G (Φ_F)**	**Φ_F (%)**
$(HR)_3C(HR)_3$-GNC	0.0905	9
$(HK)_3C(HK)_3$-GNC	0.1438	14
$(H)_3C(H)_3$-GNC	0.1076	11

Table 13: Quantum yield of three different oligopeptide-gold nanoclusters calculated using the comparative method with Rhodamine 6G.

Many noble metal nanoclusters have long fluorescence lifetime with one or two magnitudes higher than quantum dots and organic dyes (Le Guével X *et al.*, 2011). These metal nanoclusters commonly have multiple lifetime components depending on the excitation wavelength. The fluorescence lifetime of $(HR)_3C(HR)_3$-GNC, $(HK)_3C(HK)_3$-GNC and $(H)_3C(H)_3$-GNC is shown in figure 84. All the synthesized oligopeptide-gold nanoclusters exhibit remarkably long fluorescence lifetime with biexponential decay: one short component (τ_1) and one long component (τ_2) (table 14), with long lifetime component > 330 ns. The abundance of the long lifetime component τ_2 expressed in percentage is plotted in figure 85. Patel S et al., 2009 and Le Guével X *et al.*, 2012 reported that the long lifetime component of metal nanoclusters is related to the electron transfer between the metal clusters and the ligand during the reduction process.

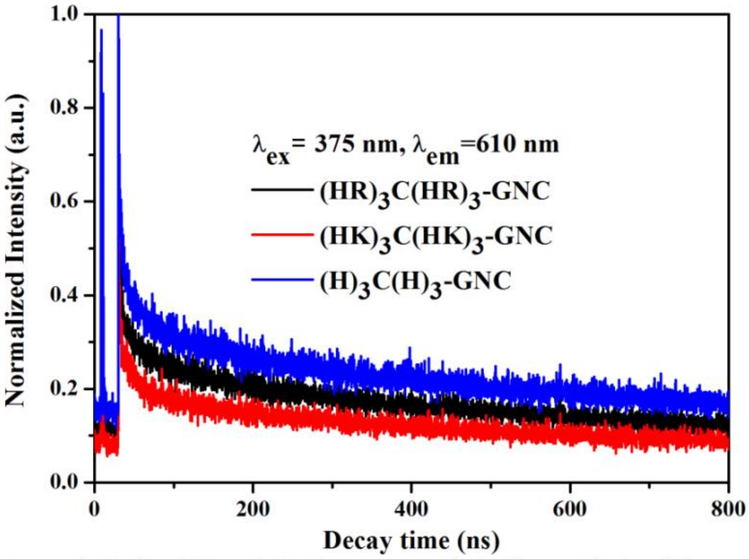

Figure 84: Fluorescence lifetime of oligopeptide-gold nanoclusters @ 610 nm emission and @ 375 nm excitation.

Sample	λ_{em}	τ_1 (ns)	A_1(%)	τ_2 (ns)	A_2(%)	χ^2
$(HR)_3C(HR)_3$-GNC	610	20.0	4.26	379.9	95.74	1.0
$(HK)_3C(HK)_3$-GNC	610	13.8	5.09	347.9	94.91	1.1
$(H)_3C(H)_3$-GNC	610	14.7	4.39	333.8	94.73	1.2

Table 14: Summary of lifetimes of oligopeptide-gold nanoclusters @ 375 nm excitation and 610 nm emission. τ_1 and τ_2 represents short and long lifetime of gold nanoclusters in nanoseconds (ns), A1 and A2 represents relative amplitude in %, χ^2 represents Chi square value.

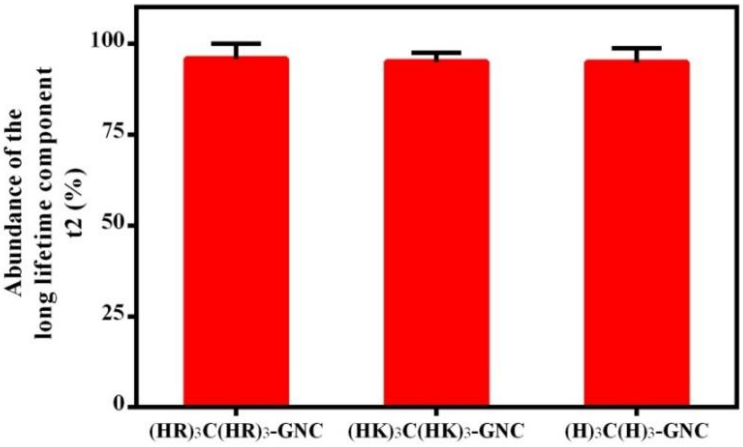

Figure 85: Relative amplitude of long lifetime component (τ_2) for different oligopeptide-gold nanoclusters @ 375 nm excitation and 610 nm emission.

4.3.4.2. Size, surface charge and surface chemistry

The size, size distribution and shape of oligopeptide-gold nanoclusters $(HR)_3C(HR)_3$-GNC, $(HK)_3C(HK)_3$-GNC and $(H)_3C(H)_3$-GNC were analyzed by HR-TEM. All the oligopeptide-gold nanoclusters have spherical shape and narrow size distribution with an average diameter below 3 nm. Figure 86 shows the HR-TEM image and size distribution of different oligopeptide-gold nanoclusters. HR-TEM image clearly illustrated the size as 2.7±0.72 nm, 2.3±0.11 and 2.4±0.18 nm for $(HR)_3C(HR)_3$-GNC, $(HK)_3C(HK)_3$-GNC and $(H)_3C(H)_3$-GNC respectively. These ultra-small sizes strongly support the metal quantum confinement effect as mentioned in section 1.4.3, i.e., the emergence of attractive fluorescent property in these oligopeptide-gold nanoclusters is due to the ultra-small size of gold nanoclusters. All the oligopeptide-gold nanoclusters showed aggregation in TEM image, which indicates the contribution from aggregation-induced emission (AIE) in these gold nanoclusters.

The surface charge or zeta potential of the as-prepared oligopeptide-gold nanoclusters were then analyzed by Malvern zeta sizer. The zeta potential of all the oligopeptide-gold nanoclusters is shown in figure 87. From the results, the surface charge of $(HR)_3C(HR)_3$-GNC, $(HK)_3C(HK)_3$-GNC and $(H)_3C(H)_3$-GNC was found to be +14.03 mV, +13.02 mV, and +7.47 mV respectively. The amino acids histidine (His or H), arginine (Arg or R) and lysine (Lys or K) in the peptides are positively charged under physiological conditions and hence the surface charge of all these gold nanoclusters is positive in as-prepared condition (pH 7). But the usage of additional arginine and lysine amino acids provides more positive charge to $(HR)_3C(HR)_3$-GNC and $(HK)_3C(HK)_3$-GNC respectively, compared with the histidine alone fabricated gold nanocluster $(H)_3C(H)_3$-GNC. It is reported that the functionalization of gold nanoclusters with arginine moieties greatly improves the cellular uptake of gold nanoclusters due to anchoring ability of positively charged arginine to the negatively charged cell membrane (Broekgaarden M et al., 2020). Similarly, the positive charge of lysine and histidine also offers increased cellular uptake to the gold nanoclusters fabricated with them.

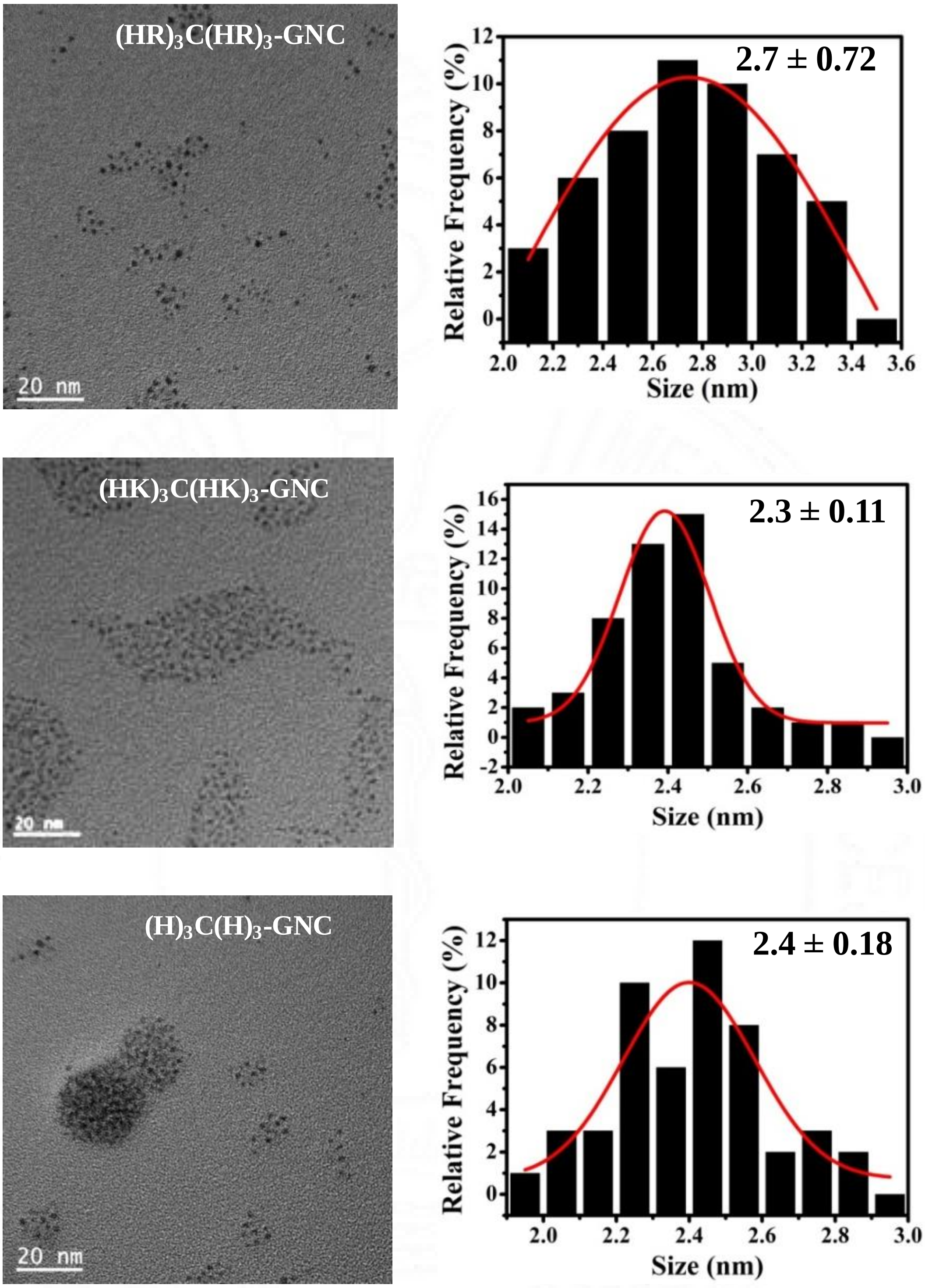

Figure 86: HR-TEM image (left) and size distribution (right) of oligopeptide-gold nanoclusters (Scale bar = 20 nm).

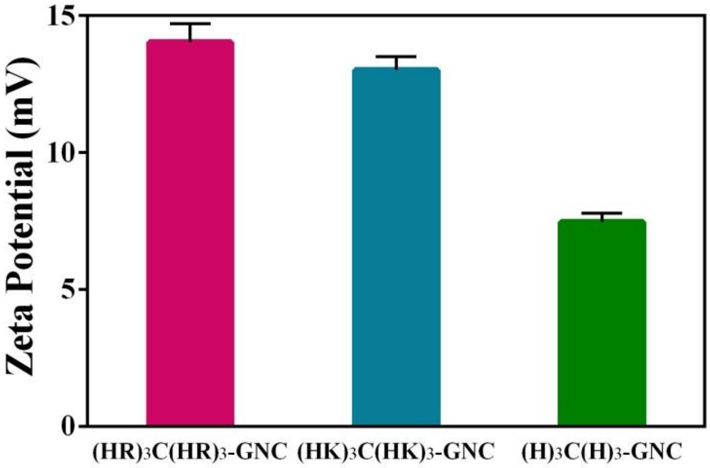

Figure 87: Surface charge of oligopeptide-gold nanoclusters.

FTIR spectral analysis was done to understand the surface chemistry and functional properties of oligopeptide-gold nanoclusters. Figure 88 shows the FTIR spectra of different oligopeptides $(HR)_3C(HR)_3$, $(HK)_3C(HK)_3$ and $(H)_3C(H)_3$ and its respective gold nanoclusters $(HR)_3C(HR)_3$-GNC, $(HK)_3C(HK)_3$-GNC and $(H)_3C(H)_3$-GNC. The characteristic peak @ 2524 cm^{-1} in all the oligopeptides attributes to the –SH group present in cysteine. The infrared measurements confirmed the covalent binding of oligopeptides to the metal nanoclusters by the disappearance of peak @ 2524 cm^{-1} in the gold nanoclusters and hence confirming the formation of Au-S bond in gold nanoclusters. In addition to the –SH peak, the broadening of band between 1750 to 1030 cm^{-1} in gold nanoclusters compared to the oligopeptides also confirmed the covalent binding between oligopeptides and metal clusters. In addition, the typical IR peaks @ 1658 cm^{-1} and 1531 cm^{-1} was observed for amide I band (C=O) and amide II band (N-H) respectively in all gold nanoclusters. The wide absorption band @ 3450 cm^{-1} corresponds to $–NH_2$ and -C-NH groups in the peptide at the surface of gold nanoclusters. The peak @ 2921 cm^{-1} and 1409 cm^{-1} are assigned to C-H stretching and O-H bending respectively.

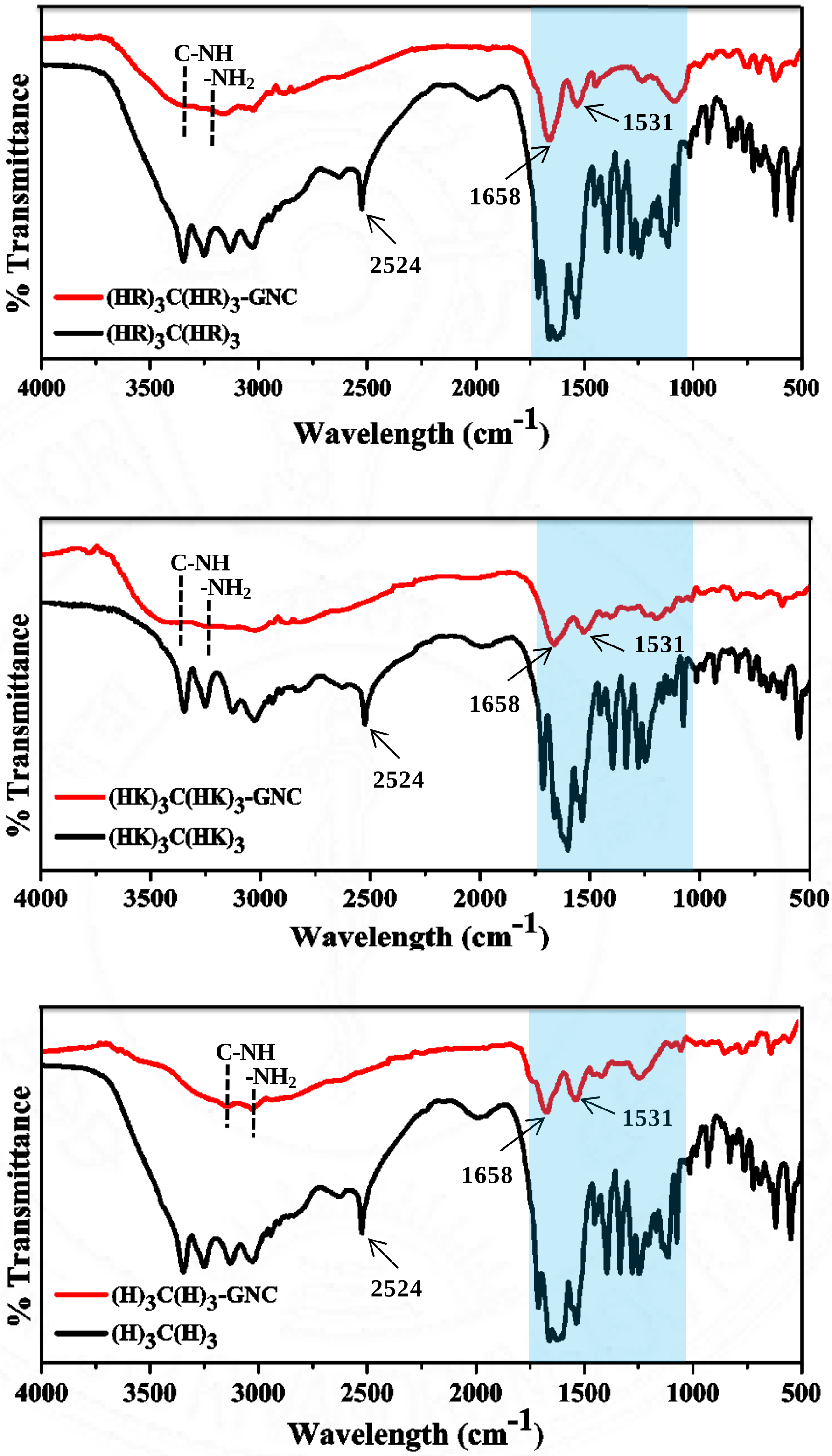

Figure 88: FTIR spectra of oligopeptides and its respective gold nanoclusters.

Followed by FTIR analysis to study the nature of ligand-metal interaction, XPS analysis was done to understand the oxidation state of metals in the oligopeptide-gold nanoclusters. The high resolution XPS core-level spectra in figure 89 shows the binding energy of gold (Au $4f_{7/2}$ and Au $4f_{5/2}$) and silver (Ag $3d_{5/2}$ and Ag $3d_{3/2}$) in all oligopeptide-gold nanoclusters. The maximum peak value of the binding energies is given in table 15. All the oligopeptide-gold nanoclusters showed the presence of both gold and silver with its characteristic binding energies, which is in good agreement with the silver-doped gold nanoclusters reported by Le Guével X *et al.*, 2012. The binding energy value obtained for Au $4f_{7/2}$ is ~84 eV for all oligopeptide-gold nanoclusters corresponds to Au(0) state, which clearly indicates the complete reduction of gold salt by oligopeptides. These results are in good agreement with the previous reported peptide capped gold quantum clusters (Baral A *et al.*, 2017) and thiol/protein directed synthesized gold nanoclusters (Shibu E *et al.*, 2009, Xie J *et al.*, 2009). The binding energy value obtained for Ag $3d_{5/2}$ is ~368 eV for all oligopeptide-gold nanoclusters corresponds to Ag(0) state, correlated with silver-doped gold nanoclusters reported by Le Guével X *et al.*, 2012. The doublet separation energy between high-resolution elemental spectra of Au $4f_{7/2}$ and $4f_{5/2}$ is ~3.7 eV and the doublet separation energy between Ag $3d_{5/2}$ and $3d_{3/2}$ is around ~5.9 eV. The observed peak values and the doublet separation energies are consistent with Au(0) and Ag(0) oxidation states. The electronic transistion between metal core and the peptide caused the minor shift observed in the binding energy of both Au and Ag. These observations also confirm that these oligopeptide-gold nanoclusters are bimetallic in nature because of the silver doping to gold nanoclusters.

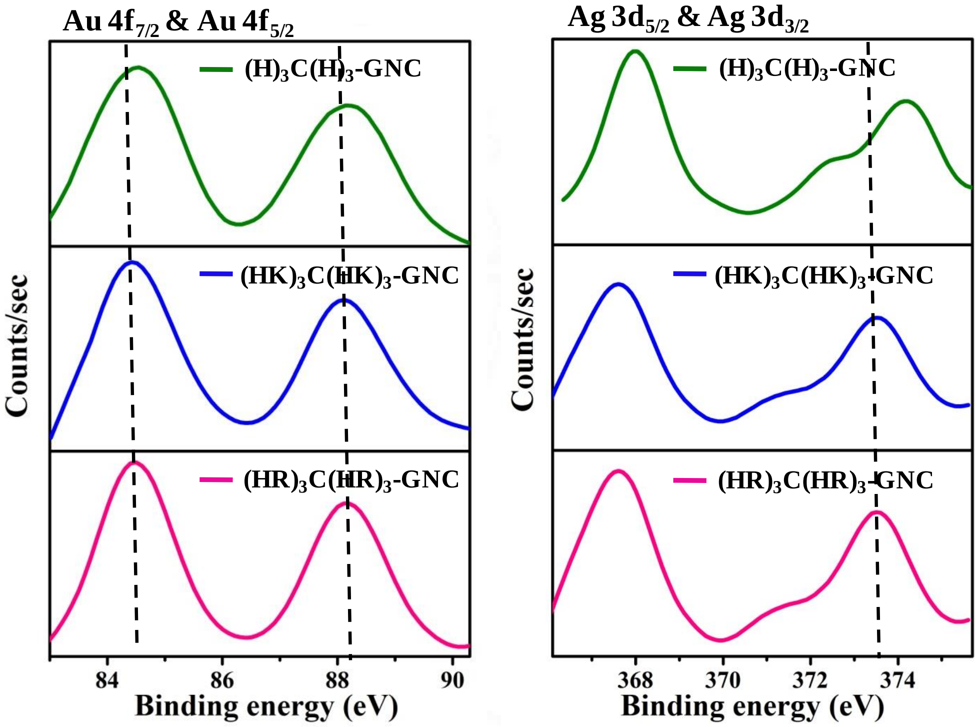

Figure 89: High resolution XPS spectra of oligopeptide-gold nanoclusters showing the binding energies of Au 4f and Ag 3d.

Sample	Au $4f_{7/2}$	Au $4f_{5/2}$	Ag $3d_{5/2}$	Ag $3d_{3/2}$
$(HR)_3C(HR)_3$-GNC	84.50	88.20	367.60	373.50
$(HK)_3C(HK)_3$-GNC	84.41	88.11	367.61	373.51
$(H)_3C(H)_3$-GNC	84.54	88.14	368.24	374.14

Table 15: The binding energies of Au $4f_{7/2}$, Au $4f_{5/2}$, Ag $3d_{5/2}$ and Ag $3d_{3/2}$ in respective oligopeptide-gold nanoclusters.

4.3.4.3. Stability of oligopeptide-gold nanoclusters

To study the fluorescence stability of oligopeptide-gold nanoclusters $(HR)_3C(HR)_3$-GNC, $(HK)_3C(HK)_3$-GNC and $(H)_3C(H)_3$-GNC at different pH, their respective emission maximum at pH 4, 5, 6, 7, 8 and 9 was measured. As shown in figure 90, significant difference was observed between the emission maximum at different pH for all the oligopeptide-gold nanoclusters. All the gold nanoclusters showed similar pattern from pH 4 to pH 9 (Figure 90). The fluorescent intensity at acidic pH (pH 4) is low. When the pH is increased to 6, the fluorescent intensity of all these gold nanoclusters drastically increased and at pH 7, the fluorescent intensity reached its peak. However, the fluorescence intensity decreased on increasing the pH from 7 to 9. It is observed that the fluorescent intensity of these gold-nanoclusters is high at acidic pH 4 and 5 compared to the alkaline pH 9. Hence it is clear that these gold nanoclusters might exhibit good fluorescence even inside acidic endosomal or lysosomal compartments in cells. The pH stability pattern of these highly positive charge oligopeptide-gold nanoclusters is similar to the slightly positive tripeptide-gold nanoclusters HCS-GNC and HCG-GNC (Figure 65). Hence the pH stability results also correlated with the zeta potential study. Even though different pH influences the fluorescent stability, all the oligopeptide-gold nanoclusters retain maximum fluorescence intensity at pH 7 and hence these oligopeptide-gold nanoclusters are highly favourable for bioimaging.

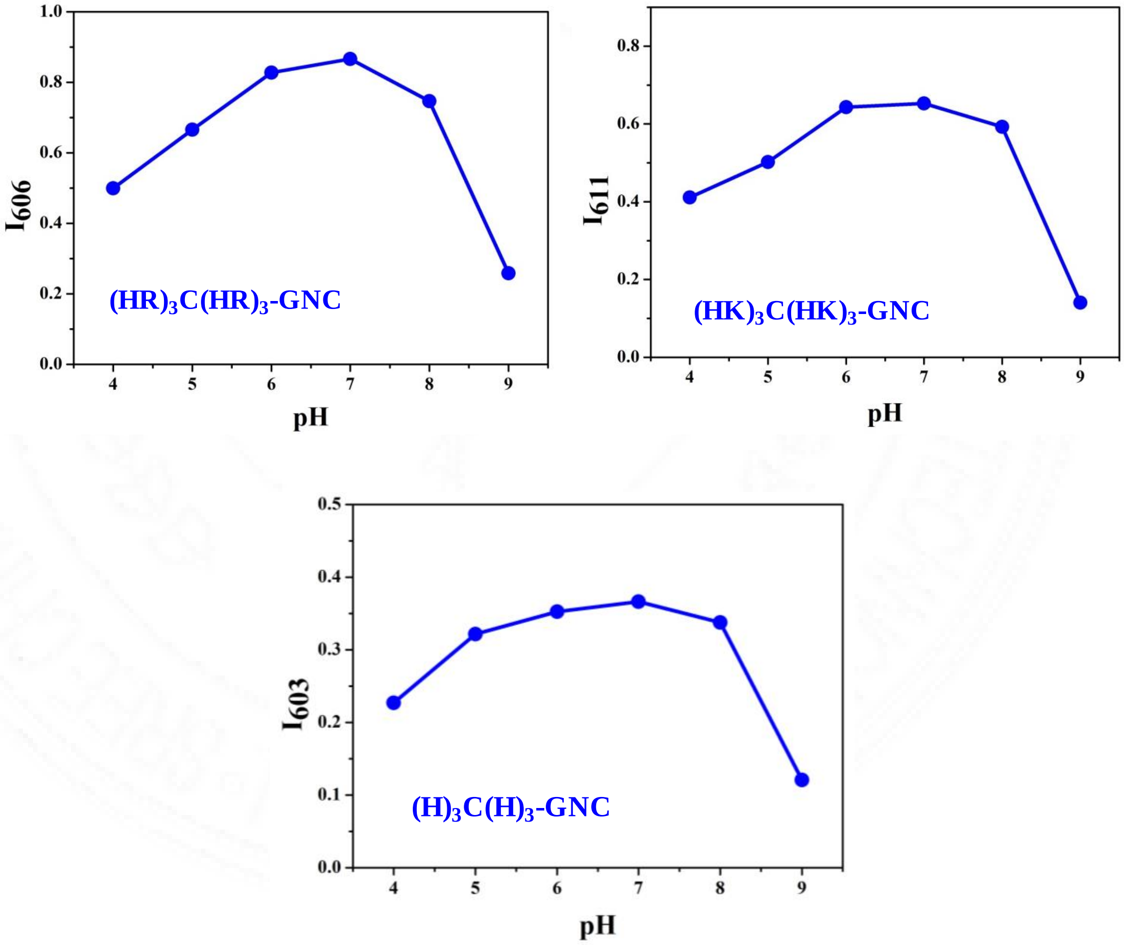

Figure 90: Influence of different pH on the fluorescent stability of oligopeptide-gold nanoclusters.

Further to evaluate the stability of oligopeptide-gold nanoclusters against photodestruction, a simple photobleaching experiment was carried out by continuously illuminating the aqueous solution of oligopeptide-gold nanoclusters with the hand-held UV lamp (λ_{ex} = 365 nm) for 10 min. The fluorescence intensity of $(HR)_3C(HR)_3$-GNC, $(HK)_3C(HK)_3$-GNC and $(H)_3C(H)_3$-GNC at their respective emission maximum 606, 611 and 603 nm was measured before and after UV illumination. Rhodamine 6G, an organic dye was used as reference. The stability of fluorescence was plotted in percentage by dividing the intensity after illumination with initial intensity (I/I_O). The results showed that all the oligopeptide-gold nanoclusters have a strong resistance to photobleaching (Figure 91), while the fluorescence intensity of Rhodamine 6G drastically decreased after continuous UV illumination. All the oligopeptide-gold nanoclusters retained maximum fluorescence stability (> 75 %) after UV illumination compared with Rhodamine 6G, which retained only 7 % of its fluorescence intensity. Thus these oligopeptide-gold nanoclusters are highly photostable and can be used for long term, biological time lapse imaging with continuous excitation.

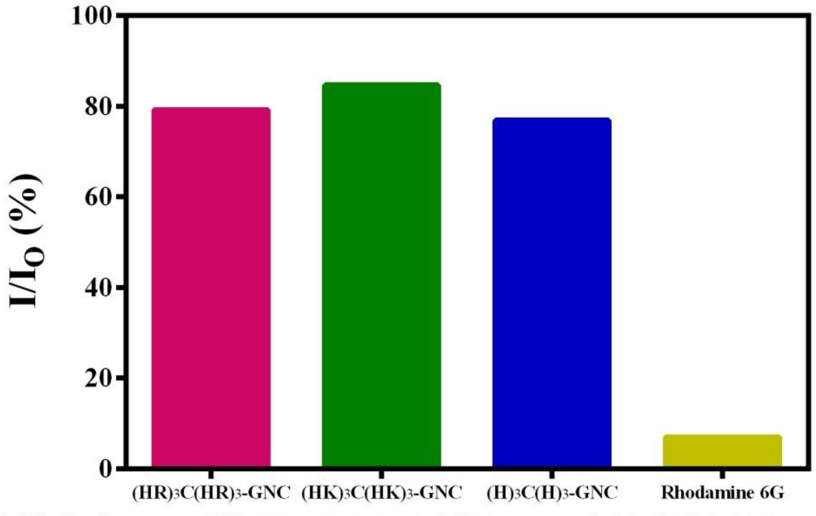

Figure 91: Photobleaching measurements of oligopeptide-gold nanoclusters and Rhodamine 6G after continuous UV illumination.

The fluorescence stability is one of the important factors that limit the practical use of nanoparticles. Hence, to evaluate the fluorescent stability of oligopeptide-gold nanoclusters during long period storage, the synthesized oligopeptide-gold nanoclusters $(HR)_3C(HR)_3$-GNC, $(HK)_3C(HK)_3$-GNC and $(H)_3C(H)_3$-GNC were redissolved in ultrapure RNase free water and stored @ 4°C. The respective emission maximum of all oligopeptide-gold nanoclusters stored @ 4°C for different time points (1, 10, 30, 60, 120, 180 days) was measured. The fluorescence of all the tripeptide-gold nanoclusters was stable even after 6 months with only a slight decrease in fluorescent intensity (Figure 92). Thus these oligopeptide-gold nanoclusters can be stored for longer period of time @ 4°C without losing its fluorescence stability. Hence it is clear that these oligopeptide-gold nanoclusters have long shelf life and can be used for bioimaging even after 6 months of storage.

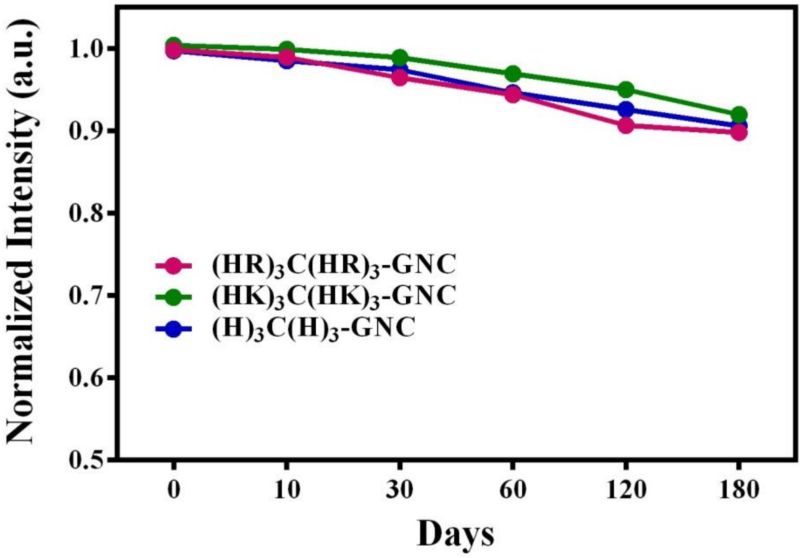

Figure 92: Effect of storage time on the fluorescence stability of oligopeptide-gold nanoclusters.

4.3.5. Biological evaluation of oligopeptide-gold nanoclusters

Inspired by the fluorescent property and photostability of oligopeptide-gold nanoclusters $(HR)_3C(HR)_3$-GNC, $(HK)_3C(HK)_3$-GNC and $(H)_3C(H)_3$-GNC, the biological interaction of these oligopeptide-gold nanoclusters was then studied for use in bioimaging application. SK-BR-3 cancer cells were used to study the biological interaction of these oligopeptide-gold nanoclusters.

4.3.5.1. *In vitro* cytocompatibility of oligopeptide-gold nanoclusters

Even though quantum dots or other nanoparticles have excellent fluorescent property for imaging application, its toxicity towards cells limits their practical application in clinical usage or for long term bioimaging. Hence it is necessary to evaluate the long term cytocompatibility of nanoparticles before being tested for cellular imaging. In order to use the oligopeptide-gold nanoclusters $(HR)_3C(HR)_3$-GNC, $(HK)_3C(HK)_3$-GNC and $(H)_3C(H)_3$-GNC for bioimaging application, the long term cytocompatibility of these gold nanoclusters was first studied in SK-BR-3 cancer cells using MTT assay. Metabolically active cells reduce the soluble MTT into insoluble coloured formazan crystals by mitochondrial dehydrogenase. The absorbance of these formazan crystals dissolved in respective solvent indicates the total cell viability with or without material treatment.

Figure 93 shows the percentage of SK-BR-3 cell viability after respective oligopeptide-gold nanoclusters treatment. All the oligopeptide-gold nanoclusters showed a concentration dependent slight decrease in cell viability @ 24, 48 and 72 h. The cells retained more than 85 % viability with $(HK)_3C(HK)_3$-GNC and $(H)_3C(H)_3$-GNC treatment after 24 h even at high concentration (1 mg/ml) except for $(HR)_3C(HR)_3$-GNC, which showed 75 % viability at high concentration. This slight decrease of cell viability $(HR)_3C(HR)_3$-GNC at high concentration might be due to the presence of more number of arginine on the surface of these gold nanoclusters, which exerts little cytotoxicity. 100 µg/ml (0.1 mg/ml) was chosen for further cell studies as all the cells retained more than 85 % viability at this concentration even after long term (72 h) treatment. Hence the results of MTT assay proved the cytocompatibility of all oligopeptide-gold nanoclusters at 0.1 mg/ml and the feasibility of these nanoclusters at this concentration to be safely exploited for bioimaging applications.

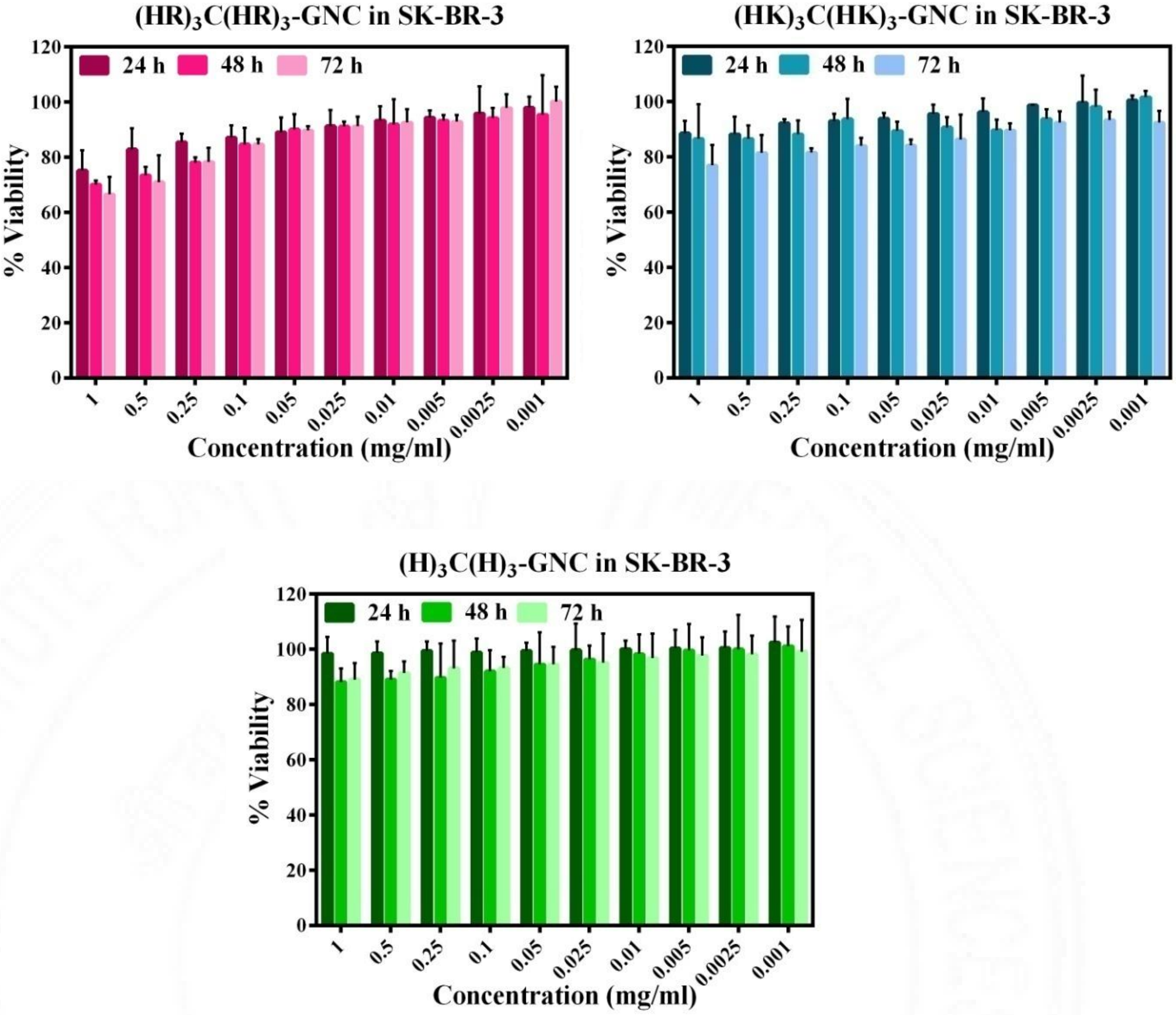

Figure 93: *In vitro* cytocomapatibility study of oligopeptide-gold nanoclusters in SK-BR-3 cancer cells showing the percentage of cell viability at different concentrations. Error bar represents the standard deviation (n=5).

4.3.5.2. Cellular uptake of oligopeptide-gold nanoclusters

In order to use the oligopeptide-gold nanoclusters, $(HR)_3C(HR)_3$-GNC, $(HK)_3C(HK)_3$-GNC and $(H)_3C(H)_3$-GNC for bioimaging application, the cellular internalization of these gold nanoclusters in SK-BR-3 cancer cells was first studied. The fluorescence emission of these oligopeptide-gold nanoclusters was employed to assess the cellular uptake, by incubating 100 µg/ml of respective gold nanoclusters in SK-BR-3 cells for 3 h. As shown in figure 94, all oligopeptide-gold nanoclusters are found to be present in the cytoplasm of cells after 3 h of incubation. Nucleus of the cells was differentially visualized with Hoechst stain. It is noted that these gold nanoclusters are not distributed uniformly in the cytoplasm of cells, but are found as aggregates inside cells. The results correlates with the findings reported in previous literatures which states that the uptake of nanoparticles by endocytosis resulted in accumulation of nanoparticles inside cells in the form of large aggregates (Chen H *et al.*, 2013).

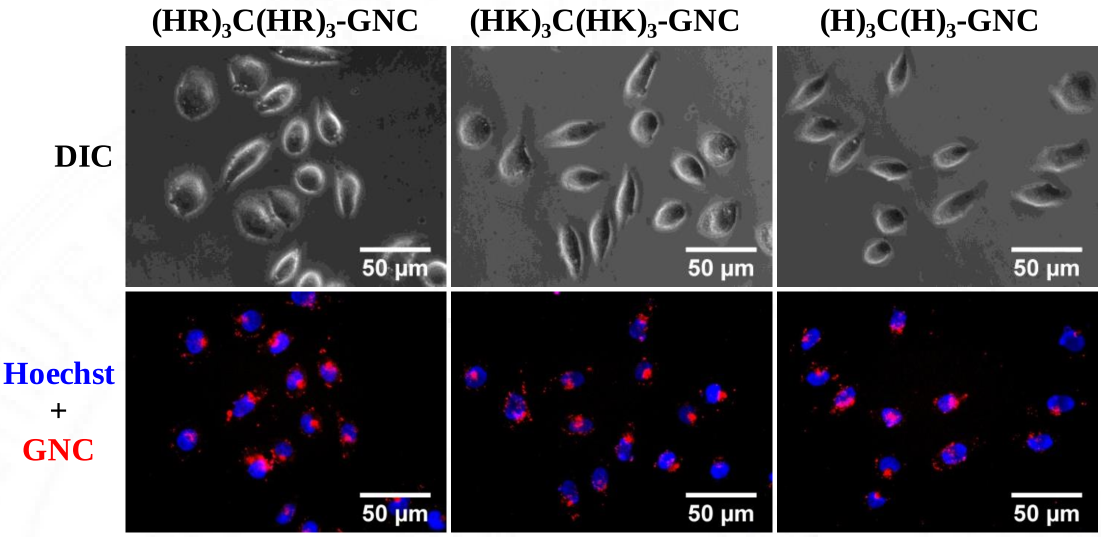

Figure 94: Cellular uptake and accumulation of oligopeptide-gold nanoclusters in SK-BR-3 cells after 3 h of incubation. The top row represents the differential interference contrast images showing the morphology of SK-BR-3 cells. Red fluorescence represents the emission from gold nanoclusters; Blue fluorescence represents the Hoechst staining of nuclei. Scale bar = 50 µm.

It has been proposed that the cellular internalization rate is influenced by nanoparticles size, charge and surface properties as well as the cell type (Behzadi S *et al.*, 2017). It is known that the cell membrane has negative charge and hence more positive charged nanoparticles penetrates cell membrane easily. The surface charge of these oligopeptide-gold nanoclusters greatly influences the nanocluster attraction towards cell entry and thereby influences cellular uptake, accumulation and cell viability percentage. As shown in the results of figure 87, the surface charge of $(HR)_3C(HR)_3$-GNC and $(HK)_3C(HK)_3$-GNC is more positive than $(H)_3C(H)_3$-GNC and hence both the former nanoclusters are found to be accumulated more in SK-BR-3 cells than the latter nanocluster (figure 94).

4.3.6. Complexation of siRNA to oligopeptide-gold nanoclusters

The complexation of siRNA with different oligopeptide-gold nanoclusters $(HR)_3C(HR)_3$-GNC, $(HK)_3C(HK)_3$-GNC and $(H)_3C(H)_3$-GNC was done in RNase free water. Each gold nanoclusters were mixed with different weight ratio of siRNA (1:0, 1:0.5, 1:1, 1:1.5, 1:2, 1:4, 1:8, 1:16) and the prepared samples were mentioned as $(HR)_3C(HR)_3$-GNC-siRNA, $(HK)_3C(HK)_3$-GNC-siRNA and $(H)_3C(H)_3$-GNC-siRNA. The positively charged amino acids arginine, lysine and histidine on the surface of gold nanoclusters allow the electrostatic interaction of negatively charged phosphate groups in siRNA resulting in gold nanocluster-siRNA complex formation.

4.3.6.1. Characterization of oligopeptide-GNC-siRNA complex

The GNC-siRNA complex $(HR)_3C(HR)_3$-GNC-siRNA, $(HK)_3C(HK)_3$-GNC-siRNA and $(H)_3C(H)_3$-GNC-siRNA prepared in different ratio were characterized using zeta potential analysis to evaluate the maximum loading capacity of each gold nanoclusters (figure 95). At 1:0 ratio, the $(HR)_3C(HR)_3$-GNC, $(HK)_3C(HK)_3$-GNC and $(H)_3C(H)_3$-GNC exhibited the surface charge of +14, +13 and +7 respectively. The addition of siRNA resulted in decrease of the surface charge of these GNC-siRNA complexes. At 1:1 of GNC-siRNA ratio, $(H)_3C(H)_3$-GNC-siRNA showed negative surface charge, while the other two $(HR)_3C(HR)_3$-GNC-siRNA and $(HK)_3C(HK)_3$-GNC-siRNA complexes showed positive surface charge. $(H)_3C(H)_3$-GNC-siRNA complex showed negligible change in surface charge after 1:1 ratio, while the surface charge of $(HR)_3C(HR)_3$-GNC-siRNA and $(HK)_3C(HK)_3$-GNC-siRNA complexes decreased further till 1:4 ratio. The maximum loading capacity of $(HR)_3C(HR)_3$-GNC, $(HK)_3C(HK)_3$-GNC and $(H)_3C(H)_3$-GNC was found to be 1:4, 1:4 and 1:1 respectively (figure 95).

From these results, it is clear that the arginine and lysine fabricated gold nanoclusters have a more positive surface charge than histidine alone fabricated gold nanoclusters and hence have high loading capacity of siRNA. A typical 21 mer duplex siRNA has a molecular weight of 13,300 daltons. Accordingly, it is calculated that per milligram of $(H)_3C(H)_3$-GNC can carry 75 nmol of siRNA, while

(HR)$_3$C(HR)$_3$-GNC and (HK)$_3$C(HK)$_3$-GNC can carry 301 nmol of siRNA. Hence, it is proved that (HR)$_3$C(HR)$_3$-GNC and (HK)$_3$C(HK)$_3$-GNC have extremely high siRNA loading capacity than other siRNA delivery vectors reported till date. This high loading capacity is due to ultra small size, high surface to volume ratio and the sufficient positive charge on the surface of oligopeptide-gold nanoclusters.

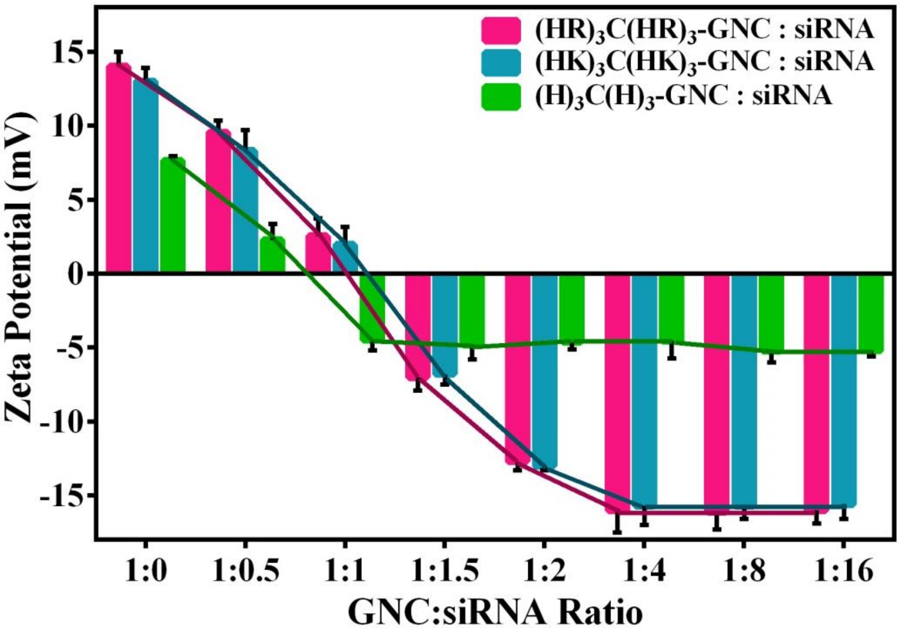

Figure 95: Charge reversal study using zeta potential analysis showing the siRNA loading capacity of three different oligopeptide-gold nanoclusters.

The surface chemistry of all GNC-siRNA complexes was further studied using FTIR spectroscopy. (HR)$_3$C(HR)$_3$-GNC, (HK)$_3$C(HK)$_3$-GNC and (H)$_3$C(H)$_3$-GNC showed characteristics FTIR spectra of gold nanoclusters with the disappearance of –SH group from their respective oligopeptides due to the formation of Au-S bond and the covalent binding between peptides and gold atoms. All GNC-siRNA complexes showed additional C-O-C glycosidic bridge and PO_4^{3-} @ 1155 and 1038 cm^{-1} respectively compared to bare GNCs (figure 96). The C-O-C glycosidic bond is due to the presence of ribose sugar in the siRNA molecule and PO_4^{3-} is due to the sugar-phosphate backbone of siRNA (Islam N *et al*., 2019). Hence, these results confirmed the complexation of siRNA with the gold nanoclusters.

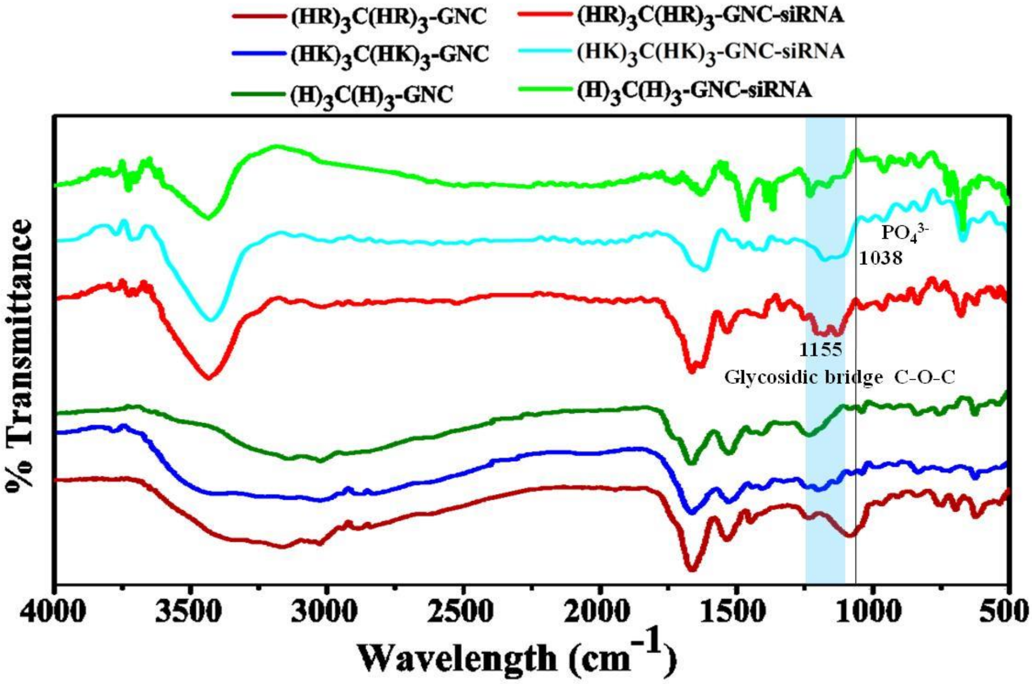

Figure 96: FTIR spectra of oligopeptide-gold nanoclusters and their complexation with siRNA.

As $(H)_3C(H)_3$-GNC has a very low siRNA loading capacity, it was omitted from further studies. In addition to FTIR spectroscopy, the complexation of siRNA with $(HR)_3C(HR)_3$-GNC and $(HK)_3C(HK)_3$-GNC was further investigated using XPS analysis. The high resolution XPS spectra in the figure 97 shows the binding energy of major elements in $(HR)_3C(HR)_3$-GNC and $(HK)_3C(HK)_3$-GNC and their complexation with siRNA. Both the bare GNCs and GNC-siRNA complexes showed the binding energies characteristic to gold, silver and nitrogen atoms. Compared to $(HR)_3C(HR)_3$-GNC and $(HK)_3C(HK)_3$-GNC, their respective GNC-siRNA complexes showed negligible changes in the surface Au and Ag contents. However, a marked increase of N content is observed in GNC-siRNA complexes compared to GNCs. This increase is due to the presence of additional N contents in the base pairs of nucleotides in siRNA. In addition to the increase in N content, a substantial presence of P atom (0.9 atomic %) was noticed in GNC-siRNA complexes compared to GNCs alone, which showed only < 0.1 atomic %. This is because of the presence of phosphate groups of nucleotides in siRNA. These results correlate with the previous finding reported by Lei Y *et al*., 2017.

(HR)$_3$C(HR)$_3$-GNC

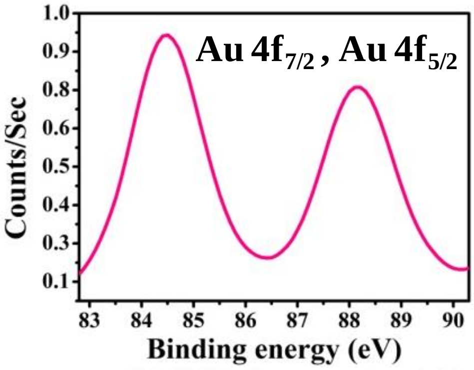

(HR)$_3$C(HR)$_3$-GNC-siRNA

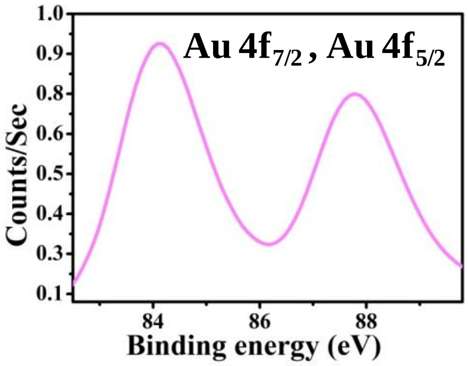

(HR)$_3$C(HR)$_3$-GNC

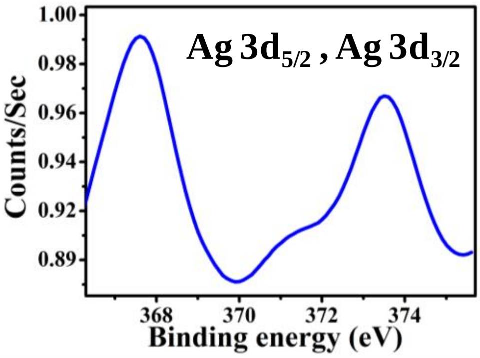

(HR)$_3$C(HR)$_3$-GNC-siRNA

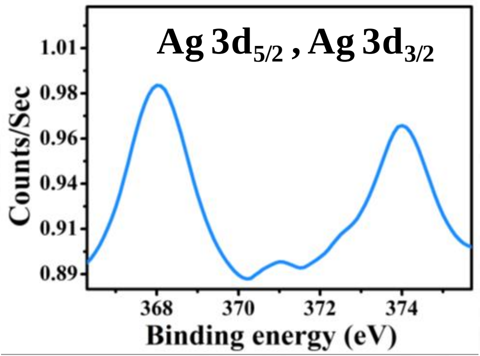

(HR)$_3$C(HR)$_3$-GNC

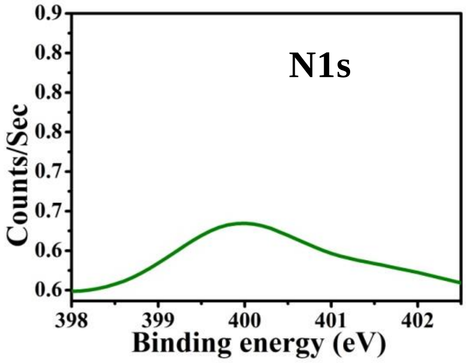

(HR)$_3$C(HR)$_3$-GNC-siRNA

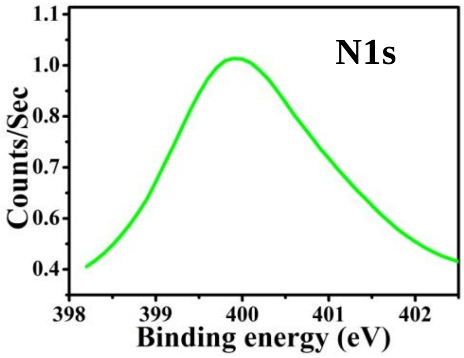

(HR)$_3$C(HR)$_3$-GNC

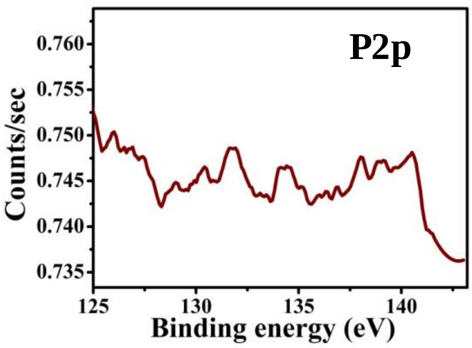

(HR)$_3$C(HR)$_3$-GNC-siRNA

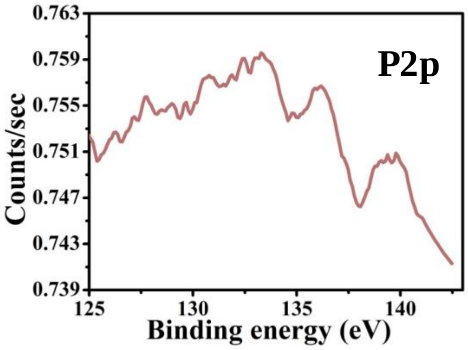

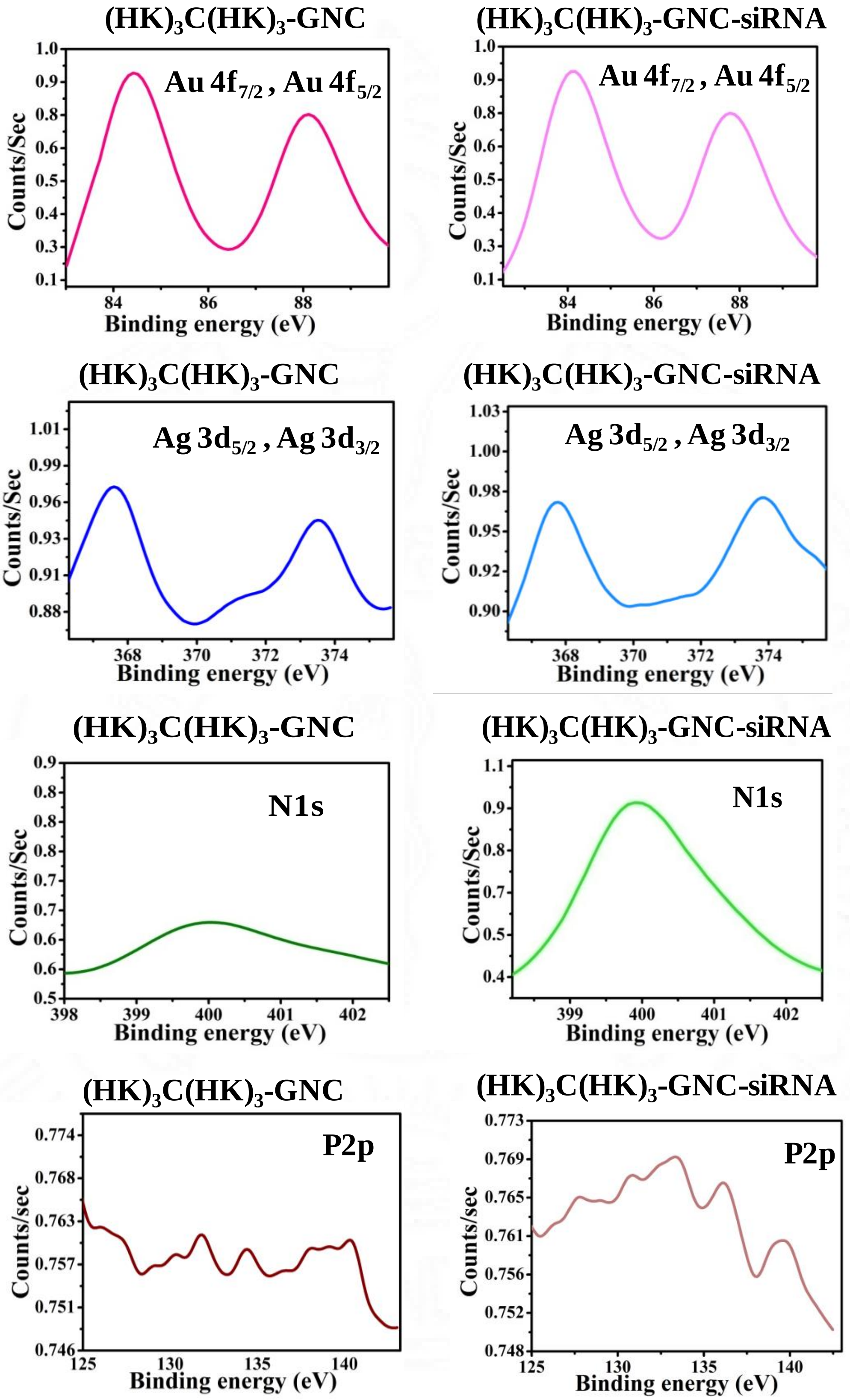

Figure 97: High resolution XPS spectra showing the binding energies of major elements in (HR)$_3$C(HR)$_3$-GNC and (HK)$_3$C(HK)$_3$-GNC and their siRNA complex formation.

4.3.7. In vitro evaluation of siRNA delivery using oligopeptide-gold nanoclusters

The prerequisite for efficient siRNA mediated gene silencing/knockdown is the high cellular uptake of siRNA. So, an efficient siRNA delivery vector should possess high siRNA loading capacity for the increased uptake in cells. The delivery vector should not only allow/increase the entry of siRNA inside cells, but also exert efficient endosomal escape for the successful delivery of siRNA inside cytoplasm. To evaluate the potential of oligopeptide-gold nanoclusters for siRNA delivery, the cellular uptake of siRNA and the cytocompatibility of different siRNA transfection methods are studied with non-specific siRNA, which consists of a scrambled sequence that will not lead to the specific degradation of any cellular message. The studies were carried out in comparison with commercially available lipofectamine 2000 reagent. The endosomal escape effect of oligopeptide-gold nanoclusters is also described in this section.

4.3.7.1. Cellular uptake of siRNA using different transfection methods

To evaluate the siRNA delivery efficiency of oligopeptide-gold nanoclusters, the cellular uptake/internalization of siRNA using different transfection methods was carried out in SK-BR-3 cells including delivery of free-siRNA (without any carrier), lipofectamine mediated transfection, $(HR)_3C(HR)_3$-GNC and $(HK)_3C(HK)_3$-GNC mediated transfection. For *in vitro* imaging of siRNA delivery, non-specific siRNA tagged with FITC (NSsiRNA-FITC) was used. This NSsiRNA consists of a scrambled sequence that will not lead to the specific degradation of any cellular message.

Figure 98 shows the cellular uptake of siRNA using the above mentioned transfection methods. The free-siRNA transfection without any carrier showed negligible cellular uptake owing to their high molecular weight and negative charge. Lipofectamine2000 mediated siRNA transfection showed the presence of NSsiRNA-FITC inside the cytoplasm of SK-BR-3 cells compared with free-siRNA transfection method. Here, lipo2000-siRNA acts as a positive control to evaluate the delivery of siRNA in this study. Compared with free-siRNA, the oligopeptide-GNC-siRNA complexes showed much larger quantity of cellular uptake, which indicates that the oligopeptide-GNC facilitate the internalization of siRNA rather than the free form. Also, both (HR)$_3$C(HR)$_3$-GNC-siRNA and (HK)$_3$C(HK)$_3$-GNC-siRNA showed increased green fluorescence in the cells compared with lipo2000-siRNA treated cells. This clearly indicates that both these oligopeptide-gold nanoclusters delivered siRNA effectively than lipo2000-siRNA, because of its high siRNA loading capacity. The co-localized signal from NSsiRNA-FITC and GNC in the merged image (figure 98) confirms the signal is due to GNC-siRNA complexes and not GNC alone.

Compared with (HK)$_3$C(HK)$_3$-GNC-siRNA, the cellular uptake of (HR)$_3$C(HR)$_3$-GNC-siRNA is high. This result correlates with the enhanced cellular uptake shown by (HR)$_3$C(HR)$_3$-GNC compared with (HK)$_3$C(HK)$_3$-GNC in figure 94. The quantification of cellular uptake of NSsiRNA-FITC using different transfection methods was also calculated by measuring the mean fluorescence intensity (MFI) per cell (Figure 99). Significant differences were observed between each transfection method, confirming the differences in uptake are influenced by different transfection methods. Compared with (HR)$_3$C(HR)$_3$-GNC-siRNA and (HK)$_3$C(HK)$_3$-GNC-siRNA, the MFI of lipo2000-siRNA is very low, thus confirmed the high transfection efficiency of oligopeptide-GNCs with respect to the positive control lipofectamine2000 mediated transfection. The quantification results correlates with the fluorescence imaging data. Hence, it is proved that these oligopeptide-gold nanoclusters acts as an efficient siRNA delivery vector with its high loading capacity compared with the commercially available lipofectamine 2000 transfection reagent.

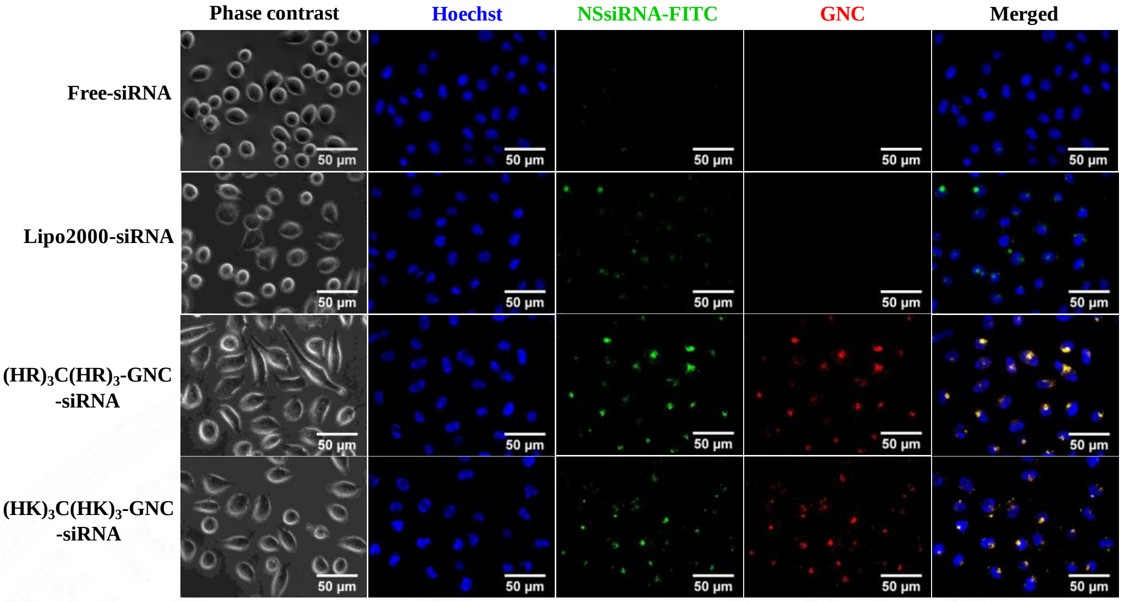

Figure 98: Fluorescent images of the cellular internalization of NSsiRNA-FITC by different transfection methods.

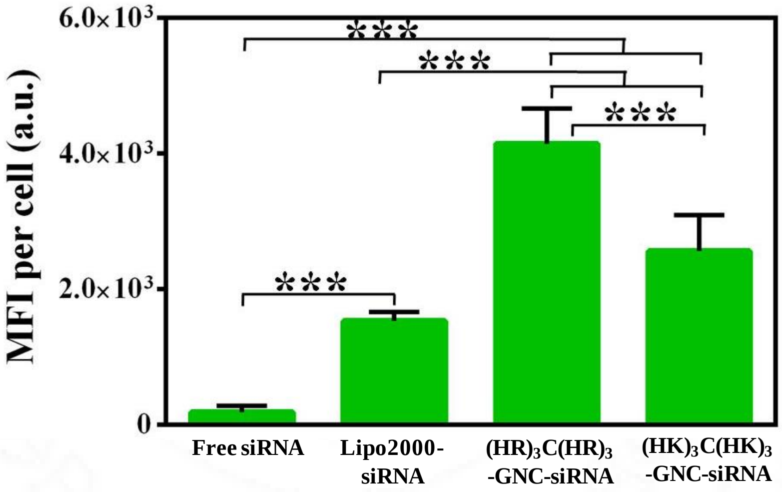

Figure 99: Quantification of cellular uptake of NSsiRNA-FITC using different transfection methods, showing the mean fluorescence intensity of NSsiRNA-FITC per cell. Mean±s.d. (n=10), *** $p < 0.001$.

4.3.7.2. Cytocompatibility of different siRNA carriers

The cytocompatibility of the oligopeptide-gold nanoclusters were already proved in section 4.3.5.1., the siRNA complexed form of GNCs is further studied for its cytocomaptibility in SK-BR-3 cells compared with the commercially available siRNA transfection reagent lipofectamine 2000. The cytocompatibility of different concentration of $(HR)_3C(HR)_3$-GNC-NSsiRNA, $(HK)_3C(HK)_3$-GNC-NSsiRNA and lipo2000-NSsiRNA complexes was studied in SK-BR-3 cells with 48 h of incubation using MTT assay. Figure 100 shows the cell viability percentage after treatment with different siRNA transfection carriers for 48 h. From the results, it is clear that both $(HR)_3C(HR)_3$-GNC-NSsiRNA and $(HK)_3C(HK)_3$-GNC-NSsiRNA complexes are non-toxic to SK-BR-3 cells from 1 to 500 nM siRNA concentration. In contrast, lipofectamine mediated siRNA transfection (lipo2000-NSsiRNA) caused significant toxicity to SK-BR-3 cells at the same concentrations. Even at high concentration of siRNA (500 nM), the cells retained more than 75% viability in case of $(HR)_3C(HR)_3$-GNC-NSsiRNA and $(HK)_3C(HK)_3$-GNC-NSsiRNA complexes, whereas the cells treated with lipofectamine at the same concentration retained only 30 % cell viability. This result confirms the cytocompatibility of oligopeptide-gold nanocluster siRNA carriers compared with the commercially available siRNA transfection reagent. This is attributed to the cytocompatibility of gold and hence it is proved that the synthesized oligopeptide-gold nanoclusters ($(HR)_3C(HR)_3$-GNC and $(HK)_3C(HK)_3$-GNC) are safe and efficient siRNA delivery vectors with both cytocompatibility and high siRNA loading capacity.

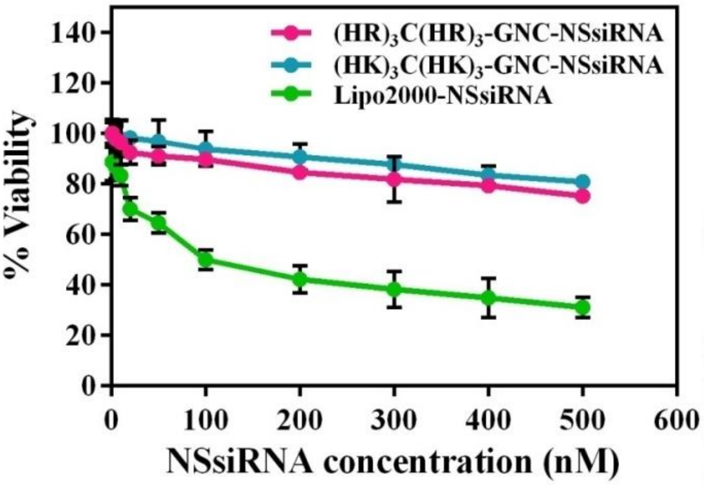

Figure 100: Cytocompatibility study of oligopeptide-gold nanocluster siRNA carrier compared with the commercially available lipofectamine siRNA carrier. Mean±s.d. (n=4).

4.3.7.3. Endosomal escape effect of oligopeptide-GNC-siRNA complex

As discussed, an efficient siRNA delivery vector should possess endosomal escape effect for delivering siRNA successfully to the cytoplasm of cells, where the RNAi machinery resides which helps in gene silencing along with siRNA. Upon entering the cells via endocytosis, the siRNA delivery vector should escape from the endosome before being fused with the lysosomes. Otherwise, the enzymes present in the acidic lysosomal compartment will degrade the siRNA before being released into the cytoplasm.

Figure 101 shows the endosomal escape of oligopeptide-gold nanocluster-siRNA complex in SK-BR-3 cells. The endo and lysosomal compartments in the cells were stained with Celllight early endosomes-GFP BacMam reagent and LysoTracker Green respectively. The co-localized signal (yellow) at 1 h incubation of oligopeptide-GNC-siRNA complex indicates both the $(HR)_3C(HR)_3$-GNC-NSsiRNA and $(HK)_3C(HK)_3$-GNC-NSsiRNA complex are present in the endosomal compartment. It is evident from the figure 101 that the separate green (LysoTracker Green) and red (GNC-siRNA complex) signal in cells indicates that these GNC-siRNA complexes did not enter lysosomes at this time point of incubation. After 4 h of incubation, the red fluorescence is seen near the perinuclear space in cytoplasm away from the green signal. This confirms that these GNC-siRNA complexes (red signal) are released into the cytoplasm from the endosomal compartments before being fused with the lysosomes (green signal).

The efficient endosomal escape effect is due to the fabrication of gold nanoclusters with more number of histidine amino acids. Histidine has excellent buffering capacity in acidic conditions (Bilalis P *et al*., 2016, P Sun *et al*., 2017). Hence, the fabrication of gold nanoclusters with histidine provided them high buffering capacity to induce “proton-sponge” effect inside the acidic endosomal compartments of cells. This “proton-sponge” caused swelling and bursting of endosome, rupturing the lipid bilayer membrane followed by the release of siRNA into cytoplasm. Thus these oligopeptide-gold nanoclusters were proved to act as an efficient siRNA delivery vector with excellent endosomal escape effect. In addition, the simultaneous tracking of siRNA delivery is also proved.

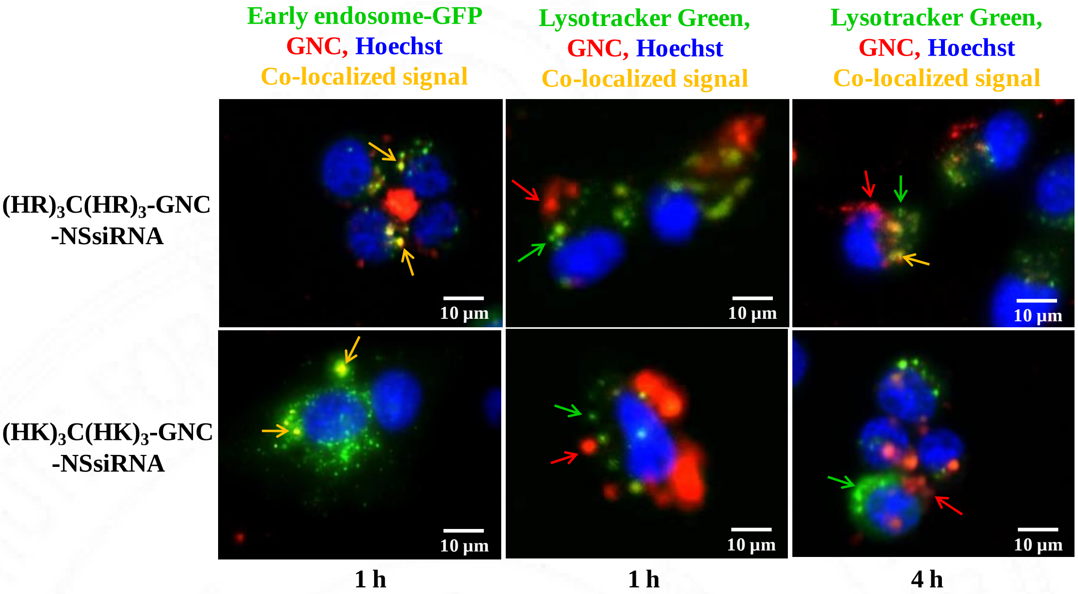

Figure 101: Fluorescent microscopic images showing the endosomal escape effect of oligopeptide-goldnanoclusters-siRNA complexes in SK-BR-3 cells at different time points.

4.3.8. Evaluation of survivin and Her2 overexpression in cancer cells

A number of studies have reported that survivin, an important member of the inhibitors of apoptosis protein family is highly overexpressed in most cancers and during foetal development, but is undetectable in terminally differentiated adult tissues (Uchida H *et al.*, 2004, Salzano G *et al.*, 2014, P Sun *et al.*, 2017). The expression of this survivin is closely correlated with the diagnosis, therapy, and prognosis of breast cancer. Hence, in breast cancer therapy, survivin gene is generally chosen as a target molecule as its inhibition can effectively induce tumour cell apoptosis which further suppress the growth of tumour. Here, the survivin expression in SK-BR-3 cells is evaluated using immunocytochemistry. Figure 102 shows the differential expression of survivin (green) in SK-BR-3 cells at different stages of cell cycle. In contrast, the WI-38 normal fibroblast cells showed negligible green fluorescence which indicates the under expression of survivin in these cells (figure 103).

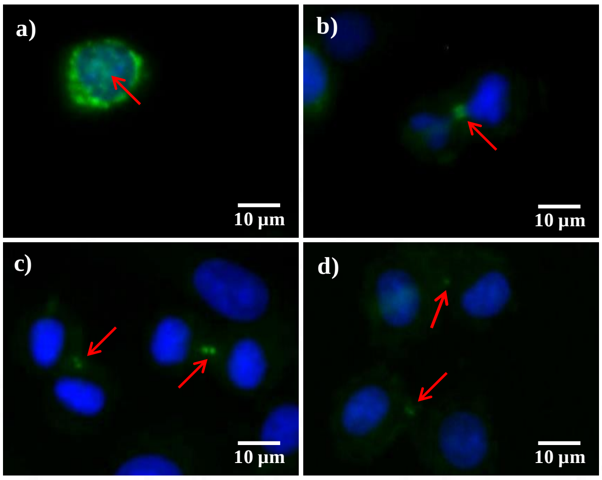

Figure 102: Fluorescent microscopic images showing the survivin over expression in SK-BR-3 cells at different stages of cell cycle: a) late prophase, b) anaphase, c) telophase, d) cytokinesis. Green and blue signals represent the survivin and nuclear staining respectively.

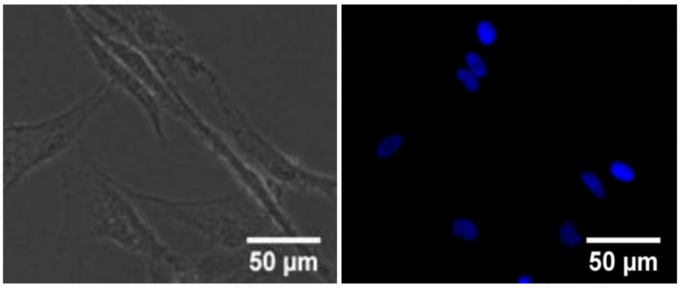

Figure 103: Fluorescent microscopic images showing the survivin under expression in WI-38 cells. Blue signal represent the nuclear staining with DAPI.

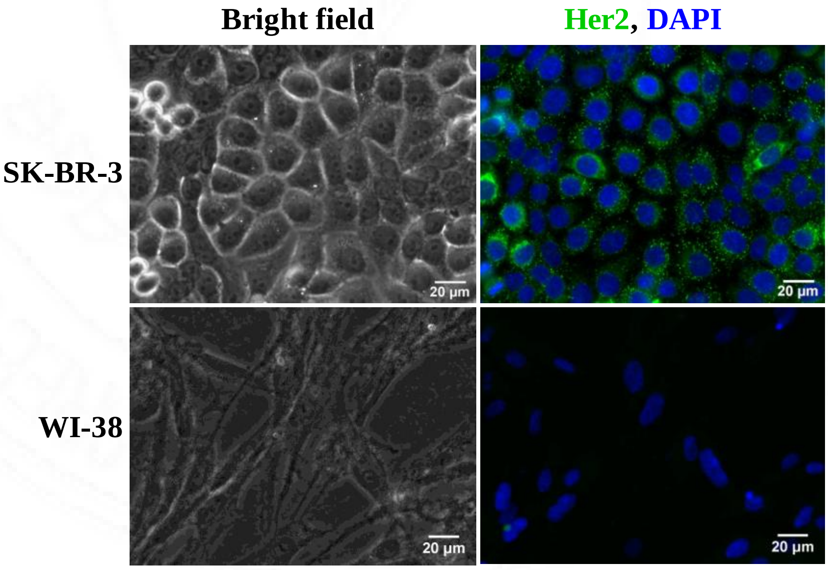

Figure 104: Fluorescent microscopic images showing the Her2 over and under expression in SK-BR-3 and WI-38 cells respectively. Green and blue signal represent the Her2 and nuclear staining with DAPI.

In addition to the survivin over expression, SK-BR-3 cells are reported to show over expressed Her2 (ERBB2) receptors in their cell surface (Ram *et al.*, 2014). Most of the breast cancer is reported to show over expression of Her2 with poor prognosis (Okarvi S *et al.*, 2018). Here, the over expression of Her2 in SK-BR-3 cancer cells compared with the WI-38 normal lung fibroblast cells were studied using immunocytochemistry. Figure 104 shows the overexpression of Her2 (green) in SK-BR-3 cells. In contrast, the WI-38 normal fibroblast cells showed negligible green fluorescence, which indicates the under expression of Her2 in these cells (figure 104).

4.3.9. Evaluation of gene silencing/knockdown by oligopeptide-GNC-siRNA complex

The knock down effect of oligopeptide-gold nanocluster-siRNA complexes was assessed by measuring survivin gene silencing in SK-BR-3 cells using qRT-PCR. The cells transfected with free SURsiRNA, Lipo2000-SURsiRNA, $(HR)_3C(HR)_3$-GNC-SURsiRNA, $(HK)_3C(HK)_3$-GNC-SURsiRNA, $(HR)_3C(HR)_3$-GNC-NSsiRNA and $(HK)_3C(HK)_3$-GNC-NSsiRNA with siRNA concentration of 100 nM for 48 h were analyzed for the quantitative survivin mRNA expression. Figure 105 shows the relative mRNA expression of survivin with respect to the homogenous control GAPDH using $2^{-\Delta\Delta Ct}$ method. The free SURsiRNA treated cells showed relatively low level of survivin mRNA expression (0.9), compared with the untreated control cells, which showed 1.07 level of survivin mRNA expression. From this, it is clear that the free-SURsiRNA caused 9 % survivin gene knockdown in cells after 48 h treatment. Lipo2000-SURsiRNA treated cells showed low level of survivin mRNA expression (0.47) with 53 % gene knockdown efficiency, which is very high than the free-SURsiRNA transfection method. Both $(HR)_3C(HR)_3$-GNC-SURsiRNA and $(HK)_3C(HK)_3$-GNC-SURsiRNA showed excellent gene silencing/knockdown effect of about 78 and 73 % respectively with very low level of survivin mRNA expression (0.22 and 0.27) in treated cells. These results confirmed the efficient siRNA delivery and knockdown efficiency of oligopeptide-gold nanocluster carriers. Compared with $(HK)_3C(HK)_3$-GNC-SURsiRNA, $(HR)_3C(HR)_3$-

GNC-SURsiRNA showed high gene silencing effect (figure 105) due to the increased cellular internalization shown by arginine fabricated gold nanoclusters than lysine fabricated gold nanoclusters (figure 99). The gene silencing results shown by different carriers correlated with the cellular uptake results. The non-specific siRNA complexed with both the GNCs showed negligible survivin gene knockdown in the treated cells. Overall, the oligopeptide-gold nanoclusters were proved as an excellent siRNA delivery carrier with increased cellular uptake and high gene knockdown efficiency compared with the commercially available lipofectamine mediated siRNA transfection.

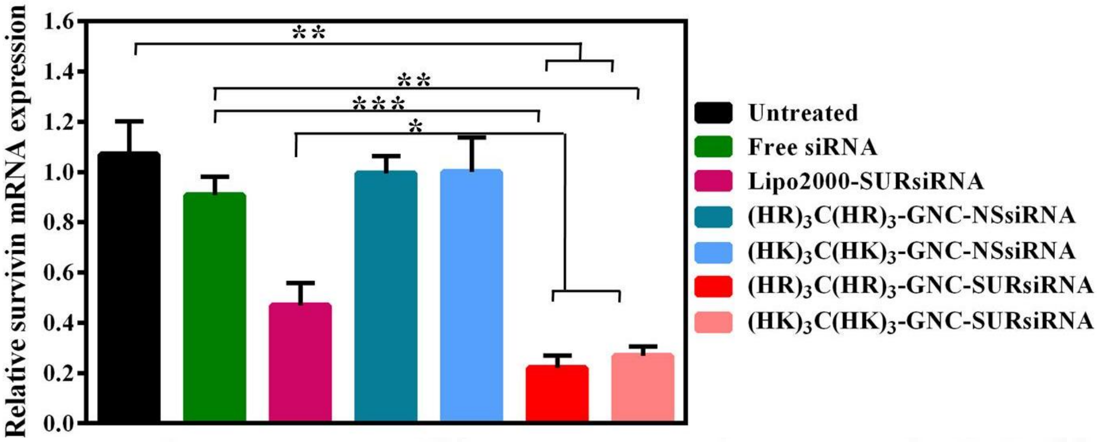

Figure 105: Relative mRNA expression of survivin in SK-BR-3 cells with different siRNA delivery vectors analyzed by qRT-PCR. Mean±s.d. (n=3), * $p < 0.05$, ** $p < 0.01$, *** $p < 0.001$.

4.3.10. Anti-migration or anti-metastatic effect of oligopeptide-GNC-siRNA complex

Inspired by the efficient gene silencing effect of oligopeptide-gold nanocluster-SURsiRNA complex, the after effects of survivin gene knockdown on SK-BR-3 cell migration was further evaluated by wound healing assay. The cells transfected with free SURsiRNA, $(HR)_3C(HR)_3$-GNC-SURsiRNA and $(HK)_3C(HK)_3$-GNC-SURsiRNA, with siRNA concentration of 100 nM were compared with untreated control cells. Figure 106 shows the migration of cells into the wound area in untreated, free-SURsiRNA, $(HR)_3C(HR)_3$-GNC-SURsiRNA and $(HK)_3C(HK)_3$-GNC-SURsiRNA incubated cells after 1, 24 and 48 h of treatment.

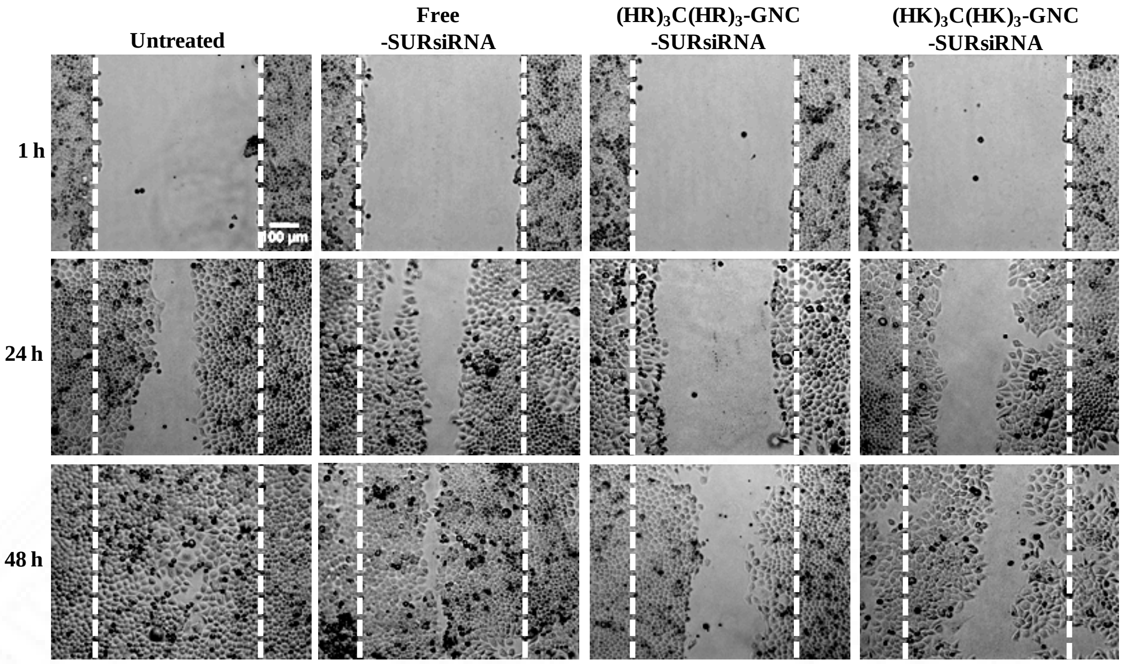

Figure 106: Wound healing assay showing the migration of SK-BR-3 cells after transfection with different survivin siRNA carriers for 1, 24 and 48 h. The dotted lines indicate the initial wound creation area in all cases.

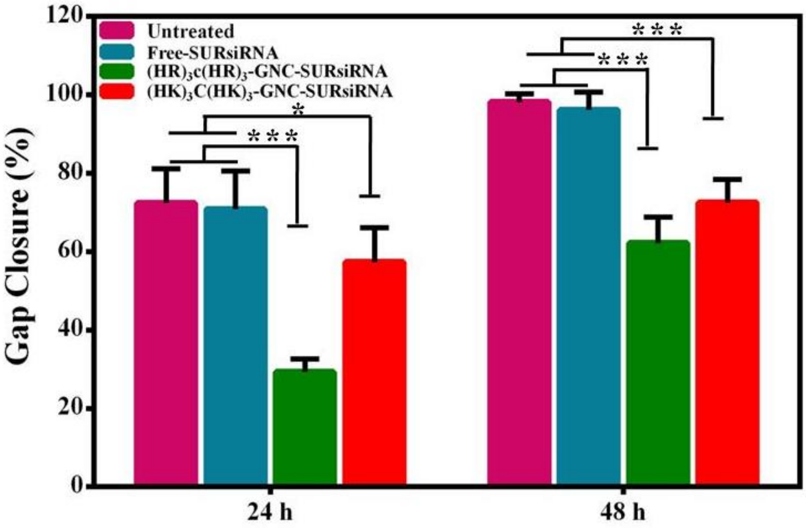

Figure 107: Extent of Gap closure % shown by SK-BR-3 cells in migration assay after 24 and 48 h treatment with GNC-SURsiRNA complexes and free-SURsiRNA. Mean±s.d. (n=5), * $p < 0.05$, *** $p < 0.001$.

After 24 h of treatment, the untreated and free-SURsiRNA treated cells showed increased migration into the wound area, and the wound is almost closed after 48 h of treatment. This indicates that the SK-BR-3 cells rapidly proliferated in these two groups. In contrast, $(HR)_3C(HR)_3$-GNC-SURsiRNA and $(HK)_3C(HK)_3$-

GNC-SURsiRNA treated cells showed less migration @ 24 h and the wound remained open even after 48 h treatment, indicating the cell proliferation is affected by the gene knockdown effect.

The extent of gap closure percentage after 24 and 48 h treatment was also quantified by randomly selecting 5 fields from each treatment. Figure 107 shows the percentage of gap closure with each treatment. Untreated cells showed around 72 % and 98 % of gap closure after 24 and 48 h treatment respectively, compared with free-SURsiRNA treated cells, which showed 70 and 90 % gap closure after 24 and 48 h treatment respectively. In contrast, the extent of gap closure in both the gold nanocluster-SURsiRNA complex is very low compared with the above two treatments. $(HK)_3C(HK)_3$-GNC-SURsiRNA showed 57 and 72 % of gap closure after 24 and 48 h treatment respectively, whereas $(HR)_3C(HR)_3$-GNC-SURsiRNA showed only 29 and 62 % of gap closure after 24 and 48 h treatment respectively. Hence, from these results it is clear that the effective survivin depletion caused by both the GNC-SURsiRNA complex inhibited the proliferation and migration of SK-BR-3 cells. $(HR)_3C(HR)_3$-GNC-SURsiRNA inhibited the migration of SK-BR-3 cells effectively than $(HK)_3C(HK)_3$-GNC-SURsiRNA, as these arginine fabricated gold nanoclusters showed increased cellular uptake than the latter one and hence their high gene knockdown efficiency which resulted in higher migration inhibition. Thus it is proved that these oligopeptide-gold nanocluster-SURsiRNA complexes showed anti-proliferative/anti-metastatic effect in SK-BR-3 cells.

4.3.11. Effect of oligopeptide-gold nanocluster-siRNA complex in inducing apoptosis

As the silencing of survivin expression in cancer cells is reported to induce apoptosis, it is expected that the survivin knockdown by oligopeptide-gold nanocluster-siRNA complex might also induce apoptosis in SK-BR-3 cells. Hence, the after effect of oligopeptide-gold nanocluster-siRNA complex in inducing apoptosis was evaluated by Dead Cell Apoptosis Kit with Annexin V Alexa Fluor® 488 & Propidium Iodide (PI). Phosphotidyl serine, a phospholipid component of cell membrane generally resides in the inner leaflet of cell membrane. In contrast with live cells, the early apoptotic cells are reported to translocate this phosphotidyl serine to outer leaflet (P Sun *et al.*, 2017) and this act as an apoptosis marker. Annexin V-Alexa Fluor® 488 specifically binds to this Phosphotidyl serine in outer leaflet of cell membrane, whereas PI enters the cell and stains the nucleus only if the cell membrane is damaged. Hence, the combined application of Annexin V- Alexa Fluor® 488 and PI helps in distinguishing live, early apoptotic, late apoptotic and necrotic cells. Even though phosphotidyl serine is found in the outer leaflet of early apoptotic cells, these cells do not lose membrane integrity and hence doesn't incorporate PI. But the late apoptotic cells and necrotic cells have membrane integrity loss and thus stain with PI. Thus, with Annexin V Alexa Fluor® 488 & PI staining, early apoptotic cells appear green, late apoptotic cells stain green and red and the necrotic cells appear with only red nuclear staining, as these cells do not have phosphotidyl serine in the outer leaflet of cell membrane.

Figure 108 shows the Annexin V- Alexa Fluor® 488 and PI staining of SK-BR-3 cells after 48 h exposure with free-SURsiRNA, $(HR)_3C(HR)_3$-GNC-SURsiRNA and $(HK)_3C(HK)_3$-GNC-SURsiRNA. From the figure 108, it is clear that both the untreated and free-SURsiRNA treated cells showed minimum number of early apoptotic cells (green cell membrane) after 48 h treatment, indicating the inefficiency of free-SURsiRNA to enter inside cells for inducing survivin gene knockdown. Both $(HR)_3C(HR)_3$-GNC-SURsiRNA and $(HK)_3C(HK)_3$-GNC-SURsiRNA treated cells showed large number of late apoptotic cells with green cell membrane and red nucleus. A minimum number of necrotic cells are also observed with both treatments. From the low magnification image (10X) of figure 108, it is clear that $(HR)_3C(HR)_3$-GNC-SURsiRNA induced more apoptosis with the appearance of large number of late apoptotic cells, whereas $(HK)_3C(HK)_3$-GNC-SURsiRNA showed more number of early apoptotic cells. This results correlates with the increased cellular uptake shown by arginine fabricated GNC-siRNA complex, resulted in increased apoptosis than the lysine fabricated GNC-siRNA complex. Hence it is proved that both these oligopeptide-GNC-siRNA complexes can efficiently induce apoptosis in SK-BR-3 cancer cells with survivin gene knockdown.

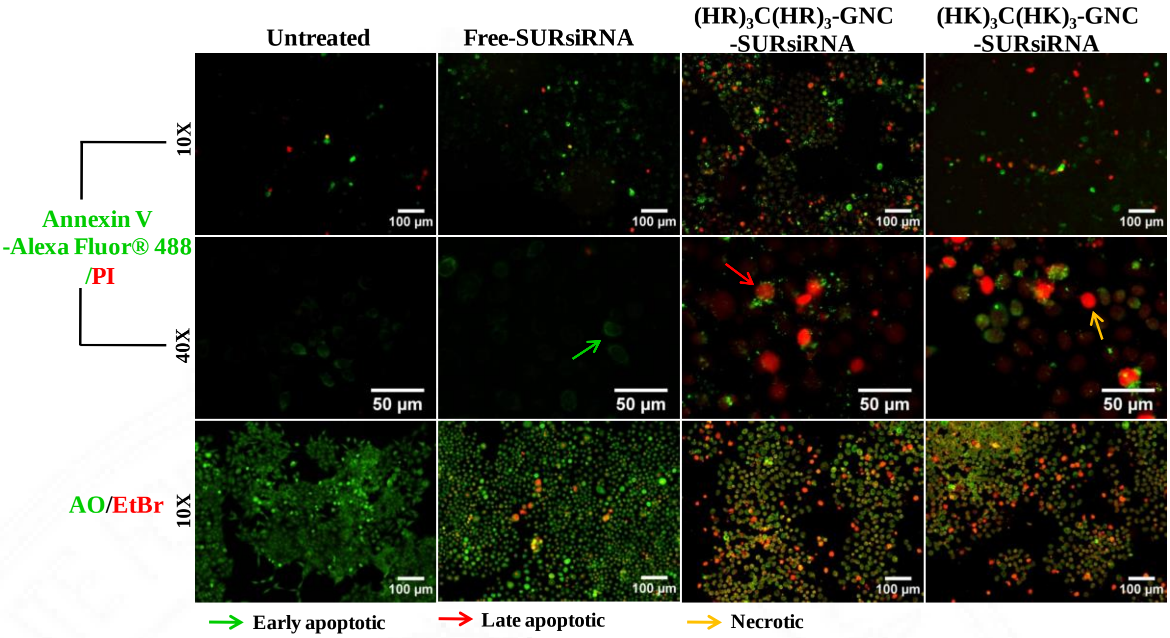

Figure 108: Fluorescence microscopic images of SK-BR-3 cells stained with Annexin-Alexa Fluor 488 & PI (low magnification-top and high magnification-bottom) and with acridine orange/ethidium bromide dual staining after 48 h of different SURsiRNA delivery transfection methods.

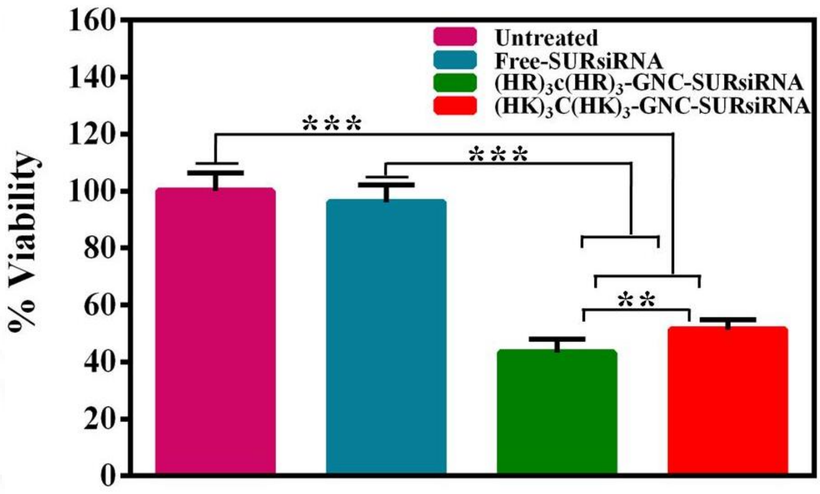

Figure 109: Quantitative cell viability percentage by MTT assay after 48 h treatment with different siRNA delivery carriers. Mean±s.d. (n=5), ** $p < 0.01$, *** $p < 0.001$.

In addition with apoptotic staining, the live dead analysis was done by dual staining with acridine orange and ethidium bromide. Acridine orange stains both live and dead cells, while ethidium bromide stains only dead cells which lost membrane integrity. Thus with this dual staining, live cells appear uniformly green, early apoptotic cells show green fluorescence with bright green dots in nucleus due to chromatin condensation, late apoptotic cells appear orange by ethidium bromide incorporation with condensed chromatin and necrotic cells appear uniformly orange with no chromatin condensation.

Figure 108 clearly show the appearance of large number of late apoptotic as well as necrotic cells in both oligopeptide-gold nanocluster-SURsiRNA treated cells, whereas a minimum number of early apoptotic cells is noted in untreated and free-SURsiRNA treated cells. The quantitative measurement of cell death after 48 h with respective treatment was also measured using MTT assay. The percentage viability of cells in figure 109 indicates the viable number of cells after each treatment. Both $(HR)_3C(HR)_3$-GNC-SURsiRNA and $(HK)_3C(HK)_3$-GNC-SURsiRNA treated cells showed high percentage of cell death compared with the untreated and free-SURsiRNA treated cells. 43 and 51 % of cell viability was observed with $(HR)_3C(HR)_3$-GNC-SURsiRNA and $(HK)_3C(HK)_3$-GNC-SURsiRNA treatment respectively. This result also correlates with the above apoptosis staining assay and live dead assay. $(HR)_3C(HR)_3$-GNC-SURsiRNA caused more cell death than $(HK)_3C(HK)_3$-GNC-SURsiRNA because of the increased cellular uptake, survivin gene knockdown efficiency shown by the former GNC-siRNA complex than the latter one. Hence it is confirmed that these oligopeptide-GNC-SURsiRNA complexes have excellent survivin siRNA delivering efficiency for knockdown induced apoptosis.

4.3.12. Evaluation of caspase 3/7 activity

Caspases are a family of cysteine proteases activated in response to diverse cell death stimuli. Caspases such as caspase-8, caspase-9 and caspase-10 are initiator caspases that activates executioner caspases (caspase-3, caspase-6 and caspase-7) (Shim M *et al.*, 2017, Walsh J *et al.*, 2008). As it is evident that the oligopeptide-GNC-SURsiRNA complexes induced apoptotic cell death, the activity of caspase 3/7 was measured to further confirm the mode of cell death. Figure 110 shows the caspase 3/7 activity in SK-BR-3 cells treated with free-SURsiRNA, $(HR)_3C(HR)_3$-GNC-SURsiRNA and $(HK)_3C(HK)_3$-GNC-SURsiRNA compared with the untreated control. Both untreated and free-SURsiRNA treated cells showed very low caspase 3/7 activity compared with the oligopeptide-GNC-SURsiRNA complexes. Both

$HR)_3C(HR)_3$-GNC-SURsiRNA and $(HK)_3C(HK)_3$-GNC-SURsiRNA complexes showed 3 fold increase in caspase 3/7 activity compared with the untreated and free-SURsiRNA treated cells, thus reconfirming the apoptotic mode of cell death.

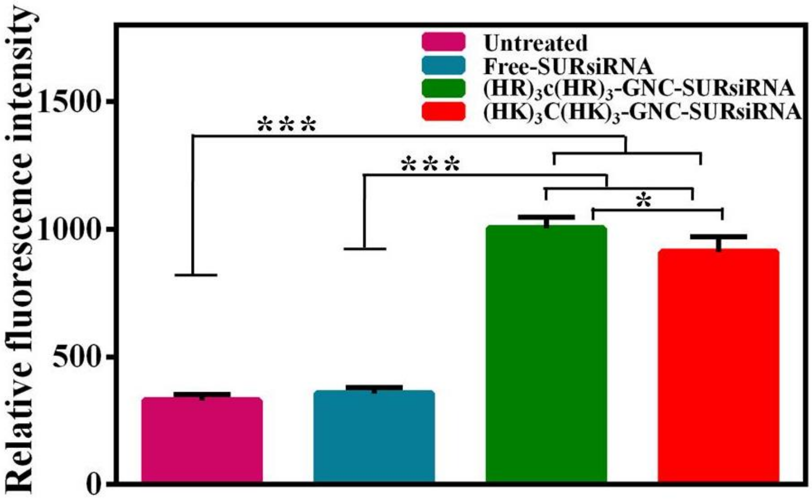

Figure 110: Relative fluorescent intensity showing caspase 3/7 activity in SK-BR-3 cells treated with different siRNA transfection methods. Mean±s.d. (n=5), * $p < 0.05$, *** $p < 0.001$.

4.3.13. Her2 conjugation to GNC-siRNA complex

Most of the cancer cells including SK-BR-3 cells are known to over expressed Her2 (ERBB2) receptors on their cell surface. Hence this Her2 receptor can be targeted with specific ligand (Her2) for targeted drug delivery specifically to cancer cells. To prove the targeted delivery of siRNA to cancer cells, here Her2 antibody was conjugated with GNC-siRNA complex. As $(HR)_3C(HR)_3$-GNC showed excellent siRNA delivery, this oligopeptide-GNC was chosen for Her2 conjugation. Figure 111 shows the UV-visible absorbance spectra of Her2 antibody, $(HR)_3C(HR)_3$-GNC-siRNA and $(HR)_3C(HR)_3$-GNC-Her2-siRNA complexes. Her2 antibody showed a peak at 280 nm, whereas $(HR)_3C(HR)_3$-GNC-siRNA showed peak at 260 nm. Conjugation of Her2 antibody to $(HR)_3C(HR)_3$-GNC-siRNA complex shifted the peak from 260 to 280 nm, thus confirming the successful conjugation of Her2 to GNC-siRNA complex.

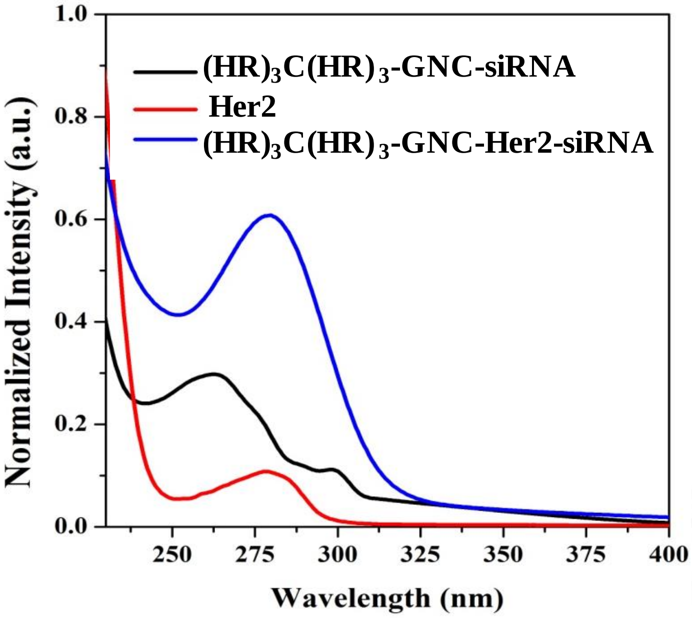

Figure 111: UV visible absorption spectra of Her2, $(HR)_3C(HR)_3$-GNC-siRNA and $(HR)_3C(HR)_3$-GNC-Her2-siRNA complex.

The conjugation of Her2 to GNC-siRNA complex was further confirmed with FTIR spectroscopy. Figure 112 shows the FTIR spectra of $(HR)_3C(HR)_3$-GNC-siRNA and $(HR)_3C(HR)_3$-GNC-Her2-siRNA complex. The strong peaks @ 1644 cm^{-1} and 1569 cm^{-1} in $(HR)_3C(HR)_3$-GNC-Her2-siRNA complex compared to $(HR)_3C(HR)_3$-GNC-siRNA indicates the additional amide I band (C=O) and amide II band (N-H) from successful Her2 conjugation.

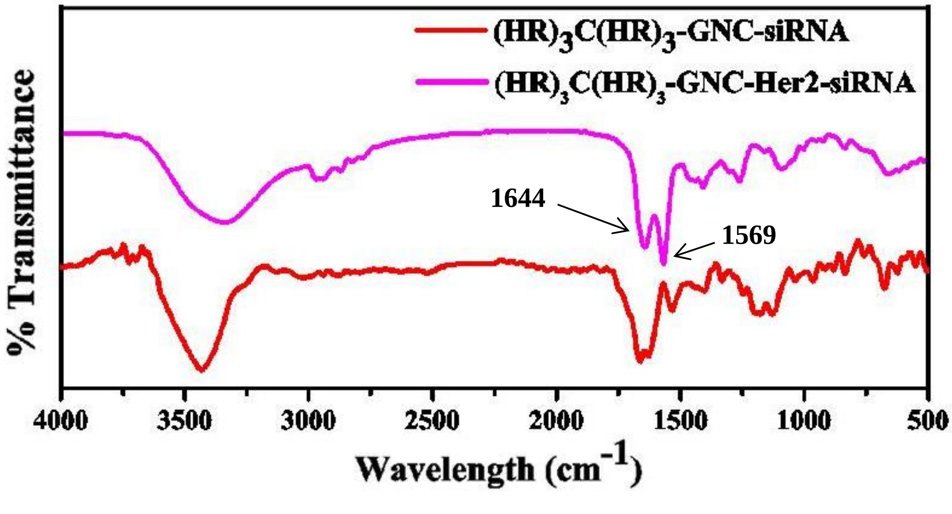

Figure 112: FTIR spectra of $(HR)_3C(HR)_3$-GNC-siRNA and $(HR)_3C(HR)_3$-GNC-siRNA-Her2 complexes.

4.3.14. Evaluation of GNC-Her2-siRNA complex uptake in co-culture model

For successful siRNA based cancer therapy, an efficient siRNA delivery vector should not only induce gene knockdown but also it should deliver siRNA specifically to cancer cells without affecting the surrounding normal cells. Hence to prove the cancer targeting specificity of $(HR)_3C(HR)_3$-GNC-Her2-siRNA complex, a co-culture model was established using SK-BR-3 cancer cells and WI-38 normal cells with an optimized ratio of 1:3. Figure 113 shows the cellular uptake of $(HR)_3C(HR)_3$-GNC-Her2-siRNA complex. The bright field image in figure 113 shows the morphology of co-cultured cells, in which the more elongated cells represents WI-38 normal cells and the slightly rounded cells represent SK-BR-3 cancer cells. The cellular internalization of $(HR)_3C(HR)_3$-GNC-Her2-siRNA complex is observed only in SK-BR-3 cells showing red fluorescence from GNC, whereas WI-38 normal cells showed negligible red fluorescence. Thus these results confirms the cancer targeting specificity of $(HR)_3C(HR)_3$-GNC-Her2-siRNA complex.

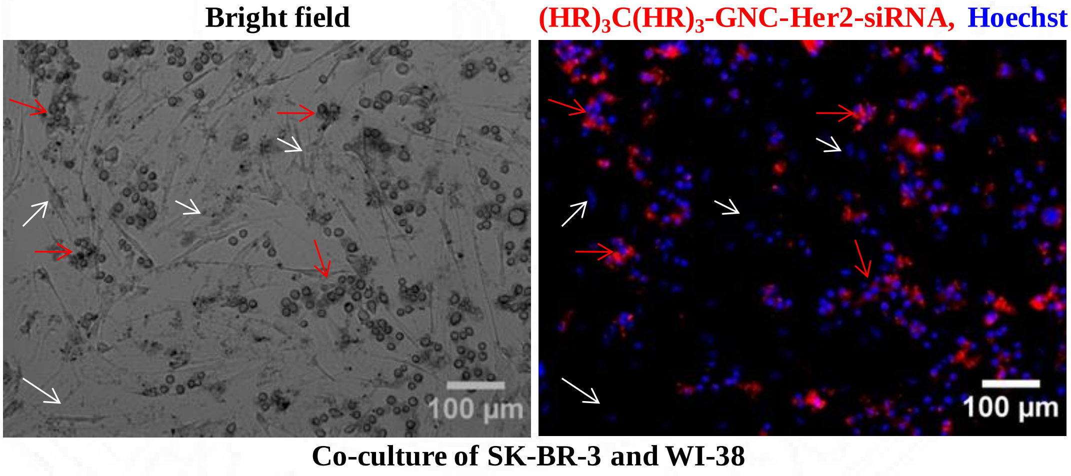

Figure 113: Evaluation of GNC-Her2-siRNA complex uptake in co-culture model. Red and white arrow indicates SK-BR-3 cells and WI-38 cells respectively.

Therefore, it is confirmed that the fluorescent nano gene downregulator developed with a complex of oligopeptide-gold nanoclusters, survivin siRNA and Her2 antibody act as a bioimaging as well as therapeutic agent. In detail, the fluorescent nano gene downregulator specifically targeted cancer cells, downregulated the overexpressed gene with efficient siRNA delivery, which was tracked simultaneously using fluorescence imaging and induced apoptotic cell death in cancer cells. Hence, the image guided cancer gene therapy of nano gene downregulator is confirmed *in vitro*.

CHAPTER 5: SUMMARY AND CONCLUSION

5. SUMMARY AND CONCLUSION

5.1. SUMMARY

Fluorescence imaging finds special attraction in biomedical field as it is non-invasive, selective, sensitive, less hazardous, rich in contrast, rapid signal acquisition ability and so on. But the main barrier for fluorescence imaging is the autofluorescence from endogenous molecules (mostly emit in blue and green fluorescence) of tissues which hinder with the desired signal visualization. Thus fluorescent probes with red emission are preferable for biological imaging. Over the years, different fluorescent molecular probes (organic dyes) were developed for various biological applications. Nowadays, fluorescent nanoprobes are replacing the organic dyes because of its several advantages. The thesis deals with the application of fluorescent molecular and nanoprobes in the field of biosensing, bioimaging and therapy. The fluorescent molecular probe mentioned in the first part of study is a Zn^{2+} sensor, bipyridine bridged bispyrrole probe, which is used for simultaneous Zn^{2+} sensing and imaging. The fluorescent nanoprobe mentioned in the second and third part of the study is gold nanocluster (tripeptide and oligopeptide stabilized gold nanoclusters), which is used for simultaneous cancer imaging and therapy.

The thesis “Design and fabrication of fluorescent probes for biomedical applications: potential tool for *in vitro* and *in vivo* bioimaging, sensing and siRNA delivery for cancer therapy” consists of three main sections: the bioimaging and sensing potential of a fluorescent ratiometric molecular probe and the exploitation of this probe to study the Zn^{2+} dynamics under epileptic condition *in vitro* and *in vivo,* development of fluorescent nanoprobe for cancer imaging cum therapy and development of fluorescent nano gene downregulator for cancer imaging cum therapy.

The first section is focused on studying the optical properties of fluorescent molecular probe, bipyridine bridged bispyrrole (BP) in physiological buffer condition, whose green emission upon Zn^{2+} binding shifts to red. The cellular imaging, Zn^{2+} sensing and ratiometric imaging potential of BP were studied in C6 glioma cells with the addition of exogenous Zn^{2+}. The endogenous Zn^{2+} sensing and the ratiometric imaging potential of BP in hippocampal slices were also confirmed. The dynamics of Zn^{2+} under neuropathological condition was also studied using BP in chemically stimulated epileptic hippocampal slices. The *in vivo* brain Zn^{2+} quantification and imaging was also proved by BP. BP is a dual function molecular probe with its change in emission from green to red upon Zn^{2+} binding which allows clear visualization of Zn^{2+} sensing, avoids autofluorescence and the ratiometric imaging potential shown by BP allows quantification of Zn^{2+} eliminating the artifacts from fluorescence imaging. Finally, the deep tissue imaging potential of BP is also proved *in vivo*. To summarize, the bioimaging cum sensing efficiency of molecular probe is proved *in vitro* and *in vivo*.

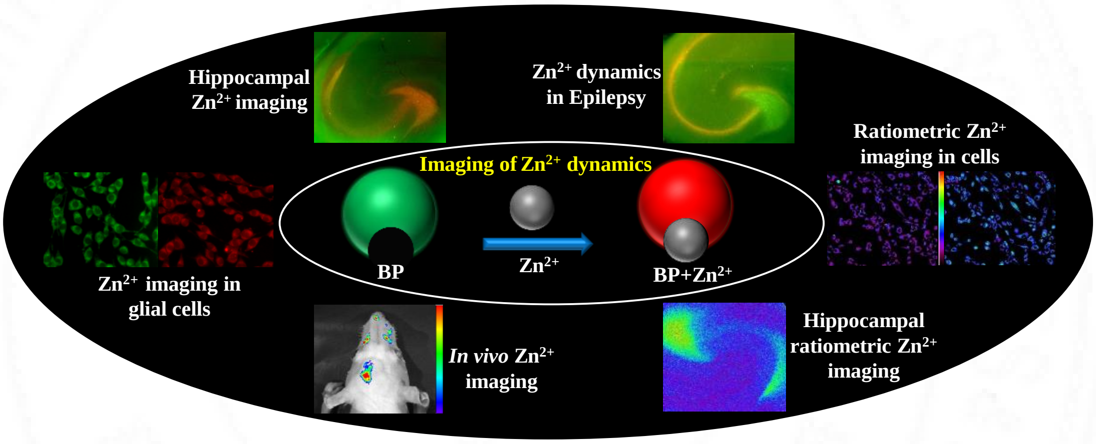

Figure 114 depicts the summary of fluorescent molecular probe property and its application

The second section is focused on the design and development of fluorescent tripeptide stabilized gold nanoclusters for simultaneous cancer imaging and therapy. Six different tripeptides were designed and synthesized towards this namely, DCG, DCS, DCH, SCG, HCS and HCG. These custom designed tripeptides were used to prepare gold nanoclusters (DCG-GNC, DCS-GNC, DCH-GNC, SCG-GNC, HCS-GNC and HCG-GNC) with different emission properties in near red region to overcome autofluorescence. All these tripeptide-gold nanoclusters have ultra small size, excellent red and near red fluorescent property, high quantum yield, long fluorescence lifetime, photostability, non-toxicity and good cellular internalization potential. Hence all the tripeptide-gold nanoclusters act as outstanding bioimaging agent. The cellular interaction of these tripeptide-gold nanoclusters was studied in different cancer cell lines. The cellular internalization of tripeptide-gold nanoclusters is highly influenced by their surface charge and different cell type. Irrespective of cell type, the internalization and accumulation efficiency is high for positively charged gold nanoclusters than negatively charged gold nanoclusters. Accordingly, the accumulation percentage was found to be HCG-GNC > HCS-GNC > DCH-GNC > SCG-GNC > DCG-GNC > DCS-GNC. These tripeptide-gold nanoclusters have limited dark toxicity but exert photoinduced ROS generation in cancer cells with 532 nm laser irradiation, leading to mitochondrial membrane potential loss followed by photoinduced cell death. Thus these tripeptide-gold nanoclusters can itself act as an efficient photosensitizer for photodynamic therapy (PDT). Also compared with all the cancer cells, the toxicity of tripeptide-gold nanoclusters in WI-38 normal cells is very low. This clearly indicates the increased uptake and accumulation of these tripeptide-gold nanoclusters in cancer cells due to high metabolic activity of cancer cells *in vitro*, while it is negligible in normal cells. This might be an added advantage for efficient cancer cell PDT without affecting normal cells *in vivo* due to the fact that *in vivo* cancer cells have enhanced permeation and retention (EPR) effect. To summarize, the image guided PDT efficiency of tripeptide-gold nanoclusters was confirmed *in vitro*.

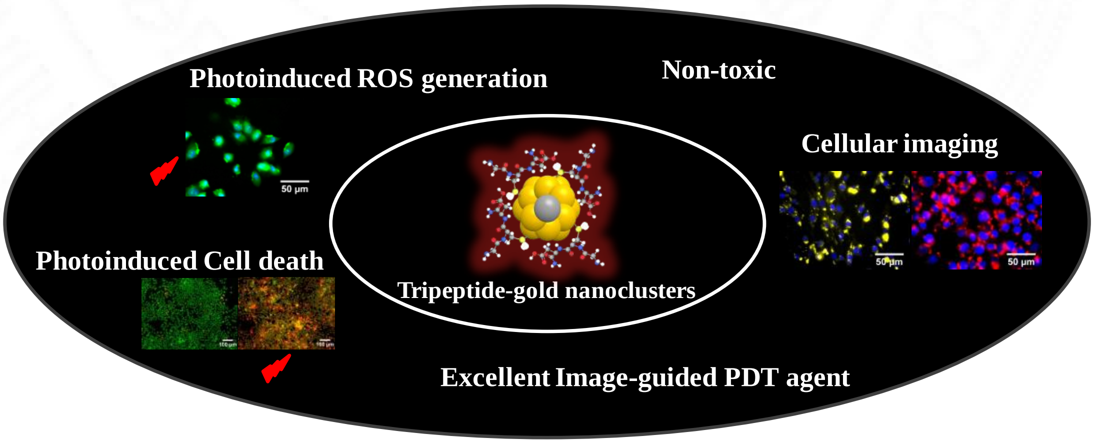

Figure 115 depicts the summary of fluorescent nano probe property and its application

The third section is focused on the design and development of fluorescent nano gene downregulator for simultaneous cancer imaging cum siRNA based cancer therapy. Three different oligopeptides namely $(HR)_3C(HR)_3$, $(HK)_3C(HK)_3$ and $(H)_3C(H)_3$ were designed and synthesized towards this with positive charge amino acids histidine, arginine and lysine. These custom designed oligopeptides were used to prepare gold nanoclusters [$(HR)_3C(HR)_3$-GNC, $(HK)_3C(HK)_3$-GNC and $(H)_3C(H)_3$-GNC] with different emission properties in near red region to overcome autofluorescence and to provide sufficient positive charge for the complexation of siRNA. The oligopeptide-gold nanoclusters have ultra small size, excellent red fluorescent property, high quantum yield, long fluorescence lifetime, photostability, non-toxicity and good cellular internalization efficiency. Hence, all these oligopeptide-gold nanoclusters act as outstanding bioimaging agents. The cellular internalization and accumulation percentage highly depends on their surface charge and hence the accumulation percentage was found to be $(HR)_3C(HR)_3$-GNC > $(HK)_3C(HK)_3$-GNC > $(H)_3C(H)_3$-GNC. As these oligopeptide-gold nanoclusters are fabricated with positively charged amino acids, the complexation with negative charge siRNA is effectively achieved. The complexation of siRNA to oligopeptide-gold nanoclusters was confirmed with FTIR and XPS. $(HR)_3C(HR)_3$-GNC and $(HK)_3C(HK)_3$-GNC have high loading capacity of siRNA because of their increased positive surface charge than $(H)_3C(H)_3$-GNC. It is found that per gram of both these oligopeptide-gold nanoclusters can carry 301 µmol of siRNA, which is very high than the reported siRNA delivery vectors so far. Both these oligopeptide-gold nanoclusters efficiently deliver siRNA into the cytoplasm of cells compared with commercially available lipofectamine 2000 reagent. Both these oligopeptide-gold nanoclusters complexed with siRNA showed excellent endosomal escape effect, which was tracked simultaneously and it showed efficient survivin gene knockdown ability than lipofectamine2000 reagent. The anti-metastatic effect in cancer cells shown by these nano gene downregulator is much appreciable. Apoptosis induction in cancer cells with increased caspase 3/7 activity by these nano gene downregulator is also proved *in vitro.* Also, these fluorescent nano gene downregulator specifically targeted cancer cells for its mechanism of action in presence of normal cells. Hence, the fluorescent nano gene downregulator constructed using these oligopeptide-gold nanoclusters, survivin siRNA and Her2 antibody is suitable for breast cancer targeting, imaging and simultaneous RNAi therapy. To summarize, the image guided siRNA delivery and cancer gene therapy of fluorescent nano gene downregulator is confirmed *in vitro*.

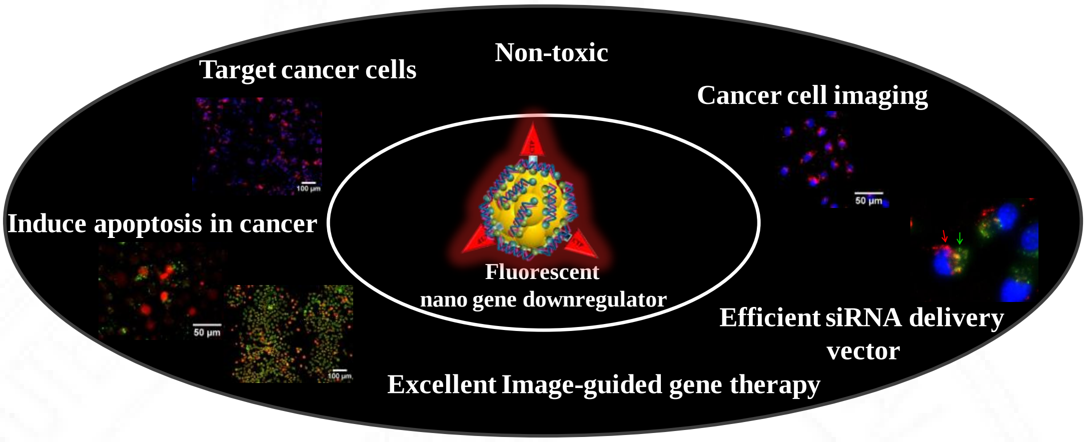

Figure 116 depicts the summary of fluorescent nano gene downegulator property and its application

5.2. CONCLUSION

To conclude, fluorescent molecular and nanoprobes were developed with desirable properties for various biomedical applications like bioimaging, sensing and therapy. Fluorescent ratiometric molecular probe was used to sense, quantify and study the dynamic of zinc ions with dual function of fluorescence and ratiometric imaging under neuropathological condition. Fluorescent nanoprobes (tripeptide-gold nanoclusters) were developed and used for simultaneous cancer imaging and photodynamic therapy. A novel fluorescent nano gene downregulator was developed and used for targeted cancer imaging, combined siRNA delivery cum tracking and cancer gene therapy. The thesis starts with the use of basic fluorescent molecular probe for bioimaging and sensing and ends with an advanced fluorescent nanoprobe for bioimaging and futuristic gene therapy for cancer. The future perspective of the study is to make these fluorescent probes available for clinical application along with the *in vivo* study. The future perspective also includes the further characterization of gold nanoclusters to uncover the position of silver doping and to study the exact mechanism of fluorescence enhancement in these nanoprobes.

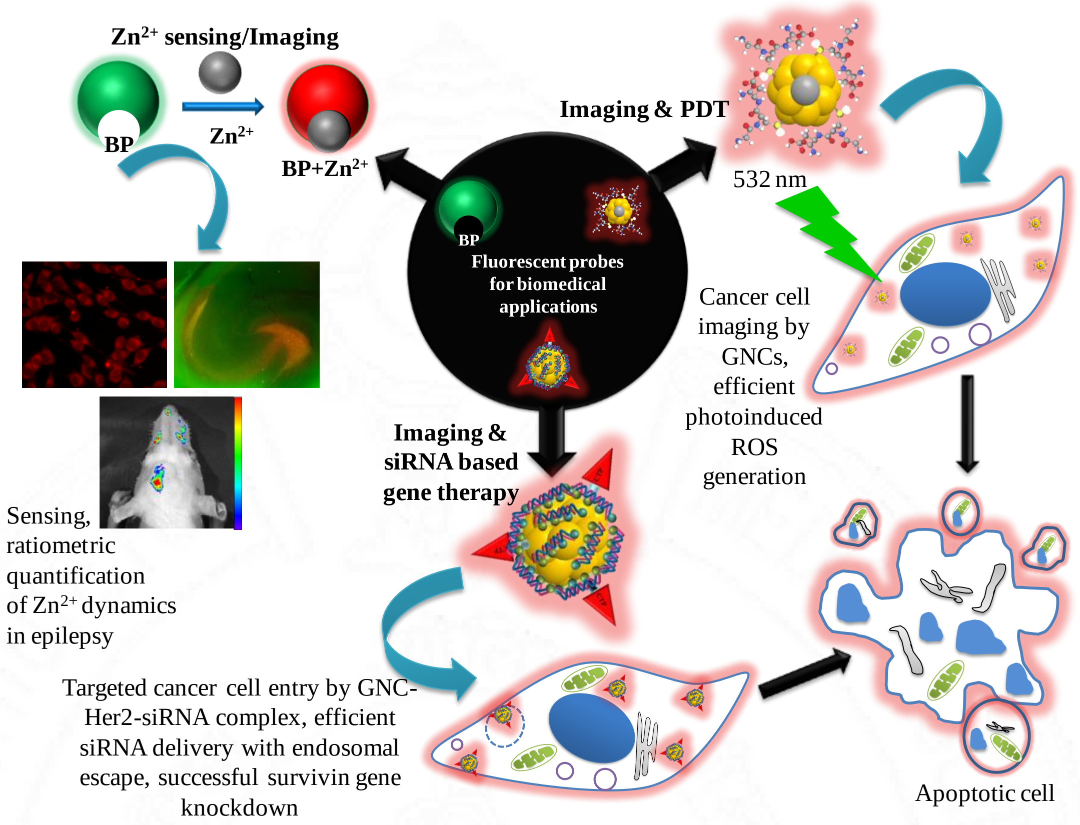

Figure 117 Illustration showing potential biomedical applications of fluorescent probes used in this study

BIBLIOGRAPHY

Ajayaghosh A, Carol P, Sreejith S (2005) A Ratiometric Fluorescence Probe for Selective Visual Sensing of Zn^{2+}. *J. Am. Chem. Soc*. 127: 14962-14963.

Ameres S, Martinez J, Schroeder R (2007) Molecular Basis for Target RNA Recognition and Cleavage by Human RISC. *Cell*. 130: 101-112.

Annie Ho J, Chang H, Su W (2012) DOPA-Mediated Reduction Allows the Facile Synthesis of Fluorescent Gold Nanoclusters for Use as Sensing Probes for Ferric Ions. *Anal. Chem*., 84: 3246-3253.

Baral A, Basu K, Ghosh S, Bhattacharyya K, Roy S, Datta A, Banerjee A (2017) Size specific emission in peptide capped gold quantum clusters with tunable photoswitching behavior. *Nanoscale*. 9: 4419-4429.

Behzadi S, Serpooshan V, Tao W, Hamaly M, Alkawareek M, Dreaden E, Brown D, Alkilany A, Farokhzad O, Mahmoudi M (2017) Cellular uptake of nanoparticles: journey inside the cell. *Chem. Soc. Rev*. 46: 4218-4244.

Bi F, Yin H, Zheng S, Zhu Q, Yang H, Kang M, Gan F, Chen X (2016) One-step synthesis of peptide conjugated gold nanoclusters for the high expression of FGFR2 tumor targeting and imaging. RSC Adv. 6: 4627-4633.

Bilalis P, Tziveleka L, Varlas S, Iatrou H (2016) pH-Sensitive nanogates based on poly(l-histidine) for controlled drug release from mesoporous silica nanoparticles. *Polym. Chem.* 7: 1475-1485.

Borges K (2003) Neuronal and glial pathological changes during epileptogenesis in the mouse pilocarpine model. *Exp. Neurol.* 182: 21-34.

Bozym R, Thompson R, Stoddard A, Fierke C (2006) Measuring Picomolar Intracellular Exchangeable Zinc in PC-12 Cells Using a Ratiometric Fluorescence Biosensor. *ACS Chem. Biol*. 1: 103-111.

Broekgaarden M, Bulin A, Porret E, Musnier B, Chovelon B, Ravelet C, Sancey L, Elleaume H, Hainaut P, Coll J, Le Guével X (2020) Surface functionalization of gold nanoclusters with arginine: a trade-off between microtumor uptake and radiotherapy enhancement. *Nanoscale.* 12: 6959-6963.

Buskila Y, Breen P, Tapson J, Van Schaik A, Barton M, Morley J (2014) Extending the viability of acute brain slices. *Sci Rep.* 4: 5309.

Calixto G, Bernegossi J, de Freitas L, Fontana C, Chorilli M (2016) Nanotechnology-Based Drug Delivery Systems for Photodynamic Therapy of Cancer: A Review. *Molecules.* 21: 342.

Chen H, Li B, Wang C, Zhang X, Cheng Z, Dai X, Zhu R, Gu Y (2013) Characterization of a fluorescence probe based on gold nanoclusters for cell and animal imaging. *Nanotechnology*, 24: 055704.

Chen W, Lan G, Chang H (2011) Use of Fluorescent DNA-Templated Gold/Silver Nanoclusters for the Detection of Sulfide Ions. *Anal. Chem.* 83: 9450-9455.

Chertok B, David A, Yang V (2010) Polyethyleneimine-modified iron oxide nanoparticles for brain tumor drug delivery using magnetic targeting and intra-carotid administration. *Biomaterials*. 31: 6317-6324.

Chien C, Liu C, Wu Z, Chen P, Chu C, Lin S (2014) Co-caged gold nanoclusters and methyl motifs lead to detoxification of dendrimers and allow cytosolic access for siRNA transfection. *J. Mater. Chem. B.* 2: 6730-6737.

Choi D, Koh J (1998) Zinc and brain injury. *Annu Rev Neurosci*. 21: 347-75.

Coin I, Beyermann M, Bienert M (2007) Solid-phase peptide synthesis: from standard procedures to the synthesis of difficult sequences. *Nat Protoc*. 2: 3247-3256.

Cui H, Hu D, Zhang J, Gao G, Zheng C, Gong P, Xi X, Sheng Z, Cai L (2017) Theranostic gold cluster nanoassembly for simultaneous enhanced cancer imaging and photodynamic therapy. *Chin. Chem. Lett*. 28: 1391-1398.

De Leon-Rodriguez L, Lubag A, Dean Sherry A (2012) Imaging free zinc levels *in vivo* – What can be learned?. *Inorganica Chim. Acta.* 393: 12-23.

DeWitt J, Sandrasegaran K, O'Neil B, House M, Zyromski N, Sehdev A, Perkins S, Flynn J, McCranor L, Shahda S (2019) Phase 1 study of EUS-guided photodynamic therapy for locally advanced pancreatic cancer. *Gastrointest. Endosc*. 89: 390-398.

Divya K, Sreejith S, Ashokkumar P, Yuzhan K, Peng Q, Maji S, Tong Y, Yu H, Zhao Y, Ramamurthy P, Ajayaghosh A (2014) A ratiometric fluorescent molecular probe with enhanced two-photon response upon Zn^{2+} binding for *in vitro* and *in vivo* bioimaging. *Chem. Sci*. 5: 3469-3474.

Dudek F (2001) Zinc and Epileptogenesis. *Epilepsy Curr*. 1: 66-70.

Dykxhoorn D, Lieberman J (2006) Knocking down Disease with siRNAs. *Cell.* 126: 231-235.

Foley C, Rubin D, Santillan A, Sondhi D, Dyke J, Pierre Gobin Y, Crystal R, Ballon D (2014) Intra-arterial delivery of AAV vectors to the mouse brain after mannitol mediated blood brain barrier disruption. *J Control Release*. 196: 71-78.

Franklin R, Costello L (2009) The important role of the apoptotic effects of zinc in the development of cancers. *J. Cell. Biochem.* 106: 750-757.

Frederickson C, Danscher G (1990) Zinc-containing neurons in hippocampus and related CNS structures. *Prog Brain Res*. 83: 71-84.

Frederickson C, Giblin L, Balaji R, Masalha R., Frederickson C, Zeng Y, Lopez E, Koh J, Chorin U, Besser L, Hershfinkel M, Li Y, Thompson R, and Krężel A (2006) Synaptic release of zinc from brain slices: Factors governing release, imaging, and accurate calculation of concentration *J. Neurosci. Meth. 154*:19–29.

Frederickson C, Kasarskis E, Ringo D, Frederickson R (1987) A quinoline fluorescence method for visualizing and assaying the histochemically reactive zinc (bouton zinc) in the brain. *J. Neurosci. Methods.* 20: 91-103.

Frederickson C, Koh J, Bush A (2005) The neurobiology of zinc in health and disease. *Nat. Rev. Neurosci.* 6: 449-462.

Fukahori M, Itoh M (1990) Effects of dietary zinc status on seizure susceptibility and hippocampal zinc content in theEl (epilepsy) mouse. *Brain Res*. 529: 16-22.

Gee K, Zhou Z, Qian W, Kennedy R (2002) Detection and Imaging of Zinc Secretion from Pancreatic β-Cells Using a New Fluorescent Zinc Indicator. *J. Am. Chem. Soc*. 124: 776-778.

Ghavami S, Hashemi M, Ande S, Yeganeh B, Xiao W, Eshraghi M, Bus C, Kadkhoda K, Wiechec E, Halayko A, Los M (2009) Apoptosis and cancer: mutations within caspase genes. *J. Med. Genet*. 46: 497-510.

Giljohann D, Seferos D, Prigodich A, Patel P, Mirkin C (2009) Gene Regulation with Polyvalent siRNA−Nanoparticle Conjugates. *J. Am. Chem. Soc*. 131: 2072-2073.

Grabrucker A, Knight M, Proepper C, Bockmann J, Joubert M, Rowan M, Nienhaus G, Garner C, Bowie J, Kreutz M, Gundelfinger E, Boeckers T (2011). Concerted action of zinc and ProSAP/Shank in synaptogenesis and synapse maturation. *EMBO J.* 30: 569-581.

Guo Y, Wang Z, Shao H, Jiang X (2012) Stable fluorescent gold nanoparticles for detection of Cu^{2+} with good sensitivity and selectivity. *Analyst.* 137: 301-304.

Guo Y, Zhao X, Long T, Lin M, Liu Z, Huang C (2015) Histidine-mediated synthesis of chiral fluorescence gold nanoclusters: insight into the origin of nanoscale chirality. *RSC Adv*. 5: 61449-61454.

Guo Z, Kim G, Shin I, Yoon J (2012) A cyanine-based fluorescent sensor for detecting endogenous zinc ions in live cells and organisms. *Biomaterials.* 33: 7818-7827.

Han R, Zhao M, Wang Z, Liu H, Zhu S, Huang L, Wang Y, Wang L, Hong Y, Sha Y, Jiang Y (2019) Super-efficient *in vivo* Two-Photon Photodynamic Therapy with a Gold Nanocluster as a Type I Photosensitizer. *ACS Nano.* 14: 9532-9544.

Hong E, Choi D, Shim M (2016) Targeted and effective photodynamic therapy for cancer using functionalized nanomaterials. *Acta Pharm. Sin. B.* 6: 297-307.

Houser C, Esclapez M (2003) Downregulation of the α5 subunit of the GABAA receptor in the pilocarpine model of temporal lobe epilepsy. *Hippocampus.* 13: 633-645.

Huang E (1997) Metal ions and synaptic transmission: Think zinc. *Proc Natl Acad Sci*. 94: 13386-13387.

Huang Y, Pan E, Xiong Z, McNamara J (2008) Zinc-Mediated Transactivation of TrkB Potentiates the Hippocampal Mossy Fiber-CA3 Pyramid Synapse. *Neuron,* 57: 546-558.

Huschka R, Barhoumi A, Liu Q, Roth J, Ji L, Halas N (2012) Gene Silencing by Gold Nanoshell-Mediated Delivery and Laser-Triggered Release of Antisense Oligonucleotide and siRNA. *ACS Nano*. 6: 7681-7691.

Islam N, Wang H, Maqbool F, Ferro V (2019). *In Vitro* Enzymatic Digestibility of Glutaraldehyde-Crosslinked Chitosan Nanoparticles in Lysozyme Solution and Their Applicability in Pulmonary Drug Delivery. *Molecules*. 24: 1271.

Jandova K, Pasler D, Antonio L, Raue C, Ji S, Njunting M, Kann O, Kovacs R, Meencke H, Cavalheiro E, Heinemann U, Gabriel S, Lehmann T (2006) Carbamazepine-resistance in the epileptic dentate gyrus of human hippocampal slices. *Brain*. 129: 3290-3306.

Jha K, Shukla M, Pandey M (2012) Survivin expression and targeting in breast cancer. *Surg. Oncol*. 21: 125-131.

Jiang M (2003) Bcl-2 constitutively suppresses p53-dependent apoptosis in colorectal cancer cells. *Genes Dev*., 17: 832-837.

Jin R, Qian H, Wu Z, Zhu Y, Zhu M, Mohanty A, Garg N (2010) Size Focusing: A Methodology for Synthesizing Atomically Precise Gold Nanoclusters. *J. Phys. Chem. Lett*. 1: 2903-2910.

Kapara A, Brunton V, Graham D, Faulds K (2020) Investigation of cellular uptake mechanism of functionalised gold nanoparticles into breast cancer using SERS. *Chem. Sci*. 11: 5819-5829.

Ketterman J, Li Y (2008) Presynaptic evidence for zinc release at the mossy fiber synapse of rat hippocampus. J Neurosci Res. 86: 422-434.

Kim J, Jang B, Choi B, Kwon L, Sohn M, Song H, Suh S (2012) Zinc Chelation Reduces Hippocampal Neurogenesis after Pilocarpine-Induced Seizure. PLoS One, 7: e48543.

Kim J, Jang D (2017) Metal-enhanced fluorescence of gold nanoclusters adsorbed onto Ag@SiO_2 core–shell nanoparticles. *J. Mater. Chem. C*. 5: 6037-6046.

Kim J, Lee C, Lim S, Adhikari A, Andring J, McKenna R, Ghim C, Kim C (2020) Elucidating the role of metal ions in carbonic anhydrase catalysis. *Nat. Commun.* 11: 4557.

Klitgaard H, Matagne A, Grimee R, Vanneste-Goemaere J, Margineanu D (2003) Electrophysiological, neurochemical and regional effects of levetiracetam in the rat pilocarpine model of temporal lobe epilepsy. *Seizure*. 12: 92-100.

Kodirov S, Takizawa S, Joseph J, Kandel E, Shumyatsky G, Bolshakov V (2006) Synaptically released zinc gates long-term potentiation in fear conditioning pathways. *Proc Natl Acad Sci*. 103: 15218-23.

Komatsu K, Kikuchi K, Kojima H, Urano Y, Nagano T (2005) Selective Zinc Sensor Molecules with Various Affinities for Zn^{2+}, Revealing Dynamics and Regional Distribution of Synaptically Released Zn^{2+} in Hippocampal Slices. *J. Am. Chem. Soc*. 127: 10197-10204.

Komatsu K, Urano Y, Kojima H, Nagano T (2007) Development of an Iminocoumarin-Based Zinc Sensor Suitable for Ratiometric Fluorescence Imaging of Neuronal Zinc. *J. Am. Chem. Soc*. 129: 13447-13454.

Le Guével X, Hötzer B, Jung G, Hollemeyer K, Trouillet V, Schneider M (2011) Formation of Fluorescent Metal (Au, Ag) Nanoclusters Capped in Bovine Serum Albumin Followed by Fluorescence and Spectroscopy. *J. Phys. Chem. C*. 115: 10955-10963.

Le Guével X, Trouillet V, Spies C, Li K, Laaksonen T, Auerbach D, Jung G, Schneider M (2012) High photostability and enhanced fluorescence of gold nanoclusters by silver doping. *Nanoscale.* 4: 7624.

Lee B, Choi B, Hong D, Kim J, Lee S, Kho A, Kim H, Choi H, Suh S (2017) The cancer chemotherapeutic agent paclitaxel (Taxol) reduces hippocampal neurogenesis via down-regulation of vesicular zinc. *Sci. Rep.* 7: 11667.

Lee E, Lee H, Huang T, Chung C, Shin W, Kim K, Koh J, Hsueh Y, Kim E (2015) Trans-synaptic zinc mobilization improves social interaction in two mouse models of autism through NMDAR activation. *Nat. Commun*. 6: 7168.

Lei Y, Tang L, Xie Y, Xianyu Y, Zhang L, Wang P, Hamada Y, Jiang K, Zheng W, Jiang X (2017) Gold nanoclusters-assisted delivery of NGF siRNA for effective treatment of pancreatic cancer. *Nat. Commun*. 8: 15130.

Lengyel I, Fieuw-Makaroff S, Hall A, Sim A, Rostas J, Dunkley P (2000) Modulation of the phosphorylation and activity of calcium/calmodulin-dependent protein kinase II by zinc. *J Neurochem*. 75: 594-605.

Li B, Wang X, Shen X, Zhu W, Xu L, Zhou X (2016) Aggregation-induced emission from gold nanoclusters for use as a luminescence-enhanced nanosensor to detect trace amounts of silver ions. *J. Colloid Interface Sci*. 467: 90-96.

Li D, Hu C, Li H (2018) Survivin as a novel target protein for reducing the proliferation of cancer cells (Review). *Biomed Rep*. 8: 399-406.

Li D, Wang Z, Cui J, Wang X, Miao J, Zhao B (2017) A new fluorescent probe for colorimetric and ratiometric detection of sulfur dioxide derivatives in liver cancer cells. *Sci. Rep.* 7: 45294.

Li W, Liu Z, Fang B, Jin M, Tian Y (2020). Two-photon fluorescent Zn^{2+} probe for ratiometric imaging and biosensing of Zn^{2+} in living cells and larval zebrafish. *Biosens. Bioelectron*. 148: 111666.

Li Y, Yuan M, Khan A, Wang L, Zhang F (2019) Peptide-gold nanocluster synthesis and intracellular Hg^{2+} sensing. *Colloids Surf. A Physicochem. Eng. Asp*. 579: 123666.

Lian S, Hu D, Zeng C, Zhang P, Liu S, Cai L (2012) Highly luminescent near-infrared-emitting gold nanoclusters with further natural etching: photoluminescence and Hg^{2+} detection. *Nanoscale Res. Lett.* 7: 348.

Link S, Beeby A, FitzGerald S, El-Sayed M, Schaaff T, Whetten R (2002) Visible to Infrared Luminescence from a 28-Atom Gold Cluster. The *J. Phys. Chem. B.* 106: 3410-3415.

Liu X, Li C, Xu J, Lv J, Zhu M, Guo Y, Cui S, Liu H, Wang S, Li Y (2008) Surfactant-Free Synthesis and Functionalization of Highly Fluorescent Gold Quantum Dots. *J. Phys. Chem. C.* 112: 10778-10783.

Long J, Shen B, Luo T, Stewart L, McMurran T. Leung L (2009) Pilocarpine model of temporal lobe epilepsy shows enhanced response to general anesthetics. *Exp. Neurol.* 219: 308-318.

Luo Z, Yuan X, Yu Y, Zhang Q, Leong D, Lee J, Xie J (2012) From Aggregation-Induced Emission of Au(I)–Thiolate Complexes to Ultrabright Au(0)@Au(I)–Thiolate Core–Shell Nanoclusters. *J. Am. Chem. Soc*. 134: 16662-16670.

Luo Z, Zheng K, Xie J (2014) Engineering ultrasmall water-soluble gold and silver nanoclusters for biomedical applications. *Chem. Commun*. 50: 5143-5155.

Ly J, Grubb D, Lawen A (2003) The mitochondrial membrane potential ($\Delta\Psi$m) in apoptosis; an update. *Apoptosis*. 8: 115-28.

MacDonald R (2000) The Role of Zinc in Growth and Cell Proliferation. *J. Nutr*. 130: 1500S-1508S.

Malinska D, Kulawiak B, Kudin A, Kovacs R, Huchzermeyer C, Kann O, Szewczyk A, Kunz WS (2010) Complex III-dependent superoxide production of brain mitochondria contributes to seizure-related ROS formation. *Biochim Biophys Acta*. 1797:1163-70.

Mancini M, Kairdolf B, Smith A, Nie S (2008) Oxidative Quenching and Degradation of Polymer-Encapsulated Quantum Dots: New Insights into the Long-Term Fate and Toxicity of Nanocrystals *in vivo*. *J. Am. Chem. Soc*. 130: 10836-10837.

Maret W (2009) Molecular aspects of human cellular zinc homeostasis: redox control of zinc potentials and zinc signals. *BioMetals.* 22: 149-157.

Maruyama S, Kikuchi K, Hirano T, Urano Y, Nagano T (2002) A Novel, Cell-Permeable, Fluorescent Probe for Ratiometric Imaging of Zinc Ion. *J. Am. Chem. Soc*. 124: 10650-10651.

Matés J, Segura J, Alonso F, Márquez J (2008) Intracellular redox status and oxidative stress: implications for cell proliferation, apoptosis, and carcinogenesis. *Arch. Toxicol*. 82: 273-299.

McMullan J, Sasson C, Pancioli A, Silbergleit R (2010) Midazolam Versus Diazepam for the Treatment of Status Epilepticus in Children and Young Adults: A Meta-analysis. *Acad. Emerg. Med.* 17: 575-582.

McRae R, Bagchi P, Sumalekshmy S, Fahrni C (2009) In Situ Imaging of Metals in Cells and Tissues. *Chem. Rev*. 109: 4780-4827.

Medarova Z, Pham W, Farrar C, Petkova V, Moore A (2007). *In vivo* imaging of siRNA delivery and silencing in tumors. Nat. Med. 13: 372-377.

Murakami M, Hirano T (2008) Intracellular zinc homeostasis and zinc signaling. *Cancer Sci.* 99: 1515-1522.

Nair L, Nazeer S, Jayasree R, Ajayaghosh A (2015) Fluorescence Imaging Assisted Photodynamic Therapy Using Photosensitizer-Linked Gold Quantum Clusters. *ACS Nano.* 9: 5825-5832.

Nakashima A, Dyck R (2009) Zinc and cortical plasticity. *Brain Res. Rev.* 59: 347-373.

Nguyen P, Cong V, Baek C, Min J (2017) Fabrication of peptide stabilized fluorescent gold nanocluster/graphene oxide nanocomplex and its application in turn-on detection of metalloproteinase-9. *Biosens. Bioelectron*. 89: 666-672.

Nolan E, Lippard S (2009) Small-Molecule Fluorescent Sensors for Investigating Zinc Metalloneurochemistry. *Acc. Chem. Res*. 42: 193-203.

Nydegger I, Rumschik S, Zhao J, Kay A (2012) Evidence for an Extracellular Zinc-Veneer in Rodent Brains from Experiments with Zn-Ionophores and ZnT3 Knockouts. *ACS Chem. Neurosci.* 3: 761-766.

Okarvi S, Aljammaz I (2018) Preparation and *In Vitro* and *In Vivo* Characterization of the Tumor-specific Antigen-derived Peptide as a Potential

Candidate for Targeting Human Epidermal Growth Factor Receptor 2-positive Breast Carcinomas. *Anticancer Res*. 38: 2823-2830.

P Sun, W Huang, L Kang, M Jin, B Fan, H Jin, Q Wang, Z Gao (2017) siRNA-loaded poly(histidine-arginine)$_6$-modified chitosan nanoparticle with enhanced cell-penetrating and endosomal escape capacities for suppressing breast tumor metastasis. *Int. J. Nanomedicine* 12: 3221–3234.

Pal N, Kryschi C (2015) A facile UV-light mediated synthesis of l-histidine stabilized silver nanocluster for efficient photodegradation of methylene blue. *J Mol Catal A Chem*. 404: 27-35.

Paoletti P, Vergnano A, Barbour B, Casado M (2009) Zinc at glutamatergic synapses. *J Neurosci.* 158: 126-136.

Patel S, Cozzuol M, Hales J, Richards C, Sartin M, Hsiang J, Vosch T, Perry J, Dickson R (2009) Electron Transfer-Induced Blinking in Ag Nanodot Fluorescence. *J. Phys. Chem. C*. 113: 20264-20270.

Philips D, Sreejith S, He T, Menon N, Anees P, Mathew J, Sajikumar S, Kang Y, Stuparu M, Sun H, Zhao Y, Ajayaghosh A (2016) A Three-Photon Active Organic Fluorophore for Deep Tissue Ratiometric Imaging of Intracellular Divalent Zinc. *Chem. Asian J*. 11: 1523-1527.

Poderys V, Jarockyte G, Bagdonas S, Karabanovas V, Rotomskis R (2020) Protein-stabilized gold nanoclusters for PDT: ROS and singlet oxygen generation. *J. Photochem. Photobiol. B, Biol*. 204: 111802.

Prakash A, Bharti K, Majeed A (2015) Zinc: indications in brain disorders. *Fundam Clin Pharmacol.* 29: 131-149.

Pyo K, Thanthirige V, Kwak K, Pandurangan P, Ramakrishna G, Lee D (2015) Ultrabright Luminescence from Gold Nanoclusters: Rigidifying the Au(I)–Thiolate Shell. *J. Am. Chem. Soc*. 137: 8244-8250.

Qian J, Xu K, Yoo, J, Chen T, Andrews G, Noebels J (2011) Knockout of Zn Transporters Zip-1 and Zip-3 Attenuates Seizure-Induced CA1 Neurodegeneration. *J. Neurosci.* 31: 97-104.

Qu X, Li Y, Li L, Wang Y, Liang J, Liang J (2015) Fluorescent Gold Nanoclusters: Synthesis and Recent Biological Application. *J. Nanomater*. 2015: 1-23.

Ram S, Kim D, Ober R, Ward E (2014) The level of HER2 expression is a predictor of antibody-HER2 trafficking behavior in cancer cells. *mAbs*. 6: 1211-1219.

Reddy S, Reddy D (2015) Midazolam as an anticonvulsant antidote for organophosphate intoxication-A pharmacotherapeutic appraisal. *Epilepsia*. 56: 813-821.

Rink L (2000) Zinc and the immune system. *Proc. Nutr. Soc.* 59: 541-552.

Roohani N, Hurrell R, Kelishadi R, Schulin R (2013) Zinc and its importance for human health: An integrative review. *J Res Med Sci.*18: 144-157.

Rumschik S, Nydegger I, Zhao J, and Kay A (2009) The interplay between inorganic phosphate and amino acids determines zinc solubility in brain slices. *J Neurochem.* 108:1300-1308.

Salzano G, Riehle R, Navarro G, Perche F, De Rosa G, Torchilin V (2014) Polymeric micelles containing reversibly phospholipid-modified anti-survivin siRNA: a promising strategy to overcome drug resistance in cancer. *Cancer Lett.*343: 224–231.

Santhakumar H, Nair R, Philips D, Shenoy S, Thekkuveettil A, Ajayaghosh A, Jayasree R (2018) Real time imaging and dynamics of hippocampal Zn^{2+} under epileptic condition using a ratiometric fluorescent probe. *Sci Rep.* 8: 9069.

Santiago González B, Rodríguez M, Blanco C, Rivas J, López-Quintela M, Martinho J (2010) One Step Synthesis of the Smallest Photoluminescent and Paramagnetic PVP-Protected Gold Atomic Clusters. *Nano Lett*. 10: 4217-4221.

Sensi S, Paoletti P, Bush A, Sekler I (2009) Zinc in the physiology and pathology of the CNS. *Nat. Rev. Neurosci*. 10: 780-791.

Shibu E, Radha B, Verma P, Bhyrappa P, Kulkarni G, Pal S, Pradeep T (2009) Functionalized Au22 Clusters: Synthesis, Characterization, and Patterning. *ACS Appl. Mater. Interfaces.* 1: 2199-2210.

Shim M, Yoon H, Lee S, Jo M, Park J, Kim J, Jeong S, Kwon I, Kim K (2017) Caspase-3/-7-Specific Metabolic Precursor for Bioorthogonal Tracking of Tumor Apoptosis. *Sci. Rep.* 7(1).

Singh A, Trivedi P, Jain N (2018) Advances in siRNA delivery in cancer therapy. *Artif Cells Nanomed Biotechnol.* 46: 274-283.

Smart T, Hosie A, Miller P (2004) Zn^{2+} Ions: Modulators of Excitatory and Inhibitory Synaptic Activity. *The Neuroscientist.* 10: 432-442.

Song W, Liang R, Wang Y, Zhang L, Qiu J (2015) Green synthesis of peptide-templated gold nanoclusters as novel fluorescence probes for detecting protein kinase activity. *ChemComm*. 51: 10006-10009.

Sreejith S, Divya K, Jayamurthy P, Mathew J, Anupama V, Philips D, Anees P, Ajayaghosh A (2012) Heteroaromatic donors in donor–acceptor–donor based fluorophores facilitate zinc ion sensing and cell imaging. *Photochem. Photobiol. Sci.* 11: 1715-1723.

Sreejith S, Divya K, Manojkumar T, Ajayaghosh A (2010) Multiple Analyte Response and Molecular Logic Operations by Excited-State Charge-Transfer Modulation in a Bipyridine Integrated Fluorophore. *Chem. Asian J.* 6: 430-437.

Sreenath K, Allen J, Davidson M, Zhu L (2011) A FRET-based indicator for imaging mitochondrial zinc ions. *Chem Commun.* 47: 11730.

Su S, Wang H, Liu X, Wu Y, Nie G (2013) iRGD-coupled responsive fluorescent nanogel for targeted drug delivery. *Biomaterials*, 34: 3523-3533.

Suh S (2009) Detection of zinc translocation into apical dendrite of CA1 pyramidal neuron after electrical stimulation. *J. Neurosci. Methods*. 177: 1-13.

Szewczyk B (2013) Zinc homeostasis and neurodegenerative disorders. *Front. Aging Neurosci.* 5: 33.

Taetz S, Bochot A, Surace C, Arpicco S, Renoir J, Schaefer U, Marsaud V, Kerdine-Roemer S, Lehr C, Fattal E (2009) Hyaluronic Acid-Modified DOTAP/DOPE Liposomes for the Targeted Delivery of Anti-Telomerase siRNA to CD44-Expressing Lung Cancer Cells. *Oligonucleotides,* 19: 103-116.

Takeda A (2000) Movement of zinc and its functional significance in the brain. *Brain Res. Rev.* 34: 137-148.

Tamano H, Nishio R, Shakushi Y, Sasaki M, Koike Y, Osawa M, Takeda A (2017) *In vitro* and *in vivo* physiology of low nanomolar concentrations of Zn^{2+} in artificial cerebrospinal fluid. *Sci. Rep.* 7: 42897.

Tóth K (2011) Zinc in Neurotransmission. *Annu. Rev. Nutr.* 31: 139-153.

Trisciuoglio D, Tupone M, Desideri M, Di Martile M, Gabellini C, Buglioni S, Pallocca M, Alessandrini G, D’Aguanno S, Del Bufalo D (2017) BCL-XL overexpression promotes tumor progression-associated properties. *Cell Death Dis*. 8: 3216.

Uchida H, Tanaka T, Sasaki K, Kato K, Dehari H, Ito Y, Kobune M, Miyagishi M, Taira K, Tahara H, Hamada H (2004) Adenovirus-Mediated Transfer of siRNA against Survivin Induced Apoptosis and Attenuated Tumor Cell Growth in Vitro and in Vivo. *Mol. Ther*. 10: 162-171.

Walsh J, Cullen S, Sheridan C, Luthi A, Gerner C, Martin S (2008) Executioner caspase-3 and caspase-7 are functionally distinct proteases. *PNAS*,105: 12815-12819.

Wang S, Meng X, Das A, Li T, Song Y, Cao T, Zhu X, Zhu M, Jin R (2014) A 200-fold Quantum Yield Boost in the Photoluminescence of Silver-Doped Ag_xAu_{25-x}Nanoclusters: The 13 th Silver Atom Matters. *Angew. Chem. Int*. 126: 2408-2412.

Wolfbeis O (2015) An overview of nanoparticles commonly used in fluorescent bioimaging. *Chem. Soc. Rev.* 44: 4743-4768.

Wong R (2011) Apoptosis in cancer: from pathogenesis to treatment. *J. Exp. Clin. Cancer Res*. 30: 87.

Woodroofe C, Won A, Lippard S (2005) Esterase-Activated Two-Fluorophore System for Ratiometric Sensing of Biological Zinc(II). *Inorg. Chem.* 44: 3112-3120.

Xie J, Zheng Y, Ying J (2009) Protein-Directed Synthesis of Highly Fluorescent Gold Nanoclusters. ***J**. Am. Chem. Soc*. 131: 888-889.

Xu C, Wang J (2015) Delivery systems for siRNA drug development in cancer therapy. *Asian J. Pharm. Sci*. 10: 1-12.

Xue L, Liu C, Jiang H (2009) A ratiometric fluorescent sensor with a large Stokes shift for imaging zinc ions in living cells. *Chem. Commun*. 9: 1061-1063.

Yahia-Ammar A, Sierra D, Mérola F, Hildebrandt N, Le Guével X (2016) Self-Assembled Gold Nanoclusters for Bright Fluorescence Imaging and Enhanced Drug Delivery. *ACS Nano*, 10: 2591-2599.

Yang H, Liu R, Xu Y, Qian L, Dai Z (2021) Photosensitizer Nanoparticles Boost Photodynamic Therapy for Pancreatic Cancer Treatment. *Nanomicro Lett.* 13: 35.

Yang T, Peng B, Shan B, Zong Y, Jiang J, Wu P, Zhang K (2020) Origin of the Photoluminescence of Metal Nanoclusters: From Metal-Centered Emission to Ligand-Centered Emission. *Nanomaterials.* 10: 261.

Yang X, Shi M, Zhou R, Chen X, Chen H (2011) Blending of $HAuCl_4$ and histidine in aqueous solution: a simple approach to the Au10 cluster. *Nanoscale*, 3: 2596 -2601.

Yezhelyev M, Qi L, O'Regan R, Nie S, Gao X (2008) Proton-Sponge Coated Quantum Dots for siRNA Delivery and Intracellular Imaging. *J. Am. Chem. Soc*. 130: 9006-9012.

Zalewski P, Forbes I, Betts W (1993) Correlation of apoptosis with change in intracellular labile Zn(II) using zinquin [(2-methyl-8-p-toluenesulphonamido-6-quinolyloxy)acetic acid], a new specific fluorescent probe for Zn(II). *Biochem. J*. 296: 403-408.

Zastrow M, Radford R, Chyan W, Anderson C, Zhang D, Loas A, Tzounopoulos T, Lippard S (2015) Reaction-Based Probes for Imaging Mobile Zinc in Live Cells and Tissues. *ACS Sens*. 1: 32-39.

Zhai J, Wang Y, Xu C, Zheng L, Wang M, Feng W, Gao L, Zhao L, Liu R, Gao F, Zhao Y, Chai Z, Gao X (2015) Facile Approach To Observe and Quantify the $\alpha_{IIb}\beta_3$ Integrin on a Single-Cell. Anal. Chem. 87: 2546-2549.

Zhang C, Zhou Z, Zhi X, Ma Y, Wang K, Wang Y, Zhang Y, Fu H, Jin W, Pan F, Cui D (2015) Insights into the Distinguishing Stress-induced Cytotoxicity of Chiral Gold Nanoclusters and the Relationship with GSTP1. *Theranostics.* 5: 134-149.

Zhang E, Xiang S, Fu A (2016) Recent Progresses of Fluorescent Gold Nanoclusters in Biomedical Applications. *J. Nanosci. Nanotechnol.* 16: 6597-6610.

Zhang L, Li S, Hong M, Xu Y, Wang S, Liu Y, Qian Y, Zhao J (2014) A colorimetric and ratiometric fluorescent probe for the imaging of endogenous hydrogen sulphide in living cells and sulphide determination in mouse hippocampus. *Org. Biomol. Chem*. 12: 5115.

Zhang Y, Li S, Liu H, Long W, Zhang X (2020) Enzyme-Like Properties of Gold Clusters for Biomedical Application. *Front. Chem*. 8: 219.

Zhang Y, Zhang X, Yuan Q, Niu W, Zhang C, Li J, He Z, Tang Y, Ren X, Zhang Z, Cai P, Gao L, Gao X (2018) Peptide-Templated Gold Clusters as Enzyme-Like Catalyst Boost Intracellular Oxidative Pressure and Induce Tumor-Specific Cell Apoptosis. *Nanomaterials.* 8: 1040.

Zhang Z, Yang X, Zhang Y, Zeng B, Wang S, Zhu T, Roden RB, Chen Y, Yang R (2006) Delivery of telomerase reverse transcriptase small interfering RNA in complex with positively charged single-walled carbon nanotubes suppresses tumor growth. *Clin Cancer Res.* 12: 4933-9.

Zheng J, Petty J, Dickson R (2003) High Quantum Yield Blue Emission from Water-Soluble Au_8 Nanodots. *ChemInform*, 34: 7780–7781.

Zhong X, Zhang D, Xiong M, Zhang L (2016) Noncoding RNA for Cancer Gene Therapy. *Recent Results Cancer Res*. 209: 51-60.

LIST OF PUBLICATIONS

1. **Hema Santhakumar,** Resmi. V. Nair, Divya Susan Philips, Sachin J. Shenoy, Anoopkumar Thekkuveettil, Ayyappanpillai Ajayaghosh and Ramapurath. S. Jayasree "Real Time Imaging and Dynamics of Hippocampal Zn^{2+} under Epileptic Condition Using a Ratiometric Fluorescent Probe", ***Scientific Reports*** **8**, 9069, (2018).

2. Resmi. V. Nair, **Hema Santhakumar** and Ramapurath. S. Jayasree "Gold nanorods decorated with a cancer drug for multimodal imaging and therapy", ***Faraday discussions*** **207**, 423-435, (2018) **(Equal Contribution).**

3. Shania M Soman, Charuvil Radhakrishna Pillai Rekha, **Hema Santhakumar**, Uttamchand Narendrakumar, Ramapurath S Jayasree "Semi-Supervised Nonnegative Matrix Factorization of Wide-Field Fluorescence Microscopic Images for Tissue Diagnosis", **Microscopy and Microanalysis 26**, 419-428, (2020).

4. Resmi V Nair, Lakshmi V Nair, Divya Maldepalli Govindachar, **Hema Santhakumar**, Shaiju S Nazeer, Charuvil Radhakrishnapillai Rekha, Sachin J Shenoy, Ganga Periyasamy, Ramapurath S Jayasree "Luminescent Gold Nanorods To Enhance the Near-Infrared Emission of a Photosensitizer for Targeted Cancer Imaging and Dual Therapy: Experimental and Theoretical Approach", ***Chemistry – A European Journal 26,*** 2826-2836, (2020).

5. Ariya Saraswathy, Shaiju S. Nazeer, Nirmala Nimi, **Hema Santhakumar**, Parvathy Radhakrishnapillai Suma, Kunnumpurathu Jibin, Marina Victor, Francis Boniface Fernandez, Sabareeswaran Arumugam, Sachin J. Shenoy, PR Varma, Ramapurath S. Jayasree "Asialoglycoprotein receptor targeted optical and magnetic resonance imaging and therapy of liver fibrosis using pullulan stabilized multi-functional iron oxide nanoprobe" ***Scientific Reports*** **11**, 1-11, (2021).

6. Kunnumpurathu Jibin, Marina Victor, Giridharan Saranya, **Hema Santhakumar**, Vishnupriya Murali, Kaustabh K Maiti, Ramapurath S Jayasree "Nanohybrids of Magnetically Intercalated Optical Metamaterials for Magnetic Resonance/Raman Imaging and In Situ Chemodynamic/Photothermal Therapy" ***ACS Applied Bio Materials*** **4**, 5742-5752, (2021).

7. Nisha Narayanan, **Hema Santhakumar**, Varsha Karunakaran, Manu M. Joseph, Kunnumpurathu Jibin, Giridharan Saranya, Palasseri T. Sujai, Ramapurath S. Jayasree, Kaustabh K. Maiti "Highly Synchronized Methylene Blue-Loaded Cucurbituril [8] Coupled Gold Nanorod: A Targeted Nanotheranostic Probe for

Enhanced Phototherapy in Combination with SERS and Fluorescence Dual Imaging Modalities on Breast Tumor Cells”, **(Communicated).**

8. Rekha Koshy, Siji Mary, **Hema Santhakumar**, Yogesh Dalvi, Tressia Paulose, Jayasree Ramapurath, Laly Pothen “Sustainable vermicompost for the simultaneous synthesis of carbon quantum dots for cancer cell imaging and hydrochar for dye adsorption” (C**ommunicated**).

CONFERENCES

1. Hema Santhakumar, Jayasree R S (2019) Synthesis and characterization of a highly fluorescent tripeptide stabilized gold nanocluster for bioimaging applications, National Conference on Materials Science and Technology-NCMST-2019, IIST, Trivandrum.

2. Hema Santhakumar, Jayasree R S (2018) Detection of hippocampal zinc ions and its dynamics under epileptic condition using a fluorescent ratiometric probe, Satellite meeting to the International Congress of Cell Biology 2018, Estuary Island Resort, Poovar.

3. Hema Santhakumar, Jayasree R S (2018) Detection of zinc ions and its dynamics in epileptic condition using a ratiometric fluorescent probe, Kerala Science Congress-2018, Govt. Brennen college, Thalassery.

4. Hema Santhakumar, Jayasree R S (2017) Detecting the dynamics of zinc ions in hippocampus under epileptic condition using a fluorescent ratiometric probe, Science Fete’2017, SCTIMST, Trivandrum - Best presentation award.

5. Hema Santhakumar, Jayasree R S (2017) Bipyridine based bispyrrole ratiometric probe for real time imaging of hippocampal zinc ions and its dynamics under epileptic condition, Nanobioteck-2017, KDTC Samudra, Kovalam.

6. Hema Santhakumar, Jayasree R S (2016) Detection of zinc ions in hippocampus using a fluorescent ratiometric probe, International conference on Advanced materials – SCICON’16, Amrita Vishwa Vidyapeetham, Coimbatore.